ILLUMINATING MARTIAN ATMOSPHERIC MYSTERIES: VARIABILITY IN WATER ICE, DUST AND METHANE

ALEX C. INNANEN

A DISSERTATION SUBMITTED TO THE FACULTY OF GRADUATE STUDIES IN PARTIAL FULFILLMENT OF THE REQUIREMENTS FOR THE DEGREE OF

DOCTOR OF PHILOSOPHY

GRADUATE PROGRAM IN EARTH AND SPACE SCIENCE
YORK UNIVERSITY
TORONTO, ONTARIO

JUNE 2026

© Alex C. Innanen, 2026

Abstract

This dissertation explores variability in three constituents of the martian atmosphere with the aims of better understanding atmospheric processes and informing future exploration. I present the results of five projects, four of which look at light interactions with atmospheric water-ice and dust and the last of which deals with methane variability in an analogue environment and the implications for martian exploration.

The Mars Science Laboratory has an extensive record of cloud observations from Gale Crater, including the yearly Aphelion Cloud Belt (ACB). I present a five-year dataset of ACB cloud movies from which I derive a single scattering phase function, which I use to comment upon ice crystal habit and variability. The ACB clouds at Gale Crater are shown to have little interannual, seasonal or diurnal variability and are likely composed of irregularly shaped water-ice crystals.

I compare MSL ACB cloud movies with images taken from the CaSSIS instrument on the Trace Gas Orbiter to explore its limits of detection. I find CaSSIS cannot see clouds with opacities of ~ 0.2 and lower, and it is not clear if these clouds impact the reflectance CaSSIS observes.

I use an eight Mars year dataset of temperature retrievals from the Mars Climate Sounder (MCS) to determine the minimum altitude MCS can see before the atmosphere becomes too opaque. There is a strong preference for cut-off altitudes above 20 km in the cloudy season, while in the dusty season there is more of a spread in altitudes.

I examine the utility of imaging backscatter from low-powered lasers to determine the properties of near-surface aerosols. I find that we can distinguish particle size and track layers of fog above the surface with this backscatter and suggest improvements for an instrument of this type.

Finally, I explore methane plume variability in a martian analogue environment in the Canadian arctic. High frequency measurements can help localise methane sources, as variability in the methane signal increases with proximity to the source of the plume. Furthermore, I look at the frequency of methane plumes of different magnitudes. These findings will both inform future sampling plans on Mars.

Acknowledgements

There are so many people who have touched this dissertation in some way and without whom it would not be what it is. This is an attempt to remember a small subset of them.

My thanks to everyone who provided support for the fieldwork which was integral to Chapter 6.

The CaSSIS team were very supportive of my trying to see invisible clouds with their instrument. Thank you in particular to Livio Tornabene for his guidance.

Margaret Landis went above and beyond her role as an internship supervisor in my masters when my four month remote project spiralled into a multi-year investigation. I'm so grateful to have had the opportunity to work with her then, and to visit in 2023, out of which Chapter 4 was born. Thank you also to the others in Paul Hayne's group for making me feel so welcome and for taking me hiking in the mountains.

Working with the MSL team has been one of the highlights of my time at PVL. The connection and support I've had from members of the science team as a whole and the ENV theme group in particular have made these last six plus years on the mission so special. I would especially like to thank Scott Guzewich for his continuing encouragement and guidance.

In my winter term of 2017 I asked John Moores if he had any summer undergraduate positions in his lab. I then procrastinated on telling him that yes, I did want to work at PVL until I think April. Despite this, and the many, many times since that I've dragged my feet and complained about having to do stats and cried in his office he has always been an incredibly compassionate, encouraging and supportive supervisor, without whom I do not think I would have continued on to or completed my PhD.

The support and friendship of the past and present members of PVL have gone a great way to keeping me sane throughout my degrees – I have learned so much from and appreciate you all. A particular thank you to denizens of CB 348: Charissa Campbell, who remained a great friend even after you went on to Goddard; Elisa Dong, my plant pal and tea friend; Grace Bischof, my subway companion (until I rudely moved to campus) and fellow bookworm; and Diana Hayes, my desk neighbour, my favourite distraction from work, my partner in cloud crime – thank you for holding my hand whenever vectors got scary, and all the other times too.

Finally, my family and my closest friends have had to weather a lot these last several years. Thank you for all the calls, for all the hugs, for marathon complaint sessions, for providing distractions, for bringing me food or tea or anything you thought I might like, for being with me and taking care of me when I was sick or had two major-ish surgeries six months apart. Rose, Tanis, Lizzie and Diana – I love you all so much. Thank you for loving me too. Mamma, Daddy and Kk – I love you to Mars and back. Thank you for coming on the journey with me.

Contents

Abstract ii

Acknowledgements iii

Contents iv

List of Tables vii

List of Figures viii

1 Introduction 1
- 1.1 An Overview of the Martian Atmosphere . . . 1
- 1.2 Martian Water-Ice Clouds . . . 3
  - 1.2.1 The Aphelion Cloud Belt . . . 5
- 1.3 Dust in the Martian Atmosphere . . . 8
- 1.4 Light Scattering in the Martian Atmosphere . . . 11
- 1.5 Atmospheric Observations by the Mars Science Laboratory . . . 14
- 1.6 Methane in the Martian Atmosphere . . . 17
- 1.7 Motivation and Structure of the Dissertation . . . 20

2 The Water-ice Cloud Phase Function at Gale Crater 22
- 2.1 Motivation & Author Contribution . . . 22
- 2.2 Methods . . . 23
  - 2.2.1 The Navcam Phase Function Sky Survey . . . 23
  - 2.2.2 Deriving the Phase Function . . . 24
  - 2.2.3 Constraining Ice Crystal Habit . . . 27
- 2.3 Results . . . 29
  - 2.3.1 Temporal Distribution . . . 29
  - 2.3.2 Interannual Comparison . . . 30
  - 2.3.3 Seasonal Comparison . . . 31
  - 2.3.4 Diurnal Comparison . . . 33
  - 2.3.5 The Henyey-Greenstein Function . . . 33
- 2.4 Discussion . . . 35
  - 2.4.1 Variability in the Mean Phase Functions . . . 35
  - 2.4.2 Comments Upon Ice Crystal Habit . . . 36

3 Can CaSSIS see Suboptical Clouds? 40
- 3.1 Motivation & Author Contribution . . . 40
- 3.2 Dataset . . . 41
  - 3.2.1 CaSSIS Observations . . . 41
  - 3.2.2 MSL Cloud Movies . . . 42
  - 3.2.3 Coordinated Imaging Campaign with MSL . . . 43
- 3.3 Methods . . . 44
  - 3.3.1 Determining Cloud Opacity from MSL Movies . . . 44
  - 3.3.2 Examining Channel Statistics . . . 45
- 3.4 Results & Discussion . . . 46
  - 3.4.1 Coordinated CaSSIS-MSL ACB Images . . . 46
  - 3.4.2 Behaviour of a Cloudy Scene . . . 49
  - 3.4.3 Comparing Clear and Cloudy Scenes . . . 51
  - 3.4.4 Limitations of the Dataset . . . 53

4 The Impact of Atmospheric Aerosols on MCS Retrieval Altitudes **54**
4.1 Motivation & Author Contribution . . . 54
4.2 Methods . . . 55
4.3 Results and Discussion . . . 56
4.3.1 Minimum Retrieval Altitudes . . . 56
4.3.2 Tracking the Decay of Global Dust Storms . . . 58

5 Determining Near-Surface Aerosol Properties using Low-Powered Lasers **61**
5.1 Motivation & Author Contribution . . . 61
5.2 Methods . . . 62
5.2.1 The Camera and Lasers . . . 62
5.2.2 Camera Calibration and Image Correction . . . 63
5.2.3 Mie Scattering Models . . . 64
5.2.4 Laboratory Testing . . . 65
5.2.5 Field Testing . . . 67
5.3 Results . . . 71
5.3.1 Simulated Particle Scattering Behaviour . . . 71
5.3.2 Laboratory Experiments . . . 74
5.3.3 Field Experiments . . . 76
5.4 Discussion . . . 80
5.4.1 Comparison of Laboratory Results with Modelled Microspheres . . . 80
5.4.2 Effects of Laser Wavelength and Particle Size on Observed Scattering Properties . . . 82
5.4.3 Impact of Assumed Fog Droplet Size . . . 83
5.4.4 Limitations of the Experiments . . . 84
5.4.5 Implications for Future Instruments . . . 87

6 Variability of Methane Plumes and Implications for Martian Exploration **91**
6.1 Motivation & Author Contribution . . . 91
6.2 Methods . . . 92
6.2.1 The OA-ICOS Instrument . . . 92
6.2.2 Study Location . . . 93
6.2.3 Sampling Procedure . . . 95
6.3 Results . . . 97
6.3.1 Background Methane Measurements . . . 97
6.3.2 Gypsum Hill Springs . . . 97
6.3.3 Wolf Spring . . . 102
6.4 Discussion . . . 105
6.4.1 Relative Frequency of Methane Spikes . . . 105
6.4.2 Variation in Methane Signal with Respect to Source . . . 106
6.4.3 Implications for Future Martian Missions . . . 108
6.4.4 Limitations of the Experiment . . . 109

7 Conclusions **111**
7.1 Summary of the Dissertation . . . 111
7.2 The Water-ice Cloud Phase Function at Gale Crater . . . 111
7.3 Can CaSSIS see Suboptical Clouds? . . . 112
7.4 The Impact of Atmospheric Aerosols on MCS Retrieval Altitudes . . . 113
7.5 Determining Near-Surface Aerosol Properties using Low-Powered Lasers . . . 113
7.6 Variability of Methane Plumes and Implications for Martian Exploration . . . 114

8 Future Work **116**
8.1 The Water-ice Cloud Phase Function at Gale Crater 116
8.2 Can CaSSIS see Suboptical Clouds? 116
8.3 The Impact of Atmospheric Aerosols on MCS Retrieval Altitudes 117
8.4 Determining Near-Surface Aerosol Properties using Low-Powered Lasers 118
8.5 Variability of Methane Plumes and Implications for Martian Exploration 118

References **120**

List of Acronyms & Abbreviations **132**

Appendices **133**

A CaSSIS Images Acquired over Gale Crater **133**

B Analysis of CaSSIS ACB Cloud Images **135**

C Methane Concentration at Wolf Spring in 2024 **146**

List of Tables

2.1 b and c values for fit HG functions. 34

3.1 CaSSIS observations at Gale Crater with likely clouds 42
3.2 Coordinated CaSSIS and MSL cloud observations 44
3.3 Qualities and opacities of MSL cloud movies 46
3.4 Coefficients of variation for ACB CaSSIS images 49
3.5 Coefficients of variation of a cloudy scene 50
3.6 Coefficients of variation between two CaSSIS images 53

5.1 Laser Characteristics 63
5.2 Calculated spectral radiance for each laser 63
5.3 Micropshere scattering efficiencies 73
5.4 Extinction coefficients in cm^{-1} for aquarium observations 75
5.5 Extinction coefficients in cm^{-1} for aquarium observations 81
5.6 Laser powers needed to overcome planetary sky brightness 90

6.1 Mean free paths of near-surface methane on Earth and Mars 95
6.2 Summary of measurements taken at Gypsum Hill traveling along the wind direction 98
6.3 Summary of measurements taken at Gypsum Hill traveling from the spring towards the Expedition River 99
6.4 Summary of measurements taken at Wolf Spring in 2022 102
6.5 Summary of measurements taken at Wolf Spring in 2024 104

A1 CaSSIS images acquired over Gale Crater 133

List of Figures

1.1 Insolation on Mars throughout its orbit . . . 2
1.2 Different cloud types seen on Mars . . . 4
1.3 MARCI water-ice optical depth retrievals . . . 6
1.4 EMIRS water-ice optical depths at six LTSTs . . . 7
1.5 Global dust cover of Mars . . . 8
1.6 Global dust optical depth over eight Mars years . . . 10
1.7 Scattering angle geometry . . . 12
1.8 Examples of scattering effects . . . 13
1.9 A diagram of MSL with instruments labelled . . . 14
1.10 Cloud observations by MSL . . . 15
1.11 A model of the Sample Analysis At Mars suite . . . 18
1.12 SAM-TLS enrichment measurements . . . 19

2.1 Projection of the PFSS pointings onto a dome . . . 23
2.2 An example of an unusable PFSS frame . . . 23
2.3 Three PFSS frames before and after mean frame subtraction . . . 26
2.4 Spectral radiance map of a PFSS frame . . . 27
2.5 Examples of different HG functions . . . 28
2.6 Navcam PFSS temporal distribution . . . 29
2.7 Unnormalised mean phase functions for MYs 34-38 . . . 30
2.8 Mean phase functions for MYs 34-38 . . . 31
2.9 Three seasonal mean curves for MYs 34-38 . . . 32
2.10 MY 34-38 mean phase functions for three seasonal bins . . . 32
2.11 Diurnal variability in each Mars year . . . 33
2.12 Fit HG functions for each Mars year . . . 34
2.13 b vs c values for MYs 34-35 . . . 34
2.14 Fit b and c values plotted over Figure 2 from Hapke (2012a) . . . 38
2.15 Comparison of fit HG parameters with those of martian dust and modelled water-ice crystals 39

3.1 A CaSSIS image of clouds . . . 40
3.2 Locations of CaSSIS observations around Gale Crater . . . 41
3.3 Locations of CaSSIS observations coordinated with MSL cloud movies . . . 43
3.4 Four frames of the sol 4682 SHM . . . 47
3.5 The MY38_035125_187_0 CaSSIS image . . . 47
3.6 BLU and NIR channels of MY38_035125_187_0 and their ratio . . . 48
3.7 Image statistics of MY38_035125_187_0 . . . 49
3.8 Two areas of cloud in and near a northern crater . . . 50
3.9 Mean reflectance and standard deviation of northern clouds . . . 51
3.10 CaSSIS images of the same area in Gale Crater . . . 51
3.11 Comparing image statistics between two CaSSIS images . . . 52

4.1 MCS area of interest around Gale Crater . . . 55
4.2 MCS Confetti Plot . . . 56
4.3 Frequencies of cut-off altitudes during cloudy and dusty seasons . . . 57
4.4 MCS water-ice retrievals plotted next to estimated MSL cloud altitudes . . . 58
4.5 Cut-off altitudes for MY 34 . . . 59
4.6 Cut-off altitudes for MY 28 . . . 60

5.1 Spectral response of the Basler camera . . . 62
5.2 Example of the Mie Simulator GUI . . . 64
5.3 The MAPLE aquarium setup . . . 65
5.4 Schematic of the aquarium setup . . . 66
5.5 Fisheye and undistorted aquarium photos . . . 67
5.6 Elevation and azimuth angles of the MAPLE camera . . . 69
5.7 Scattering angle along the laser beam . . . 70
5.8 Modelled phase functions of three sizes of microspheres . . . 71
5.9 The middle section of the three microsphere phase functions . . . 72
5.10 Scattering efficiencies of three microspheres . . . 72
5.11 Modelled phase function of fog . . . 73
5.12 Modelled scattering efficiency of fog . . . 74
5.13 Radiance-Distance curves for the red laser in 3-μm microspheres . . . 74
5.14 Extinction curves for each microsphere and laser wavelength . . . 75
5.15 Phase functions of the three sizes of microspheres at three wavelengths . . . 76

5.16 June 29 images before and after bias and dark correction . . . 77
5.17 Spectral radiance along each laser beam for measurements taken June 29 . . . 78
5.18 Phase function corrected spectral radiance for measurements taken June 29 . . . 79
5.19 Experimentally derived phase functions compared with the modelled curves . . . 80
5.20 Extinction curves for each laser wavelength in water alone . . . 81
5.21 Spectral radiances along the beam with three different fog droplet sizes . . . 83
5.22 Modelled and manually selected laser beams . . . 86
5.23 Three example laser beam geometries . . . 87
5.24 Portions of the laser beam captured by cameras with smaller FoVs . . . 88

6.1 A schematic of the ICOS instrument . . . 92
6.2 The ultraportable OA-ICOS instrument . . . 93
6.3 Gypsum Hill and Wolf Springs . . . 94
6.4 Location of background methane measurements . . . 95
6.5 Sampling plan at Wolf Spring in 2024 . . . 96
6.6 Measured methane concentration at MARS . . . 97
6.7 Wind Direction transect methane concentrations at Gypsum Hill . . . 100
6.8 Measured methane concentration downstream from the Gypsum Hill spring . . . 101
6.9 Measured methane concentration at Wolf Spring in 2022 . . . 103
6.10 Location of measurements taken in 2024 at Wolf Spring . . . 104
6.11 Power spectral density estimate for Wolf Spring . . . 105
6.12 Methane diffusing in the wind direction from Wolf Spring . . . 106
6.13 Average concentration and variation in methane with increasing distance from plume . . . 107

B1 BLU channel coefficient of variation versus cloud optical depth . . . 135
B2 CaSSIS image MY35_007380_357_0 . . . 136
B3 CaSSIS image MY37_024431_355_3 . . . 137
B4 CaSSIS image MY37_026416_186_3 . . . 138
B5 CaSSIS image MY38_033831_184_0 . . . 139
B6 CaSSIS image MY38_034055_185_0 . . . 140
B7 CaSSIS image MY38_034297_353_0 . . . 141
B8 CaSSIS image MY38_034409_354_0 . . . 142
B9 CaSSIS image MY38_034521_354_1 . . . 143
B10 CaSSIS image MY38_034521_354_2 . . . 144

B11 CaSSIS image MY38_034901_190_0 145

C1 Measured methane concentrations at Wolf Spring acquired in 2024 151

Chapter 1

Introduction

1.1 An Overview of the Martian Atmosphere

In March of 1666, Italian-French astronomer Giovanni Domenico Cassini made a series of telescopic observations of Mars from which he determined that the rotational period of the planet was only 40 minutes longer than our own (Cassini, 1666). Over a century later, German-British astronomer Frederick William Herschel inferred the existence of seasons like Earth's by noting the changing size of Mars' polar caps. In the same work, he suggested that Mars "has a considerable but moderate atmosphere, so that its inhabitants probably enjoy a situation in many respects similar to ours" (Herschel, 1784).

This view of Mars, as habitable and indeed inhabited with a moderately thick atmosphere and liquid surface water, persisted into the 20th Century (Kieffer et al., 1992). More powerful telescopes, new methods of detection and the advent of spacecraft exploration of Mars have since revealed the Mars we know today - a lifeless, dry planet with a thin atmosphere. This is not to say that the martin atmosphere and climate are not worth studying. Indeed, these systems are quite complex and dynamic, and each has attributes similar to their terrestrial analogues and others which are quite different.

The two major drivers of the martian climate are the planet's obliquity of 25.2° giving rise to seasons similar to those we experience on Earth and its high orbital eccentricity of 0.0934 which results in significant differences in insolation and temperature at different points in its orbit. Thus, as well as the four seasons we are accustomed to on Earth, Mars experiences an aphelion season during northern spring and summer characterised by increased cloud formation and a perihelion season during northern autumn and winter characterised by increased dust loading. These seasons are sometimes known simply as the 'cloudy' and 'dusty' seasons, respectively[1].

As is customary, we use the system for numbering Mars years (MY) first defined by Clancy et al. (2000) and enumerated by Piqueux et al. (2015) in which MY 1 began at UTC 00:00:00 on April 11, 1955. Seasons and the passage of time within a Mars year are represented by degrees of solar longitude (L_s) with $L_s = 0°$

[1]While the exact solar longitude bounds for these seasons vary in the literature, for the purposes of this work we define the cloudy season as $L_s = 0 - 150°$ and the dusty season as $L_s = 150 - 360°$.

being the start of northern spring (Figure 1.1). A martian day, known as a *sol*, is divided into local hours of 1/24th of the sol, with 60 equal minutes per hour and 60 equal seconds per minute. Because of these equal divisions of the sol, martian hours, minutes and seconds differ from those used in terrestrial timekeeping.

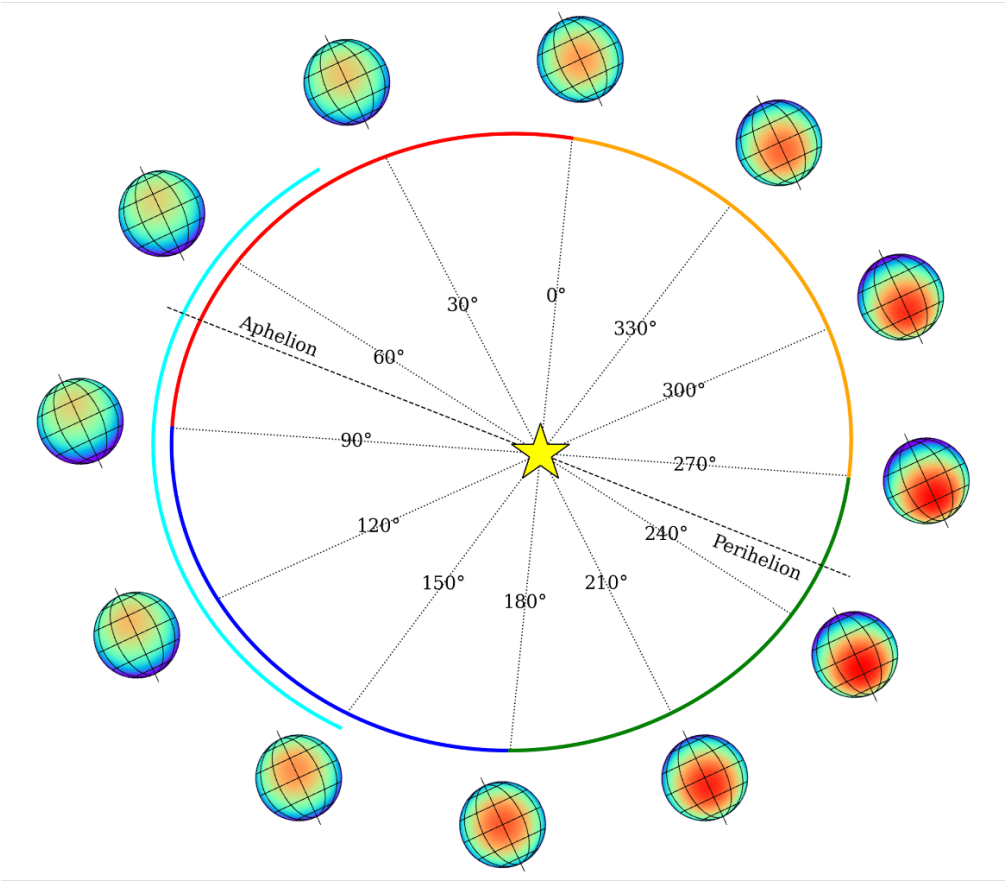


Figure 1.1: Mars' orbit with solar longitude indicated in 30° intervals. The high eccentricity can be seen, with aphelion and perihelion also indicated. Seasons are represented by different colours: northern spring/southern summer, red; northern summer/southern winter, blue; northern autumn/southern spring, green; northern winter/southern summer, yellow. Colours on the globes represent insolation at the surface. The cyan region covers Aphelion Cloud Belt Season (Section 1.2). Illustration by Hayes (2025).

At an abundance of $\sim$ 95%, carbon dioxide (CO_2) is the major constituent of Mars' atmosphere with molecular nitrogen (N_2, $\sim$ 2.8%), argon (Ar, $\sim$ 2.1%), molecular oxygen (O_2, $\sim$ 0.17%) and carbon monoxide (CO, $\sim$ 0.07%) as the next most abundant species (Franz et al., 2017). Also present are a number of trace gases including water vapour (H_2O) and methane (CH_4), both of which vary in abundance throughout the Mars year (see Sections 1.2 and 1.6 for respective discussions of these trace gases).

Mars' surface pressure is quite low, with an average pressure of 610 Pa (compared to Earth's of $\sim$ 101 kPa), though this can vary significantly seasonally and with location. The CO_2 which makes up the majority of Mars' atmosphere is in equilibrium with the polar caps, where CO_2 condenses during the cold polar winters and is released back into the atmosphere as temperatures warm in the spring and summer, impacting

atmospheric surface pressures (Tillman et al., 1993). Additionally, the large differences in elevation across the planet — notably, the fact that the northern hemisphere is on average a few kilometres lower in elevation than the southern — mean that surface pressure is typically higher in the northern hemisphere of the planet than in the southern (Hourdin et al., 1993).

While these two factors broadly describe the variations in surface pressure across the planet and through its year, the martian atmosphere is much more dynamic than can easily be captured in a few sentences, especially in the region closest to the surface. This region of the atmosphere is known as the Planetary Boundary Layer (*PBL*) — the portion of the atmosphere directly impacted by interactions with the surface. Extending upwards as high as 10 km above the surface during the day (Hinson et al., 2008) and collapsing at night (Spiga, 2019), the PBL is characterised by relatively short timescale fluctuations in meteorological properties such as temperature, pressure and wind and the movement of aerosols such as dust and of molecular species such as water vapour and methane. Dynamics within the PBL also influence the broader global climate, through the transfer of heat and momentum from the surface to the atmosphere as a whole, as well as the injection of aerosols and molecular species into the atmosphere above the PBL, impacting global circulation (Petrosyan et al., 2011).

1.2 Martian Water-Ice Clouds

Despite its relatively low abundance in the martian atmosphere compared to our own, water vapour plays an important role in influencing the martian climate throughout the Mars year. The most significant water reservoirs on Mars are the polar caps, whose yearly cycles of sublimation and deposition drive a global water cycle. During the northern spring and summer (southern autumn and winter, $L_s = 0 - 180°$), water vapour is released from the north polar cap and is transported southwards by the solstitial, cross-equatorial Hadley cell. Around this time, Mars reaches its aphelion ($L_s = 71°$) and the atmosphere cools, causing this water vapour to reach its saturation point and leading to the formation of water-ice clouds. This enhanced cloud formation gives rise to the yearly Aphelion Cloud Belt (*ACB*, Section 1.2.1) around the tropics, interrupting the southward transport of water vapour and trapping it just north of the equator (Wolff et al., 1999). This hemispheric asymmetry may explain why the south polar water ice reservoir is not as extensive as that in the north and why northern hemisphere water vapour has a peak abundance of 60-70 precipitable microns (pr μm) while the southern hemisphere peak is only 20 pr μm (Trokhimovskiy et al., 2015).

The southern spring and summer (northern autumn and winter, $L_s = 180 - 360°$) see a similar sublimation from the south polar cap and subsequent transport of water vapour northwards. However, due to Mars' closer proximity to the sun around perihelion ($L_s = 251°$), the atmosphere is not cooled sufficiently to generate the

wide-scale saturation of water vapour and subsequent global-extent cloud formation in the tropics.

Still, both polar caps see seasonal cloud formation in the form of the "polar hoods", which form in the hemispheres' respective late summers. The timing and types of polar hood clouds are similar in both hemispheres. In the late summer, local dust storms lead to the formation of water-ice clouds which extend to latitudes of up to $\sim 35°$N in the northern hemisphere and $\sim 35°$S in the southern hemisphere. Both polar hoods retreat in their hemispheres' early springs (Wang and Ingersoll, 2002).

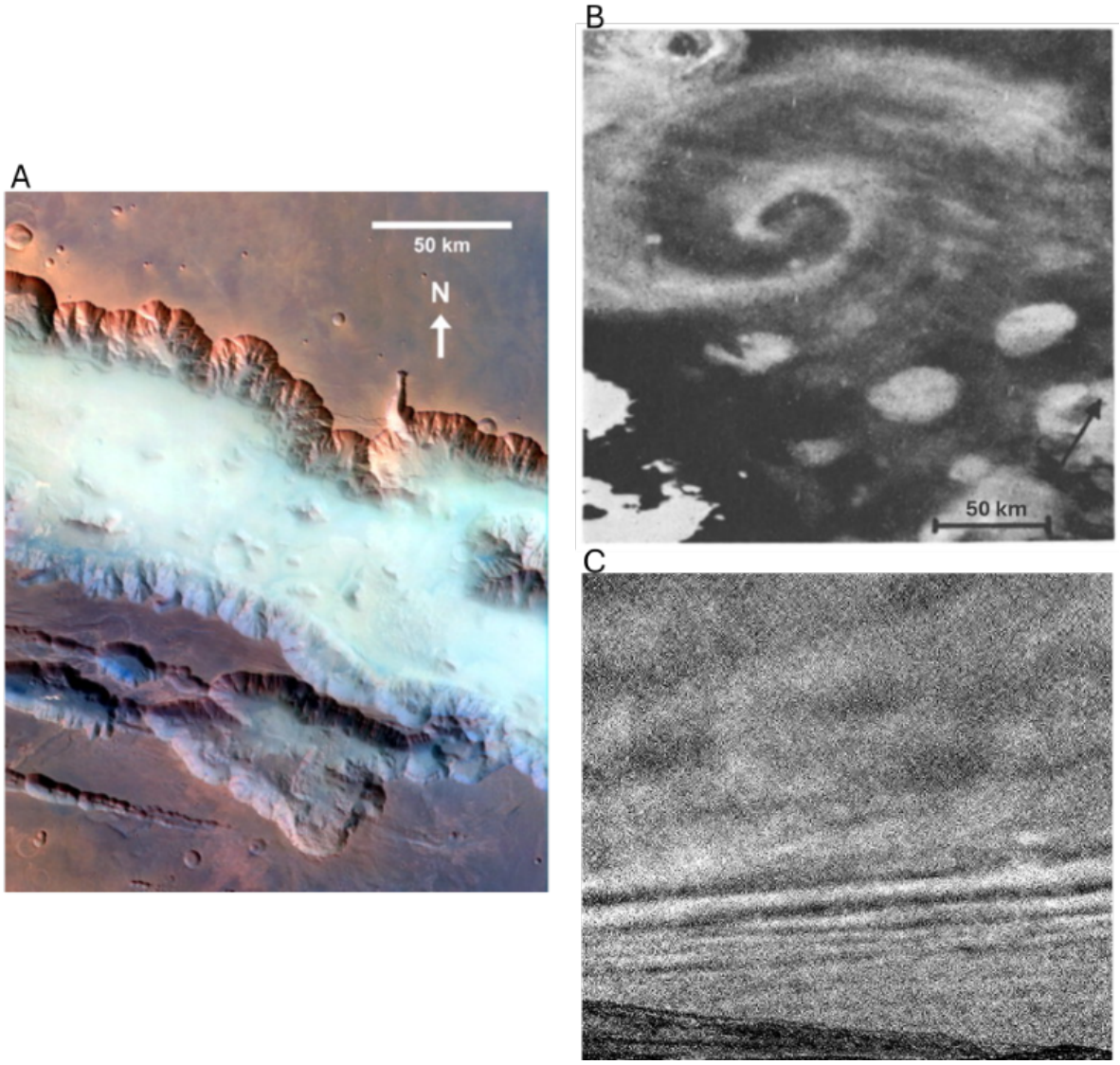


Figure 1.2: Three different cloud types seen on Mars. (A) Fog in Valles Marineris imaged by the High Resolution Stereo Camera onboard Mars Express. The image is centred at 14.17°S, 302°E and was taken at local time 09:20 at $L_s = 30°$. Figure 1 in Möhlmann et al. (2009). (B) A spiral cloud above the north pole imaged by the Viking 1 Orbiter Visual Imaging System. It is located at 81°N, 162°W and was taken at local time 10:00 at $L_s = 105°$. Figure 1 in Gierasch et al. (1979). (C) Gravity waves above Gale Crater captured by the Navigation Cameras on the Mars Science Laboratory following processing to ehance cloud features. This image is part of a movie taken at local time 08:51 and $L_s = 132°$.

Martian water-ice clouds exhibit a variety of different morphologies, which can vary based on formation mechanism, time of year and location. These include spiral clouds which tend to form in high northern latitudes as part of the polar hood; gravity and lee waves, which are seen in both ACB and polar hood clouds; and hazes or fogs which occur both near the surface and at higher altitudes up to 50 km (Kahre et al., 2017). Examples of these cloud types can be seen in Figure 1.2. Some martian clouds are associated with specific topography, such as orographic clouds forming around the Tharsis mountains, or morning fogs within Valles Marineris. However, others have more to do atmospheric instabilities, as in the case of clouds formed by gravity waves.

Clouds have been observed at Mars since the arrival of Mariner 4 in 1965 (Leighton et al., 1965). Currently, both orbiters and landed spacecraft observe martian clouds in a range of different wavelengths and using many different observational strategies. The Mars Colour Imager (*MARCI*) on board the Mars Reconnaissance Orbiter (*MRO*) perhaps has the largest dataset of daily water-ice cloud optical depths covering large portions of the planet and taking advantage of its UV bands which are particularly well suited for distinguishing water-ice clouds (Wolff et al., 2019). The High Resolution Stereo Camera (*HRSC*) on board Mars Express has built up a large catalogue of cloud images along with information about cloud characteristics and morphologies as well as their spatial and temporal distribution from 2017 to the present (Tirsch et al., 2025). The ability of orbiters to observe most or all of the martian surface daily allows us to get an idea of planet-wide trends and processes associated with clouds.

In contrast, surface cloud observations are more spatially limited. We are only able to observe clouds in the area of the lander or rover making the observation. Still, surface observations have provided great insights into cloud processes. Cloud observations have been taken by every landed spacecraft beginning with the Viking landers in the 1970s (Pollack et al., 1977) and continuing to the present day. Dedicated cloud movies[2] taken by various landed spacecraft have enabled the study not only of cloud properties such as opacity, morphology, and behaviour (E.g. Moores et al., 2015; Hayes et al., 2024b; Lemmon et al., 2024c) but also the indirect study of winds aloft (E.g. Campbell and Moores, 2025). The Phoenix lander was also equipped with a LIDAR which was able to measure cloud heights and observe precipitation (Whiteway et al., 2009).

1.2.1 The Aphelion Cloud Belt

The Aphelion Cloud Belt is a yearly, equatorial belt of water-ice clouds. As described above, it is driven by the southward transport of water vapour from the north polar cap combined with the cooling of the atmosphere as Mars reaches aphelion. The ACB forms around $L_s = 40 - 60°$ and persists until about

[2]See Section 1.5 for further discussion of cloud movies from the Mars Science Laboratory.

$L_s = 150°$ and stretches from $\sim 30°$N to $\sim 10°$S latitude (Clancy et al., 1996; Wolff et al., 1999).

The ACB has a significant impact on the martian climate and atmospheric circulation. It interrupts the cross-equatorial flow of water vapour, sequestering water vapour in the northern tropics during the aphelion season and leading to an imbalance in north and south water vapour (Montmessin et al., 2004). Additionally, the ability of ACB clouds to absorb and scatter solar radiation impacts atmospheric temperature and associated dynamics (Wilson and Guzewich, 2014).

Orbital observations have been able to examine the temporal and spatial behaviour of the ACB. ACB clouds generally range in altitudes from 15-40 km (Heavens et al., 2010) with opacities which can range from sub-optical ($\tau < 0.1$) to ~ 0.6 (Wolff et al., 1999). These peaks in opacity occur around $L_s = 60° - 100°$ near the heart of the ACB at $10 - 20°$N. The ACB typically has very low interannual variability on a global scale (Wolff et al., 2019, Figure 1.3).

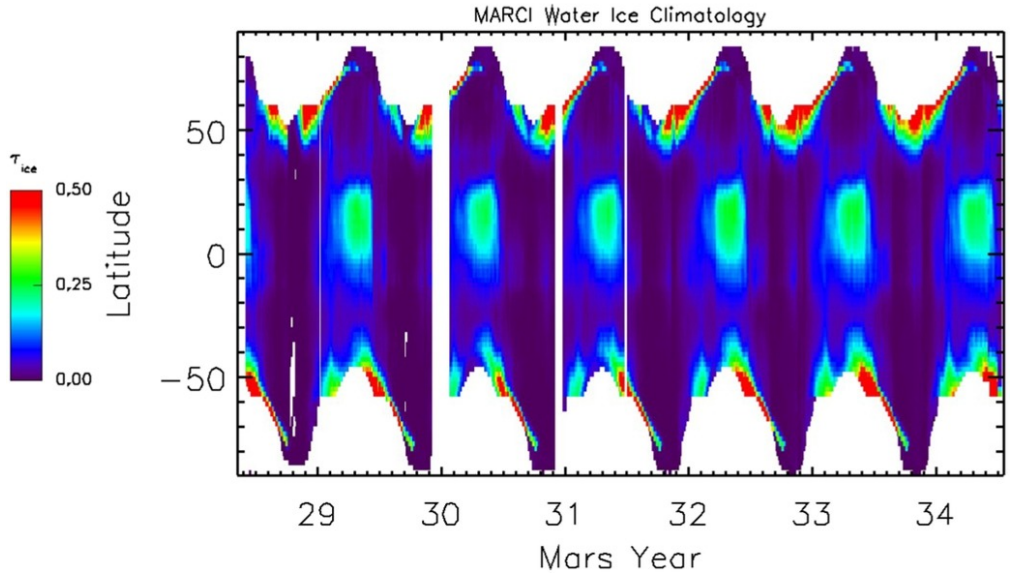


Figure 1.3: MARCI water-ice optical depth retrievals from MYs 28-34 showing the changes with latitude and L_s over that span of time and averaged over 14-16 LST. The interannual repeatability of the ACB is very apparent. Figure 11 in Wolff et al. (2019).

Diurnally, ACB cloud opacity peaks overnight and reaches a minimum around local noon. While observations by the planetary Fourier Spectrometer (*PFS*) show the diurnal behaviour of ACB cloud opacity to be nearly symmetric around local noon (Giuranna et al., 2021), visible-UV observations by the Emirates Exploration Imager (*EXI*) on board the Emirates Mars Mission (*EMM*) orbiter show higher overall morning cloud opacities than afternoon (Wolff et al., 2022). The differences between morning and afternoon clouds, with greater cloud enhancement in the morning than afternoon, has been linked to different formation mechanisms: morning clouds form overnight at cooler temperatures and persist into the mornings, while afternoon clouds form as a result of increased convection during the warmer, midsol hours which delivers cloud condensation

nuclei and water vapour to altitudes at which clouds form (Tamppari et al., 2003).

It appears that the diurnal variability in the ACB is location-dependant. Observations around the Tharsis region (Madeleine et al., 2012) and Jezero Crater (Patel et al., 2023) have displayed diurnal variability in ACB clouds, while observations at Gale Crater (Hayes et al., 2024b; Innanen et al., 2025a) have shown little difference between morning and afternoon cloud properties. Indeed, from global observations of the ACB by the Emirates Mars Infrared Spectrometers (*EMIRS*) on board EMM, we are able to see that the magnitude of the diurnal difference varies across the planet (Atwood et al., 2022, Figure 1.4).

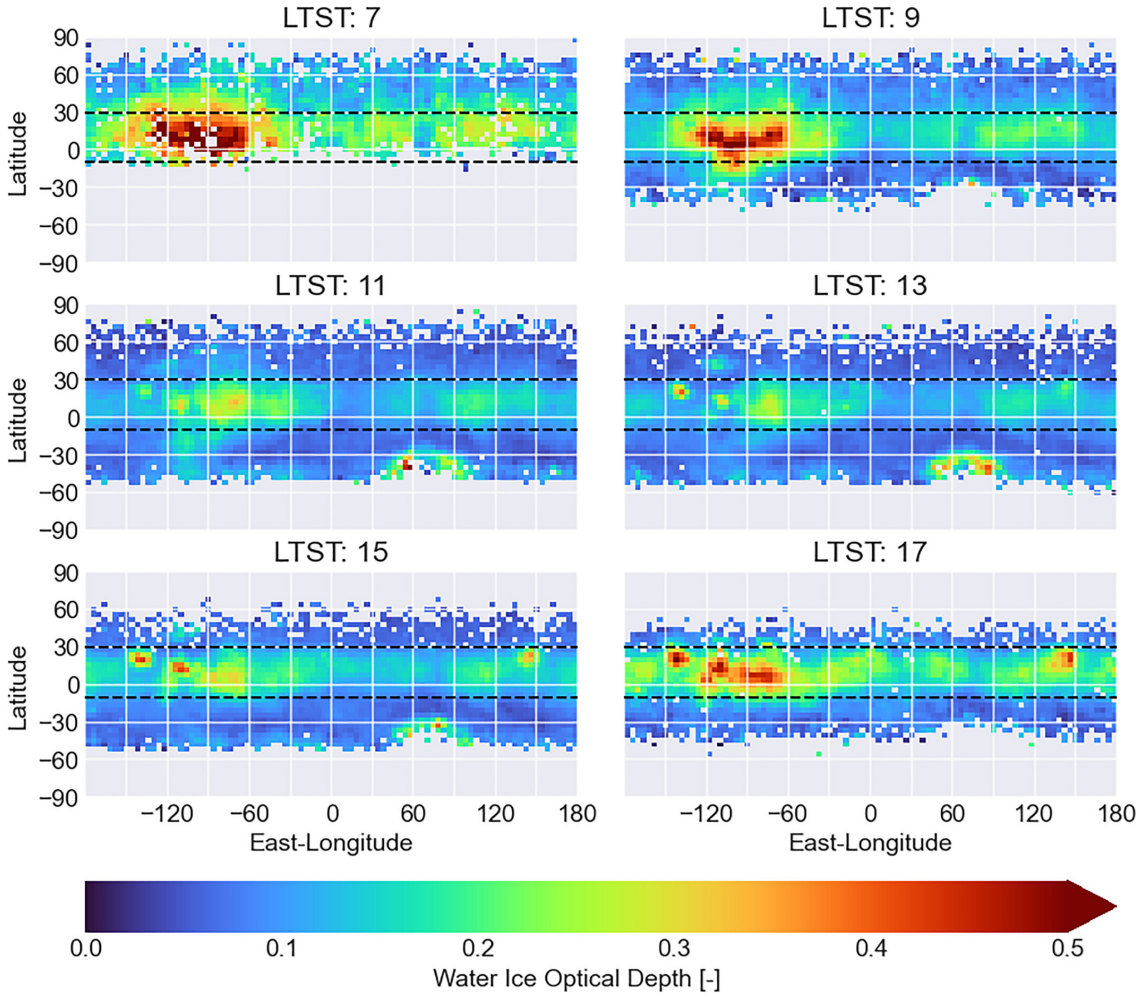


Figure 1.4: Water-ice optical depths retrieved by EMIS averaged over the ACB season for six LTSTs over Mars. The extent of the ACB is given by dashed black lines. Figure 1 in Atwood et al. (2022).

While the ACB extends over all longitudes in its latitudinal range, localised areas of cloud increased cloud opacity occur especially in areas of high topographic variation such as Tharsis and Elysium (Giuranna et al., 2021). Additionally, as mentioned above, the ACB tends to exhibit the thickest clouds towards the centre of its latitudinal range with clouds nearer to the edges being thinner.

Orbital investigations have also attempted to determine water-ice crystal geometry within the ACB clouds. The clouds are suggested to have effective radii between 2-5 μm (Kahre et al., 2017) and with a droxtal geometry (Wolff et al., 2019). However, the presence of a 22° halo imaged by the Perseverence Rover during the MY 36 ACB season suggests that, at that location at least, the clouds contain hexagonal water-ice crystals (Lemmon et al., 2022).

1.3 Dust in the Martian Atmosphere

The martian atmosphere is particularly well suited to lofting fine grained dust particles through near-surface wind stress and convective vortices (Kahre et al., 2017). Dust lifting events can range from transient and local, as in the case of dust devils and linear wind stress lifting events (e.g. Guzewich et al., 2023b), to sustained and global, as in the case of global dust storms (*GDS*) (e.g. Guzewich et al., 2019). Atmospheric dust is composed primarily of silicates with a wide range of particle sizes based on location and altitude (Kahre et al., 2017). This suspended dust is an effective absorber and scatterer of radiation, resulting in heating of both the dust and the atmosphere around it. As a result, airborne dust significantly impacts the thermal structure of the martian atmosphere (Gierasch and Goody, 1972).

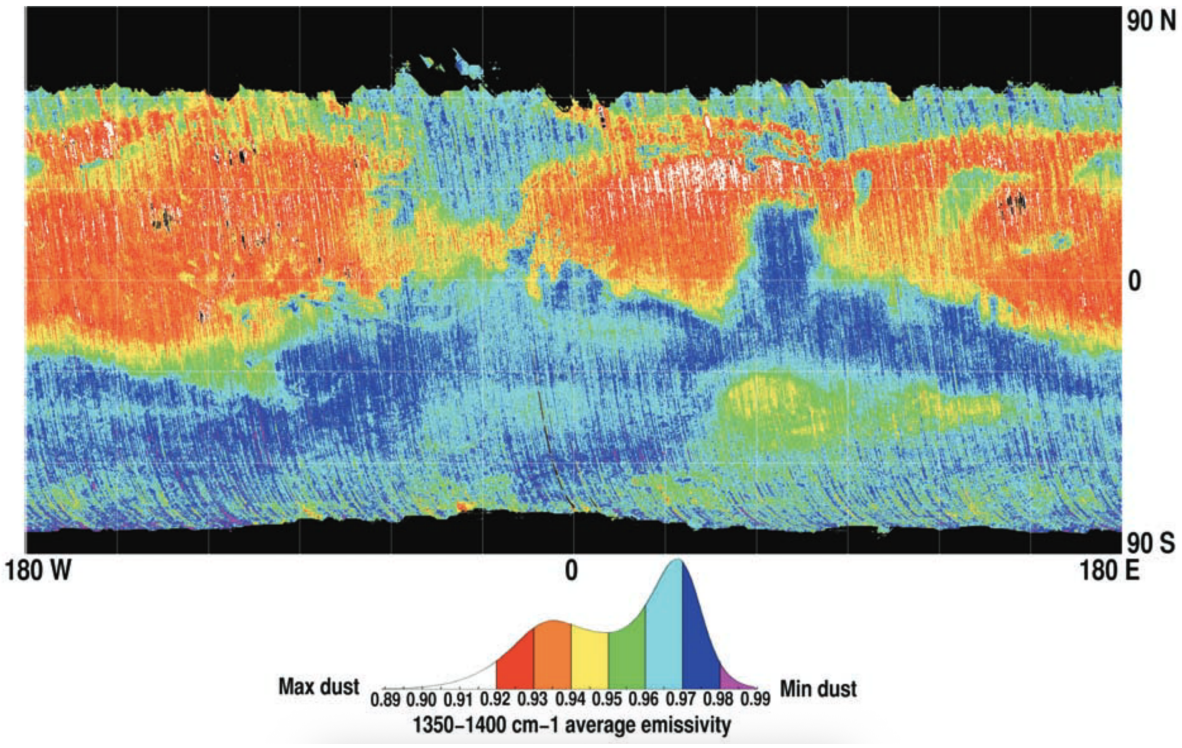


Figure 1.5: The dust cover index derived from MGS/TES data for the surface of Mars. Figure 14 in Ruff and Christensen (2002).

This thermal impact subsequently affects many other processes and cycles within the martian climate. The dust cycle is heavily linked to both the CO_2 and water cycles, all of which in turn impact global circulation. Unlike water and CO_2, whose main reservoirs are at the poles, the entire martian surface acts as a dust reservoir, though the amount of dust varies with location (see Figure 1.5). Dust is also transported to and from these reservoirs through the action of global and regional dust storms.

While atmospheric dust is present throughout the martian year, there is typically less dust loading in northern spring and summer (the cloudy season) and higher through northern autumn and winter (the dusty season). The dusty season is characterised not only by this increased dust loading but also the presence of dust storms at local, regional and global scales. Dust loading begins to increase in the low latitudes of the southern hemisphere around $L_s = 150°$ as well as around the edge of the southern polar cap. The increase in dust continues across the planet, peaking around $L_s = 210 - 240°$ before decreasing after $L_s \sim 260°$. There is another, typically smaller peak in dust loading around $L_s \sim 310°$ before opacity once again decreases into the start of the next Mars year (Montabone et al., 2015).

The dusty season is also characterised by local and regional dust storms, with local dust storms having surface areas $< 1.6 \times 10^6$ km^2 and regional dust storms having surface areas $> 1.6 \times 10^6$ km^2 (Cantor et al., 2001), though the locations and intensities of these storms can vary from year to year. Local dust storms contribute significantly to the dust cycle due to their pervasiveness, appearing across the planet throughout the Mars year. However, there also exist localised cycles particularly along the edges of the seasonal ice caps and in the mid-latitudes as well as in areas of high topography (such as the Tharsis region) in the northern hemisphere. Regional dust storms occur less frequently than their local counterparts, on the order of 8-35 times per Mars year, through they tend to persist longer (Kahre et al., 2017).

Global dust storms, the largest and longest-lasting of all the dust storms, occur on average every few Mars years. Since 1924 (MY -16), there have been eleven potential GDSs observed, eight of which are confirmed to have been global in extent, with the extents remaining three unknown due to observational limitations. Of these, the most well documented are those in MYs 25, 28 and 34, all of which were observed by multiple spacecraft in orbit or on the surface of Mars (Wolkenberg et al., 2020). The majority of these storms originate in the southern hemisphere (and indeed the most recent MY 34 GDS is the sole exception) as local and regional storms form and combine. Typically, GDSs form around perihelion ($L_s = 271°$), though they have also been observed earlier around the southern spring equinox ($L_s = 180°$) (Kahre et al., 2017). There is only one Mars year known to have two GDSs, MY 12, occurring around $L_s = 205°$ and $L_s = 275°$ and observed by the Viking orbiters (Briggs et al., 1979).

The mechanisms that control the initiation of GDS are not fully understood, though they likely depend on feedbacks between the thermal structure of the atmosphere and dust loading and are thus influenced by the

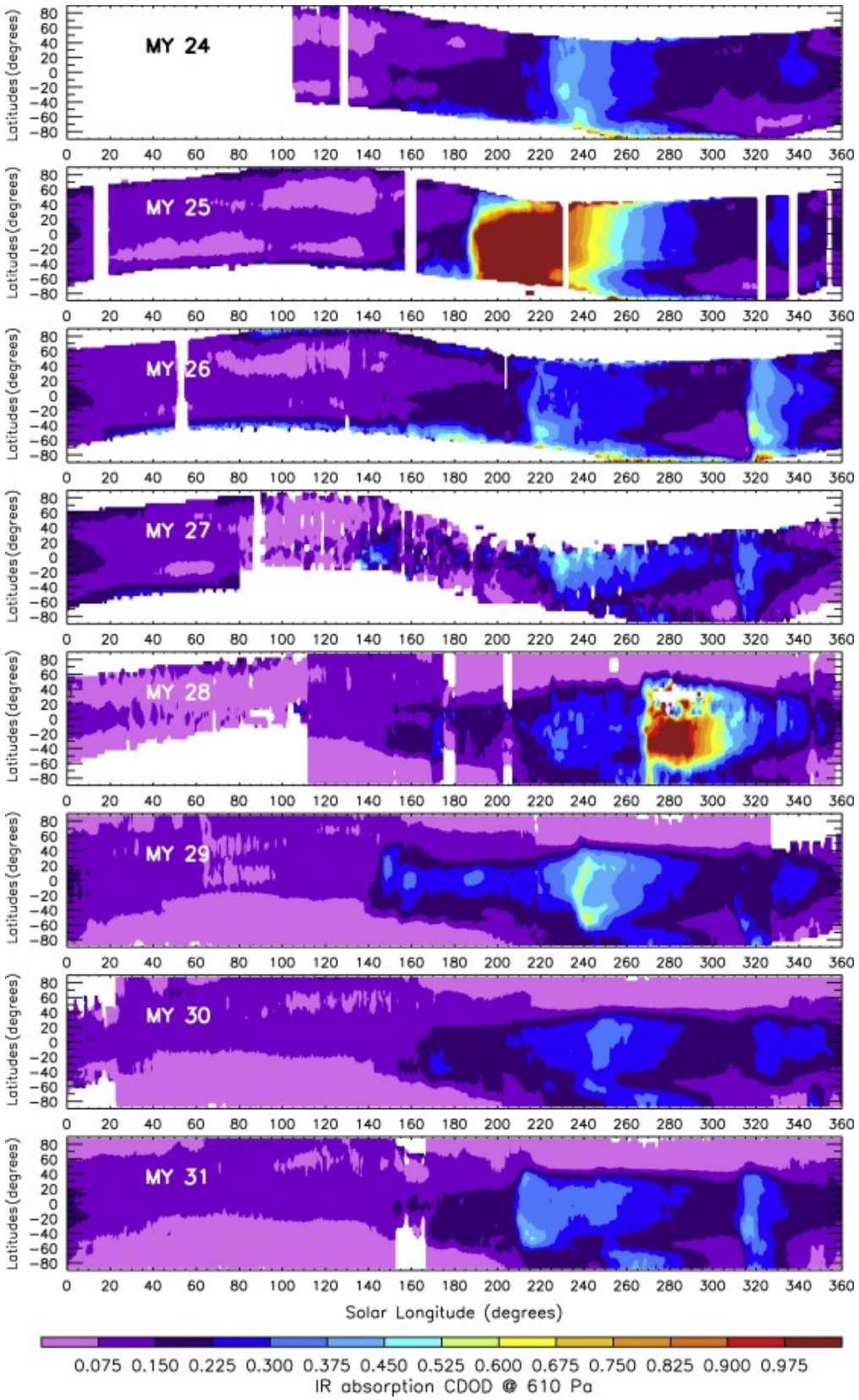


Figure 1.6: Zonal mean column dust optical depth from My 24–31. Data are taken from TES, MCS and THEMIS at the 9.3 μm absorption band. Figure 16 in Montabone et al. (2015).

combined effects of Mars' eccentric orbit and its topographic dichotomy (Newman et al., 2019). As mentioned above, GDS go through an initiation phase characterised by the growth and combination of multiple regional and local dust storms which lead to a rapid increase in global dust opacities. This initiation phase is followed by a decay phase as dust lifting stops. As with dust storm initiation, the reason for the halting of dust lifting is unknown, though it could be due to the removal either of all surface dust or surface dust which is sufficiently easy to lift (Kahre et al., 2017). In the three most recent GDS, the lengths of the expansion phases were within 1° of L_s of each other, while the decay phases had more variation (Wolkenberg et al., 2020).

The size, composition and subsequent geometry of dust varies across the planet and thus is not well represented by a single particle size or shape. The distribution of dust sizes and types have been studied across the planet by both orbiters and landers, and the transport of dust has likewise been modelled (Guzewich et al., 2023b). Long-term surface missions such as the Mars Exploration Rover Opportuinity and the Mars Science Laboratory (see Section 1.5) have been able to build up extensive records of dust behaviour in their regions (Lemmon et al., 2015, 2024a); however these are constrained to specific regions. Orbital measurements can also determine dust properties (e.g. Clancy and Lee, 1991); however they may miss the lower portions of the atmosphere due to interactions with the very aerosols they are trying to study (Innanen et al., 2024b).

1.4 Light Scattering in the Martian Atmosphere

Radiative transfer describes the transport of electromagnetic energy through some medium, and involves the absorption, emission and scattering of photons as they interact with the constituents of this medium. In simplest terms, the transfer of radiance (I) through an atmosphere can be understood with the Beer-Lambert law, $I = I_0 \exp(-\tau)$, where I_0 is the radiance at the top of the atmosphere, and τ is the optical depth and describes how light is attenuated through the atmosphere. This attenuation typically consists of components of absorption and scattering by both gases and aerosols in the atmosphere. Absorption here refers to light which has been captured by a particle, while scattering refers to an incident wave of light being redirected in all directions by a particle.

In this work, we are concerned primarily with the scattering of light by water ice and dust in the atmosphere of Mars. The scattering of radiation from the sun is important in understanding radiative transfer, which impacts not only the radiation budget of the planet but also atmospheric dynamics.

Scattering by dust, for instance, can have large radiative effects on the atmosphere, impacting temperature, pressure, and global circulation, as described in Section 1.3. Water-ice clouds, though initially assumed to be less impactful than dust, can have similar radiative impacts (e.g. Clancy et al., 1996). While this effect

may be more obvious in the case of thick clouds, which can clearly attenuate light reaching the surface as we observe on any cloudy day, even sub-optical clouds, those which cannot be seen by eye, may impact radiative transfer. Dust and water ice can also be linked and influence each other, especially given that dust acts as a condensation nucleus for water ice. A dramatic example of their influence on each other is during the MY 34 GDS when unusual high altitude cloud formation was observed due to increased dust lifting and the altered thermal structure of the atmosphere (Stcherbinine et al., 2020).

Understanding light scattering is not just important for its effects on radiative transfer alone. The scattering properties of particles can also provide insight into their characteristics, and bulk scattering properties can be used to remotely understand planetary atmospheres (Hansen and Travis, 1974).

Particles scatter light in different ways depending on their size, shape and the wavelength of the incident light. Scattering is divided into different regimes based on the size of the particle compared to the wavelength of the incident light. When the particle's radius is much less than the light's wavelength, Rayleigh scattering applies. A basic example of this is the scattering of visible sunlight by gas molecules in Earth's atmosphere, giving rise to its blue sky. When the particle has a radius comparable to or larger than the wavelength, we move into the Mie and geometric scattering areas, with Mie theory being more applicable to smaller particles and geometric optics applying better to larger particles (Hansen and Travis, 1974).

Scattering of light in an atmosphere can be divided into single- and multiple-scattering, depending on the number of scattering centres or particles present and their separation from each other. Single scattering is typically applied to a small volume element, from which a multiple scattering solution may be inferred; however in some cases, such as those of optically thin clouds where multiple scattering is negligible, a single scattering approximation may be used (E.g. Moores et al., 2015). The single scattering properties of some particle may be described by the scattering coefficient (μ_{sca}) and the phase matrix ($\mathbf{P}$).

The scattering coefficient has units of per length and is described as the scattering cross section per unit volume. The scattering cross section (σ_{sca}), which as units of area, gives the amount of incident light removed from the original direction by a single scattering event and redistributed over the area of a sphere centred on the scatterer (Liou, 2002). The ratio of the scattering cross section to the geometric cross section of the scatterer can be described by the scattering efficiency (Q_{sca}) (Hansen and Travis, 1974).

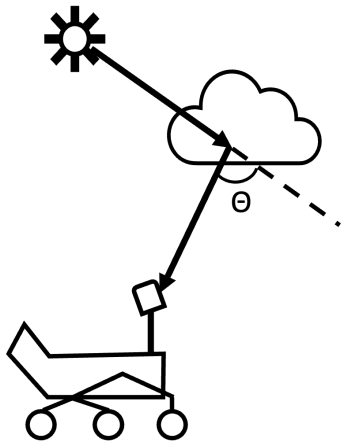


Figure 1.7: An example of the geometry of the scattering angle, the angle the sunlight incident on a cloud particle makes to the observer.

The phase matrix describes the distribution and polarization of scattered light, and its first term, P^{11} contains the scattering phase function (Hansen and Travis, 1974). The scattering phase function (or simply phase function), usually given on its own by $P(\theta)$, is unitless and describes how much light is scattered by the scatterer over scattering angles $0 < \theta < 180°$. The magnitude of the phase function gives the fractional amount of light scattered, and is normalised such that the area under its curve is 4π (Hansen and Travis, 1974). The geometry of the scattering angle is given in Figure 1.7. The phase function is sometimes described in terms of the complementary phase angle, g, where $g = \theta - 180°$ (e.g. Hapke, 2012b).

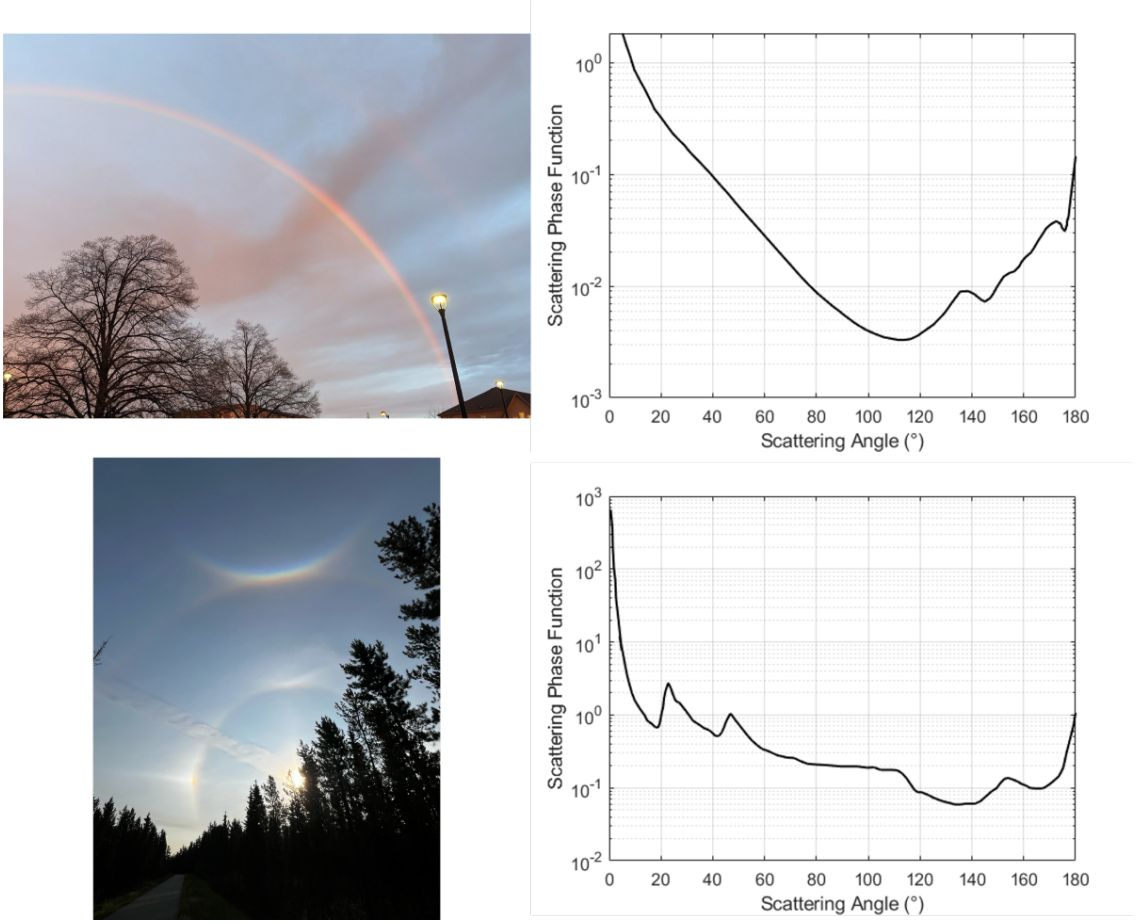


Figure 1.8: Top left: an example of a rainbow, caused by increased light scattering by cloud droplets at a scattering angle of $\sim 138°$. A faint secondary arc can be seen, as well as the increased brightening within the primary arc. Photo taken by the author. Top right: the phase function for cloud droplets, adapted from Sassen and Liou (1979). A local maximum around 138° can be seen. Lower left: A number of atmospheric optical phenomena caused by hexagonal water-ice crystals. Both the 22° and 46° halos can be seen, as well as a sundog to the left of the sun, a upper tangent arc on the inner halo and a circumzenithal arc on the outer. Photo taken by Scott Guzewich, used with permission. Lower right: the phase function for hexagonal plates, adapted from Yang and Liou (1996). Local maxima around 22° and 46° can be seen.

The phase function can encode information on a particle's size and shape, with size strongly impacting behaviour at high and low scattering angles and shape more strongly impacting behaviour at middle scattering

angles. For instance, a smaller particle will tend to scatter light more evenly in all directions, whereas a larger particle will become more strongly forward scattering (Liou, 2002). The shape of the particle can influence scattering features across the range of scattering angles, which in turn can give rise to scattering phenomena such as halos and rainbows (Figure 1.8).

Since the size and shape of the particles influence the scattering phase function, they also necessarily influence the transfer of solar radiation through the atmosphere, so having a good understanding of the properties of aerosols in the martian atmosphere is important in understanding radiative transfer as a whole. Currently, many Mars climate models assume a single water-ice crystal geometry, often spherical (e.g. Kleinböhl et al., 2009) or droxtal (Wolff et al., 2019). However, it is very likely that ice crystal geometry, or habit, varies across Mars, and potentially also temporally throughout the year, between seasons or even within a single sol. For instance, while hexagonal water-ice crystal geometry has been inferred at Jezero Crater through the detection of a halo (Lemmon et al., 2022), no such optical phenomena have been observed at Gale Crater through over six Mars years of cloud observations, suggesting the crystal habit of the clouds there may differ.

1.5 Atmospheric Observations by the Mars Science Laboratory

The Mars Science Laboratory (*MSL, Curiosity*) landed on Mars at the tail end of the MY 31 ACB season ($L_s = 151°$). Its landing site, Gale Crater (5.4°S 137.8°E), is a large impact basin just over 150 km in diameter with a 5 km layered interior mound known as Aeolis Mons or Mount Sharp.

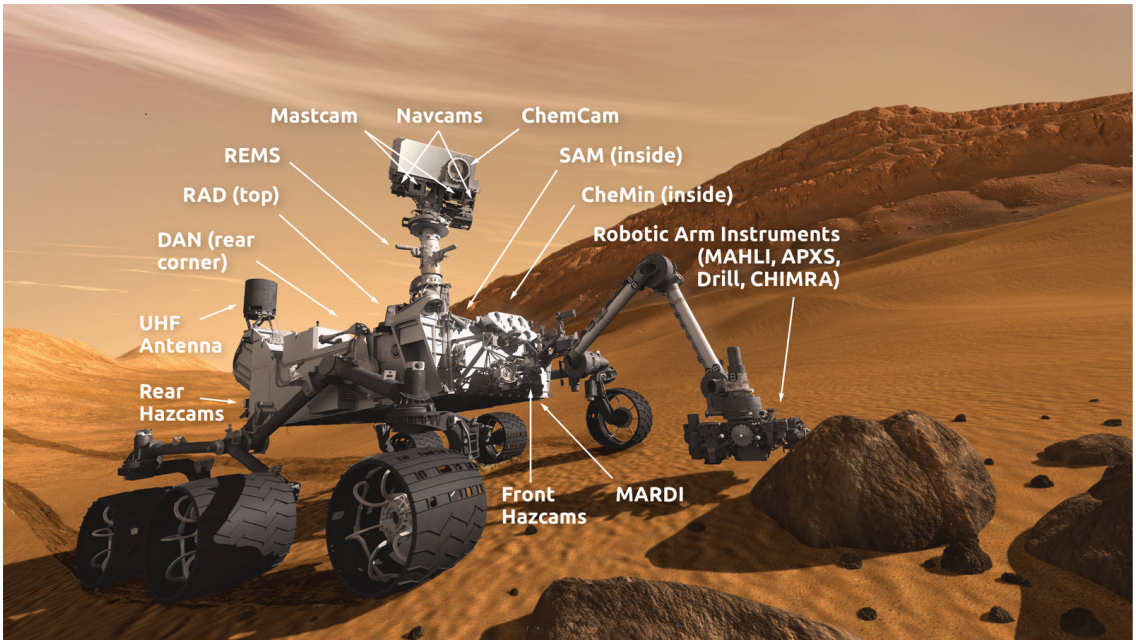


Figure 1.9: A diagram of MSL with its scientific and engineering instruments labelled. NASA/JPL-Caltech.

Over more than seven Mars years, MSL has built up an extensive record of the present environment in and around Gale Crater. MSL also takes part in network meteorology, with both other landers such as Mars 2020 and Insight (e.g. Lemmon et al., 2024b; de la Torre Juárez et al., 2024) and with orbiters (e.g. Guzewich et al., 2017).

All of the rover's ten science instruments as well as its engineering cameras have been used for environmental science activities ranging from continuous, long-term meteorological monitoring with the Rover Environmental Monitoring Station (*REMS*) to studying aeolian activity with the Mars Hand Lens Imager (*MAHLI*) and Mars Descent Imager (*MARDI*) (Guzewich et al., 2023a). Amongst these activities are extensive, long-term studies of both martian clouds and atmospheric dust.

Since the very start of the mission, MSL's Navigation Cameras (*Navcams*) have been used to take regular cloud movies. Initially, these were eight-frame Zenith and Suprahorizon movies (*ZM* and *SHM*, respectively) which were intended to document cloud properties such as morphology, opacity, spacing and velocity (Moores et al., 2015). These movies continue to be captured, though their parameters have changed over the course of the mission (Hayes et al., 2024b). Two additional cloud observations have been added: the Phase Function Sky Survey (*PFSS*) in MY 34 (Cooper et al., 2019) and the Cloud Altitude Observation (*CAO*) in MY 35 (Hayes et al., 2024b). Late MY 35 also saw the addition of the Shunt Prevention[3] ENV Navcam Drop-In (*SPENDI*). This observation consists of two cloud movies nearly identical to the SHM and four dust lifting movies (Hayes et al., 2024b).

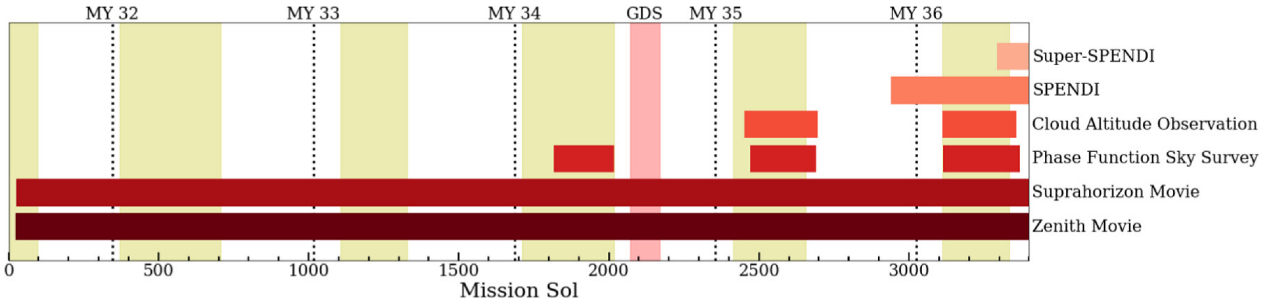


Figure 1.10: Cloud observations by MSL through the first five Mars years of its mission. Yellow shaded regions indicate the ACB season, with the red shaded region showing the extent of the MY 34 GDS. Figure 2 in Hayes et al. (2024b).

Between these cloud observations, we have a more than seven-Mars year record of the clouds at Gale Crater from which we have been able to infer cloud opacities (Kloos et al., 2016; Hayes et al., 2024b), wind speeds (Campbell and Moores, 2025), cloud altitudes (Campbell et al., 2020), and water-ice crystal habit (Cooper et al., 2019; Innanen et al., 2025a). We observe clouds at Gale Crater throughout the entirety of

[3]To extend the life of the rover's batteries, we try not to fully charge them, and when we have excess charge it is often necessary to 'shunt', or run the rover's heaters to discharge the batteries. The SPENDI was created to partially drain the rover's battery in a way that still provides a science return.

the Mars year, though they can typically be divided into twilight clouds, observed around twilight during early southern autumn to $L_s \sim 45$ (Lemmon et al., 2024c); ACB water-ice clouds; and non-ACB clouds. All these clouds tend to be relatively high altitude, and do not seem to be influenced by or interact with the topography of Gale Crater at all. The water-ice clouds observed during ACB season at Gale tend to be sub-optical ($\tau < 0.1$) (Hayes et al., 2024b) with altitudes between 15-40 km (Campbell et al., 2020). Non-ACB clouds are more difficult to characterise, as it is not always possible to tell if we are observing dust or water-ice clouds. For the most part, clouds observed during the dusty season are assumed to be lower-altitude dust clouds (Hayes et al., 2024b).

MSL uses both its Navcams and Mast Cameras (*Mastcams*) to take regular observations of atmopheric dust. These observations include various Navcam dust lifting movies, intended to capture both straight line dust lifting events and dust devils (Guzewich et al., 2023b); the single-frame Navcam Line of Sight observation to determine line-of-sight extinction to the crater rim (Bischof et al., 2024); and the Mastcam tau observation to determine column opacity through direct solar imaging (Lemmon et al., 2024a).

The LOS and tau observations both reveal seasonal variability in dust that is consistent with the greater dust cycle on Mars, with higher opacities observed in the dusty season and lower opacities in the cloudy season. Both observations also show a seasonal dependence of dust, with column opacity peaking in the morning (Lemmon et al., 2024a) and line-of-sight within the crater peaking around local noon (Bischof et al., 2024). Dust lifting shows similar trends, with a peak in frequency in the dusty season and increased dust lifting around local noon. Dust lifting is also heavily influenced by topography and the location of the rover, as the availability of surface dust is an integral part of these events (Guzewich et al., 2023b).

MSL was also present for the MY 34 GDS. As a result, it was able to capture the most extensive set of in-situ meteorological measurements of such a storm and, indeed, the first set of in situ measurements with meteorological sensors since Viking in 1977. The REMS instruments made extensive measurements of pressure, air and ground temperature, UV flux and the first surface relative humidity measurements during the storm, as well as its initiation and decay. Mastcam tau and crater rim extinction, as well as Navcam LOS measurements tracked the optical depth throughout the storm, revealing a peak column opacity of 8.5. While the GDS impacted atmospheric dynamics within Gale crater, the dust observed from it was sourced from outside the crater, and dust lifting within the crater itself was suppressed by the reduced thermal gradient (Guzewich et al., 2019).

1.6 Methane in the Martian Atmosphere

In 1971, the Mariner 9 spacecraft became the first spacecraft to orbit another planet when it reached Mars. Among its instruments was an infrared interferometer spectrometer (*IRIS*), intended to collect spectral measurements of Mars' surface and atmosphere (Hanel et al., 1970). The data obtained by IRIS were used to determine atmospheric constituents and their isotopic ratios and to place upper limits based on non-detections of other minor species which may have been present, including methane. Maguire (1977) placed an upper limit of 0.02 ppmv (20 ppbv) on methane based on a non-detection in IRIS's 1306 cm^{-1} band. The first detection of methane was made by the Earth-based Fourier Transform Spectrometer at the Canada-France-Hawaii Telescope in 1999, with an abundance of 10 $\pm$3 ppbv (Krasnopolsky et al., 2004), though this was not published until after another detection by Mars Express in 2003 (Formisano et al., 2004). Subsequent Earth-based measurements suggested high temporal and spatial variability of martian methane, with methane spikes or plumes up to $\sim$ 45 ppbv (Mumma et al., 2009). However, none of these observations agreed with each other either spatially or temporally.

Methane detection from orbit was also reported by the Planetary Fourier Spectrometer (*PFS*) onboard Mars Express. Formisano et al. (2004) initially reported an average global mixing ratio of 10 ± 5 ppbv, varying between 0 and 30 ppbv, though this average was later amended to 15 ± 5 ppbv (Geminale et al., 2011). The Thermal Emission Spectrometer (*TES*) onboard the Mars Global Surveyor (*MGS*) reported abundances up to 60 ppbv (Fonti and Marzo, 2010). Like Earth-based observations, those by PFS and TES saw seasonal variations in and localised sources of methane, suggesting some unknown sources and sinks for martian methane (Geminale et al., 2011). Also like terrestrial observations, the orbital observations did not agree well with one another.

From the martian surface, only MSL has been able to measure methane. With an effective path-length of 16.8 metres and a spectral resolution of 0.0005 cm^{-1}, MSL's Sample Analysis at Mars Tunable Laser Spectrometer (*SAM-TLS*) is capable of detecting methane in concentrations above 0.1 ppbv (Mahaffy et al., 2012). SAM-TLS uses infrared laser absorption within a 20 cm long Herriott sample cell, making 81 passes for methane measurements. Ingested martian air can also undergo a methane enrichment process which removes atmospheric CO_2 and increases methane abundance within TLS (Mahaffy et al., 2012).

SAM-TLS methane measurements have been taken using both "direct-ingest" and "enrichment" methods. In the direct-ingest method, spectra taken with the sample cell filled with martian air are compared to those taken with a sample cell that has been evacuated (Webster et al., 2013). In the enrichment method, the ingested methane is enriched 23 ± 1 times. Results from direct ingest and enrichment measurements taken back-to-back on sol 684 agreed well (Webster et al., 2015).

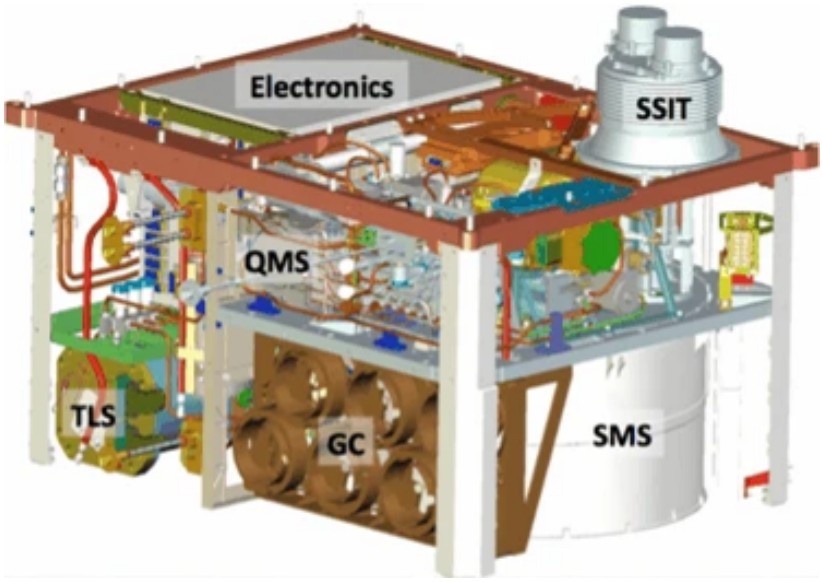


Figure 1.11: A model of SAM with TLS and the other instruments indicated. Figure 1 in Mahaffy et al. (2012).

As of 2020, SAM-TLS had taken nearly 30 direct-ingest and enrichment methane measurements. While the majority of these were taken overnight, two were taken in the daytime on sols 2615 and 2644 (Webster et al., 2021). The background enrichment measurements show a seasonal cycle, with a peak near $L_s = 160°$, towards the end of the southern winter (Webster et al., 2018). The daytime measurements showed an absence of methane, suggesting either rapid destruction or dilution of methane during the daytime (Webster et al., 2021). Indeed, the deeper planetary boundary layer (*PBL*) during the daytime would lead to enhanced mixing, while the collapse of the PBL at nighttime will suppress mixing, causing methane to build up overnight (Moores et al., 2019).

These differences in mixing would also go some way to explaining the apparent discrepancy between SAM-TLS methane measurements and the lack of any methane reported by the ExoMars Trace Gas Orbiter (*TGO*). Since the start of science operations in 2018 (MY 34), both the Atmospheric Chemistry Suite (*ACS*) and Nadir Occultation for MArs Discovery (*NOMAD*) instrument suites onboard TGO have been making methane measurements of the martian atmosphere. In that time, ACS and NOMAD have both failed to detect any methane (Korablev et al., 2017). In particular, ACS placed an upper limit on methane of 0.02 ppbv, lower than the background measurements reported by SAM-TLS (Montmessin et al., 2021). However, NOMAD and ACS are unable to see below about 5 km in altitude (Korablev et al., 2017), and thus cannot observe near-surface methane.

There is also controversy surrounding whether or not SAM-TLS is in fact measuring martian methane. There have been assertions that the spectral features for methane are contaminated by ozone or CO_2 (Olsen et al., 2020), or that the foreoptics chamber of the TLS is contaminated with methane from Earth (Viscardy

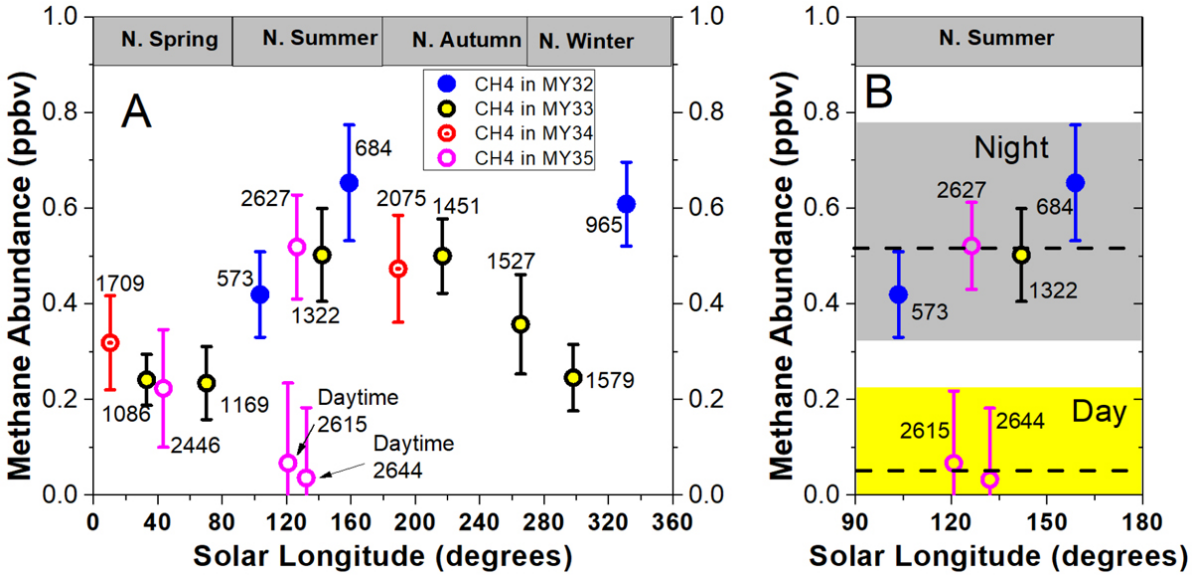


Figure 1.12: (A)SAM-TLS enrichment measurements up to mid-MY 35 (January 2020) excluding the sol 2442 measurement. Error bars are ±1 SEM. (B) Diurnal variability in measured methane abundance in late southern winter. Figure 1 in Webster et al. (2021).

et al., 2025). These assertions have been tested by the SAM-TLS team (E.g. Webster et al., 2020), who believe that the measurements do show martian methane, and that the seasonal cycle, while still not understood, is occurring in martian methane.

SAM-TLS has also observed spikes in methane well above the mean. A measurement taken on sol 2442 (19 Jun 2019) showed a mixing ratio of 20.5 ± 2 ppbv. In a subsequent measurement taken four sols later (sol 2446, 23 Jun 2019), methane concentrations had returned to typical background levels (Webster et al., 2021). This brief spike in methane concentration suggests not only the presence of occasional methane plumes, but also some rapid methane destruction mechanism. While such mechanisms have been proposed (E.g. Thøgersen et al., 2019; Zhang et al., 2022), the actual mechanism at play on Mars remains unknown.

Methane can persist in Mars' atmosphere for, at most, a few hundred years (Atreya et al., 2007); however the variability in observed methane including the rapid dissolution of methane plumes and the discrepancies between TGO and MSL methane observations suggests methane is being destroyed on scales much more rapid than this. However, the several hundred year limit does also suggest that methane is being produced by some as yet unknown process or processes occurring in the martian subsurface (Oehler and Etiope, 2017). Microseepage of methane from the subsurface would account for both the seasonal background behaviour of methane and the occasional plumes. However, the behaviour of these plumes is not well understood as their only observations by TLS are at a single point in time. Thus, plume initiation and decay have not been observed, nor is there any understanding of if these plumes are isolated incidents.

Despite the questions and controversy surrounding the current set of martian methane measurements,

there is a desire within the martian atmospheric community to understand these measurements and the implications they have for methane variability and exchange. Both the most recent Planetary Decadal Survey (National Academies of Sciences, Engineering, and Medicine, 2023) and the recent Mars Exploration Program Analysis Group Goals (Banfield et al., 2025) highlight an understanding of methane's behaviour as a priority in the coming years. It is thus important to consider how we would like to study the behaviour of methane, and what future instruments can best achieve this goal.

1.7 Motivation and Structure of the Dissertation

The work in this dissertation is largely concerned with characterising variability in three constituents of the martian atmosphere: water ice (described in Section 1.2), dust (described in Section 1.3) and methane (described in Section 1.6). In examining water ice and dust, I make use of the scattering properties of these aerosols to determine their geometric properties, and their larger interactions in the atmosphere. I make use of in-situ observations of the area around Gale Crater from both orbit and the surface of Mars, laboratory simulations, and terrestrial analogues. I examine the interactions of water vapour with aerosols in cloud formation using surface measurements (Chapter 2), study how the presence of aerosols may impact orbital instruments' ability to see through the atmosphere (Chapters 3 & 4) and use laboratory and terrestrial analogue measurements to inform future instrumentation to study near-surface aerosols (Chapter 5) and methane plumes (Chapter 6).

This dissertation begins higher in the martian atmosphere, examining water-ice clouds several to tens of kilometres above Gale Crater both from surface and from orbit. I then examine the atmospheric column with MCS from about 100 km down to within a few kilometres of the surface. The final two chapters are more concerned with the PBL, looking at aerosol and methane behaviour in the region within a few kilometres of the martian surface.

As described in Section 1.2, many climate models assume a single water-ice crystal habit for the ACB, despite the fact that there is evidence of varying water-ice crystal habit at different locations. Chapter 2 uses a five-Mars year dataset from MSL to infer the water-ice crystal habit of ACB clouds at Gale Crater. We use a five-Mars year data set to derive the single scattering phase function (Section 1.4) of these clouds. The phase function can provide information on particle size and habit, though the limited dataset from MSL only allows us to constrain crystal habit. Understanding the scattering properties of clouds can also be important in understanding radiative transfer during the ACB season. We also use the derived phase function to examine interannual, seasonal and diurnal variability of these clouds at Gale Crater.

Chapters 3 and 4 both examine the limits of detection of orbital instruments for exploring the martian

atmosphere. While much of our understanding of the atmosphere comes from orbital observations, these observations could be impeded or confounded by the presence of aerosols in the atmopshere, especially as we approach the surface. Chapter 3 uses images from TGO's Colour and Stereo Surface Imaging System (*CaSSIS*) in the area around Gale Crater taken concurrently with MSL cloud observations to probe CaSSIS' ability to see sub-optical water-ice clouds. Chapter 4 examines how dust and water-ice in the martian atmosphere may impede the ability of the Mars Climate Sounder (*MCS*) to observe down the surface through looking at minimum retrieval altitudes over nine Mars years.

Chapter 5 examines the utility of using low-powered lasers combined with an all-sky viewer to infer near-surface aerosol properties for planetary applications. This analysis continues work started by Campbell (2024), using laboratory simulations and field testing, as well as Mie scattering models to infer particle size and distribution from laser backscatter. A low-cost, relatively simple instrument could be an effective way of understanding aerosol behaviour in the lowest part of the atmosphere, a region that may be missed by orbiters.

Finally, Chapter 6 uses measurements taken in a martian analogue environment to examine methane plume variability over short timescales. As described in Section 1.6, the behaviour of martian plumes is not currently well understood. We look at the behaviour of terrestrial methane plumes from a point source and how this behaviour changes with increasing distance from the source. Additionally, we observe the release of methane over an extended time at high frequency to estimate the frequency of plumes of varying sizes. Understanding this behaviour is important in localising methane point sources, and our findings can inform instrument design and future mission concepts to better characterise martian methane.

Chapter 2

The Water-ice Cloud Phase Function at Gale Crater

2.1 Motivation & Author Contribution

MSL is well positioned to observe the southern edge of the ACB, and indeed it has done so year after year since its landing just after $L_s = 150°$ in MY 31. The ACB is a relatively invariant feature in the martian water cycle (Section 1.2), which has a significant impact on the planet's atmospheric radiation budget and thermal structure. Constraining the microphysical properties of ACB clouds provides insight into the nature of these impacts. In this chapter, I derive a phase function for the water-ice clouds of the ACB observed at Gale Crater and use it to comment upon the water-ice crystal geometry within these clouds.

Previous work constrained martian water-ice cloud phase functions from orbit (e.g. Clancy and Lee, 1991; Clancy et al., 2003) and from the surface (Kloos et al., 2016; Cooper et al., 2019). We extend the surface work at Gale Crater using a dedicated cloud observation from MSL (described in Section 2.2.1).

This work is not intended to be exhaustive or indeed to capture the entirety of the ACB. While the ACB shows high repeatability year to year, it does differ spatially (e.g. Madeleine et al., 2012; Atwood et al., 2022). As a result, this work only captures the scattering behaviour of water-ice clouds at Gale Crater, which tend to be relatively optically thin and are not strongly influenced by the topography within the crater (Hayes et al., 2024b).

This chapter is based on work published in Innanen et al. (2024a) and Innanen et al. (2025a), with added text and figures as well as an additional Mars year of data. Both papers were written by me, with all data analysis performed and figures generated by me.

2.2 Methods

2.2.1 The Navcam Phase Function Sky Survey

MSL's Navcams are two sets of cameras mounted on the rover's remote sensing mast (*RSM*). They operate in the 600-850 nm band with a field of view (*FOV*) of 45°×45° and a signal to noise ratio of 200:1 (Maki et al., 2012), making them well suited to observing optically thin Martian clouds. Additionally, the RSM is able to rotate 360° in azimuth and 178° in elevation (Maki et al., 2012), allowing the Navcams to observe an extremely wide range of angles.

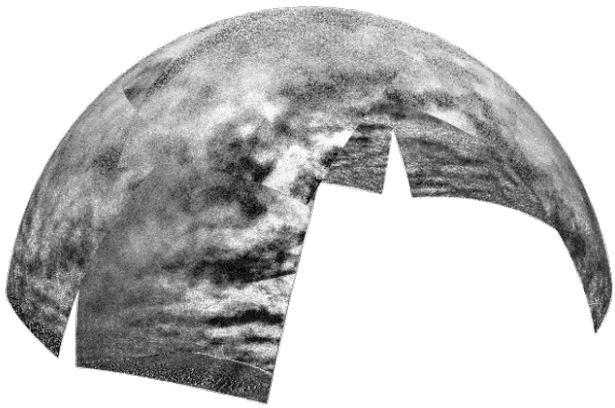


Figure 2.1: A projection of the nine pointings of the sol 1924 PFSS onto a dome. The rover is positioned at the centre, and the gap in coverage avoids imaging the sun directly.

The Navcam Phase Function Sky Survey (*PFSS*) was instituted in MY 34 and has continued in every subsequent ACB season. It consists of nine three-frame movies each at different pointings forming a dome around the rover (Figure 2.1). These nine pointings are divided into three higher elevation (+70° above the local level (*LL*) horizon) pointings at a separation of 120° of azimuth and six lower elevation (+30° LL) pointings at a separation of 48° of azimuth (Cooper et al., 2019). This procedure allows observation of a greater range of scattering angles in order to characterise the single scattering

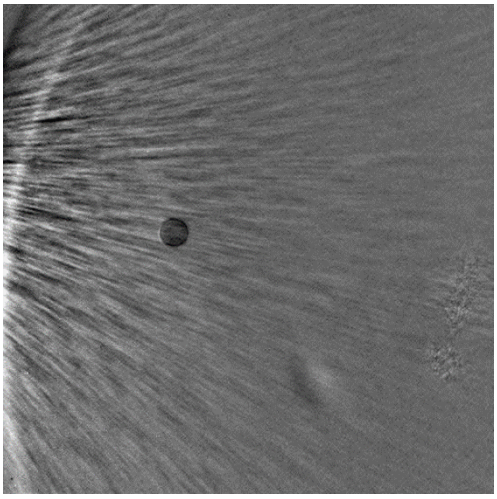


Figure 2.2: An example of an unusable PFSS frame due to sun contamination. This is pointing 9 of the PFSS taken on sol 2555 in MY 35 at 09:21:01 LTST.

phase function of ACB season water-ice clouds at Gale Crater and constrain ice crystal geometries.

The PFSS has a preferred cadence of one observation per week during the ACB season (L_s∼40° to L_s∼150°), alternating between morning and afternoon observations. It has been conducted at this approximate cadence throughout the ACB seasons of MYs 34-38.

In order to not over-saturate the Navcams by imaging the sun, there is a 2.5-hour solar keepout around local noon, and the morning and afternoon observations include a gap in their spatial coverage (Figure 2.1). However, some frames which were taken too close to the sun still proved unusable (Figure 2.2), as it was difficult or impossible to determine if clouds were present. As a result, we imposed a lower limit of 45° on the scattering angles we could confidently observe based on the FOV of the Navcams.

2.2.2 Deriving the Phase Function

The scattering phase function, $P(\theta)$, describes the angular distribution of scattered radiation – in the case of this work, sunlight scattered by water-ice clouds – as a function of scattering angle (θ). The phase function expression used in this work is derived by Cooper et al. (2019) and is based on the radiative transfer equation for plane-parallel atmospheres (Eq. 1.4.22 in Liou (2002)):

$$\mu \frac{dI(\tau, \mu, \phi)}{d\tau} = I(\tau, \mu, \phi) - J(\tau, \mu, \phi) \tag{2.1}$$

where I is the radiance from the atmosphere or cloud and J is the source term, both functions of τ, the atmospheric column optical depth, μ, the cosine of the cloud viewing angle and ϕ, the azimuthal angle. The following derivation follows Kloos et al. (2016).

Since ACB clouds observed from Gale Crater are optically thin, we can use a single-scattering approximation. The source term can be simplified to:

$$J(\tau, \mu, \phi) = \frac{\overline{\omega}}{4\pi} F_{\lambda,0} P(\theta) \exp\left[-\frac{\tau}{\mu_0}\right] \tag{2.2}$$

where $\overline{\omega}$ is the single scattering albedo and $F_{\lambda,0}$ is the in-band solar flux at the cloud. The final term, $\exp\left[-\frac{\tau}{\mu_0}\right]$, accounts for light extincted through the atmosphere, with μ_0 being the cosine of the solar zenith angle.

We then make the following three assumptions: (1) water-ice crystals have a single scattering albedo of 1 in the Navcam band (Liou, 2002; Clancy et al., 2003); (2) there is no significant scattering occurring above the clouds due to their height (Campbell et al., 2020); and (3) all radiance the Navcams observe is from sunlight scattered within the cloud. Based on these assumptions, the downward-scattered radiance from the

cloud can be given by:

$$I(\Delta\tau, \mu, \phi) = \frac{\Delta\tau}{4\pi\mu} F_{\lambda,0} P(\theta) \tag{2.3}$$

where $\Delta\tau$ is the integrated cloud optical depth. To account for light extincted by dust between the clouds and the rover, we modify Eq. 2.3 by including the term $\exp\left[-\frac{\tau_{COL}}{\mu}\right]$ where τ_{COL} is a column optical depth taken from observations by the MSL Mast Cameras (Lemmon et al., 2024a). For MYs 34 through most of 37, we interpolate a column opacity from that same Mars year. However, just after $L_s = 120°$ in MY 37, the Mastcam filter wheel suffered an anomaly, causing the method for determining column tau to change (Lemmon, 2024). As these new column tau values are still preliminary, we chose to use an average tau value calculated over the previous Mars years for the latter part of MY 37 and MY 38.

In order to get the in-band radiance, we multiply by the bandpass of the Navcams ($\Delta\lambda$). Equation 2.3 can then be reduced to:

$$I_{\lambda,VAR}\Delta\lambda = \frac{\Delta\tau}{4\pi\mu} F_{\lambda,0} P(\theta) \exp\left[-\frac{\tau_{COL}}{\mu}\right] \tag{2.4}$$

where $I_{\lambda,VAR}$ is the in-band variation in spectral radiance. Rearranging Equation 2.4 gives an expression for the phase function:

$$P(\theta) = \frac{4\pi\mu I_{\lambda,VAR}\Delta\lambda}{\Delta\tau_{WIC} F_\lambda \exp\left[-\frac{\tau_{COL}}{\mu}\right]} \tag{2.5}$$

where $\Delta\tau_{WIC}$ is the assumed cloud optical depth, derived from Navcam cloud observations (Hayes et al., 2024b). Typically, we used a cloud opacity from a cloud observation taken on the same sol or as close as possible to the corresponding PFSS. However, for MY 38 we do not have calculated cloud opacities for the cloud movies collected during that season. As a result, we take the average opacity for each L_s over the previous six Mars years. The low interannual variability we observe in the opacity (Hayes et al., 2024b) suggests that this assumption should have little impact on the phase function.

The water-ice clouds seen during ACB season with MSL are often too optically thin to be seen in raw Navcam images, so each movie undergoes mean frame subtraction (*MFS*) which removes the time-invariant component of each frame, leaving a perturbation movie of the time-varying component. As the name suggests, this is done by assembling an average frame from the three frames in each movie and then subtracting this mean frame from each individual frame pixel by pixel. Figure 2.3 shows an example of this. As in Cooper et al. (2019), we assume that scattering from dust is uniform across the Navcam images and thus it is removed by the MFS process. However, some component of time-varying dust may still be present in the MFS frames.

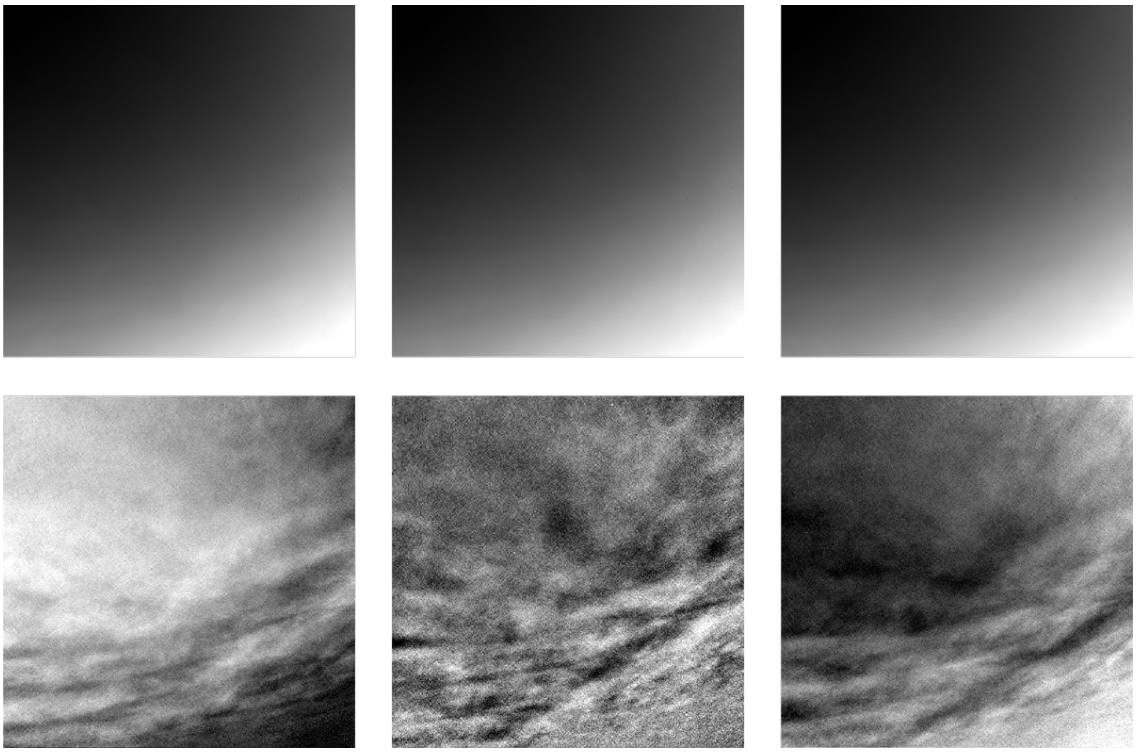


Figure 2.3: The three frames of the sol 4641 pointing 5 movie before (top) and after (bottom) MFS and contrast stretching. Cloud features that are not visible in the raw frames are clear in the MFS frames.

Following MFS, each perturbation movie is contrast-stretched and manually examined to determine if clouds are present. If they are, a radiance map of frame 2 is created from the original images to determine the variation in spectral radiance between a region of assumed cloud and a region of assumed empty sky (Figure 2.4). We select points of high spectral radiance (presumed cloud) and low spectral radiance (presumed empty sky) and average over a circle of 5-pixel radius to determine the value of $I_{\lambda,VAR}$ to be used in Eq. 2.5. The value of $I_{\lambda,VAR}$ should be taken as a lower limit, due to uncertainty in whether the low radiance region is truly empty sky or merely a thinner cloud. The selected locations of the cloud within the frame are also used to calculate the scattering angle, θ.

We select multiple adjacent points of cloud and empty sky within each movie with clouds present. The number of points extracted from each movie varies depending on how much of each frame clouds are visible in but did not exceed 16 total points.

While it is difficult to account quantitatively for all errors associated with Eq. 2.5, we can approximate the uncertainty from several sources. The MSL opacities used for this study have a mean uncertainty of around 20% (Hayes et al., 2024b), while the uncertainty on the $I_{\lambda,VAR}$ term is likewise ∼20% (Kloos et al., 2016). The contribution to uncertainty from τ_{COL} is much lower, averaging ∼6% for the ACB seasons of MYs 34, 35 and 36 (Lemmon et al., 2024a). Taken together, these give an uncertainty of around 30% for our

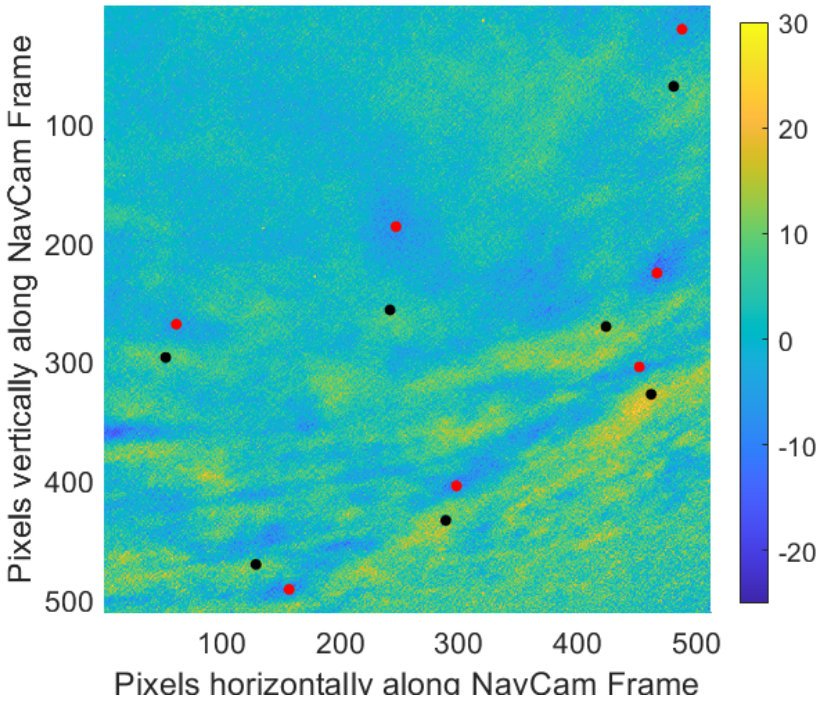


Figure 2.4: A spectral radiance map of the second frame of the sol 4641 pointing 5 movie with sample regions of high spectral radiance (black dots) and regions of low spectral radiance (red dots) indicated. The high-radiance region is assumed to be cloud, while the low-radiance region is assumed to be clear sky. The colourbar represents the change in radiance relative to the mean value of the entire image.

calculated phase function.

Typically, a phase function is normalised over scattering angles 0-180° such that the area under the curve is equal to 4π (Hansen and Travis, 1974). However, since most scattering from particles of comparable radius to Martian aerosols occurs in the forward scattering direction (scattering angles less than 40°), which the PFSS is not able to observe, it is not possible to determine what normalisation values are appropriate for our derived phase function. However, in studying the variability in the phase function and in constraining ice-crystal habit, we are more interested in the general shape of the phase function than its absolute magnitude. Normalisation of the curves will be discussed in Section 2.3.2.

2.2.3 Constraining Ice Crystal Habit

In order to comment upon ice-crystal habit, we approximate the phase function by fitting a two-term Henyey-Greenstein (*HG*, Equation 2.6) function to each Mars year's curve. HG functions are used to approximate single scattering phase functions, with a two-term equation demonstrating bidirectional scattering (Hapke, 2012b). They have a history of use in planetary applications, though are primarily used to model the phase functions of dusts and regoliths (Hapke, 2012a). However, they have been used to model atmospheric

aerosols, such as dust (e.g. Moores et al., 2015; Johnson et al., 2006), and we believe that they are a good fit for this application as at their core they are used to represent the kind of single-scattering phase functions that we derive above for the PFSS data.

The form of the two-term HG function we use is similar to that used by Moores et al. (2015):

$$P(\theta)_{HG} = \frac{(1-c)(1-b^2)}{(1+2b\cos(180-\theta)+b^2)^{3/2}} + \frac{c(1-b^2)}{(1-2b\cos(180-\theta)+b^2)^{3/2}} \tag{2.6}$$

The HG function is described by the asymmetry parameter (b) and the backscatter fraction (c). Small values of b give low, wide forward- and backscattering lobes, while larger values give higher, narrower lobes. Higher values of c correspond to smaller amounts of forward scattering, with a more strongly forward scattering particle having c< 0.5 (Hapke, 2012a). See Figure 2.5 for examples of varying b and c.

Different authors have used different formulations to define c. Hapke (2012b) uses a value of c which gives the two-term HG function as:

$$P(g)_{HG} = \frac{(1+c_H)(1-b^2)}{(1-2b\cos(g)+b^2)^{3/2}} + \frac{(1-c_H)(1-b^2)}{(1+2b\cos(g)+b^2)^{3/2}} \tag{2.7}$$

where g is the phase angle, $180° - \theta$. Thus, the value of c we use can be related to the Hapke (2012b) value (c_H) by:

$$c_H = 2c - 1 \tag{2.8}$$

This relation is important in comparing our derived b and c values from our fit HG functions to values derived for other materials. In comparing our derived values to those of materials whose properties are known, such as those of water-ice crystals and dust, we can comment upon the likely crystal habit of the ACB clouds observed by the PFSS.

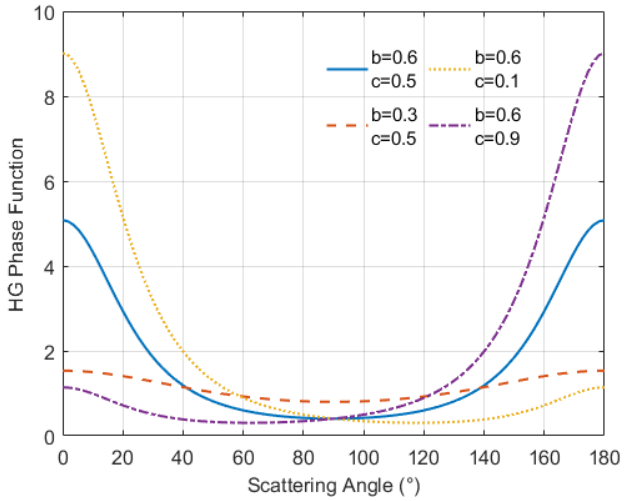


Figure 2.5: Examples of four different HG functions with different b and c values.

2.3 Results

2.3.1 Temporal Distribution

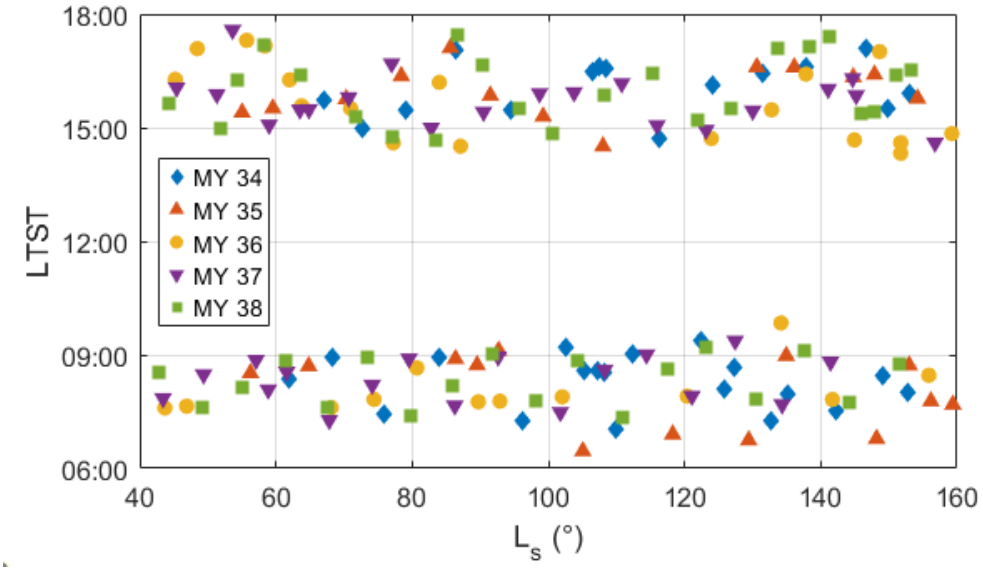


Figure 2.6: Temporal distribution of Navcam PFSS observation over the five Mars years it has executed. Observations show the distribution between morning and afternoon and the ±2.5 hour keep-out around local noon.

Figure 2.6 shows the temporal distribution of PFSS observations over the last five Mars years. In MY 34, there were a total of 35 observations over L_s range $61.9° - 156.5°$ with 20 occurring in the morning and 15 in the afternoon. In MY 35, there were 26 observations spanning L_s range $55.0° - 159.4°$ evenly split between morning and afternoon. In MY 36, there were 30 observations spanning L_s range $43.7° - 164.0°$ with 13 morning and 17 afternoon observations. The penultimate two observations (sols 3353 and 3359) were excluded from analysis as they occurred during a regional dust storm and it was not possible to differentiate water-ice clouds from dust features. In MY 37, there were 37 observations spanning L_s range $43.4° - 156.8°$ with 17 morning and 20 afternoon observations. In MY 38, there were 41 observations spanning L_s range $42.7° - 153.3°$ with 18 morning and 23 afternoon observations.

From these observations, we identified movies containing cloud features and manually selected high and low radiance points as described in Section 2.2.2. These radiance points cover scattering angles from 45° to around 160° over the four Mars years.

2.3.2 Interannual Comparison

For each Mars year, we produced a mean phase function combining all individually computed phase function values (as described in Section 2.2.2) by applying a moving average over a window size of 15° of scattering angle. This window size remains fixed regardless of the number of individual points within the 15° bin. This method produces average curves which reduce noise in the mean while preserving small yet potentially important scattering features. As mentioned in Section 2.2.2, since $I_{\lambda,VAR}$ is assumed to be a lower bound for the expected value, the resultant mean phase function should likewise be taken as a lower bound.

As discussed in Section 2.2.2, we are unable to normalise these magnitudes of these mean curves in the typical way as we are missing scattering angles below 45° and above $\sim 160°$. As a result, we normalise the phase functions around the flat portion of the MY 34 curve (scattering angles $90° - 130°$) in order to more easily compare the shape of the curve within and between Mars years.

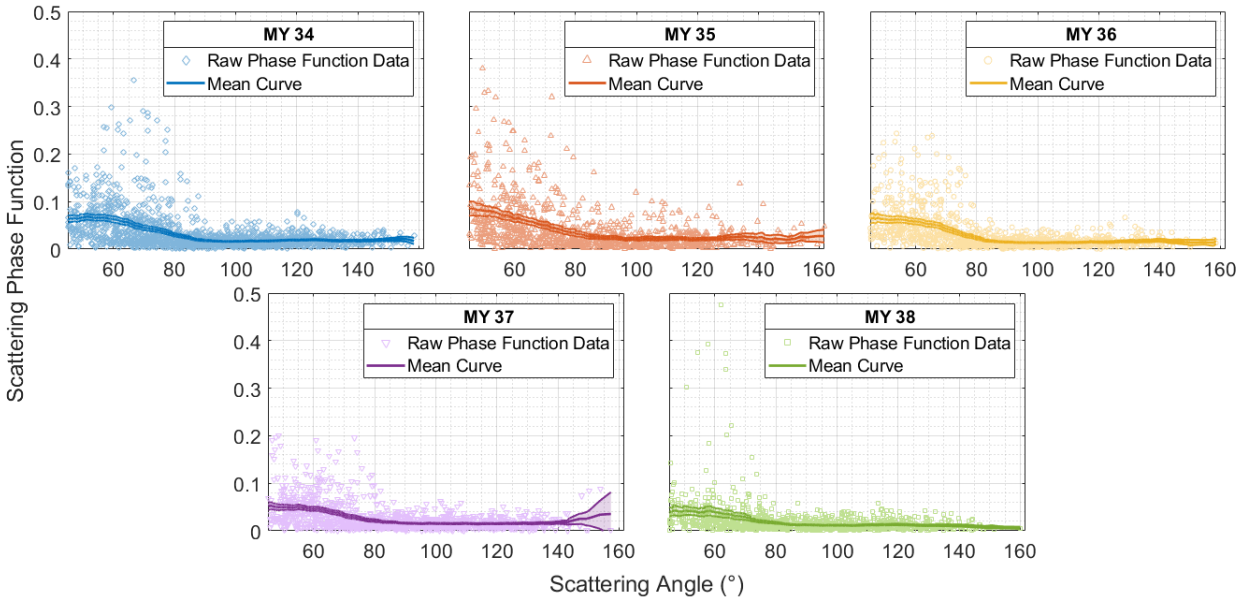


Figure 2.7: Mean curves of the derived phase functions for all five Mars years, plotted over their respective raw phase function values. The outer lines give the bounds of the 95% confidence interval. No normalisation has been applied to the curves.

The mean curves are shown in Figure 2.7 alongside the individually calculated points and 95% confidence intervals of the mean curve, which are given by $1.96\frac{\sigma}{\sqrt{n}}$. Of the individually calculated points, any that were more than 3σ away from the mean were taken to be outliers and were not included in the moving average calculation.

All four Mars years exhibit similar behaviour, with a flat region at scattering angles greater than $\sim 90°$ and an increase in magnitude towards the forward scattering direction ($45° \sim 90°$). All curves are also quite

smooth overall, with no obvious local maxima or minima.

MYs 37 and 38 both seem to have lower overall magnitudes than MYs 34-36, however since no normalisation has been performed on these curves, as discussed in Section 2.2.2, there is low confidence in the magnitudes of these curves. The MY 37 curve also has an apparent increase in magnitude around 150°. This is likely not representative of actual conditions and a result of a paucity of data at these higher scattering angles. There are only a handful of phase function values between $150° \sim 160°$, and thus the mean curve is not well constrained here, as we can see in the 95% confidence interval.

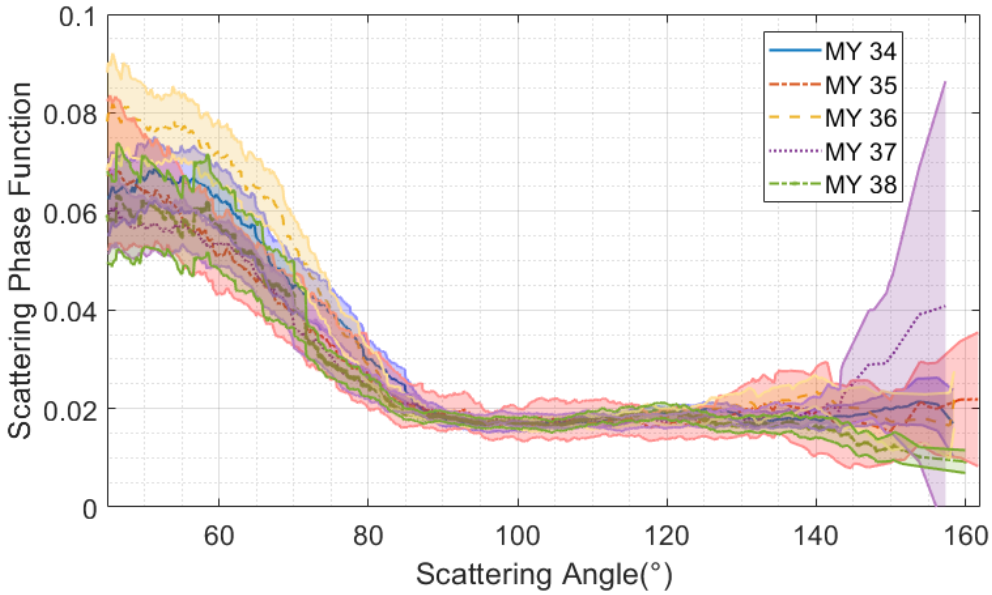


Figure 2.8: Mean phase functions for MYs 34-38. Shaded error bars give the 95% confidence interval. The phase functions have been normalised around the flat portion of the MY 34 curve to better compare their shapes.

Figure 2.8 shows the mean phase functions for each Mars year normalised and plotted over each other. All five Mars years are very similar in shape, with differences in magnitude typically falling within the 95% confidence intervals of the other curves.

2.3.3 Seasonal Comparison

We were interested in seeing if there were any changes to the phase function over the course of the ACB season. In order to examine this, we divided the phase function observations into three seasonal bins for each Mars year: early ACB, spanning $L_s = 40° - 80°$, mid ACB, spanning $L_s = 80° - 120°$, and late ACB, spanning $L_s = 120° - 160°$. As with the PFSS observations, the early and late ACB bins extend beyond the typical bounds of the ACB by about 10° of L_s. Using the same method described in Section 2.3.2, we constructed mean phase functions for each seasonal bin in each Mars year (Figure 2.9).

We can see little seasonal variability in the shapes of the curves for each Mars year. While the later ACB

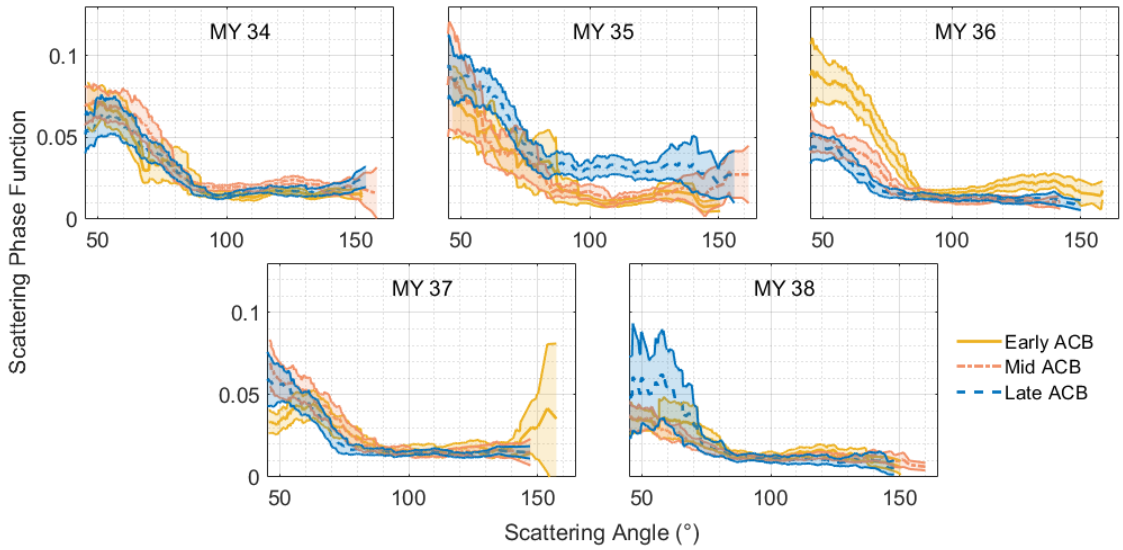


Figure 2.9: Mean curves for each Mars year divided into three seasonal bins: early ACB ($L_s = 40° - 80°$), mid-ACB($L_s = 80° - 120°$) and late ACB ($L_s = 120° - 160°$). The three seasonal curves for each Mars year have been plotted against one another to explore seasonal variability. Shaded regions show the 95% confidence interval.

curve in MY 35 seems to have a higher magnitude, these curves have not been normalised and the shape remains consistent throughout the MY. Likewise, the early ACB curve in MY 36 has a higher magnitude, which could also be due to the lack of normalisation.

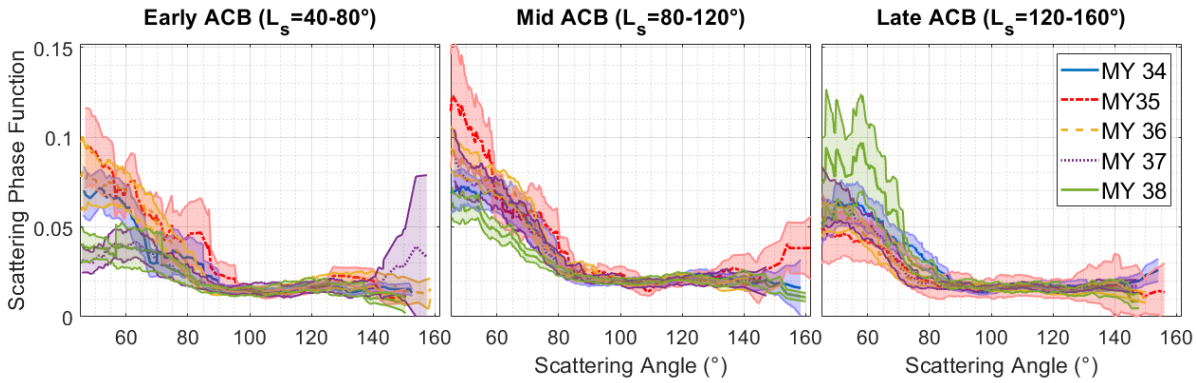


Figure 2.10: The mean curves for the three seasonal bins for each Mars year. The mean curves for the five MYs have been plotted against one another in each seasonal bin to examine interannual variability. Each phase function has been normalised around the flat portion of the MY 34 curve. Shaded regions show the 95% confidence interval.

We also examine interannual variability in the three seasonal divisions of the ACB (Figure 2.10). As in Section 2.3.2, the curves shown in Figure 2.10 were normalised around the flat portion of the MY 34 curve in each seasonal bin. Again, there is not much year-to-year variation in the shape of the phase function, except in the case of the early ACB. Here, we see much flatter curves for MYs 37 and 38, with less of a defined increase towards the forward scattering direction. Potential reasons for these trends will be discussed in Section 2.4.1.

2.3.4 Diurnal Comparison

In order to examine diurnal variability in ACB clouds at Gale Crater, we divided the PFSS observations into morning and afternoon bins for each Mars year. We applied the same moving average as in Section 2.3.2 to create mean morning and afternoon phase functions (Figure 2.11).

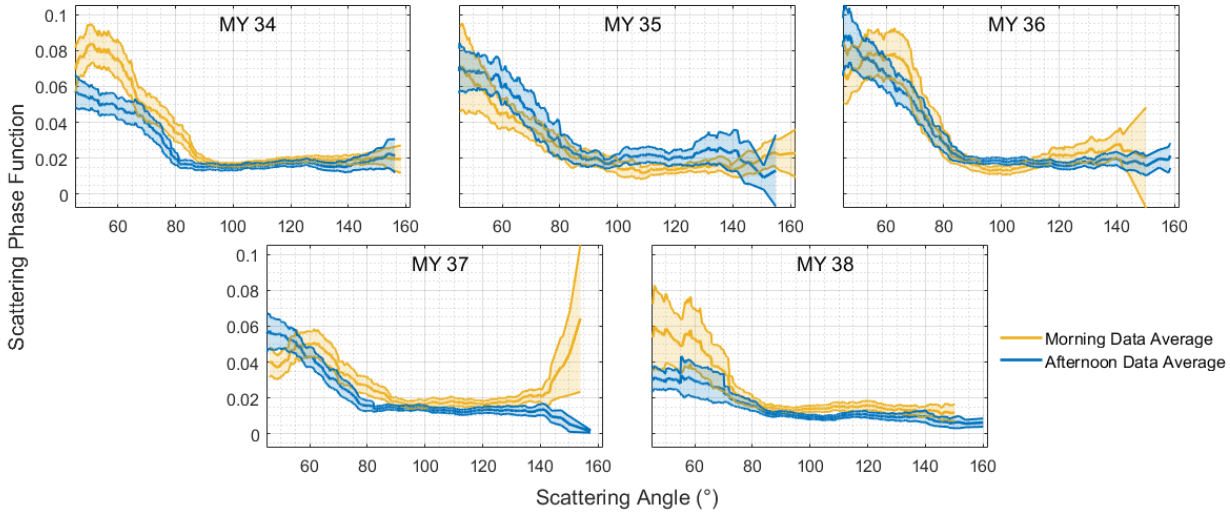


Figure 2.11: Comparisons of morning and afternoon phase functions for each Mars year. Shaded error bars give the 95% confidence intervals.

While there appears to be little diurnal variability in MYs 35-37, the MY 34 curves have distinct shapes, especially at scattering angles less than 90°. Potential reasons for this discrepancy will be discussed in Section 2.4.1. For the other Mars years, the good agreement between the morning and afternoon phase functions indicates that the phase function remains consistent throughout the sol.

2.3.5 The Henyey-Greenstein Function

To comment upon ice-crystal habit, we fit the two-term HG function (Equation 2.6) described in Section 2.2.3 to the full range of data for each Mars year using a non-linear least squares method. Figure 2.12 shows the fit HG functions for each Mars year.

While the curves all look relatively flat, especially over this range of scattering angles, the b and c values which describe the curves encode information about ice crystal habit, as described in Section 2.2.3. The b and c values for each Mars year's HG function are given in Table 2.1 and plotted with their 95% confidence intervals in Figure 2.13.

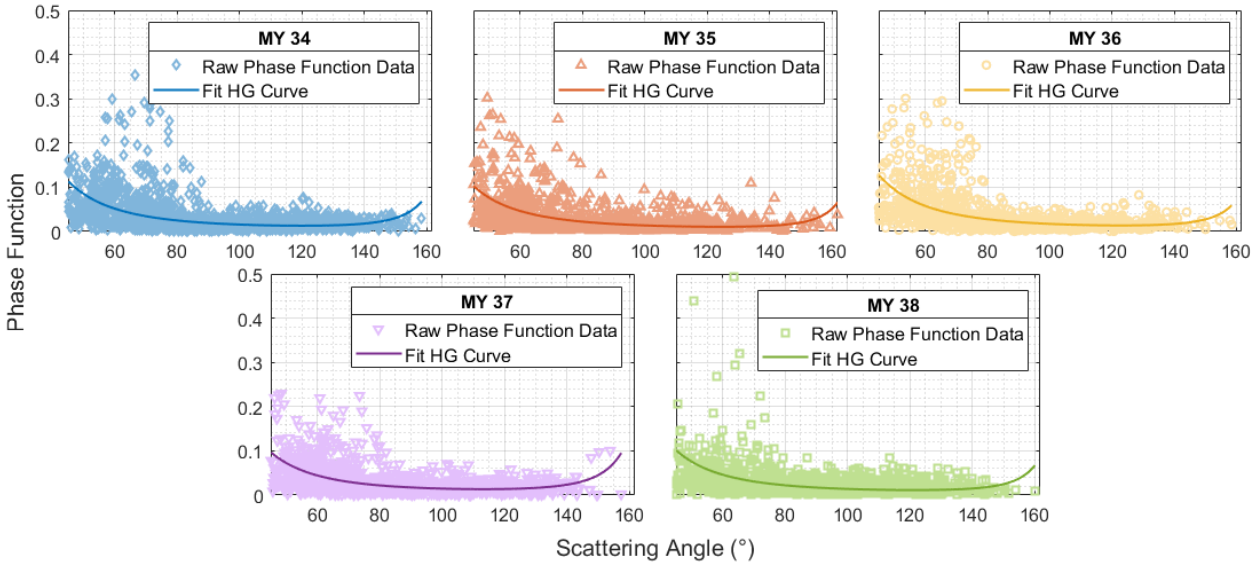


Figure 2.12: Fit HG functions for each Mars year.

Table 2.1: *b and c values for each Mars year's fit HG function.*

MY	b	c
34	0.9736	0.0606
35	0.9766	0.0403
36	0.9708	0.0450
37	0.9762	0.1123
38	0.9766	0.0538

The asymmetry parameters (b) are all very similar for each MY and while the 95% confidence intervals for MYs 34-38 do not all overlap, they are all within 0.01 of each other. In the backscatter fraction (c), we see a bit more variability and larger error bars. MY 37 is the most notably different with the highest backscatter fraction, and no overlap in the 95% confidence interval with MYs 34-36. This higher c value is likely caused by the paucity of data points at higher scattering angles, artificially giving a higher backscatter. In Figure 2.12, we can see that the HG function is increased by the three higher phase function values around 150°, as also occurs in the mean phase function (Figure 2.8).

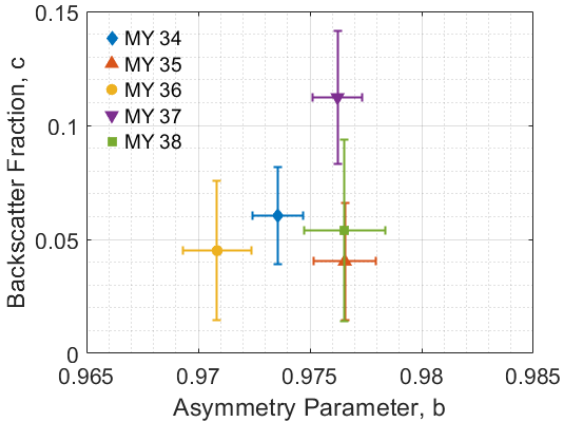


Figure 2.13: Asymmetry parameter (b) vs backscatter fraction (c) for all five Mars years. Error bars show the 95% confidence intervals in b and c.

2.4 Discussion

2.4.1 Variability in the Mean Phase Functions

The similarities in the shape of the whole Mars year curves (Figure 2.8) suggest low interannual variability in the phase function and likely also in crystal habit. This is unsurprising, given the highly repeatable nature of the ACB and the similar lack of variability in water-ice cloud opacity observed year-to-year at Gale Crater (Hayes et al., 2024b). The curves also do not exhibit any strong local maxima or minima which are indicative of scattering phenomena. Indeed, no such phenomena have been observed at Gale Crater, though a halo has been observed at Jezero Crater (Lemmon et al., 2022).

In terms of seasonal variability, we can see in Figure 2.9 that for each Mars year the phase function does not exhibit any strong seasonal dependence, which we also observe in cloud opacities at Gale (Hayes et al., 2024b). However, we see hints of interannual variability in the early ACB, with the MY 37 and 38 curves appearing flatter than those of MYs 34-36 (Figure 2.10).

It is difficult to pinpoint a reason for the flattening of the early ACB curves in MYs 37 and 38. There does not seem to be a systematic reason for this difference. All three seasonal bins for MYs 37 and 38 have the same range of scattering angles, with no obvious areas where a paucity of data may be responsible for the differences in curve shape. Additionally, the column tau in the early ACB season is very consistent with that of previous Mars years, and there is no obvious seasonal variability in cloud opacity in MY 37 (Hayes et al., 2024c). Our use of average column and cloud opacities for MY 38 likewise results in a lack of seasonal variability in the opacity.

In MYs 36-38, we began collecting PFSS observations earlier than the previous two Mars years, starting nearer to $L_s = 40°$ during the transition into ACB season (Figure 2.6). Capturing this transition could be responsible for these differences, showcasing the natural variability in water-ice crystal formation during the start of the ACB. The formation of these earliest clouds could be influenced by factors such as differing temperature, pressure, or relative humidity, which could impact water-ice crystal formation. The differences in phase function shape for the early ACB in MYs 37 and 38 could indicate a difference in water-ice crystal habit at the very start of the ACB season. The lack of agreement with MY 36, for which we also have these earlier observations, could be simply due to variation in the formation fo the ACB at Gale Crater, and the clouds we happened to capture in each of these three Mars years.

Diurnal variability in the ACB is observed at other locations on Mars (e.g. Madeleine et al., 2012; Patel et al., 2023), likely due to differences in temperature and cloud formation mechanism (Tamppari et al., 2003). However, we see little diurnal variability in cloud opacity at Gale Crater (Hayes et al., 2024b) and

more generally around the southern edge of the ACB (Atwood et al., 2022). MYs 35-38 show no diurnal variability outside the range of uncertainty, however MY 34 exhibits distinct shapes in the mean phase function curve, especially at scattering angles less than 90° (Figure 2.3.4), with the afternoon curve being slightly more flattened. It should be noted that the apparent decrease in the AM curves for MYs 34 and 36 around 45° is likely not real and is a result of the relative scarcity of points at those scattering angles. The apparent increase in the AM curve and decrease in the PM curve of MY 37 near 160° should likewise be discounted for the same reasons.

As with the early ACB interannual variability discussed above, there is no clear reason for the apparent difference in the shapes of the MY 34 morning and afternoon curves. There does not appear to be any systematic reason for the differences we see within the data themselves. However, MY 34 does have a greater number of higher opacities in the mornings, even though these are outliers, and the majority of morning cloud observations have opacities similar to those observed in the afternoon (Hayes et al., 2024b). However, higher cloud opacities would result in a lower value of the phase function, whereas we see a higher value of the morning phase function, especially at smaller scattering angles.

While the phase function depends on cloud opacity, the opacity calculation itself depends on the cloud phase function. Especially at smaller scattering angles, where the phase function becomes less flat, the opacity is more heavily dependant on the phase function. We recalculated the MY 34 phase function using an average cloud opacity value of 0.1 and saw that the flat part of the curve remains pretty much the same; however at scattering angles below $\sim 65°$, the curve becomes slightly flatter (though the 95% confidence intervals of both curves still overlap).

A number of different particle properties impact the shape of the phase function, notably particle shape and size, but also features such as the surface roughness of the particle (Eg. Yang et al., 2013) and any inclusions, such as air bubbles (Eg. Macke et al., 1996), within the particle itself. Additionally, when examining bulk scattering properties as we do here, the presence of different ice crystal habits can smooth out scattering features that may be present from a single habit (Bohren and Singham, 1991). Section 2.4.2 further discusses our attempts to constrain a water-ice crystal habit.

2.4.2 Comments Upon Ice Crystal Habit

To constrain the water-ice crystal geometry we observe, we can compare our derived b and c values to those derived for known particle geometries. Hapke (2012a) collected HG functions for 495 regolith and dust particles and plotted their b and c values (Figure 2 of Hapke, 2012a). All these values lie within a physically allowable region defined as follows (Eq. 6 in Hapke, 2012a):

$$|c_H| \leq \frac{1+3b^2}{b(3+b^2)} \tag{2.9}$$

keeping in mind that c_H is related to the c used in this work by Equation 2.8.

The b and c values for our fit HG functions all fall within this allowable region. Figure 2.14 shows the b and c values of our derived phase functions plotted over Figure 2 from Hapke (2012a). Error bars represent the 95% confidence interval on both b and c values, though the error in b is too small to be displayed at this scale. While the asymmetry parameter, b, appears to be fairly well constrained especially when compared to c, it is important to recall that our data only spans scattering angles 45°-160°. These limitations mean that we cannot see the regions of the phase function where we would expect to see the most scattered light, and therefore the HG functions for each Mars year are only a best guess within this available data.

Our b and c values align most closely with those reported by Souchon et al. (2011), which studied volcanic samples. In particular, our b and c values fall near those for irregular, rough, opaque Hawaiian basalt and round, smooth, translucent Hawaiian olivine (Figure 8 in Souchon et al., 2011). While the actual character of the observed cloud particles may differ from these regoliths, this could indicate that the cloud particles have a similarly rough, irregular habit. Furthermore, this result could point to a thin film of water ice accreted onto dust particles.

To examine how closely our observed cloud particles resemble martian dust, we compare our results with those for three martian dust particles which have had HG functions fit to them. These are taken from observations at the Spirit rover site (Johnson et al., 2006), the Phoenix lander site (Moores et al., 2015), and, most relevantly to our observations, Gale Crater (Chen-Chen et al., 2019). Johnson et al. (2006) fit an HG function to HWMK919 simulant, an analogue to martian dust (Morris et al., 2001), at a number of different wavelengths. Here, we use their results at 750 nm, which falls within the bandpass of the MSL Navcams. The Chen-Chen et al. (2019) results also use observations from the MSL Navcams, but fit a three-term HG function. We fit our two-term expression to their curve to extract b and c values. The Stereo Surface Imager on Phoenix used in the Moores et al. (2015) study has a bandcentre of 450 nm, outside the bandpass of the Navcams, but which we still include as a point of comparison. Figure 2.15 shows our b and c values plotted alongside the martian dusts.

We also fit the same HG function to the phase functions for six modelled water-ice crystals with particle sizes around 3 μm (Bi and Yang, 2014), on the order of likely martian water-ice crystal sizes (Clancy et al., 2003). Figure 2.15 shows these alongside our fit values. Also included here are the b and c values for a theoretical smooth, transparent sphere (McGuire and Hapke, 1995), as many climate models assume spherical water-ice crystal geometry.

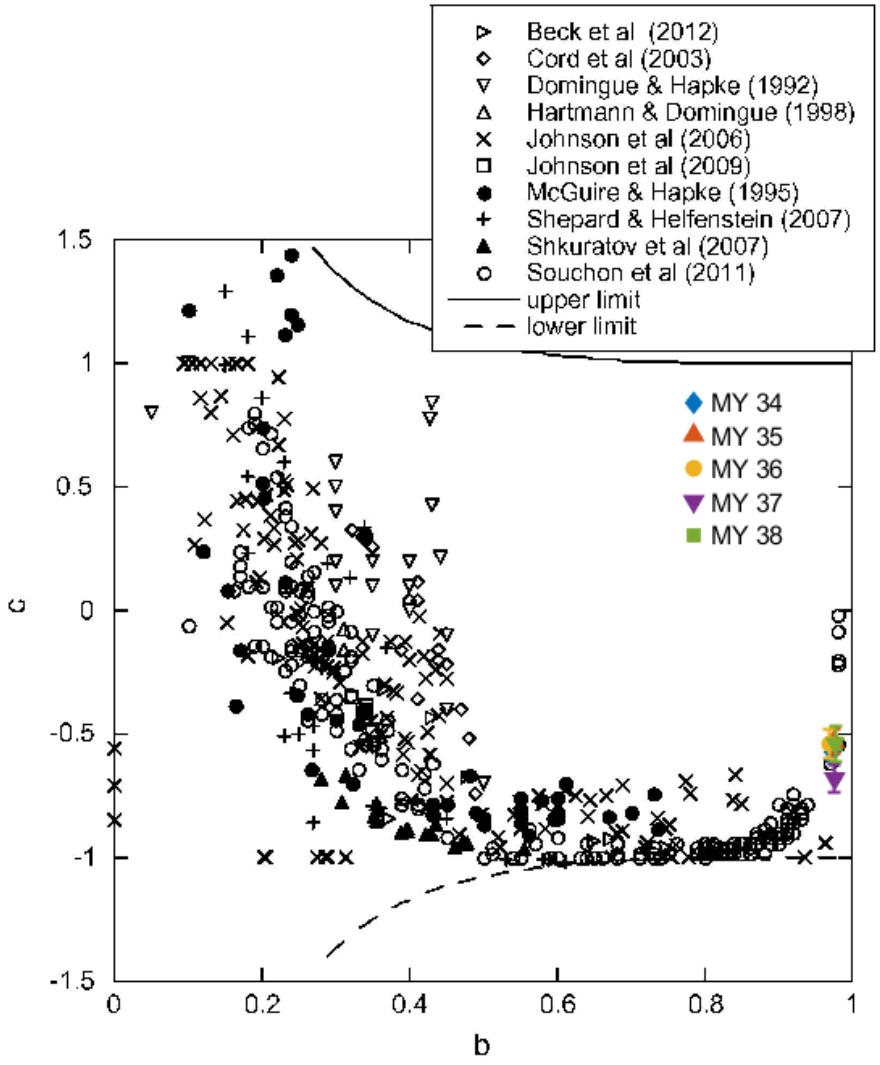


Figure 2.14: b and c values for fit HG functions for MYs 34-37 plotted over Figure 2 from Hapke (2012a) which shows b and c values of the 495 dust and regolith particles described therein. The 'hockey stick' region of allowable values is shown as solid and dashed lines. Error bars on the MY 34-37 values show the 95% confidence bounds on b and c, though only those on c are visible at this scale. Take note that the Hapke (2012a) definition of c differs from the one used in this work (Equation 2.8).

Our data do not agree closely with any of the martian dusts, nor with the modelled water-ice crystals. The lack of agreement with any of the modelled water-ice crystal geometries supports the suggestion that the cloud particles we see in the ACB at Gale are of some irregular geometry. Our phase functions also do not agree particularly closely with any of the three martian dusts. If the cloud particles we see are indeed ice-rimed dust, the accreted water-ice layer seems to be significant enough to change the scattering properties from those of dust alone.

Due to our narrow range of scattering angles, there is some inherent uncertainty associated with our fit HG functions as we cannot see either the forward- or backscattering lobes. Additionally, the practice of using

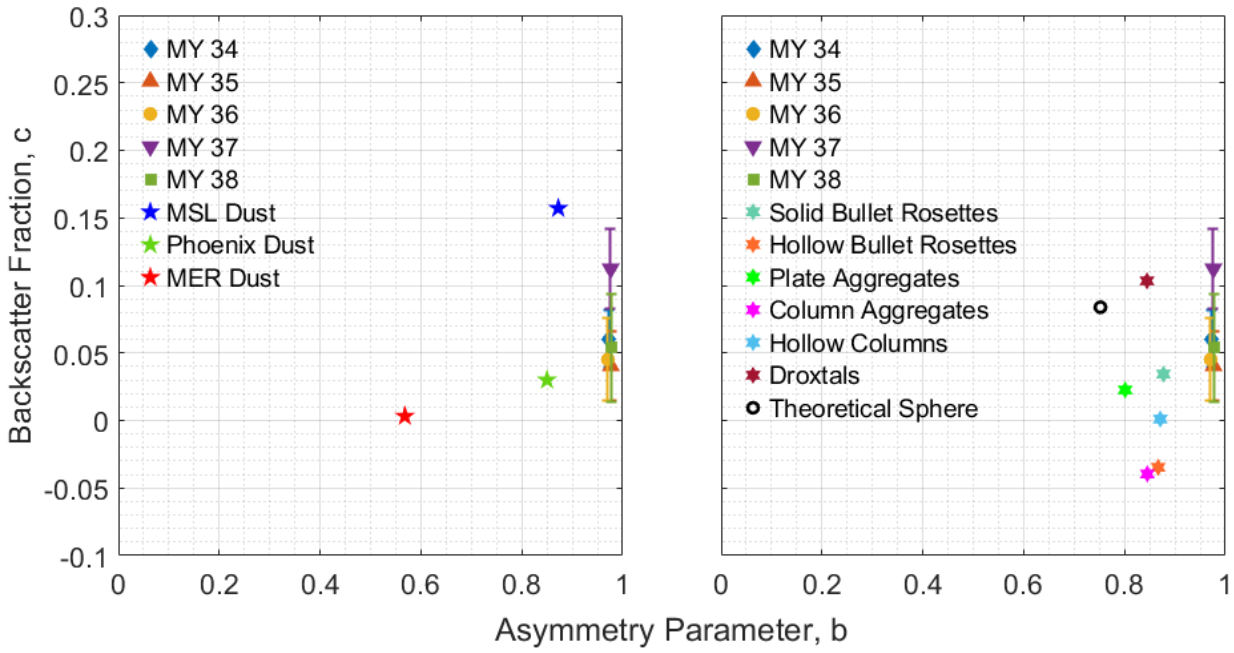


Figure 2.15: Asymmetry parameter (b) and backscatter fraction (c) values for our derived PFSS phase functions compared with b and c values for three martian dusts (left, Johnson et al., 2006; Moores et al., 2015; Chen-Chen et al., 2019) as well as six modelled water-ice cyrstal geometries (Bi and Yang, 2014) and a theoretical smooth transparent sphere (McGuire and Hapke, 1995)(right). Error bars on our PFSS phase functions give the 95% confidence bounds on b and c.

HG functions is primarily employed in planetary applications to regoliths and dusts, so there is a paucity of points of comparison for water-ice particles.

Chapter 3

Can CaSSIS see Suboptical Clouds?

3.1 Motivation & Author Contribution

The Colour and Stereo Surface Imaging System (*CaSSIS*) is the ExoMars Trace Gas Orbiter's (*TGO*) main imaging system. It is capable of taking both single images and stereo pairs at a resolution of $\sim$ 4.6 m/pix from an altitude of $\sim$ 400 km. These images may be up to $\sim$ 9.5 km wide and $\sim$ 50 km long. CaSSIS has four broadband filters optimised for Mars photometry (BLU, centred at 495 nm, PAN at 678 nm, RED at 836 nm and NIR at 939 nm). It uses a 'push-frame' image acquisition mode, building up image strips along TGO's track. Unlike other Mars orbiters, TGO's orbit is not sun-synchronous, which allows it to capture images at various local times and solar incidence angles (Thomas et al., 2017).

While CaSSIS has been used primarily as a geological instrument, it has at times observed clouds especially in the northern hemisphere (Machado et al., 2025). Optically thick clouds, like those that form around polar craters (Figure 3.1) and the Tharsis mountains, are obvious to the eye in CaSSIS images. However, optically thinner clouds including clouds which we observe above Gale Crater during the ACB season, may be missed in CaSSIS images. These clouds tend to be suboptical, meaning that they are not able to be seen in the raw Navcam images, and average opacities of $\sim$ 0.1 (Hayes et al., 2024b).

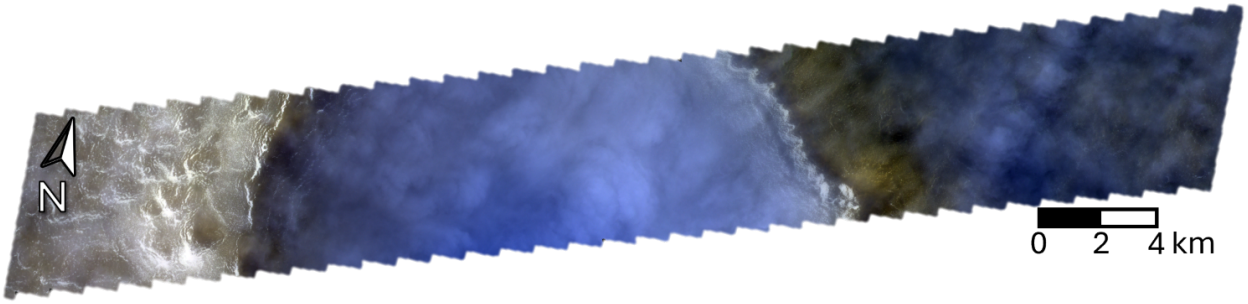


Figure 3.1: An example of a CaSSIS image (MY36_015998_085_0) of clouds in and around a northern crater at 73.3°N, 178.1°E. This image uses the NIR, PAN and BLU filters and was taken at 10:24 LST at $L_s = 63.2°$ in MY 36.

MSL has a large existing dataset of cloud observations spanning the time from MSL's landing until present (see Section 1.5). While MSL's cloud imaging happens throughout the Mars year, the most productive time

to view clouds is during the ACB season (see Section 1.2). I investigate overlapping CaSSIS and MSL cloud observations in order to determine the limits of detection of optically thin water-ice clouds by CaSSIS.

All analysis, writing and figure generation was completed by me. MSL cloud opacities up to MY 37 were calculated by Diana Hayes (Hayes et al., 2024c), while those for MY 38 were calculated by me.

3.2 Dataset

3.2.1 CaSSIS Observations

Of the thousands of CaSSIS images acquired to date, 82 have been taken in and around the vicinity of Gale Crater (Appendix A). Of these, the most recent eight were taken during a coordinated MSL-CaSSIS imaging campaign which was implemented in MY 38 (see Section 3.2.3). The remaining 74 images can be seen in Figure 3.2. 28 images were taken within a few hours of an MSL cloud movie (shown in red and green in Figure 3.2). This acts as an indication for whether clouds are likely to be present in the CaSSIS images. Of these observations, 8 were taken on sols on which there are clouds visible in the MSL cloud movies. These are summarised in Table 3.1.

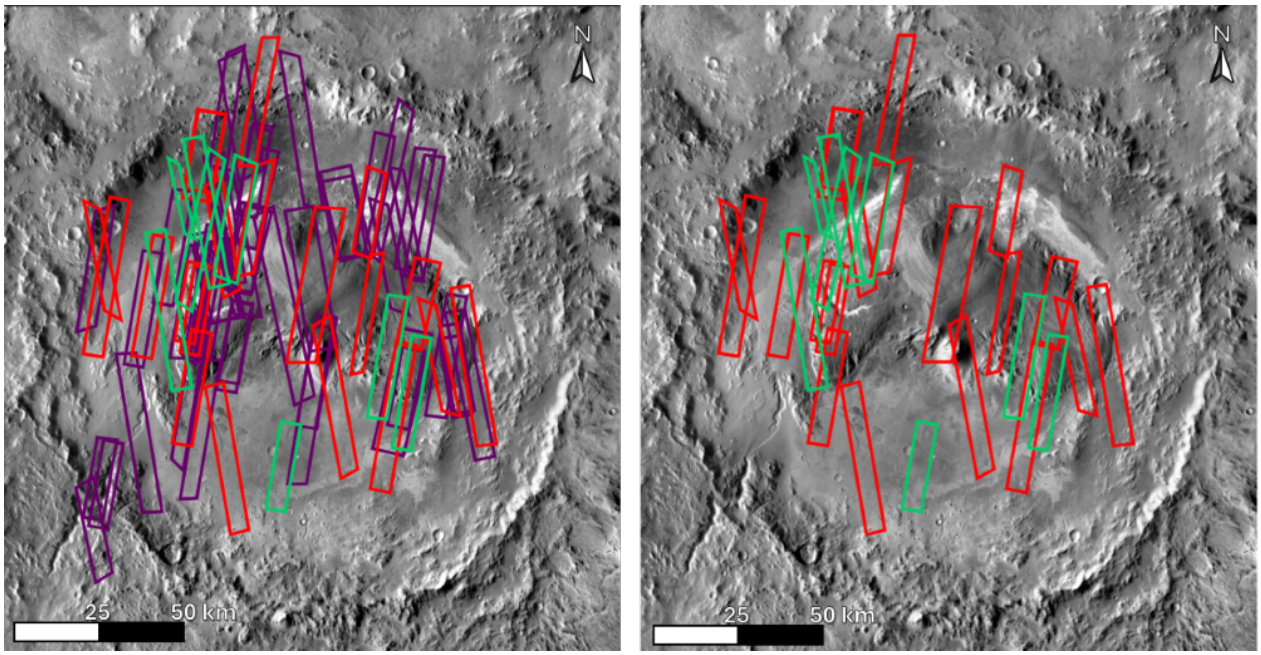


Figure 3.2: The locations of 74 CaSSIS images taken around Gale Crater prior to the coordinated imaging campaign with MSL (Section 3.2.3) shown in JMARS. (Left) All 74 images acquired. (Right) Only images acquired on days when MSL also acquired a cloud movie. In both panels, purple represents images taken on sols without a corresponding MSL cloud movie, red shows images acquired on sols with an MSL cloud movie where clouds were not seen, and green shows images aquired on sols with an MSL cloud movie in which clouds were seen.

CaSSIS can capture both single images and stereo pairs (Thomas et al., 2017). All the images listed

Table 3.1: *CaSSIS observations taken around Gale Crater at times when MSL cloud movies indicate the presence of clouds.*

CaSSIS Image ID	**L$_s$ (°)**	**Imaging Time (SCET)**	**LST**	**Cloud Movie Sol & LTST**	**MSL Cloud Movie Type**
MY35_007380_357_0	55.0203	2019-07-20 03:23:12.889	14:45:47	2471 15:18:36	CAO
MY35_012472_186_0	274.245	2020-09-09 00:50:51.559	8:15:13	2877 07:44:26	SHM & ZM
MY36_018708_356_0	167.346	2022-02-01 16:15:45.161	8:42:07	3374 08:38:31	ZM
MY36_020089_355_3	234.226	2022-05-25 18:05:10.750	9:41:07	3484 11:53:18	SHM
MY37_024431_355_3	64.7415	2023-05-16 06:37:49.709	9:39:26	3830 09:00:19	SHM & ZM
MY37_026416_186_3	138.485	2023-10-25 18:28:39.209	13:30:34	3988 11:57:01	SHM
MY37_028108_186_0	215.293	2024-03-12 07:26:16.664	9:36:22	4123 08:40:11	SHM & ZM
MY37_028462_352_0	233.364	2024-04-10 08:00:28.480	15:25:27	4151 17:38:47	SHM & ZM

in Table 3.1 are single images (indicated by the final digit of the image ID with 0 or 3 representing single images). With the exception of MY35_012472_186_0 and MY36_018708_356_0, which are only taken with the NIR, PAN and BLU bands, all images are taken with all four of CaSSIS' bands.

Only three of the cloudy CaSSIS images were taken during the ACB season (MY35_007380_357_0, MY37_024431_ 355_3 and MY37_028108_186_0). This is the only time of year where we are relatively certain that the clouds observed by MSL are water-ice clouds and not composed instead of dust.

3.2.2 MSL Cloud Movies

We used three different cloud observations in this work, all of which use MSL's Navcams: the Zenith Movie (*ZM*), Suprahorizon Movie (*SHM*) and Cloud Altitude Observation (*CAO*). The ZM consists of eight frames taken 38 seconds apart at an elevation of 85°. The azimuthal pointing of these movies changes from south pointing (180°) during $L_s = 0 - 190°$ to north pointing (0°) during $L_s = 190 - 360°$ to avoid the sun. CAOs, which were developed and implemented in MY 35 to estimate cloud height, consist of a ZM paired with a cloud shadow movie. For this analysis, we only use the ZM in the CAO to determine opacity.

From sol 1032 to sol 4044, the SHM was identical to the ZM but at an elevation of 26°. Starting on sol 4044 ($L_s \sim 168°$ of MY 37), the number of frames was increased to 16, though the duration of the observation remained the same. SHMs are sun safe at any time during the sol, and thus can be taken throughout the sunlit hours. ZMs and CAOs have a keepout of ±2.5 hours from local noon. The ZM and SHM are taken throughout the whole Mars year with a preferred cadence of one cloud movie every three sols. The CAO is only executed during the ACB season, typically in the afternoon.

3.2.3 Coordinated Imaging Campaign with MSL

During the ACB season of MY 38, we implemented a joint imaging campaign between CaSSIS and MSL, attempting to image the same clouds from orbit and from the surface. As CaSSIS's operations are more constrained due to TGO's orbit and the instrument's planning cadence, operations are planned further in advance and times of upcoming CaSSIS observations are known several weeks to months in advance. From this, we could strategically add cloud observations to MSL plans, which are created on a much shorter cadence. We attempted to capture cloud movies as close in time to CaSSIS observations as possible, keeping in mind rover operational constraints.

The eight CaSSIS observations of Gale Crater are shown in Figure 3.3. Their timings, and the timings of the corresponding MSL observations are given in Table 3.2.

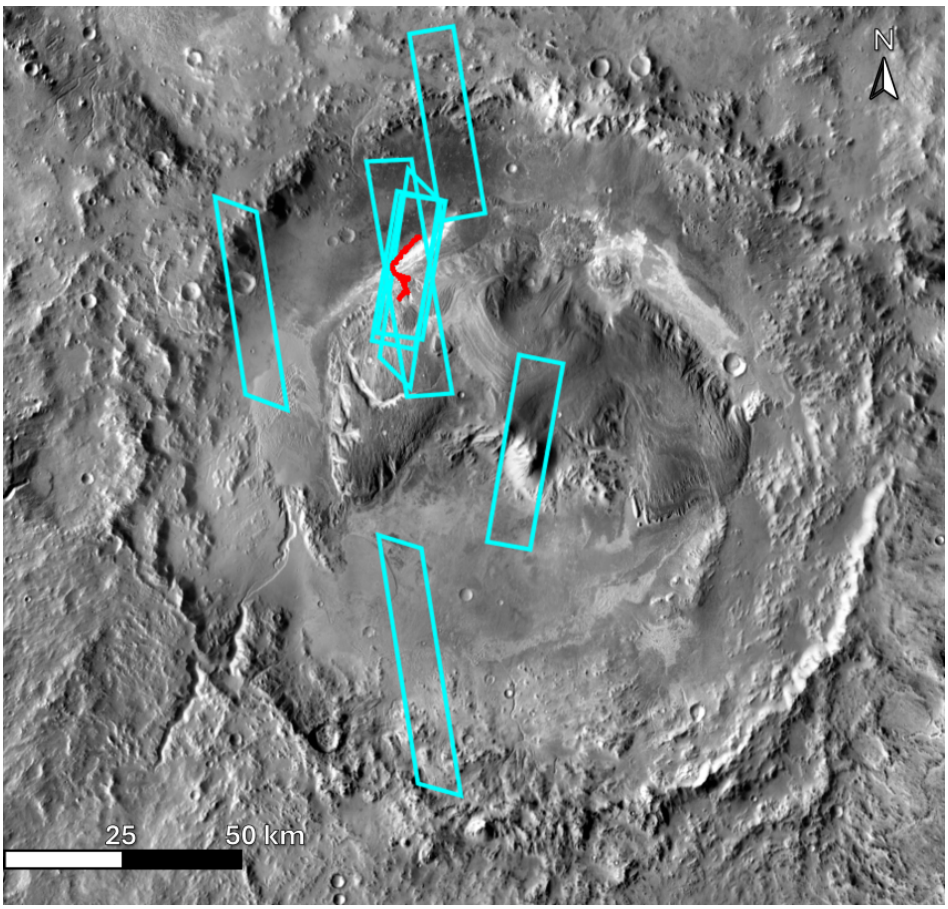


Figure 3.3: The locations of the eight CaSSIS images that has coordinated MSL cloud movies in the ACB season of MY 38, shown in JMARS. The MSL traverse is shown in red on the base map.

With the exception of MY38_034521_354_1 & _2, which are a stereo pair of images, all observations are single images using all four channels. The first image of the stereo pair uses only the BLUE, PAN and NIR channels, while the second uses only the BLU, PAN and RED channels.

Table 3.2: *Timings of Coordinated CaSSIS and MSL cloud observations.*

CaSSIS Image ID	L_s (°)	Imaging Time (SCET)	MSL Sol & LMST	Actual Time MSL Movie Executed	MSL Cloud Movie Type
MY38_033831_184_0	101.1	2025-06-23 21:48:51	4579 10:30:51	4579 10:01:46	SHM
MY38_034055_185_0	109.4	2025-07-12 06:00:17	4597 06:55:37	4597 10:30:52	SHM
MY38_034297_353_0	118.5	2025-08-01 02:28:45	4616 14:39:11	4616 14:26:13	CAO
MY38_034409_354_0	122.8	2025-08-10 06:34:39	4625 12:51:45	4625 12:47:33	SHM
MY38_034521_354_1	127.2	2025-08-19 10:40:13	4634 11:04:00	4634 11:53:56	SHM
MY38_034521_354_2	127.2	2025-08-19 10:40:59	4634 11:04:44	4634 11:53:56	SHM
MY38_034901_190_0	142.3	2025-09-19 12:30:54	4664 16:57:20	4664 16:55:53	CAO
MY38_035125_187_0	151.6	2025-10-07 20:41:44	4682 13:21:32	4682 13:55:23	SHM

There were several operational constraints which impacted the coordination of MSL cloud movies. The ±2.5 hour noon keepout of the ZM and CAO meant that we could only use SHM for the majority of the coordinated observations with CaSSIS. Additionally, the ACB season falls in the southern winter, when additional heating is required for rover operations early in the morning and late in the evening. Despite these constraints, in all but one case we were able to schedule an MSL cloud movie within an hour of the CaSSIS observation. This increases the likelihood that any clouds we observe in the cloud movies would be present at the time the CaSSIS images were taken.

3.3 Methods

3.3.1 Determining Cloud Opacity from MSL Movies

We determine cloud opacities from MSL cloud movies using the method described in Hayes et al. (2024b). While that work considers two different models to calculate opacity, in this work we use only the High Cloud (HC) model. The derivation, as described in Kloos et al. (2016), is identical to that presented in Equations 2.1 - 2.4 of this dissertation. However, instead of isolating the phase function, we rearrange to get:

$$\Delta\tau_{HC} = \frac{4\pi\mu I_{\lambda,VAR}\Delta\lambda}{P(\theta)F_0 \exp\left[-\frac{\tau_{COL}}{\mu}\right]} \tag{3.1}$$

where the terms of this equation are identical to those described in Section 2.2.2. Note that the phase function used in this expression is the average phase function derived in Hayes et al. (2024b), which was used in that work to correct opacities for the phase function effect based on the scattering angle of the observed clouds.

As with the movies of the phase function sky survey (Chapter 2), we create mean frame subtracted versions of the cloud movies to show the time-varying component of the image. We can then determine $I_{\lambda,VAR}$ from a radiance map of a single MFS frame within the movie and use this to calculate the cloud opacity at that point.

3.3.2 Examining Channel Statistics

We can look at the image statistics of each channel to determine whether the suboptical clouds are having an obvious impact on any one channel. The CaSSIS products we use contain the georeferenced and radiometrically calibrated images in each channel that was used for the observation. The radiometric calibration gives the I/F (reflected radiance over solar irradiance) reflectance values at each wavelength. We are able to stack multiple channels to create colour images, with NPB being the most commonly used in this work. Different spectra created from the four channels indicate different types of materials present within a scene.

Surface water-ice and water-ice clouds and fogs tend to show up in CaSSIS images as higher reflectances in the BLU band relative to the NIR (Tornabene et al., 2017; Rangarajan and Tornabene, 2026). To examine this, we look a the ratio of the BLU to NIR on a pixel by pixel basis. Values of this ratio greater than 1 indicate that there is more reflectance in the BLU channel, while less than 1 indicate higher reflectance in the NIR. However, features around Gale Crater such as sand patches are also highly reflective in the BLU channel, so we cannot use a simple ratio without also visually inspecting the scene.

We can also look at the mean and standard deviations in the reflectance across the scene. Moores et al. (2010) used a similar method to determine optical depth from Phoenix movies, examining the mean and varying irradiance. As the BLU channel is often much lower than the other channels over all, we also examine the corresponding coefficient of variation. The coefficient of variation is the ratio of the standard deviation to the mean and gives an idea of the dispersion of the distribution of reflectances around the mean, even if the means vary from channel to channel. A larger coefficient of variation is indicative of more variation across the scene in that channel, whereas a smaller one means the scene is reflecting fairly evenly in the channel.

3.4 Results & Discussion

3.4.1 Coordinated CaSSIS-MSL ACB Images

Because of the difficulty in distinguishing dust clouds from water-ice clouds outside the ACB season, we begin by looking only at the opacities of clouds during the ACB season. With the three movies taken concurrently with CaSSIS movies prior to MY 38 and our eight coordinated observations in MY 38, we have eleven MSL-CaSSIS pairs to examine.

We use a quality metric when evaluating MSL cloud movies from 0 to 10 with 0 indicating a movie with no cloud present and 10 indicating a movie in which clouds are visible in the raw frame (Hayes et al., 2024b). The quality is not always indicative of the opacity, and indeed the highest quality cloud movie of the eleven we examine has the lowest opacity. Table 3.3 gives the qualities of the ten ACB movies from Tables 3.1 and 3.2, as well as the opacities as determined using the method described in Section 3.3.1. Note that on sols where both a ZM and an SHM were captured together, we use the ZM to derive the opacity due to the higher uncertainty associated with the SHMs (Kloos et al., 2018; Hayes et al., 2024b). For images taken concurrently with a CAO, we likewise use the ZM component.

Table 3.3: *Qualities and opacities of MSL cloud movies which overlap ACB season CaSSIS images.*

CaSSIS Image ID	MSL Sol	Cloud Movie Type	Quality	Cloud Opacity
MY35_007380_357_0	2471	CAO	2	0.052
MY37_024431_355_3	3830	ZM	2	0.145
MY37_026416_186_3	3988	SHM	5	0.084
MY38_033831_184_0	4579	SHM	3	0.126
MY38_034055_185_0	4597	SHM	3	0.154
MY38_034297_353_0	4616	CAO	5	0.100
MY38_034409_354_0	4625	SHM	3	0.114
MY38_034521_354_1/2	4634*	SHM	6	0.135
MY38_034901_190_0	4664	CAO	7	0.041
MY38_035125_187_0	4682	SHM	4	0.260

**while there were two CaSSIS images taken on this sol, as they were a stereo pair there was only one movie captured concurrently.*

The highest opacity seen in these movies is 0.260 in the SHM taken on sol 4682, at the tail end of ACB season. This movie was taken about 30 minutes after the CaSSIS image (MY38_035125_187_0), so we can assume that the clouds visible in this movie were most likely present at the time of the CaSSIS image. While this SHM was pointed south and the CaSSIS image was taken to the west of the rover, we likewise would expect that the cloud sheet would be extensive enough that it would extend over the area covered by this CaSSIS image.

While the clouds in this movie are not as clear as those in other movies, we can still see structure in them

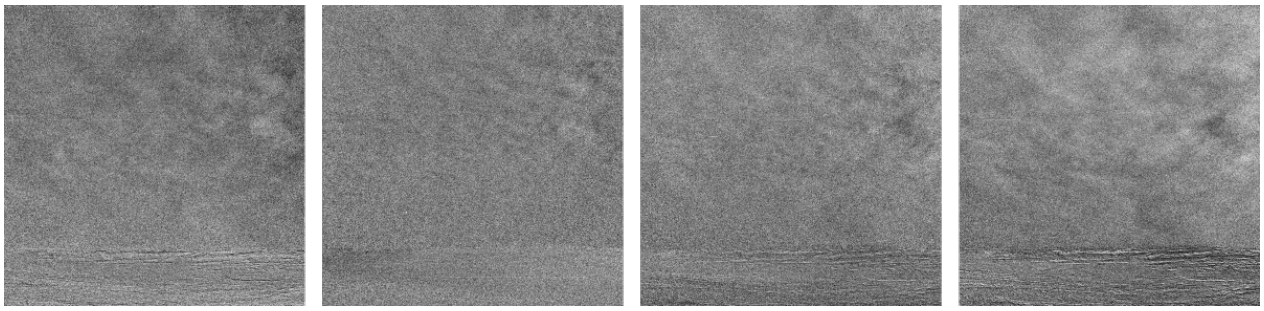


Figure 3.4: Every fourth frame of the mean fram subtracted sol 4682 SHM. Clouds are visible moving from the right of the frame to the left.

(Figure 3.4) which is missing from the respective CaSSIS image. The NPB version of this image (Figure 3.5) looks quite clear, and if there is some haze from optically thin clouds, the structure of the clouds is not visible. However, the lightness of the image is likely due to the high elevation angle of the sun, as this image was taken near local noon.

When we look at just the BLU channel alone (Figure 3.6) we see only the terrain features and not any obvious clouds. The brightest area in the BLU channel is the sand patch at the bottom of the image. Ratioing the BLU to NIR channels does not reveal any other structure, just that the BLU is much much lower than the NIR, across most of the image with the exception of the sandpatch. This agrees with the average I/F values in Figure 3.7.

The reflectance in the BLU channel is much lower than any of the other channels. While it does have a small standard deviation, it is more likely that that is due to its overall low reflectance. Its coefficient of variation is 0.098, the lowest of all the four channels (0.123, 0.171 and 0.200, respectively). While thin clouds could still be contributing to the reflectance in the BLU channel, their contributions are not sufficient enough that their effect is apparent in any of the analyses we have performed.

Indeed, we are unable to see clouds in any of the CaSSIS images in which we are reasonably certain that clouds would be present (See Appendix B), in either the NPB images or in further investigation of the BLU channel. Variations in the BLU channel seem to come overwhelmingly from the terrain in the image, where features such as sand patches and shadowing show up more brightly in the BLU. When ratioing the BLU to NIR channels,



Figure 3.5: The MY38_035125_187_0 CaSSIS image corresponding to the sol 4682 SHM in Figure 3.4. This image has been constructed from the NIR, PAN and BLU channels.

these features are what have a higher ratio. Bluer images too tend to be those with more sand.

When we plot the mean I/F across the scene, the spectra have the same general shape as we see in Figure 3.7, with the BLU channel being the least reflective by far. The standard deviations of each scene follow a similar pattern as well.

The coefficients of variation for each image and each channel are given in Table 3.4. The BLU channel consistently sees the lowest coefficient of variation, unsurprisingly given that it is also consistently the least reflective. The coefficient of variation in the BLU channel is typically much lower than the others, with MY38_034901_190_0 being the closest to the value of the other channels. This image is stronger in the BLU, but looking at the NPB image it seems that is due to the terrain reflecting quite strongly in that channel. There again is no evidence of clouds in the image itself in any band or combination.

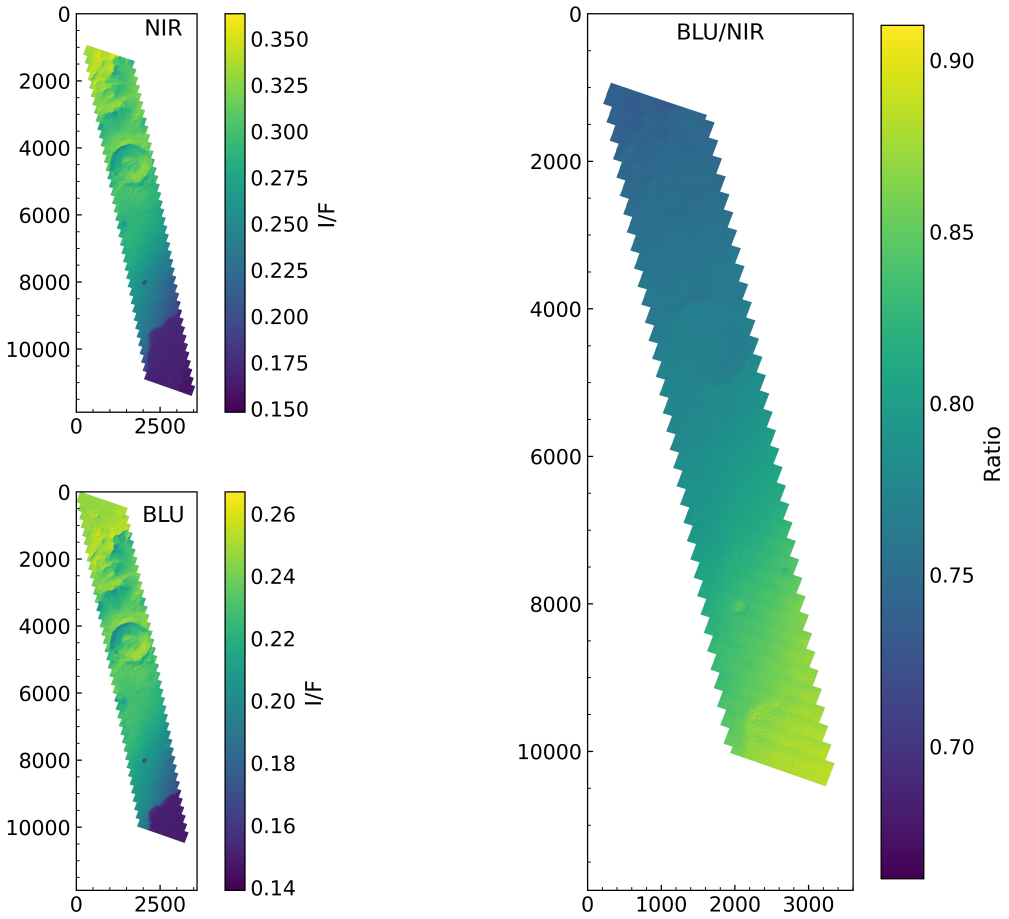


Figure 3.6: The BLU and NIR channels of MY38_035125_187_0 alone as well as the ration of BLU to NIR.

It is worth noting that the highest coefficient of variation in the BLU channel corresponds to the image taken with the most optically thick clouds. However, looking at the other coefficients of variation in the BLU channel there does not seem to be any strong agreement between cloud opacities and the coefficients

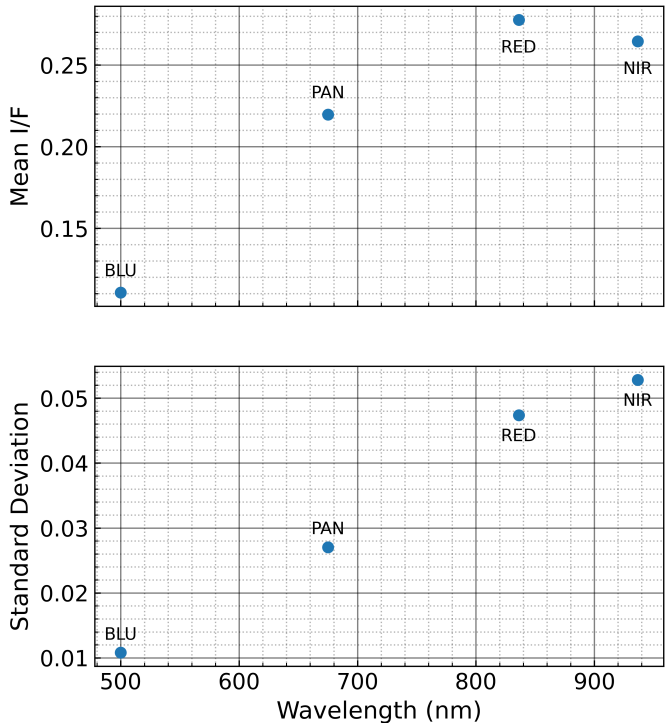


Figure 3.7: The mean I/F and standard deviations for each channel of MY38_035125_187_0.

of variation we get, so this is likely not a strong indicator of the presence of clouds influencing reflectance in the BLU channel. Thus, we can fairly reasonably conclude that CaSSIS is unable to visually see clouds with optical depths below at least 0.26.

Table 3.4: *Coefficients of variation for each of the CaSSIS images likely containing clouds.*

	BLU	**PAN**	**RED**	**NIR**
MY35_007380_357_0	0.041	0.106	0.125	0.131
MY37_024431_355_3	0.092	0.189	0.215	0.217
MY37_026416_186_3	0.082	0.177	0.191	0.196
MY38_033831_184_0	0.021	0.042	0.049	0.050
MY38_034055_185_0	0.086	0.136	0.144	0.146
MY38_034297_353_0	0.069	0.132	0.159	0.174
MY38_034409_354_0	0.046	0.131	0.150	0.157
MY38_034521_354_1	0.051	0.137	–	0.164
MY38_034521_354_2	0.055	0.141	0.161	–
MY38_034901_190_0	0.039	0.047	0.047	0.048
MY38_035125_187_0	0.098	0.123	0.171	0.200

3.4.2 Behaviour of a Cloudy Scene

The scene shown in Figure 3.1 (MY36_015998_085_0) shows very clear and distinct clouds both within the crater and outside of it. In order to understand how CaSSIS behaves in the presence of clear and

obvious clouds, we can examine the image statistics as described in Section 3.3.2 for this scene. We take two 1000×1000 pixel areas within the crater and to the ENE of the crater, both of which show obvious clouds, shown in Figure 3.8.

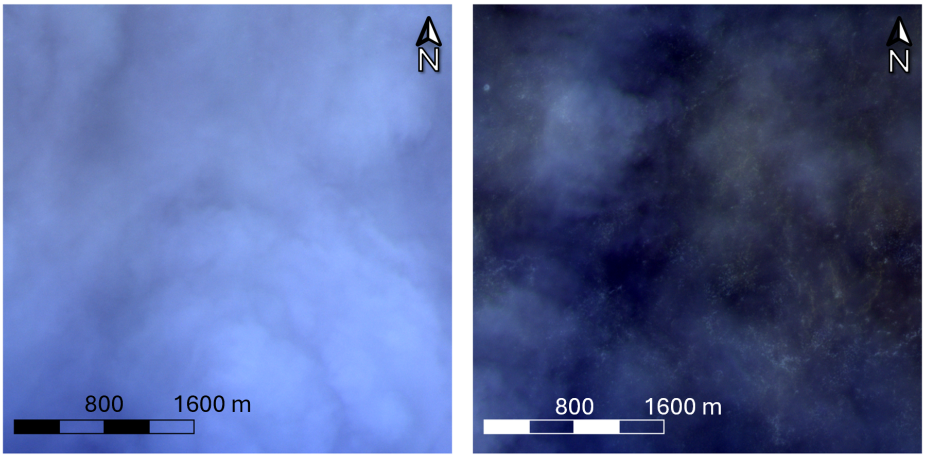


Figure 3.8: Two areas of cloud in the MY36_015998_085_0 image (Figure 3.1) within the crater (left) and ENE of the crater (right).

The area within the crater shows clear structure in the clouds, but they mostly obscure the terrain below and there are no obvious terrain features. The clouds outside the crater seem a little thinner, with thicker areas and the terrain is visible through them as well as some bright features that may be surface ice.

Looking at the statistics for the two areas, the shapes of the spectra are very similar to those we saw for the clear image and the ACB images. There is a bit more of a steep drop from the RED to NIR channels. The behaviour of the standard deviations however are quite different from those we saw in the other images. The highest standard deviations and corresponding coefficients of variation (Table 3.5) are in the BLU channel. This is perhaps to be expected with a scene mostly dominated by structured clouds.

Table 3.5: *Coefficients of variation of the two areas of cloud in MY36_015998_085_0.*

	BLU	**PAN**	**RED**	**NIR**
In crater	0.040	0.027	0.025	0.025
Outside crater	0.049	0.032	0.029	0.029

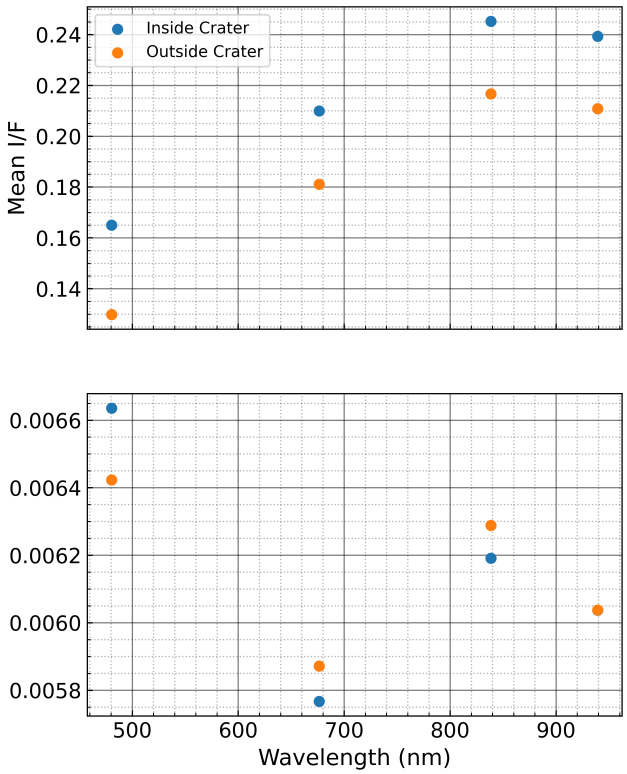


Figure 3.9: The mean reflectance and standard deviation for each channel for the two areas of cloud in Figure 3.8.

3.4.3 Comparing Clear and Cloudy Scenes

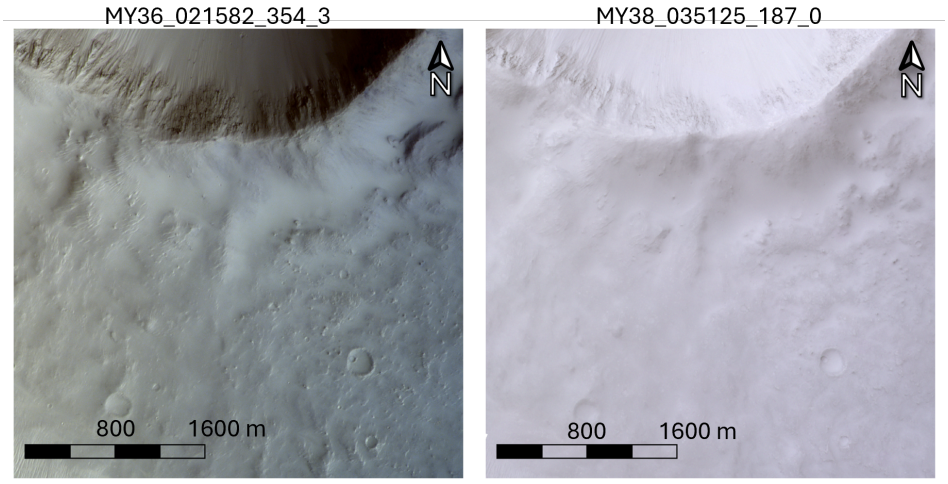


Figure 3.10: A portion of clear CaSSIS image MY36_021582_354_3 (left) and the same area of CaSSIS image MY38_035125_187_0 (right, Figure 3.5) taken while suboptical clouds were likely present.

To look at how our cloudy scenes compare to a clear scene, we can look at an overlapping CaSSIS image that we can assume is cloud free. We use CaSSIS image MY36_021582_354_3, taken in MY 36 which overlaps our MY 38 coordinated image MY38_035125_187_0 spatially on the northwest side of Gale Crater.

MY36_021582_354_3 was taken on the same sol as an MSL cloud movie which did not show any clouds, and as it was acquired at an L_s of 310°, well into the dusty season we can expect that we would not see clouds. We look at an 1000×1000 pixel patch that the two images have in common (Figure 3.10).

The MY 38 CaSSIS image appears much more washed out than the MY 36 image. This could be due in part to lighting effects. The MY 36 image was taken at 07:53:28 LST where the sun has an incidence angle of 61.5°. The MY 36 image was taken at 13:59:59 LTST with the sun at an incidence angle of 32.4°. The dramatic shadowing from the lower sun angle in the mornign is aparant in the scene. We also know that atmospheric dust loading in Gale tends to increase towards midsol (Bischof et al., 2024), so it is possible that there is more dust in the MY 38 scene. A tau of 0.683 was reported by MSL (Lemmon et al., 2024a) from an observation taken around the same time as the MY 36 CaSSIS image. There was no tau taken on the same sol as the MY 38 image, but tau measurements from surrounding sols suggest taus around 0.8.

Looking at the image statistics of the common area in Figure 3.10, the shape of the reflectance spectra are very similar in the clear and cloudy images. The cloudy image is more reflective overall in all channels, which is likely due to the higher sun angle closer to midsol. The clear image has a higher standard deviation in all channels as well, which can be attributed to the clearer features we can see in the image.

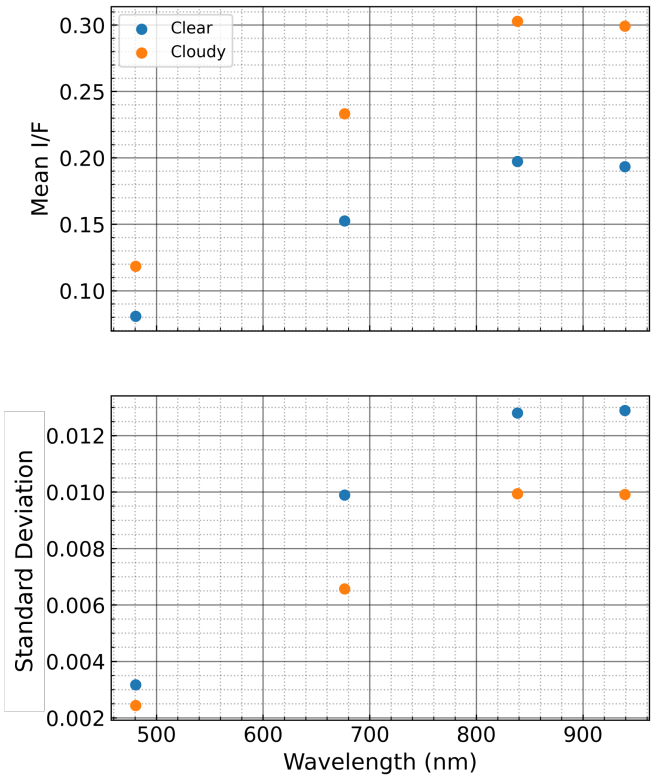


Figure 3.11: A comparison of mean I/F and standard deviation in each channel across the area of the two CaSSIS images given in Figure 3.10.

Likewise examining the coefficients of variation over just the area of interest in the two images (Table 3.6, those in the cloudy image are lower than in the clear but follow the same general pattern of increasing towards the NIR.

Table 3.6: *Coefficients of variation for the two overlapping CaSSIS images.*

	BLU	**PAN**	**RED**	**NIR**
MY36_021582_354_3	0.039	0.065	0.065	0.067
MY38_035125_187_0	0.021	0.028	0.033	0.033

Overall, the cloudless image taken in MY 36 and the image with suboptical clouds taken in MY 38 have very similar behaviours from channel to channel. The only differences in reflectance can easily be attributed to lighting effects, which suggests that the suboptical clouds present in the MY 38 image are not having an appreciable impact on reflectance in the BLU channel.

3.4.4 Limitations of the Dataset

The largest limitation of this dataset is its small size. We have only 11 images taken at times at which we know that clouds are present, and of these only three were taken prior to our dedicated imaging campaign alongside MSL. Thus, while we could conclude that CaSSIS is unable to see clouds with optical depths below 0.26, we do not know how robust this value is or what the actual limit of detection for CaSSIS may be, as we simply do not have enough images to say. We are also unable to calculate atmospheric optical depths using CaSSIS alone at this point in time, so we cannot validate the MSL-derived opacities, or determine optical depths at wavelengths outside of the range of the Navcams.

Because the CaSSIS images are taken at different locations, differences in terrain make analysis difficult as certain terrain features are more strongly reflective in the BLU themselves, as discussed above. Future work could look at smaller subframes of similar terrain to have a better one-to-one comparison, such as comparing the crater floor only.

Additionally, lighting effects influence the reflectance and the character of the terrain, as we see in Figure 3.10. Comparing similar solar incidence angles would also yield a better comparison, however the small size of the dataset does not allow this, as images are distributed through the late morning and afternoon.

Further analysis could also be done to separate atmospheric phenomena from the strong signal in the terrain. Tornabene et al. (2017) noted that the BLU to NIR or RED ratio alone will often falsely flag areas of strong illumination or certain mineral types such as basaltic dunes the same as it would water ice. Using a different spectral parameter or ratio (Eg. Rangarajan and Tornabene, 2026) may more strongly reveal the presence of water-ice clouds, especially over an area that is not as strongly reflective in the BLU channel.

Chapter 4

The Impact of Atmospheric Aerosols on MCS Retrieval Altitudes

4.1 Motivation & Author Contribution

The Mars Climate Sounder (*MCS*) is an infrared radiometer aboard the Mars Reconnaissance Orbiter (*MRO*) which has been observing the Martian atmosphere nearly continuously since its arrival in MY 28 (2006) (McCleese et al., 2007). While MCS can theoretically observe down to Mars' surface, in practice many retrievals are cut off at higher altitudes due to the presence of atmospheric aerosols, such as dust or water ice, or other atmospheric conditions producing high uncertainties in the retrievals (Kleinböhl et al., 2009).

MCS retrievals have been used in conjunction with surface measurements such as those from MSL for a variety of purposes including constructing dust profiles (Guzewich et al., 2017), validating cloud altitudes (Campbell et al., 2020), and retrieving water-ice cloud opacities (Cooper et al., 2019). However, in the case of water-ice clouds, it is uncertain whether or not MCS is observing the same clouds as MSL.

MCS does not report water-ice retrievals when visible extinctions reach above 0.001 km^{-1} (Wilson and Guzewich, 2014). Over the 5 km vertical resolution of MCS, this extinction corresponds to an optical depth of 0.005. In contrast, the ACB has a zonal average visible optical depth of around 0.45 (Heavens et al., 2011). Indeed, after the first year of MCS operations it was reported that the presence of the ACB reduced the number of sucessful retrievals in the equatorial region (Kleinböhl et al., 2009). This result suggests that even very tenuous, suboptical clouds would impede MCS' ability to observe down to the surface and sufficiently high water-ice clouds would result in retrievals being cut off tens of kilometres above the surface. However, this also means that we can use the minimum altitude retrieved by MCS to infer the altitude the opaque cloud layer.

This chapter is based on Innanen et al. (2024b), with some alterations and additions to the text and additional figures. The research note and section of this dissertation were written by me, and the data

analyses were carried out by me.

4.2 Methods

MCS' typical observation mode consists of limb measurements used to retrieve vertical profiles of temperature, water-ice and dust opacities, amongst other atmospheric properties, between 10 and 90 km above the surface from MRO's polar, sun-synchronous 03:00/15:00 LST orbit (Kleinböhl et al., 2009). MCS has nine channels: eight mid- and far-infrared channels and one broadband visible/NIR channel. Channels A1, A2 and A3 provide information on CO_2 as well as pressure and temperature, while channels A4, B2 and B1 provide information on water-ice and -vapour and channels A5 and B1 provide information about dust (McCleese et al., 2007).

MCS profiles have an altitude resolution of 4-6 km and a precision of 0.5-2 K for temperature and $10^{-4} - 10^{-5}$ km^{-1} for dust and water-ice opacity. MCS uses an iterative retrieval method which determines temperature or amount of an absorber based on the measured radiances in each channel as described in Kleinböhl et al. (2009). Because several of the retrievals, such as temperature, use multiple channels to determine the quantity in question, if the atmosphere begins to become opaque in one channel, as in the case of high CO_2 absorption in the A2 channel, the other channels may be weighted more heavily (Kleinböhl et al., 2009).

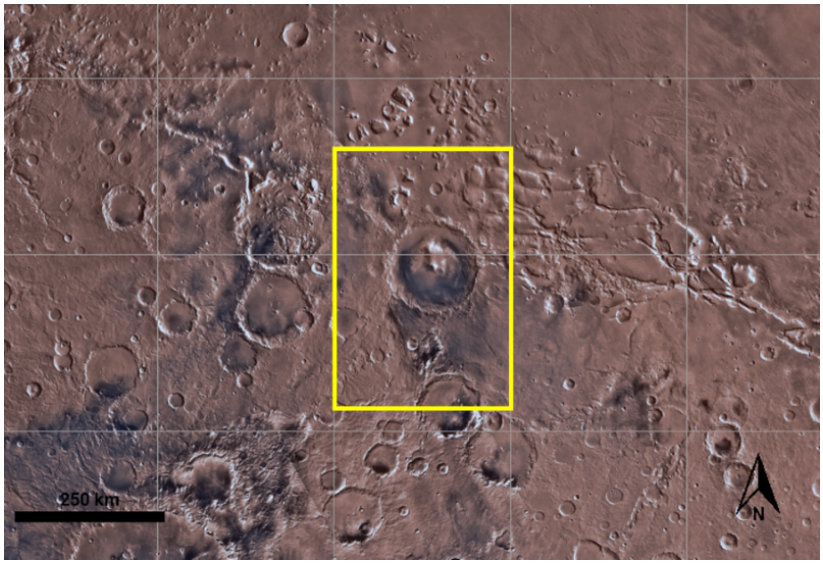


Figure 4.1: The area around Gale Crater for which we retrieved MCS temperature profiles, shown in JMARS.

We looked at MCS temperature profiles for the area around Gale Crater with longitude bounds of $135 - 140°$E and latitude bounds of $2 - 9°$S (Figure 4.1) over the period spanning the start of MCS science operations

($L_s = 111°$ of MY 28) to $L_s = 205°$ of MY 36. Positioned as it is at the southern edge of the ACB, Gale Crater was chosen for not only its yearly cloud coverage but also its extensive data set of surface cloud observations for MSL (Eg. Campbell et al., 2020; Hayes et al., 2024b). From the MCS profiles, we extract the minimum altitude at which a temperature is retrieved and take this as the 'cut-off' altitude below which the atmospheric opacity becomes too great for MCS to observe.

4.3 Results and Discussion

4.3.1 Minimum Retrieval Altitudes

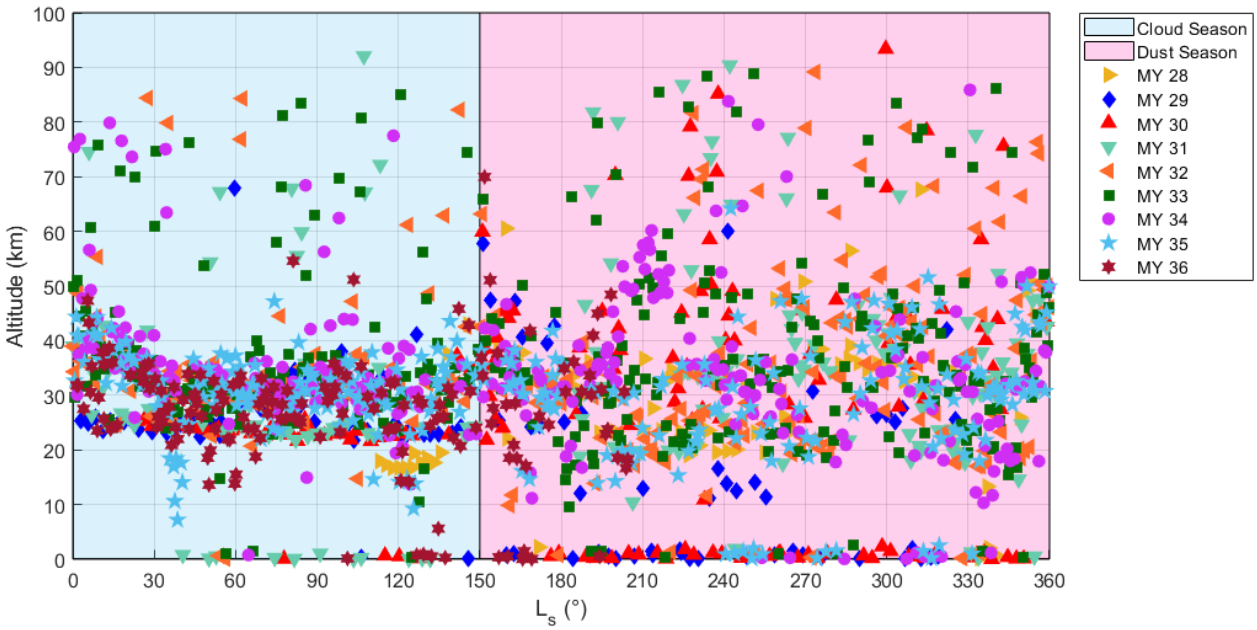


Figure 4.2: Cut-off altitudes for MCS retrievals over Gale Crater from MY 28-36. Cloudy season ($L_s = 0 - 150°$) is indicated by the shaded blue region, dusty season ($L_s = 150 - 360°$) by the shaded pink region.

The dataset used here consists of 1877 retrievals over 8 Mars years, allowing us to probe interannual and seasonal trends (Figure 4.2). The cut-off altitudes from these retrievals span the entire range that MCS can observe, from near the surface to just over 90 km. However, the retrievals exhibit a preference for cut-off altitudes between 20 and 40 km with 64% of all cut-off altitudes falling within this range.

Separating out the cloudy season ($L_s = 0 - 150°$) from the dusty season ($L_s = 150 - 360°$) (Figure 4.3), we see that this preference is more pronounced during the cloudy season with only 8% of all retrievals cutting off below 20 km. The mean cut-off altitude in the cloudy season is 30.6 km. In the cloudy season, daytime water-ice clouds tend to form between 15 and 40 km (Heavens et al., 2010), and cloud altitude estimates at Gale Crater have shown a preference for water-ice cloud formation between 15 and 30 km (Campbell et al.,

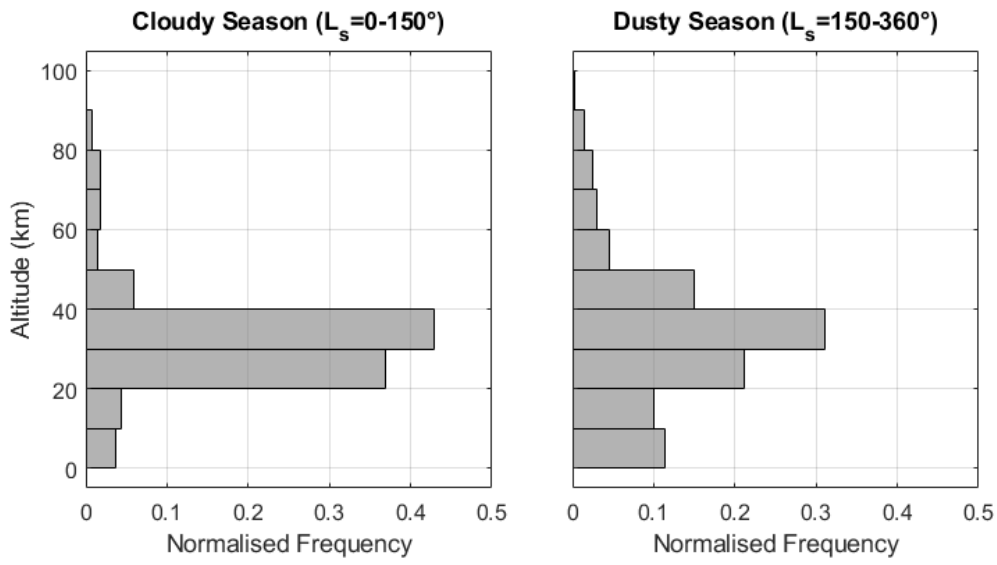


Figure 4.3: Normalised frequencies of cut-off altitudes during cloudy and dusty seasons for all Mars years.

2020). The strong preference observed in the cloud season for cut-offs between 20 and 40 km is thus likely due to the increase of water-ice clouds at these altitudes, which have a mean preferred opacity of around 0.1 (Hayes et al., 2024b), much higher than the limit for MCS' water-ice retrievals. Additionally, any clouds forming below the retrieval cut-off, as in the case of multiple cloud layers, will be missed by MCS.

Of the cloud altitudes estimated at Gale Crater in MY 34 by Campbell et al. (2020), four cloud altitude observations were taken on sols with corresponding MCS profiles over Gale Crater: MSL sols 1787, 1878, 1959 and 1990. The estimated cloud altitudes are shown in Figure 4.4 with the corresponding MCS water-ice optical depth retrievals. For all but sol 1878, the estimated altitude of the clouds seen by MSL fall below the point where the MCS retrieval cuts off. This suggests that the clouds being seen by MSL are not necessarily the same as those being observed by MCS. It is also worth noting that the optical depths of these clouds as calculated from MSL (Hayes et al., 2024b) are much higher than the optical depths reported by MCS (0.12, 0.17, 0.188 and 0.28, respectively).

In the dusty season, this strong preference becomes less pronounced with a greater spread in cut-off altitudes. The mean cut-off altitude in the dusty season is 28.7 km. In Gale Crater, there is a marked increase in dust optical depth around the end of the cloudy season ($L_s = 150°$). Dust opacity varies during the dusty season, with maxima around $L_s = 230°$ and $L_s = 330°$ before declining again to around 1 at the end of the year (Lemmon et al., 2024a). We do not see these same peaks and troughs in the MCS cut-off altitudes - rather, the dusty season seems to be characterised by a greater spread in cut-off altitudes compared to the cloudy season, as can be seen in Figure 4.3.

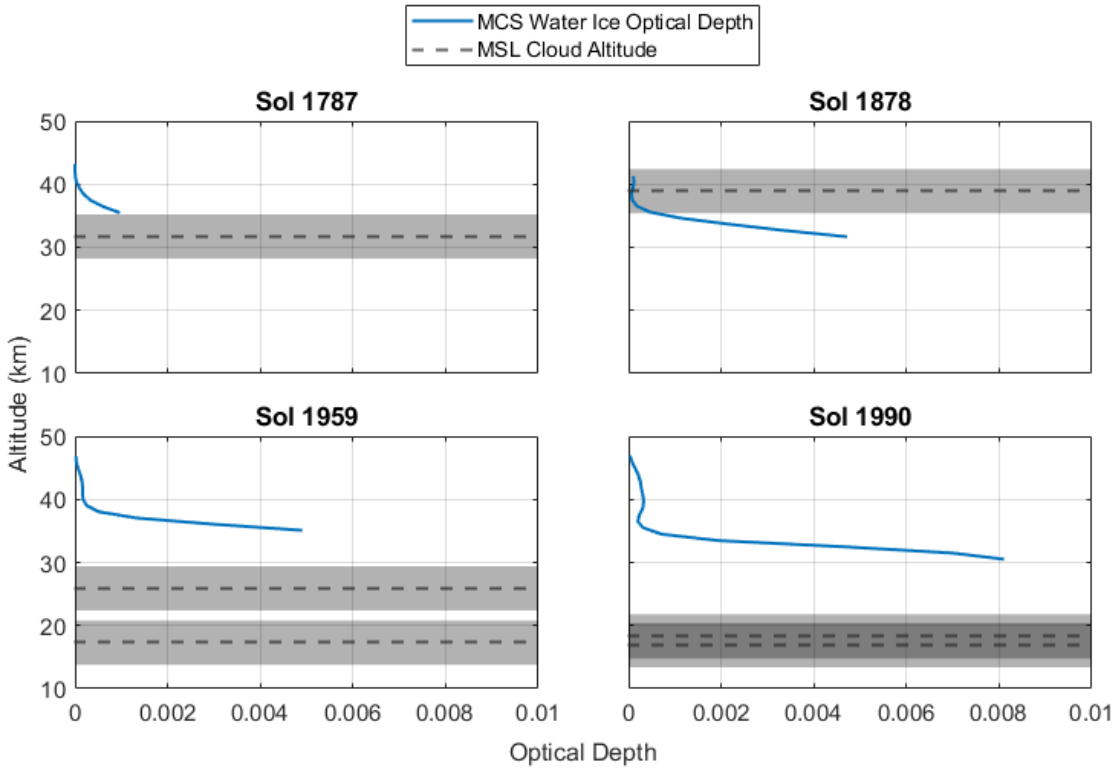


Figure 4.4: MCS water-ice retrievals (solid blue line) plotted next to estimated MSL cloud altitudes (dashed grey line) from Campbell et al. (2020). Grey shaded regions give the uncertainty in cloud altitude. Note that on sols 1959 and 1990, the altitude calculation was done using two different shadows, resulting in two different altitude estimations.

4.3.2 Tracking the Decay of Global Dust Storms

The exception to the above generalisation is in the case of global dust storms (*GDS*, see section 1.3), where sufficient dust opacity will force the retrieval cut-off altitudes higher than typical. This trend is particularly clear in the case of the MY 34 GDS, where there is an obvious increase in cut-off altitude starting a little before $L_s = 200°$ and decay starting around $L_s = 210°$ (Figure 4.5).

The MY 34 GDS occurred around $L_s = 200°$, with precursor storms forming at $L_s \sim 181°$ and the storm being termed global by $L_s \sim 193°$. The decay phase began around $L_s \sim 205°$ before dust levels returned to typical by $L_s \sim 250°$ (Guzewich et al., 2019). In the MCS retrieval cut-off altitudes (Figure 4.5), we see these altitudes beginning to fall from their peak near 60 km starting about $L_s \sim 210°$. By fitting an exponential decay curve to the decay phase of cut-off altitudes, we can see that the return to dusty season average altitudes happens at $L_s \sim 270°$, nearly 20° of L_s after opacities recovered to their pre-GDS levels.

The decay constant we retrieve from the decay curve fit to these cut-off altitudes is -0.06. In contrast, the Planetary Fourier Spectrometer (*PFS*) observed a decay constant for opacity in the MY 34 GDS of -0.1609

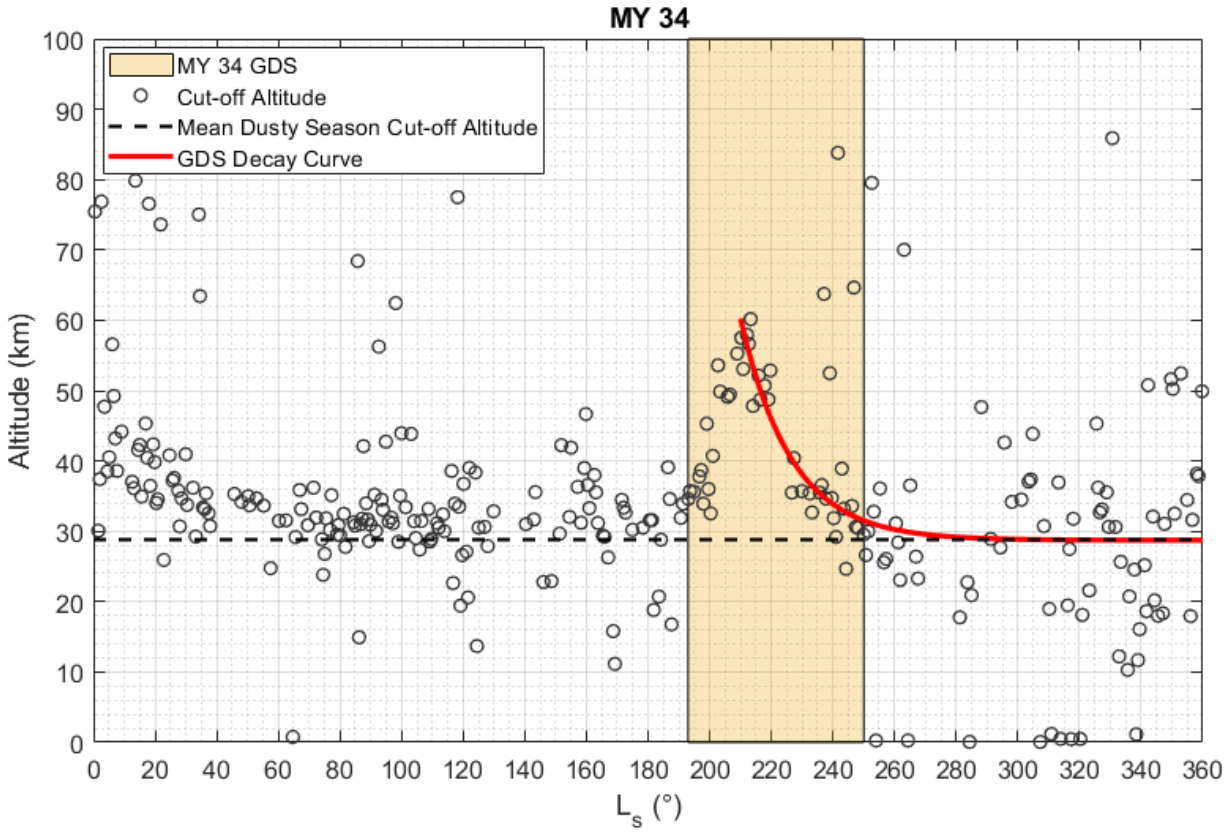


Figure 4.5: Cut off altitudes for MY 34, with the decay phase fitted with an exponential decay curve (solid red line) with the expression $y = 31.5e^{-0.0605(x-210)} + 28.73$. The temporal extent of the MY 34 GDS (Guzewich et al., 2019) is shown by the yellow patch.

(Wolkenberg et al., 2020). This delay in recovery points to the persistence of small particles lofted by the GDS to higher altitudes. Larger particles, which have a greater impact on total opacity, will sediment more rapidly than these small particles, which nonetheless seemingly impede MCS' ability to see down to the martian surface.

Beginning science operations at $L_s = 111°$ in MY 28, MCS was also able to observe the MY 28 solstitial GDS (Kleinböhl et al., 2009). This storm began around $L_s \sim 265°$, with the decay phase beginning at $L_s \sim 295°$ and reaching typical opacities by $L_s \sim 340°$ (Wolkenberg et al., 2020). As with MY 34, we can also see the signature of the MY 28 GDS, though the minimum cut-off altitudes before the decay phase of the GDS are lower, between 30 and 40 km. Despite the relative paucity of retrievals compared to MY 34, we are still able to fit a decay curve to the data (Figure 4.6). As with MY 34, we see that the cut-off altitudes return to the mean value after the opacities have recovered, though not with quite as dramatic a delay as in MY 34. The decay constant for the cut-off altitudes that we retrieve is -0.0429 while the PFS observed a decay constant for opacity of -0.0637 (Wolkenberg et al., 2020).

Using these decay curves, we can approximate the sedimentation of the high altitude dust using Stokes

flow and thus retrieve an approximate particle size. Assuming a Reynolds number << 1, the terminal velocity of a small particle (v) is given by the following expression (Melosh, 2011):

$$v = \frac{1}{18}\frac{(\sigma - \rho)d^2 g}{\eta} \tag{4.1}$$

σ is the density of martian dust, which is between 2600-3100 kg/m^3 (Perko et al., 2002). ρ is the density of the air, which varies by several orders of magnitude over the altitude range (Schofield et al., 1997). However, since the air density is so much less than the dust density, even a change of three orders of magnitude does not meaningfully impact the velocity. The three final terms of Equation 4.1 are d, the particle diameter, g, the gravitational force (3.71 m/s^2 for Mars) and η, the gas viscosity (10.6×10^{-6} Pa-s for Mars). Looking at the settling rates we see in Figures 4.5 and 4.6, the particle sizes are in the range of 1-10 μm.

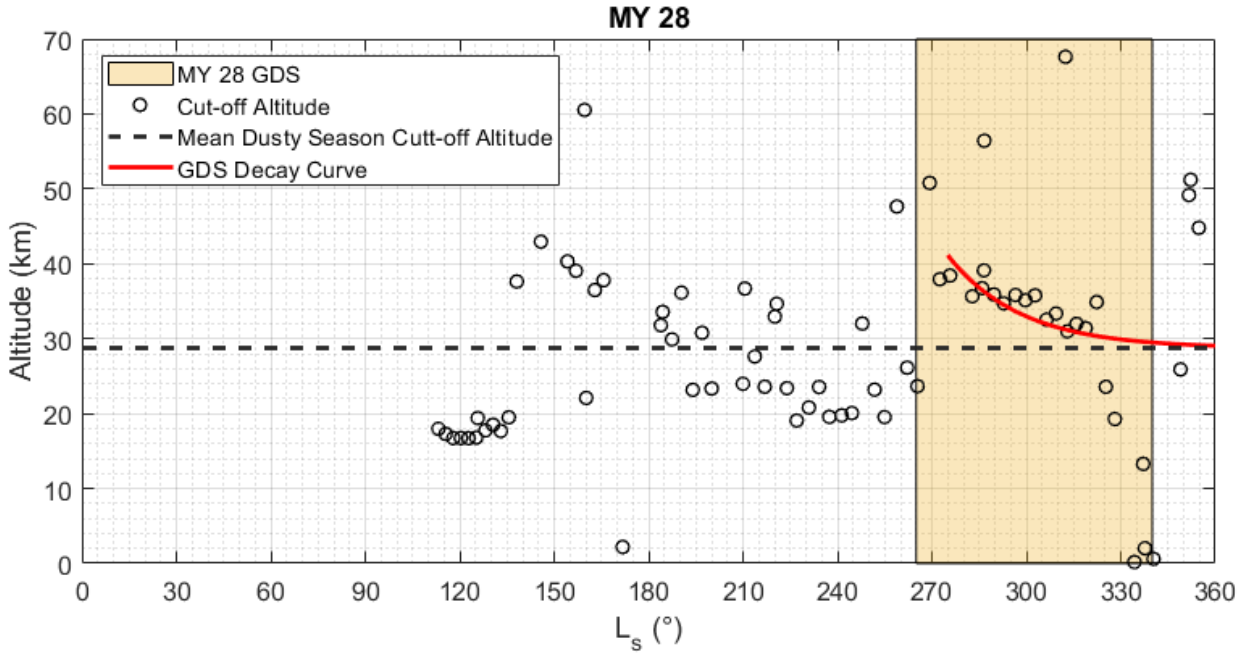


Figure 4.6: Cut off altitudes for MY 28, with the decay phase fitted with an exponential decay curve (solid red line) with the expression $y = 12.411e^{-0.0429(x-275)} + 28.73$. The temporal extent of the MY 34 GDS (Wolkenberg et al., 2020) is shown by the yellow patch.

Smaller, regional dust storms such as that observed around L$_s$ = 150° in MY 36 (Lemmon et al., 2024a) do not appear to have a similar impact on retrieval cut-off altitudes. This dust storm may have been short-lived enough or the opacities low enough (between 1.5 and 2) that dust did not have a chance to build up at higher altitudes and impede MCS' ability to see the lower atmosphere.

Chapter 5

Determining Near-Surface Aerosol Properties using Low-Powered Lasers

5.1 Motivation & Author Contribution

The work presented in this chapter builds on previous work done by Campbell (2024) as part of an overarching project looking at the feasibility of a low-cost weather station (the Mars Atmospheric Panoramic camera and Laser Experiment, *MAPLE*) to characterise near-surface aerosols (Campbell et al., 2022). My contribution to this project was the analysis of images obtained during laboratory and field testing of a prototype instrument. This project aims to characterise the behaviour and properties of near-surface aerosols such as size and concentration.

The laboratory testing has not been described to date. The experiments themselves were performed by Charissa Campbell, but all analysis of the images and data collected was undertaken by me and an undergraduate student, Brock Koch Nichol, at my direction. The laboratory experiment (described further in Section 5.2.4) consisted of imaging lasers of three wavelengths in a suspension of three sizes of polystyrene microspheres in water. This experiment was done with the aim of characterising scattering behaviour using lasers of different wavelengths through different sizes of particles. Understanding how different-sized particles interact with these lasers may help in estimating the size of unknown near-surface aerosols in future planetary missions.

The field testing (further described in Section 5.2.5) was first discussed in Campbell (2024). The instrument was used in Argentia, Newfoundland due to the frequent presence of fog with the aim of understanding its behaviour in a near-surface aerosol-rich environment and understanding the scattering properties of the fog as captured by the instrument. While Campbell (2024) performed some analysis of the images in that work, there were several methodological errors and corrections that needed to be addressed. I undertook further processing of images collected in Argentia, including image correction and conversion to spectral radiance and using modelled fog scattering properties (Section 5.2.3) to apply a phase function correction to

the measured spectral radiance to more accurately capture the the heights of the fog banks.

From the laboratory and field results, I was further able to identify the strengths and weaknesses of the instrument for characterizing particles and to suggest improvements and future work. Additionally, the results obtained in Argentia allowed me to estimate the laser powers needed to observe backscatter from comparably thick near-surface fogs on different planets' background sky brightnesses using comparable equipment.

5.2 Methods

5.2.1 The Camera and Lasers

The setup used in laboratory and field testing consists of three low-powered lasers mounted alongside an all-sky panoramic camera. A full description of the setup is given in Campbell (2024) with the relevant information for this dissertation summarised here.

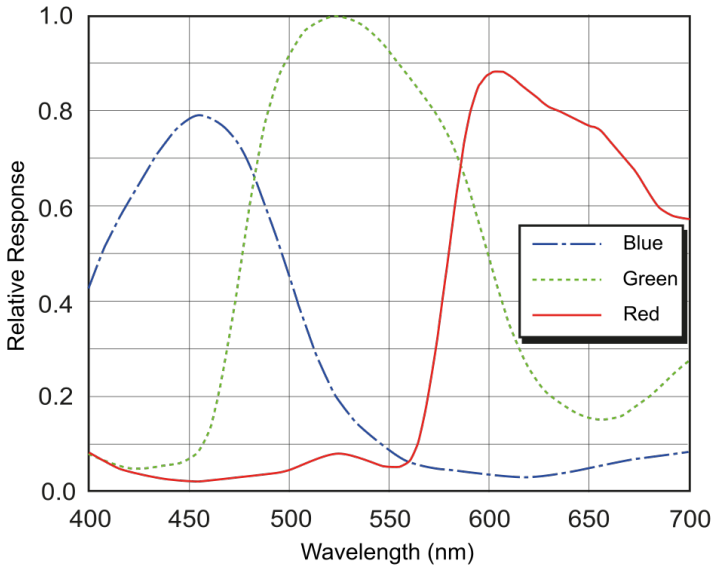


Figure 5.1: The spectral response of the Basler camera. Figure from Basler-AG (2026).

The camera used in these experiments is a Basler ace acA4024-29uc USB camera. It has a resolution of 4024×3036 pixels and was fitted with an equidistant fisheye lens of unknown origin with a 180° FOV (Campbell, 2024). The equidistant nature of the lens means that the image should maintain an equal scale for angular distances across the image (Bettonvil, 2005). For more discussion of lens properties, see Section 5.4.4. The solid angle subtended by a single pixel will change across the image.

Figure 5.1 gives the relative spectral response of the camera, which is slightly more responsive in the green than in the red and blue. It uses an 8 bit per pixel Bayer colour filter (Basler-AG, 2026).

The three lasers used in the laboratory and field tests are Thorlabs class 3R continuous wave (CW) lasers in red (635 nm), green (520 nm) and blue (450 nm), with characteristics given in Table 5.1.

Table 5.1: *Characteristics of the three CW lasers used in this study. Power was measured using an optical power meter.*

Laser	**Model Number**	**Power (mW)**	**Centre Wavelength (nm)**
Blue	CPS450	4.22	451.9
Green	CPS520	4.92	514.3
Red	CPS635	5.50	638.0

5.2.2 Camera Calibration and Image Correction

While some calibration of the Basler camera was outlined in Campbell (2024), there was some confusion in the procedure, and the results given therein did not account for either dark and bias corrections or changes due to changing exposure times. As a result, I redid the camera calibration in its entirety and captured bias and dark frames for this work.

To characterise the camera's response to the three lasers, I took the laser power ($P(\lambda)$) both directly from the laser (Table 5.1) and at the exit of the integrating sphere using a Newport 843-R optical power meter (Table 5.2). Using a Maya Pro 2000 spectrometer to determine the full width half maximum ($FWHM$) of each laser, we could determine the spectral radiance of the laser beam (L_λ) within the integrating sphere, given by:

$$L_\lambda = \frac{P(\lambda)}{\pi A_{LM} FWHM(\lambda)} \tag{5.1}$$

where A_{LM} is the area of the power meter sensor (0.1 mm). The power, FWHM and corresponding spectral radiance for each laser are given in Table 5.2.

Table 5.2: *Power, FWHM and calculated spectral radiance at the integrating sphere exit for each of the three lasers.*

Laser	**450 nm**	**520 nm**	**640 nm**
Power (mW)	0.016	0.019	0.020
FWHM (nm)	1.7528	1.6111	2.9368
Spectral Radiance ($W/m^2/Sr/nm$)	0.0291	0.0375	0.0217

We then captured images of each laser diffused within the integrating sphere with the Basler camera over exposure times between 200 and 1 000 000 μs. This allowed us to determine a conversion factor (CF) from digital number (DN) to spectral radiance at each exposure time (t), given by:

$$CF(t) = \frac{L_\lambda}{DN(t)} \tag{5.2}$$

The DN was taken by averaging over the centre of the integrating sphere in a 800×800 pixel area. Each of the images taken during the calibration procedure, as well as in the laboratory and field experiments, were dark and bias corrected. The laboratory and field experiments were all performed using an exposure time of 1 s, which resulted in conversion factors of 8.50×10^{-5} for the red laser, 1.49×10^{-4} for the blue laser and 1.17×10^{-4} for the green laser.

In order to apply bias and dark correction to the images, we took 20 dark images with the camera at the 1 s exposure time, as well as 150 bias images. From these we created an average dark image and an average bias, which we then subtracted from the experimental images on a pixel-by-pixel basis.

5.2.3 Mie Scattering Models

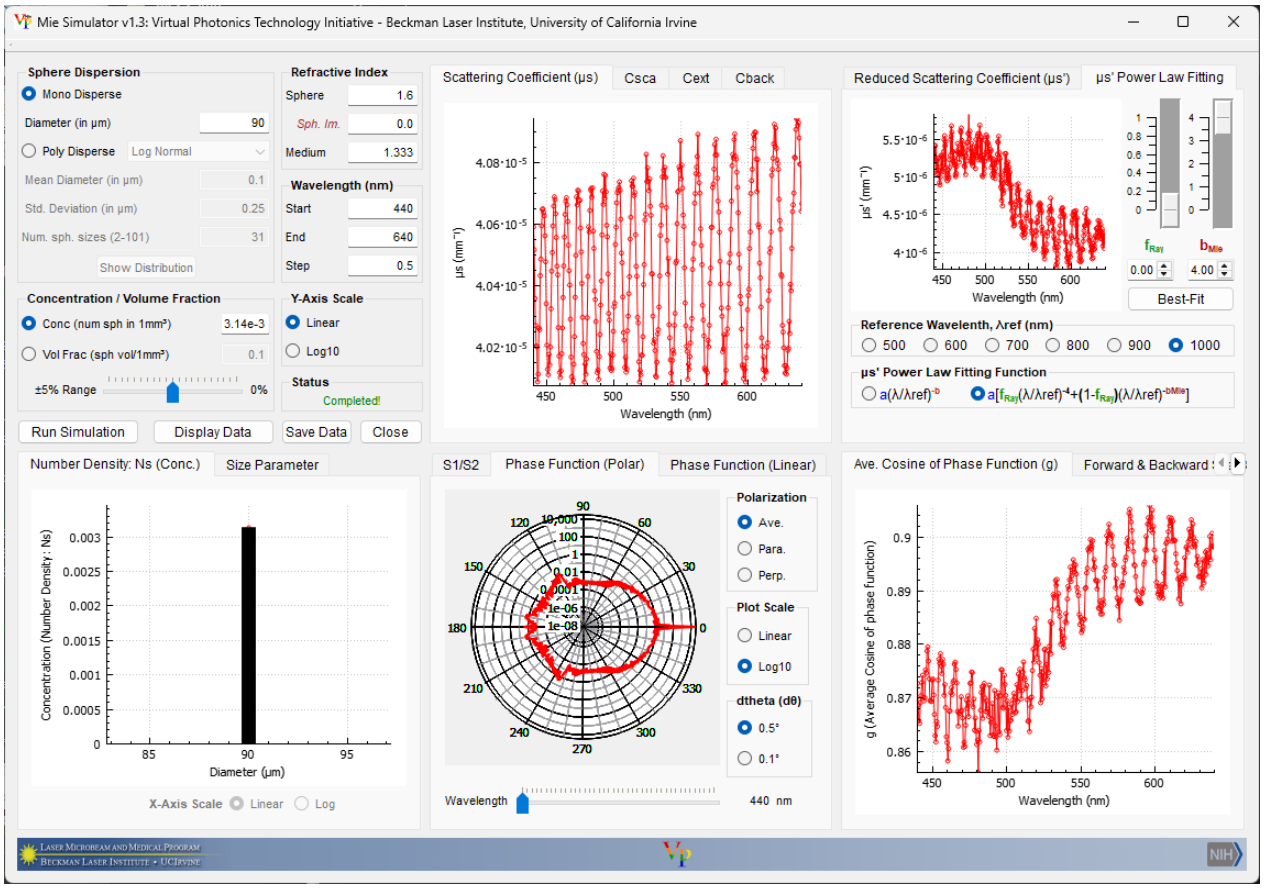


Figure 5.2: An example of the Mie Simulator GUI. The upper left hand panel shows the input parameters for 90 μm polystrene spheres. The other panels show the results of the simulation.

To model the expected scattering behaviour of the lasers with the particles used in the experiments de-

scribed below (Sections 5.2.4 & 5.2.5), I used the Mie Simulator created by the Virtual Photonics Technology Initiative at the Beckman Laser Institute, University of California, Irvine (Virtual Photonics Technology Initiative, 2025). An example of its output is shown in Figure 5.2. From this, I am able to extract the single scattering phase function and scattering coefficient (μ_s) for a given particle with known refractive index, radius and concentration in a given medium at each of the three laser wavelengths.

The scattering coefficient is given by

$$\mu_s = Q_{sca}\pi a^2 N_s \tag{5.3}$$

where Q_{sca} is the scattering efficiency, a is the particle radius and N_s is the number density.

5.2.4 Laboratory Testing

The MAPLE setup was tested in the lab using a $100 \times 40 \times 40$ cm aquarium filled with water within which were suspended polystyrene microspheres of three different sizes. This was to see how the laser backscatter would be impacted by differing particle sizes.

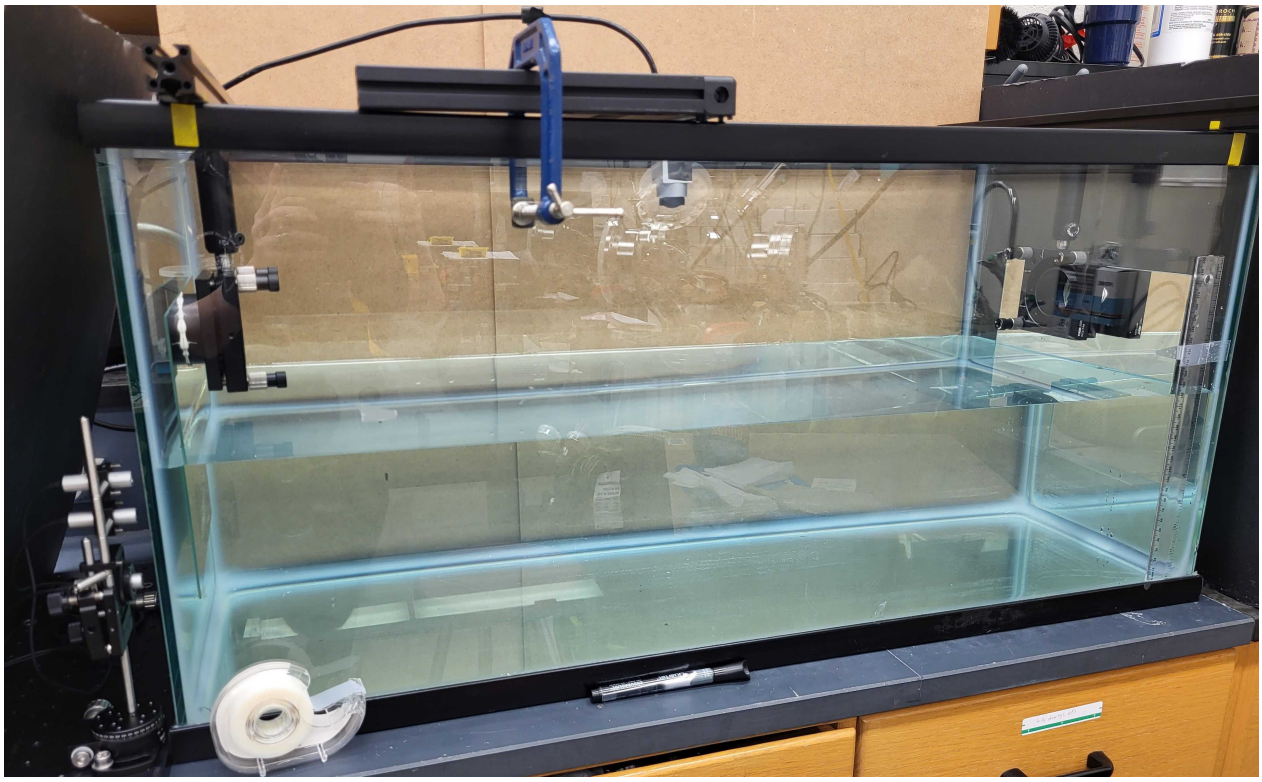


Figure 5.3: A photo of the aquarium setup for testing laser backscatter with microspheres, taken by Charissa Campbell. The lasers can be seen mounted at the left side of the aquarium. The camera is mounted in the middle above the aquarium. Two mirrors are mounted at either end inside the aquarium at a small standoff.

The microspheres used were Polybead® microspheres of sizes 3, 20 and 90 μm. They are all composed of polystyrene and suspended in water at a concentration of 2.5% (w/v). The spheres have a density of ~ 1.05 g/cm^3 and a refractive index of ~ 1.59 (Polysciences, Inc, 2009). The benefit of using these micropsheres is that they have a density very similar to that of water, so when they are mixed into a large volume of water they remain suspended for a long period of time before settling to the bottom.

The camera was mounted above the aquarium pointing downwards into the water. The lasers were positioned pointing into the side of the aquarium. Within the aquarium on either end two mirrors (25×20 cm) were mounted 9 cm above the aquarium floor. The laser beam was reflected from these mirrors a number of times (see Figures 5.4 & 5.5), increasing the effective path length that the laser beam travelled within the tank and allowing a greater distance over which to measure the extinction of the beam. The aquarium setup is shown in Figure 5.3 and diagrammatically in Figure 5.4.

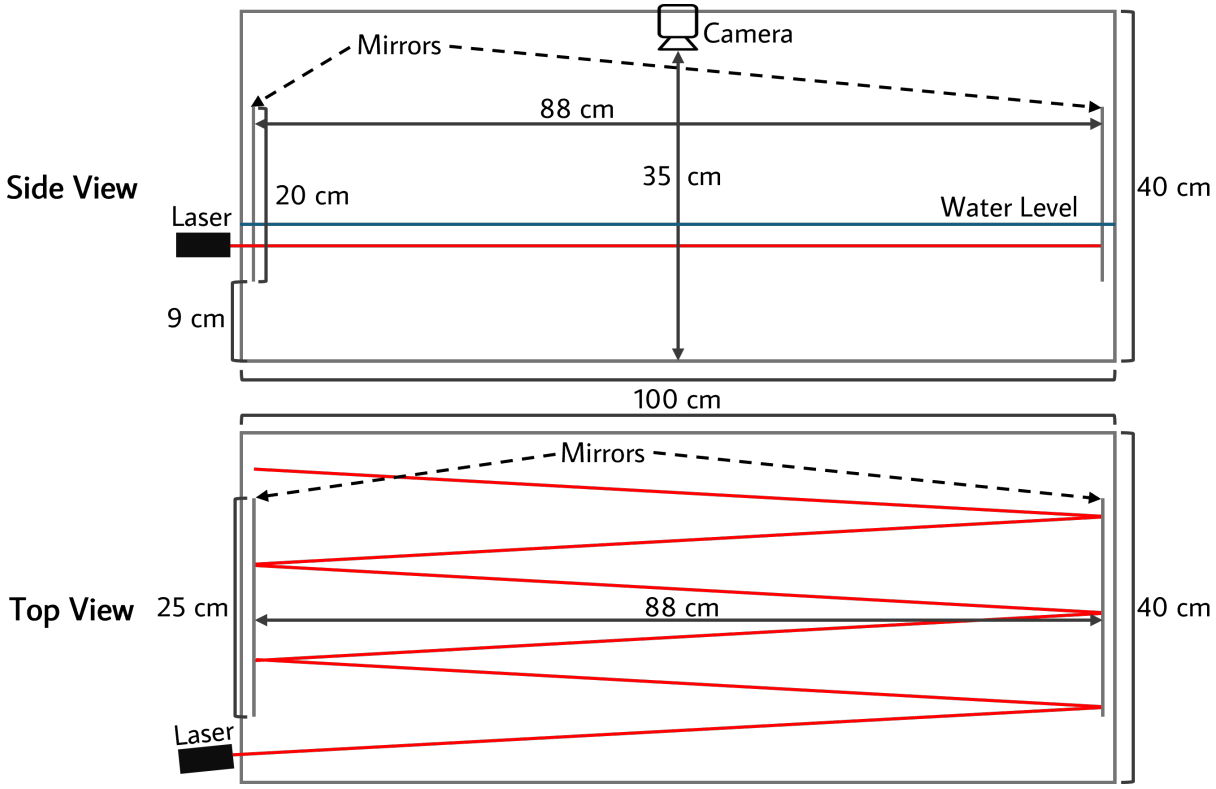


Figure 5.4: A schematic of the aquarium setup, with a side view shown above and a top down view shown below.

While the intention was to vary the concentrations of microspheres over each run through dilution, there may have been some error in this dilution. When examining the images taken in each run, the attenuation of the beam does not seem to change much by visual inspection from run to run. Likewise, analysis of the images revealed similar extinction curves for most runs (see Section 5.3 for more details). As a result, we treated the concentration as fixed at the average concentration over the runs for each size: 6.11×10^4 spheres/mL for

the 3 μm spheres, 6.75×10^2 spheres/mL for the 20 μm spheres and 3.14 spheres/mL for the 90 μm spheres.

For each size of microsphere, the camera imaged each laser through ten runs with an exposure time of 1 second. These images were then corrected in Matlab to be rectilinear (Figure 5.5). This straightens the laser beams, which appear curved due to the camera's fisheye lens.

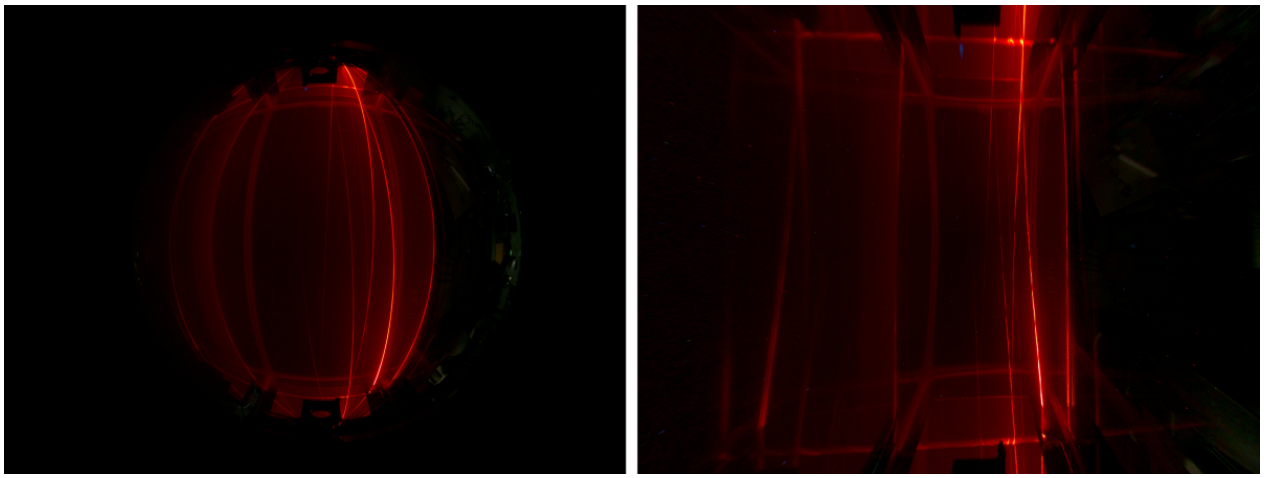


Figure 5.5: (Left) The original fisheye image of the red laser in the aquarium. (Right) The same image following rectilinear correction in Matlab, with the laser beams now straight. The undistorted image has been cropped to show just the aquarium.

From the undistorted images, we could extract the spectral radiance at each point along the laser beam. The scattering angles corresponding to each point were also computed. The spectral radiance as a function of distance, d, along the beam could then be used to determine an extinction coefficient by fitting a curve with the form

$$L_\lambda(d) = a \exp\left(b(d-h)\right) + k \tag{5.4}$$

using a nonlinear least squares method.

We use an iterative process to determine the best fit, fitting the extinction curve initially and then subtracting the residual from this curve, which was our repeated phase function. We combined these repeated curves to calculate an average phase function, which we can then subtract from the original radiance-distance curve. We then once more fit an extinction function to this reduced curve for this reduced curve, giving us the final equation for the extinction curve.

5.2.5 Field Testing

A full description of the field testing of the MAPLE setup is given in Campbell (2024). The relevant details to this dissertation are summarised here.

For the field testing, the camera and lasers were housed in a 41.8 × 33 × 17.3 cm Pelican case with polycarbonate windows inserted for the camera and lasers. The setup was deployed in Argentia, Newfoundland, in summer 2022 in order to observe fog particles. A number of daytime and nighttime experiments were performed; however only the nighttime observations yielded usable results as the laser beam was not visible against the brightness of the sky in daytime (Campbell, 2024). In this chapter we will only be analysing the June 29 nighttime observations.

The June 29 observations were taken around 21:00 local time in what was described as a "thick fog" (Campbell, 2024). The exposure time of the images was not recorded for this experiment, so an exposure time of 1 s, which was used for the other nighttime observation, has been assumed for consistency with the laboratory tests. The pelican case was left open for the June 29 observations, so neither the camera nor the lasers were behind the polycarbonate windows.

To analyse the images captured on these nights, we first applied a bias and dark correction to them (further described in Section 5.2.2). We then identified the beam in the image, following a similar procedure to that used by Campbell (2024), which in turn follows that of Moores et al. (2011).

However, the geometry of the fisheye lens complicates this procedure. For a truly equiangular image, we should be able to map spherical coordinates to each pixel in the image. In our image, the elevation angle (θ_{El}) and azimuthal angle (φ) can be mapped onto the image as shown in Figure 5.6, with an elevation of 90° at the zenith and 0° at the horizon. The position of the CCD and the lens mean the zenith of the image is not the true centre of the image and is offset in the x-axis by 137 pixels. There is no offset in the y-axis. The azimuth can be selected arbitrarily, and we have taken $\varphi = 0°$ to be at the left or 9 o'clock side of the image, with azimuth increasing clockwise.

To map pixel coordinates to azmiuth and elevation, we use the following expressions:

$$\theta_{El} = r_{px} \frac{90°}{r_{im}} \tag{5.5}$$

$$\varphi = \tan^{-1}\left(\frac{Y_{px}}{X_{px}}\right) \tag{5.6}$$

where r_{px} is the distance in pixels to the pixel of interest from the zenith; r_{im} is the radius in pixels of the image (1285.5 pixels); Y_{px} is the y-component of a line from the pixel to the zenith; and X_{px} is the x-component.

We can then identify the azimuth and elevation of the base and the top of the laser beam on the image using this pixel-to-angle mapping. As can be seen in Figure 5.6, the lasers were not truly vertical, as they were expected to be, as a vertical laser would appear to terminate at the zenith. The azimuth and elevation

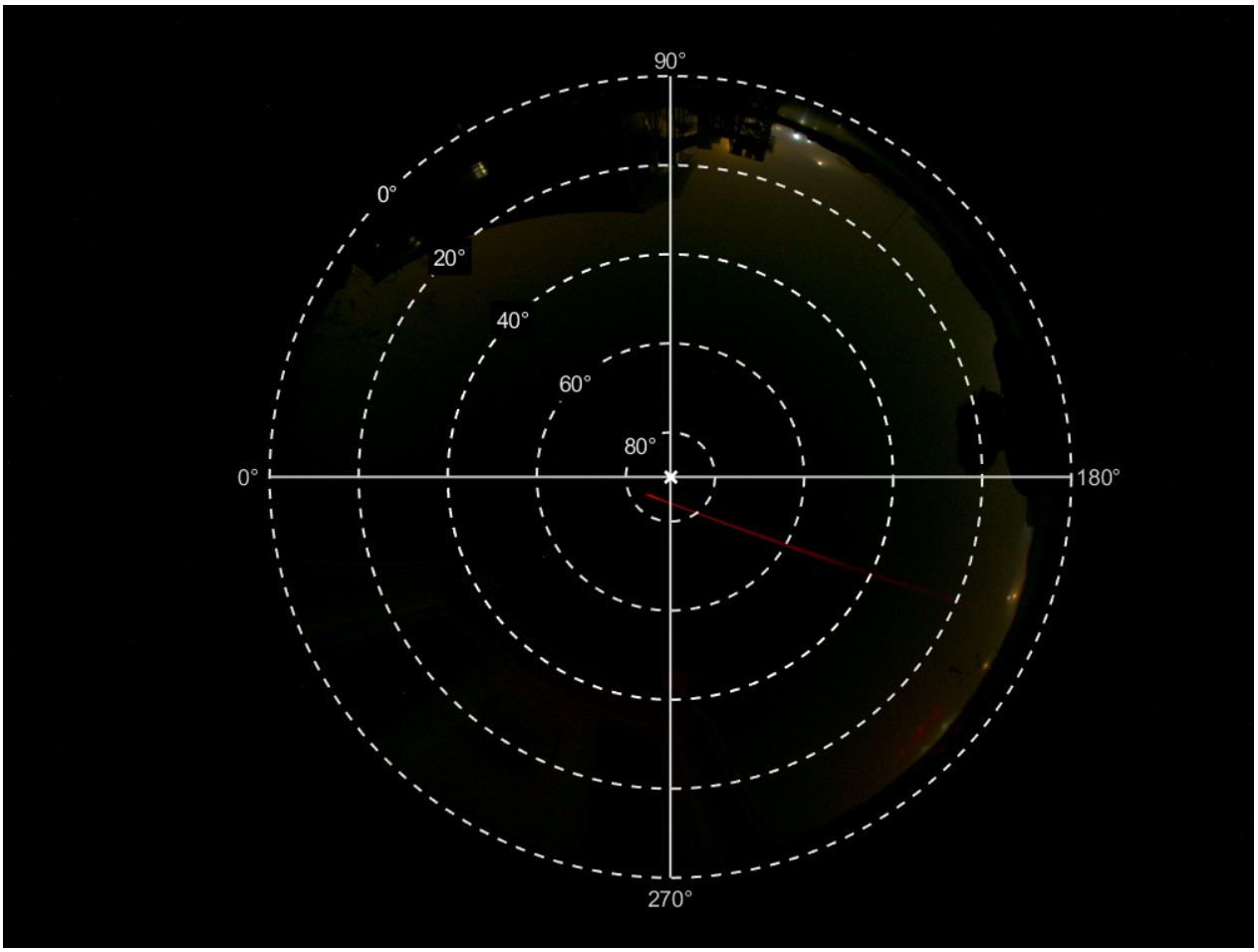


Figure 5.6: The June 29 red laser image with azimuth an elevation angles overlaid. The x in the centre represents the image zenith, at 90° of elevation.

of the laser top can give the tilt of the laser ($90° - \theta_{El,top}$) and the direction in which it is tilted (φ_{top}).

The cartesian coordinates of the base of the laser are also known, if we take the camera to be at [0,0,0] and the laser is 10 cm away (per Campbell, 2024) in the azimuthal direction of the base. Knowing the cartesian coordinates of the base and the direction of the laser beam (by creating a unit vector, $\vec{v}$, pointing from the base to the top), we can then construct a line along that vector by increasing the radius of the line by a set step size and mapping the cartesian coordinates at each step size back onto spherical and then pixel coordinates.

For this work, use a step size of 1 cm. As we approach the top of the beam, the mapped points become closer together until they converge at the apparent top of the beam on the image. Therefore, we take the highest part of the beam that we can 'see' as the distance along the beam at which there start being multiple 1 cm steps within that top pixel. See Section 5.4.4 for further discussion of how much of the beam is visible.

However, the camera lens does not appear to be fully equiangular, as discussed further in Section 5.4.4.

As a result, this drawn line does not completely match up to the laser beam in the image, especially in the middle (Figure 5.23). We therefore manually selected the coordinates of the centre of the beam at the same elevation angle, and take the distance along the beam to be approximately the same as those derived from the procedure above.

From the distance along the beam and the elevation angle, we can also determine the scattering angle at each point along the beam. For a beam tilted at some angle, the scattering angle θ is shown in Figure 5.7 and given by:

$$\theta = 180° - \cos^{-1}\left(\frac{\vec{u}\cdot\vec{v}}{|\vec{u}||\vec{v}|}\right) \tag{5.7}$$

where $\vec{u}$ and $\vec{v}$ are the vectors from the camera and along the laser beam, respectively. The scattering angles able to be seen by the camera at this geometry are between about 90° and 180°.

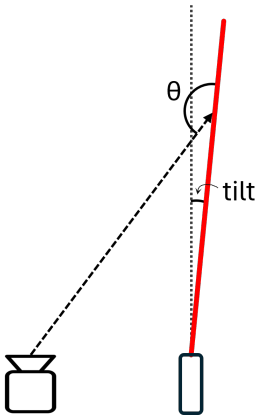


Figure 5.7: The scattering angle along the laser beam is the angle between a vector in the direction of the laser beam and a vector from the camera to a given point along the laser beam.

To estimate the brightness along the beam, we extract average spectral radiance at each 1 cm step along the beam. The image is first converted from digital number to spectral radiance as described in Section 5.2.2. We then get an average spectral radiance by taking a patch with the height in pixels of the 1 cm step, which varies along the beam, and a width of 20 pixels to either side of the centre of the beam. Two further patches of the same height and a width of 10 pixels are taken to either side of the 40 pixel wide patch to represent the background brightness. This background brightness is then subtracted from the beam to remove any stray light.

Knowing the scattering angle along the beam, we can also phase function-correct the spectral radiance using the modelled phase functions for particles with a radius of 30 μm in each of the three laser wavelengths (see Section 5.2.3). Removing any phase function effects allows us to see areas of strongest backscatter, which may indicate thicker fog layers.

5.3 Results

5.3.1 Simulated Particle Scattering Behaviour

Using the Mie Simulator as described in Section 5.2.3, I simulated the single scattering phase function and the scattering efficiency for both the microspheres and fog particles. The necessary simulation parameters are the diameter of the particle in μm, the number of spheres per 1 mm^3, the wavelength range in nm, and the refractive indices of both the medium and the spheres.

For the microspheres, the 3 μm diameter spheres have a concentration of 61.1 spheres/mm^3, the 20 μm spheres have a concentration of 6.75×10^{-1} spheres/mm^3 and the 90 μm spheres have a concentration of 3.14×10^{-3} spheres/mm^3. The latter three parameters were fixed for all three microsphere simulations with the wavelength range being 400-650 nm at a step size of 0.5 nm, the refractive index of the medium (water) being 1.333 and the refractive index of the microspheres being 1.6.

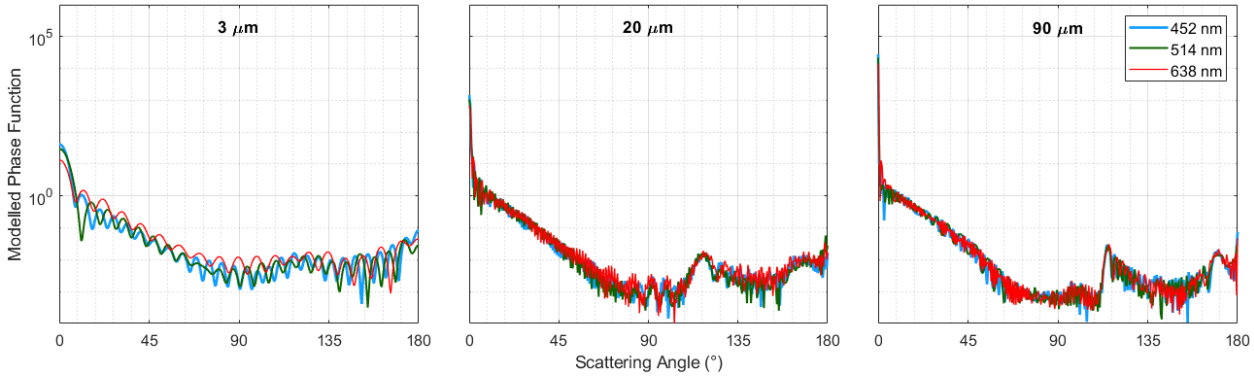


Figure 5.8: Modelled phase functions for the three sizes of microspheres at each of the three laser wavelengths, with the y-axis on a logarithmic scale. Note the differences in each y-axis.

These parameters gave nine phase functions - three curves at each laser wavelength for each of the three microsphere sizes. These curves are given in Figure 5.8. The curves all have very strong forward- and back-scatter peaks with the forward-scattering peak in particular vastly overwhelming the rest of the curve. The forward scattering becomes stronger for the larger microspheres, with the curves for those sizes also showing local maxima around 115° and 170°. If we look at the middle section of the curve using a linear y-axis (Figure 5.9), we see that the middle of the curve is almost entirely flat above about 55° for the 3 μm microspheres and for the 20 and 90 μm microspheres apart from the local maxima.

For the 20 and 90 μm, the phase functions of the three wavelengths are very similar, indicating that there is not much difference in scattering behaviour within these three wavelengths. For the 3 μm microspheres, we see differences in the phase function depending on wavelength, particularly in the forward-scattering

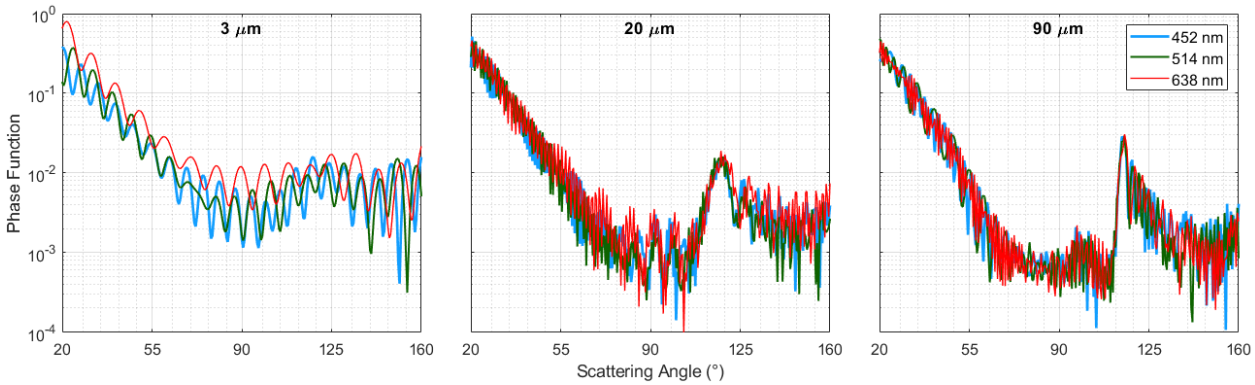


Figure 5.9: The middle 140 degrees of the modelled phase functions for the three sizes of microspheres at each of the three laser wavelengths, corresponsing to the scattering angle range seen in the aquarium experiments.

direction, with maxima and minima appearing at different scattering angles. This indicates that the scattering behaviour at smaller particle sizes is more heavily wavelength dependant.

The model also gives us a scattering coefficient (μ_s) from which we can derive a scattering efficiency (Q_{sca}) using Equation 5.3. The scattering efficiencies as a function of wavelength for each of the spheres are given in Figure 5.10 and Table 5.3. Similarly to the phase functions, we can see that the scattering efficiencies are more strongly wavelength dependant for the smaller microspheres, which are more heavily in the mie scattering regime. The scattering efficiency is also higher for these smaller micropsheres, above 3×10^{-6} in this range of wavelengths, while for the 20 and 90 μm microspheres the scattering efficiency is lower than the minimum value of the 3 μm spheres in this range. However, it is important to note that the concentration is also the highest for the 3 μm spheres.

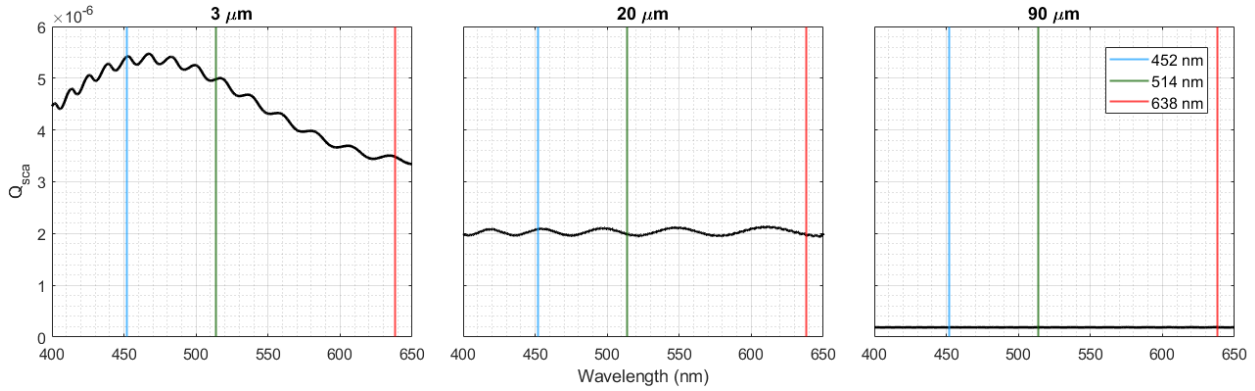


Figure 5.10: The scattering efficiencies of the three sizes of microspheres as a function of wavelength. The vertical coloured lines indicate the wavelengths of the three lasers. Note that while the scale of all three y-axes are the same, their ranges differ.

Table 5.3: *Scattering efficiencies of the three sizes of microsphere at the three laser wavelengths.*

	Blue	**Green**	**Red**
3 μm	5.42×10^{-6}	4.98×10^{-6}	3.48×10^{-6}
20 μm	2.08×10^{-6}	1.99×10^{-6}	1.96×10^{-6}
90 μm	1.86×10^{-7}	1.89×10^{-7}	1.89×10^{-7}

For fog droplets in air, we used a diameter of 30 μm, a concentration of 10 000 spheres/mm^3, based on Isaac et al. (2020), a refractive index of the medium (air) of 1.0003 and a refractive index of the fog droplets of 1.333. The phase functions at the three laser wavelengths are shown in Figure 5.11. Fog droplets of this size exhibit the strongest wavelength dependence in the forward scattering direction, while in the flat part of the curve between $\sim 55 > 160°$, the phase functions of the three wavelengths are quite similar. There are no obvious local maxima or minima.

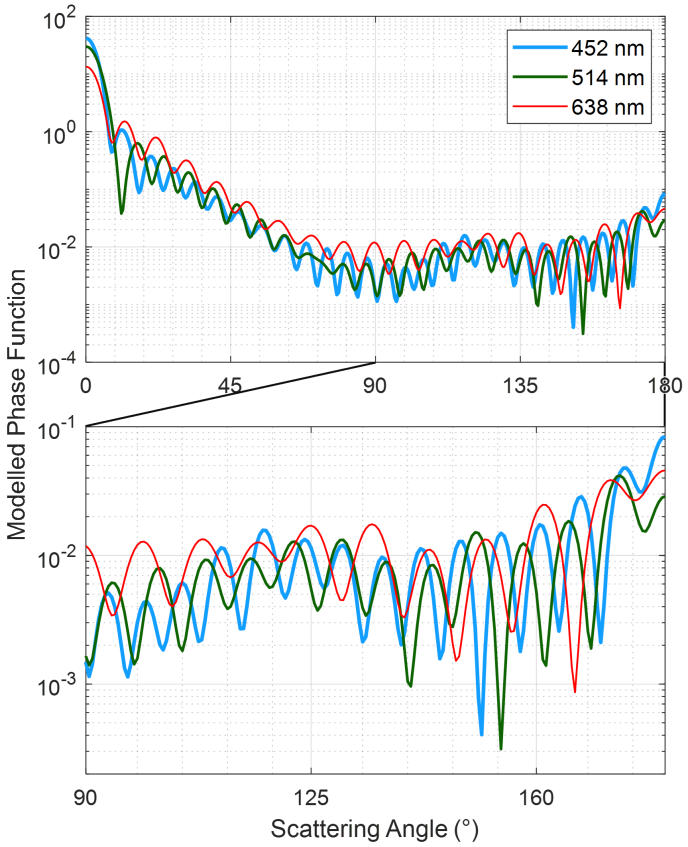


Figure 5.11: The modelled phase function of 30 μm fog. The top figure shows the full phase function while the bottom shows the region from $90° - 180°$ (the area seen in the field experiments) both on a logarithmic scale.

The scattering efficiency as a function of wavelength is shown in Figure 5.12. Similarly to the larger microspheres, the scattering efficiency has little wavelength dependence. The scattering efficiencies for the blue, green and red laser wavelengths are 0.0667, 0.0670 and 0.0694, respectively.

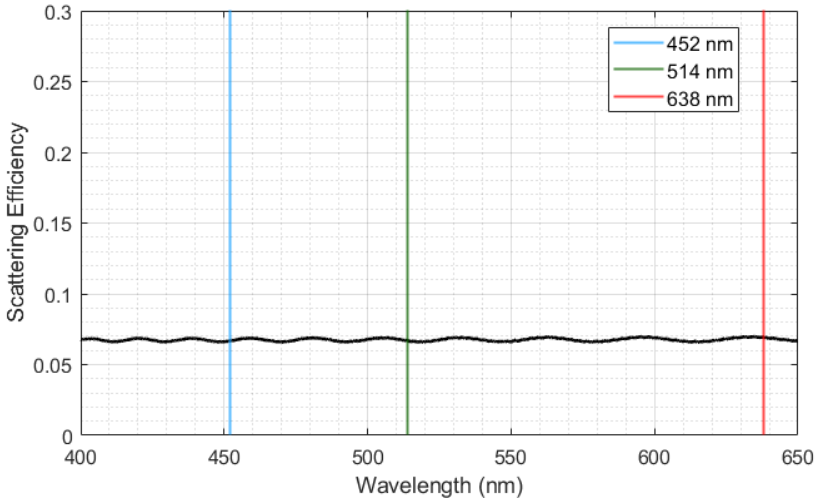


Figure 5.12: The modelled scattering efficiency of 30 μm fog as a function of wavelength. The vertical coloured lines indicated the wavelengths of the three lasers.

5.3.2 Laboratory Experiments

Figure 5.13 shows all nine observations taken with the red laser through 3 μm microspheres, labelled 'runs'. While the radiance does fall off with distance, indicative of extinction as the beam passes through the medium inside the aquarium, we also see the curve rising and falling regularly in each reflection of the laser beam. These smaller maxima and minima show the phase function of the microspheres as the scattering angle changes.

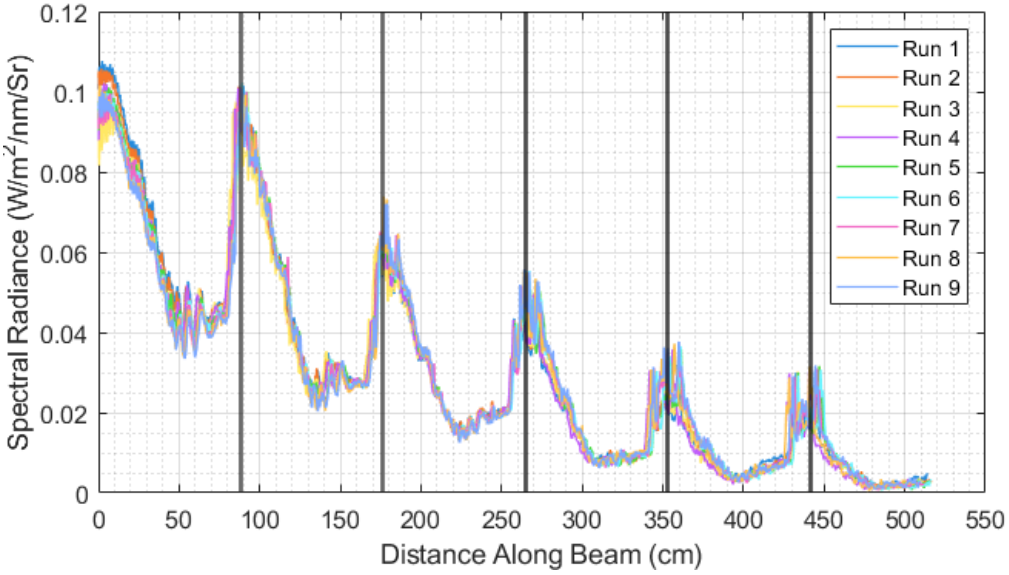


Figure 5.13: Spectral radiance of the beam distance for the red laser through three micron micropsheres over the course of nine observations. Vertical black lines show the position of the mirrors where the beam is reflected.

Since the radiance-distance curves along the beam are so similar for each run, we use an average curve to compute the extinction, as described in Section 5.2.4. The extinction curves plotted over the radiance-distance measurements for each size of microsphere at each wavelength laser are shown in figure 5.14. The extinction coefficients, given by b in Equation 5.4, are given in Table 5.4.

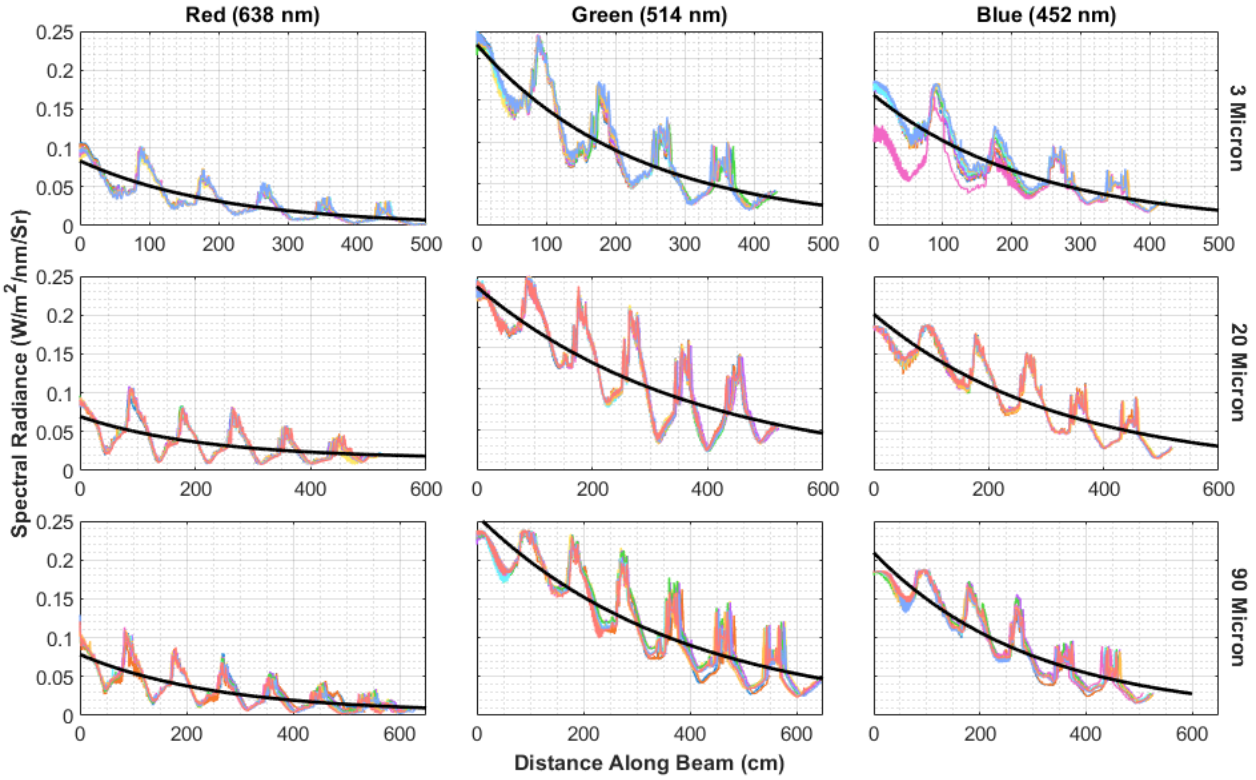


Figure 5.14: Extinction curves for each size of microsphere at each laser wavelength. The spectral radiances of the beams for each aquarium observation as a function of distance are shown in pastel colours, with the extinction curve plotted as a heavy black line overtop.

Table 5.4: *The extinction coefficients for each aquarium observation. Errors on the values are the 95% confidence intervals for the extinction curve fit.*

Wavelength / Size of Microsphere	**638 nm**	**514 nm**	**452 nm**
3 μm	$4.89 \pm 0.02 \times 10^{-3}$	$4.37 \pm 0.02 \times 10^{-3}$	$4.29 \pm 0.10 \times 10^{-3}$
20 μm	$4.62 \pm 0.12 \times 10^{-3}$	$2.66 \pm 0.06 \times 10^{-3}$	$3.110 \pm 0.01 \times 10^{-3}$
90 μm	$3.88 \pm 0.07 \times 10^{-3}$	$2.62 \pm 0.10 \times 10^{-3}$	$3.35 \pm 0.01 \times 10^{-3}$

The red laser has the lowest spectral radiance overall, followed by the blue with the green having the highest. The number of reflections we are able to confidently observe also increases as the size of the microspheres increases. The highest extinction is the red laser in 3 μm spheres, with a decay constant of 4.89×10^{-3} while the smallest is seen in the green laser in the 90 μm spheres.

The residual phase function left behind from subtracting the extinction curve from the measured spectral

radiance was then averaged over the reflections of the beam. The phase functions of each of these bounces are very similar, which increases our confidence that this residual is the phase function we are seeing.

Because of this subtraction process, the phase function ended up with some negative values, which are non-physical. Typically, we would resolve this by having the area under the phase function integrate to 4π (Hansen and Travis, 1974); however as we do not see the full angular range of the phase function and are mostly interested in the general shape, we simply shift the phase function up so that the minimum value of the experimentally derived phase function is equal to the minimum value of the corresponding modelled phase function. The averaged phase functions with their 95% confidence intervals are shown in Figure 5.15.

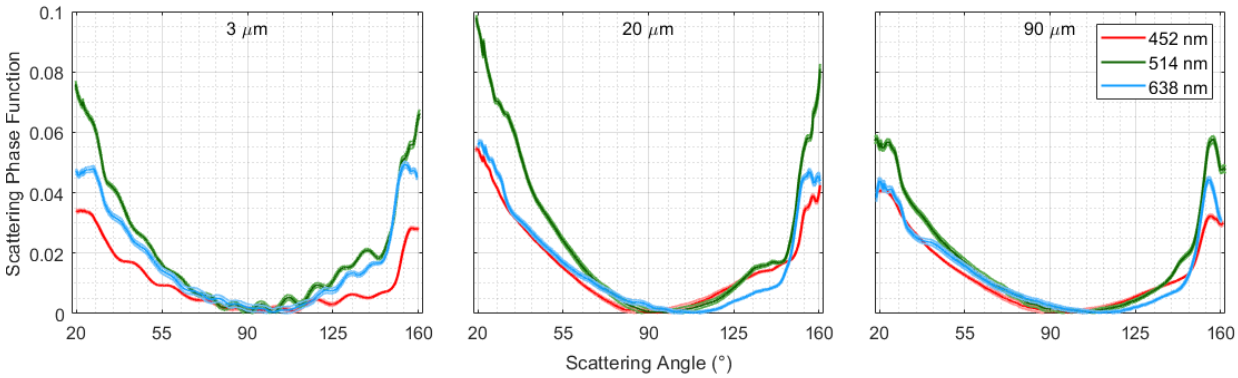


Figure 5.15: The average phase functions of the three sizes of micropsheres in the aquarium at the three different laser wavelengths. Shaded error bars represent the 95% confidence interval of the mean phase function.

The geometry of the setup means we are not able to observe scattering angles below $\sim 20°$ or above $\sim 160°$, where we expect to see the majority of scattering. Additionally, the reflected beams converge on topof each other at the mirrors, which makes distinguishing the individual beams difficult close to the mirror. The apparent increase in the phase function around 160° is likely the forward scattering of the adjacent beam or other scattering effects off the mirror. The phase function is likely only reliable out to $\sim 140°$.

5.3.3 Field Experiments

The bias- and dark-corrected images from June 29 are shown in Figure 5.16.

The red laser beam is tilted about 6.6° from vertical, the green $\sim 10.4°$ and the blue $\sim 13.8°$. We can easily convert the distance along the beam to the height above the ground using these tilt angles to infer the heights of fog banks. We also add 17 cm to this height as the approximate height above the ground of the base of the laser beam, based on the height of the pelican case. The maximum height above the ground of the red beam is 76.99 m, of the green 32.70 m and of the blue 49.45 m. The maximum height we are able to resolve decreases with increasing tilt angle.

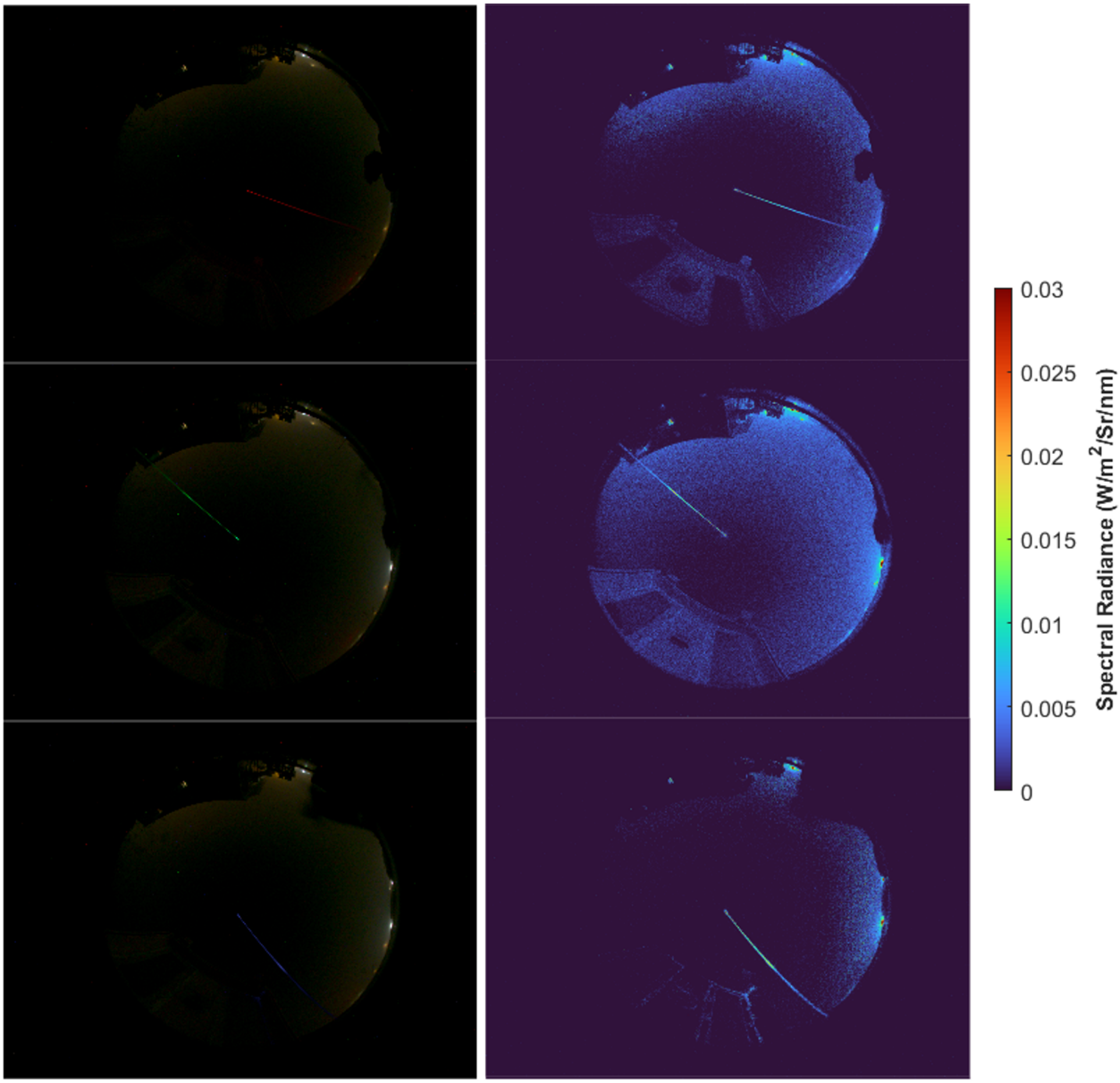


Figure 5.16: Images captured of each of the three laser beams on June 29 are shown on the left, red top, green middle, blue lower. The right images show the corresponding bias and dark corrected images (Section 5.2.2) in the relevant channels, which have been converted to spectral radiance.

We determine the spectral radiance along the beam as described in Section 5.2.5, shown in Figure 5.17. The blue beam seems to have the highest spectral radiance out of all three, despite it having the lowest power. However, the blue beam will experience the most Rayleigh scattering due to its low wavelength. Looking at the bias and dark corrected blue channel (Figure 5.16), the beam is the most distinct from the background, and there is not much stray light in the blue channel. The green beam is the most difficult to resolve from the background.

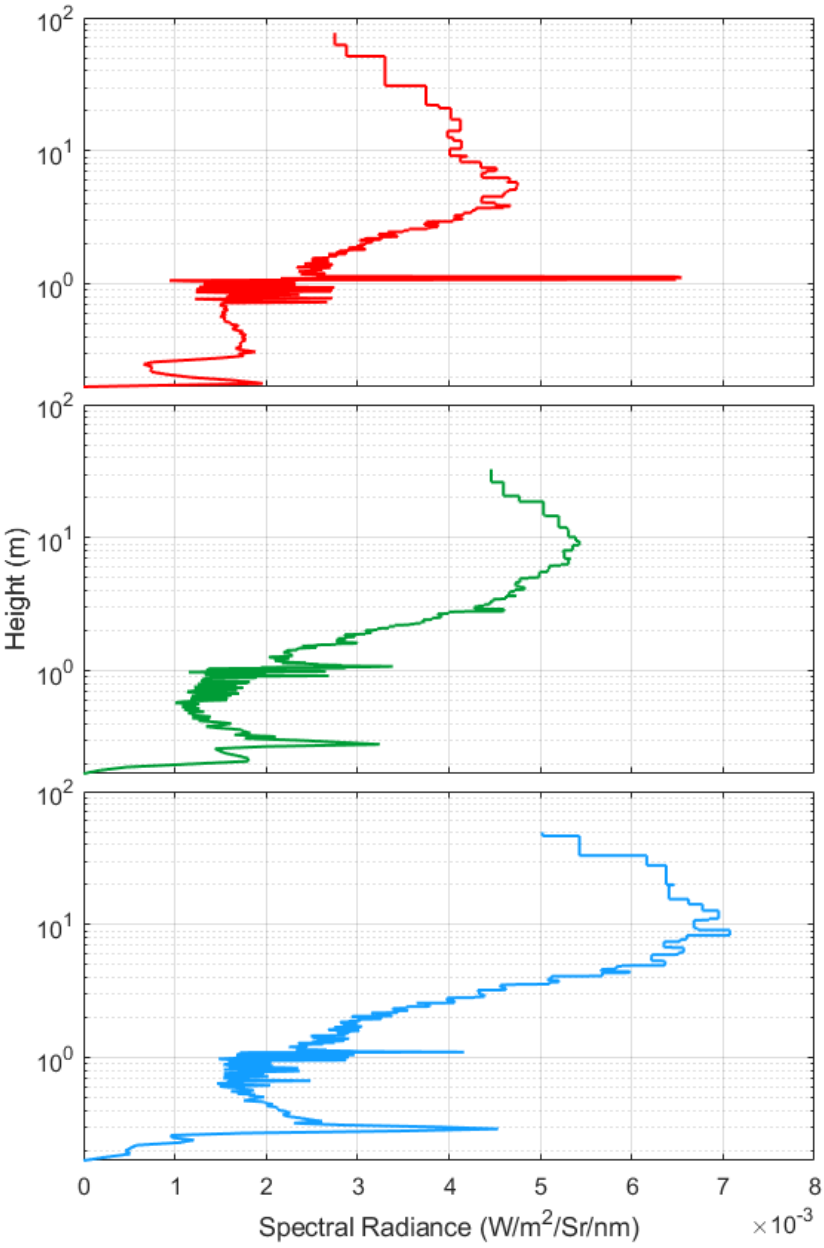


Figure 5.17: Spectral radiance as a function of distance for each laser beam (red top, green middle, blue bottom) for the measurements taken on June 29. All beams have been corrected for any stray light from the background.

The stair-step behaviour toward the top of the beam is likely due to the fact that the 1 cm steps become smaller than one pixel towards the top of the beam. We also see contamination from lights near the horizon in the lower ~ 0.4 m of the beam. Thus, we can likely safely ignore the results in this lower portion.

Dividing the curves by the modelled fog phase functions gives us the phase function corrected curves (Figure 5.18). We can see potential fog layers around 1 m and 4 m. This could also be the base of the fog layer. We do not have any notes about the character of the fog or its vertical extent, nor any meteorological

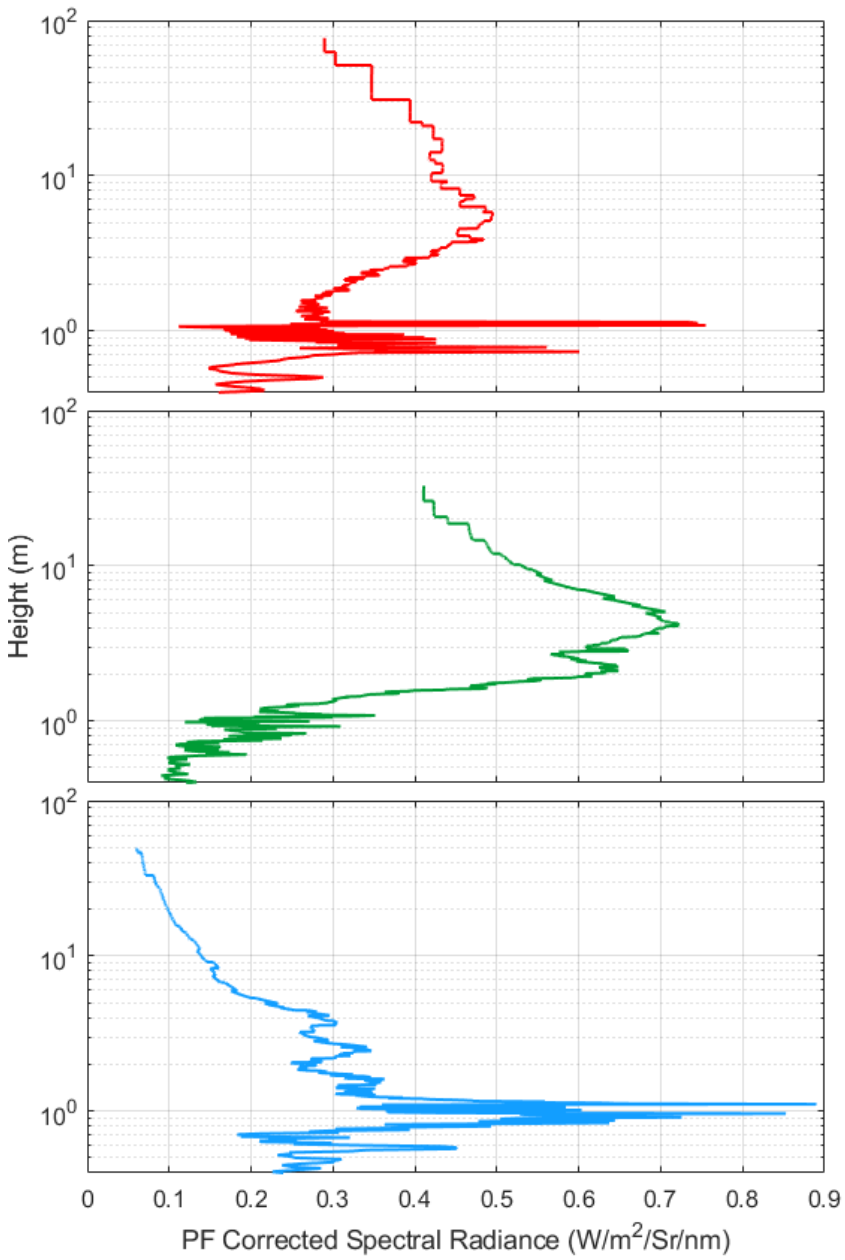


Figure 5.18: Spectral radiance as a function of distance for each laser beam (red top, green middle, blue bottom) for the measurements taken on June 29. The spectral radiances have been dicvided by the phase functions generated in Section 5.3.1. The bottom 40 cm of the beam have been removed due to contamination from nearby lights.

data to compare to the laser backscatter findings. The ~ 1 m signal is quite strong in the red and blue, but is overpowered in the green by the signal higher up.

The behaviour in the green is likely due to the strong background signal in the green (Figure 5.16). At lower altitudes along the beam, the background signal makes the laser nearly indistinguishable, but it becomes easier to resolve towards the top. When we subtract the background from the beam, these lower portions will have smaller values while the upper ones will be larger.

5.4 Discussion

5.4.1 Comparison of Laboratory Results with Modelled Microspheres

We can compare the phase functions we derived from the aquarium observations with the modelled phase functions from Section 5.3.1, shown in Figure 5.19. We have limited the phase functions to the area between 20° and 140° as the experimental curve outside that range is likely contaminated by the overlap between the incoming and reflected beam.

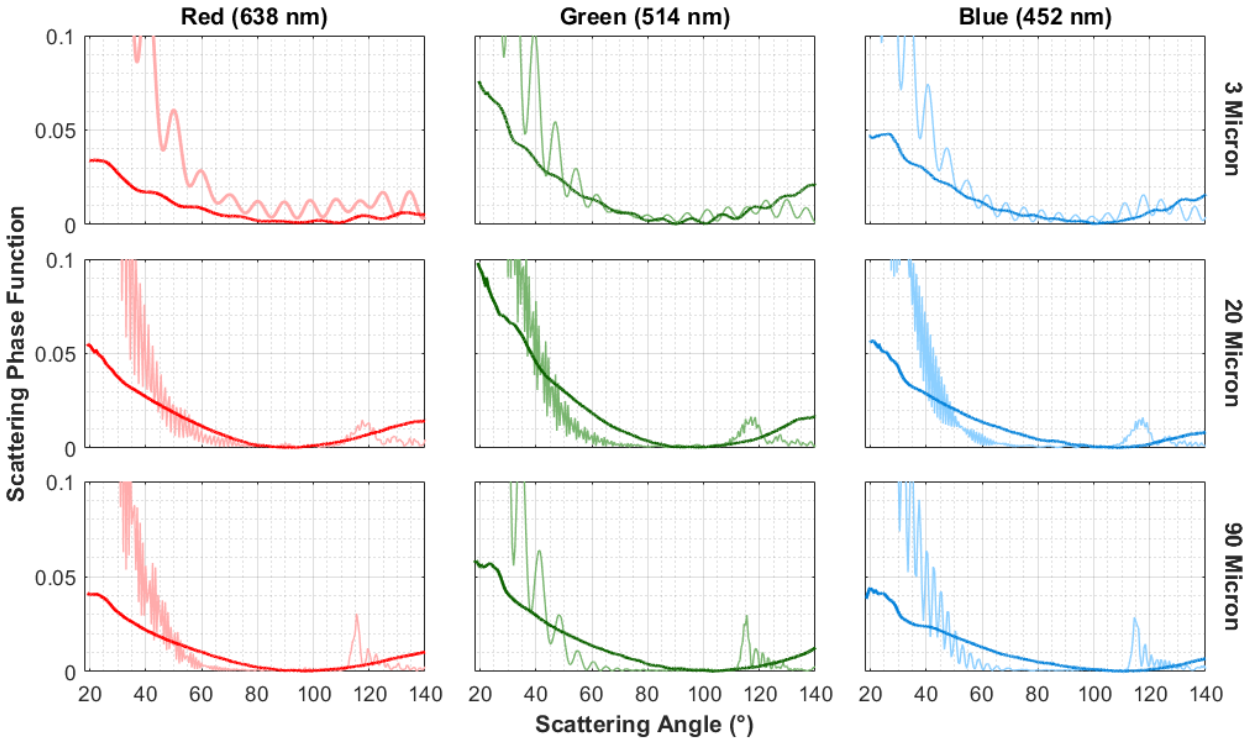


Figure 5.19: The average scattering phase functions from the aquarium observations compared with the modelled phase functions for each size of microsphere at each laser wavelength. The darker, thicker lines are the experimentally derived phase functions while the lighter, thinner lines are the modelled curves.

The 3 μm curves exhibit some of the oscillating behaviour that we see in the modelled phase functions, whereas the 20 and 90 μm curves are smoother. This oscillation is really only relevant for perfect spheres, and is not expected in real scattering materials (Hapke, 2012b). Its presence in the 3 μm runs, which have the highest concentration of microspheres, could be indicative of more backscatter from the micropsheres and less from other impurities in the water. We observe an increase in the phase function at scattering angles below $\sim 60°$ in both the modelled and experimental phase functions, though the degree to which the magnitude of the phase function increases is lower in the experimental curves.

We do not see the scattering features around 120° that are present in the modelled phase functions,

especially in the larger microspheres. It is worth noting that we are using a Mie scattering model, and the larger microspheres likely exhibit properties more in line with geometric scattering (Hansen and Travis, 1974). An analysis using geometric optics may be more appropriate in this case.

It should also be noted that the microspheres were diluted quite a bit, and in the case of the 90 μm spheres, the concentration in the aquarium is only a few spheres per mL (Section 5.2.4). This consideration does raise the question as to whether we are seeing backscatter from the spheres themselves when they are so scarce in the aquarium, or impurities in the water. At the very least, we are almost certainly seeing backscatter from a combination of water impurities and microspheres, which is likely responsible for the more flattened phase function, which is often a consequence of contributions of multiple or irregular particle geometries.

There were images taken of each of the lasers in the tap water alone, which we analysed using the same methods as in Section 5.2.4 to see the differences in extinction and phase function. This will give us an idea of the magnitude of the contribution from the microspheres versus impurities in the tap water. The spectral radiance along the beam and fit extinction curves are shown in Figure 5.20, with corresponding extinction coefficients given in Table 5.5.

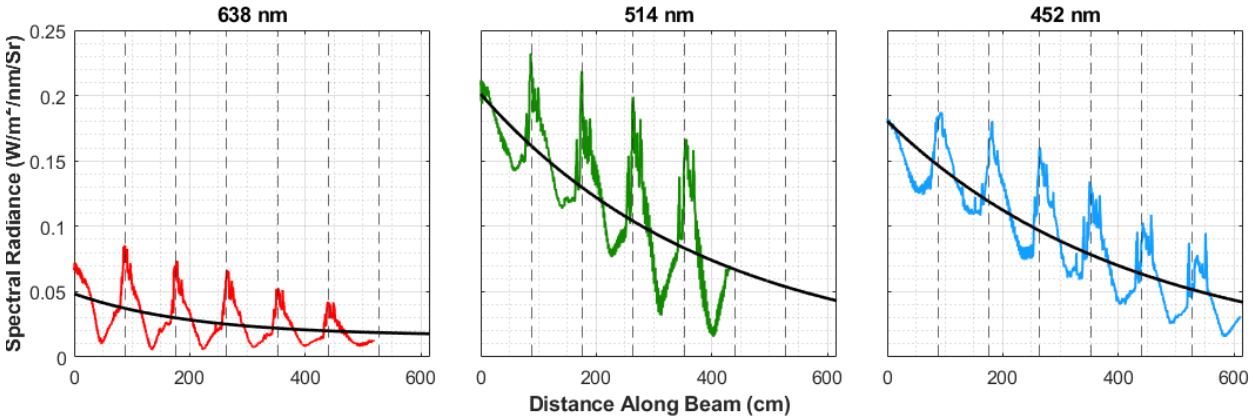


Figure 5.20: Fit extinction curves for each laser wavelength through tap water only in the aquarium. The spectral radiance along the beam is shown in red, green, and blue for each laser with the heavy black line overtop showing the extinction curve. Vertical dashed lines indicate the position of the mirrors, where the beam is reflected.

Table 5.5: *The extinction coefficients for each aquarium observation, as in Table 5.4 and the extinction coefficients for the observations taken in tap water only. Errors on the values are the 95% confidence intervals for the fit extinction curve.*

Wavelength / Size of Microsphere	**638 nm**	**514 nm**	**452 nm**
Water Only	$4.85 \pm 0.48 \times 10^{-3}$	$2.50 \pm 0.28 \times 10^{-3}$	$2.37 \pm 0.12 \times 10^{-3}$
3 μm	$4.89 \pm 0.02 \times 10^{-3}$	$4.37 \pm 0.02 \times 10^{-3}$	$4.29 \pm 0.10 \times 10^{-3}$
20 μm	$4.62 \pm 0.12 \times 10^{-3}$	$2.66 \pm 0.06 \times 10^{-3}$	$3.110 \pm 0.01 \times 10^{-3}$
90 μm	$3.88 \pm 0.07 \times 10^{-3}$	$2.62 \pm 0.10 \times 10^{-3}$	$3.35 \pm 0.01 \times 10^{-3}$

The extinction coefficients for the blue and green lasers are lower than any of those for the runs with microspheres, which we would expect given a theoretically clearer medium. However, the extinction coefficients are all very close to each other, with the coefficient in the green run for water only overlapping that for the 90 microsphere run in the 95% confidence interval. The results from the red laser are a bit more unclear, with an extinction coefficient higher than those in the 20 and 90 μm experiments. It is not clear why this would be the case, though it is worth noting that the red laser is by far the dimmest of the three. The responsivity in the red of the Basler camera does fall off above $\sim$ 600 nm (Figure 5.1), though at $\sim$ 638 nm it is still comparable to the response in the blue channel. The red extinction coefficients are overall higher than those of the blue and green, and clustered closer together.

In all cases, while it seems like the microspheres may have a small influence on the laser scattering, and it is clear that impurities in the water impact the backscatter to a large degree. Thus, it is likely that the signal from the micropsheres alone is contributing a much smaller amount than that from the tap water impurities.

We also extracted the phase functions from the spectral radiance measurements following the same method described in Section 5.2.4 and while the phase functions are similar in shape to those in Figure 5.15, they are relatively flat and smooth, as we saw with the larger microspheres, and as we would expect for a combination of irregularly shaped water impurities in the pure tap water. The similarity of the phase functions is also further indication that there is a large component of the backscatter signal we see from impurities.

5.4.2 Effects of Laser Wavelength and Particle Size on Observed Scattering Properties

As mentioned in Section 5.3.1, when we model the behaviour of microspheres and fog particles, smaller particle sizes have a greater wavelength dependence on their scattering properties. As discussed above, we do not observe the same amount of variation due to wavelength in the laboratory experiments, which could be due in part to camera and laser characteristics. Likewise, at the assumed size of the fog particles we observed in Argentia ($\sim$ 30 μm) we do not expect to see much difference between wavelengths apart from a small increase in magnitude in the red around $\sim 90° - 130°$.

In the aquarium, we can observe the impact of particle size on the behaviour of the laser beam. We do see that the extinction is highest in the 3 μm spheres and lowest in the 90 μm spheres, which agrees with the smallest modelled particles having the largest values of Q_{sca}. The smaller particles are likely extincting more light by scattering it away. This does suggest that we are able to use the observed laser backscatter to probe differences in particle size, but more effectively for the smallest particles in the Mie regime.

5.4.3 Impact of Assumed Fog Droplet Size

While we selected a fog droplet size of 30 μm based on characterizations of Newfoundland fog by Isaac et al. (2020), in reality fog contains a bimodal distribution of fog droplet sizes (Fig. 9 in Isaac et al., 2020). To determine how our assumed single fog droplet size impacts our results, we can look at the phase function corrected spectral radiances from the images with two other sizes of fog particles: 20 and 40μm (Figure 5.21).

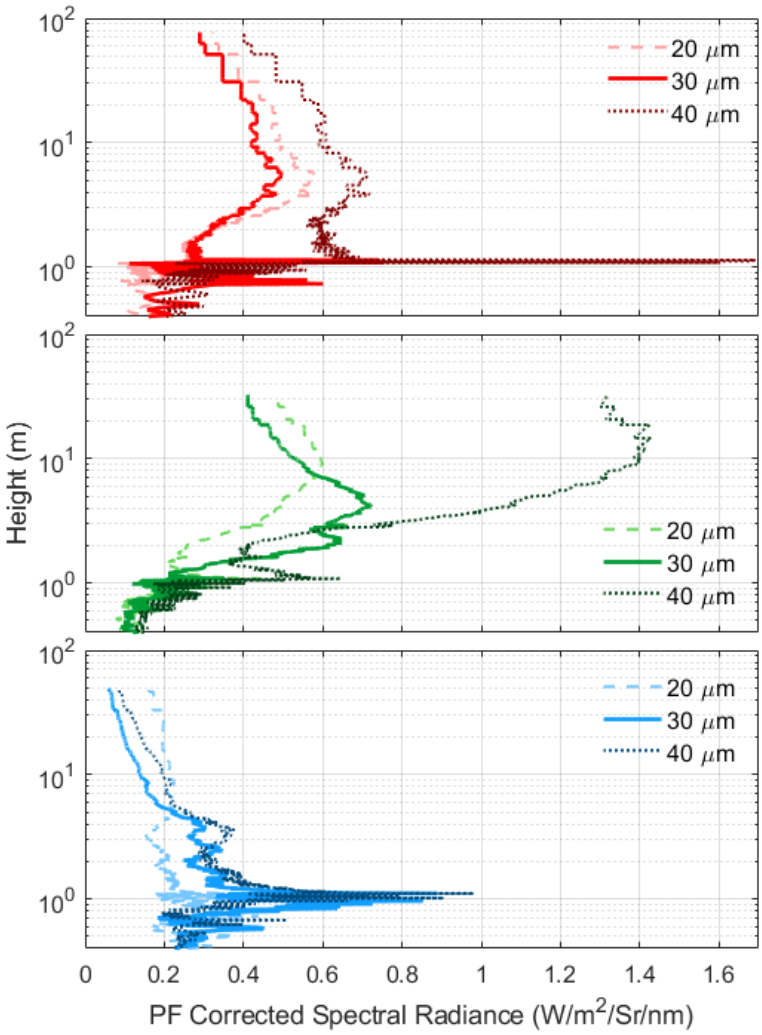


Figure 5.21: The spectral radiances as a function of distance for each laser beam (red top, green middle, blue bottom) for the observations on June 29. As in Figure 5.18, the spectral radiances have been divided by the fog droplet phase functions for droplet sizes 20 μm (light, dashed line), 30 μm (solid line), and 40 μm (dark, dotted line). The bottom 40 cm of the beam have been removed.

In the range of $0 - 180°$, the scattering angle range of the laser beams, the phase functions do not seem to differ all that much. They all display the local maxima around 140°, and the backscatter peak towards 180°. However, there are also more subtle local minima and maxima which differ in location between the three sizes of fog droplet which impact the phase function corrected spectral radiances.

The 40 μm droplet phase function does appear to mostly result in a higher spectral radiance at higher parts of the beam, which also have greater scattering angles. The exception to this is in the blue beam where the highest parts of the beam are brightest with the 20 μm droplets. The lower parts of the beam, at lower scattering angles, are more similar in spectral radiance.

The particle size seems to have the greatest impact at scattering angles closest to 180°. This is to be expected, as it is the forward- and backscattering regions of the phase function which are the most influenced by particle size. While the magnitude of the phase function corrected spectral radiance does seem to be impacted by particle size, especially at higher scattering angles, the general trends with height still hold (with the exception of the highest portion of the green beam), and we see the same increase around 1 and 4 m at all three particle sizes.

5.4.4 Limitations of the Experiments

As with any experimental work, we identified a number of limitations with our experiments. Further challenges for this work in particular arose from the fact that I did not perform the experiments and was simply working with the data after the fact. Some challenges associated with this have already been noted above - namely in the concentration of microspheres in the aquarium not seeming to change throughout the runs and in the exposure time not being noted for the June 29 observations in Argentia.

As noted in Section 5.2.4, the intention of the aquarium experiments was to vary both the size of the microspheres and their concentrations to examine the impact of particle number density on the laser scattering. As the images and the resulting radiance curves (Figure 5.14) showed little variation, and because of confusion surrounding the procedure used to dilute the concentration, we chose to assume a fixed, average concentration. Because of this assumption, we cannot explore in this work the impact of particle concentration on the laser scattering properties. Additionally, it is possible and indeed likely that the average concentrations chosen for each size of microsphere is not representative of the actual concentration of microspheres in the aquarium. This limitation mainly impacts the modelled scattering behaviour as we used these concentrations for those models. While the conclusions about behaviour at different wavelengths and particle sizes should stand independent of concentration, in comparing to the phase functions derived from the aquarium, it is likely that our modelled phase functions do not have the same concentration of microspheres.

Furthermore, the extreme dilution of the microspheres meant that there were very few spheres total in the aquarium, especially at the larger sizes. In Section 5.4.1, where we saw that the microspheres likely had a much lower contribution to the observed backscatter signal than impurities in the tap water used for the experiment. A much higher concentration of microspheres is likely needed to comment upon their behaviour,

and using deionized water likewise would perhaps remove the contribution from tap water impurities.

The aquarium was also not the best setup to observe the beam on its own. Reflections not only off the mirrors but also off the aquarium sides (Figure 5.5) added stray light in the image and made distinguishing the laser beam itself from these background reflections difficult. This problem was especially visible in extracting the phase function, as discussed in Section 5.3.2. The ends of the phase function that we were able to observe, around 20° and 160°, exhibit unusual behaviour, especially the steep increase towards 160°. This behaviour is likely a result of the reflection at the mirrors, with adjacent reflections of the beam overlapping. As a result, we cannot be very confident in the phase functions we extracted from these images.

Campbell (2024) gives a full description of the Argentia experiments, which included three daytime and two nighttime experiments. While we only look at the June 29 nighttime experiment in this work, the daytime experiments showed that the lasers were not visible against the daytime sky brightness. The laser power required to overcome sky brightness will be discussed more in Section 5.4.5.

The June 29 experiment suffered from both a lack of documentation and what Campbell (2024) describes as "an act of haste". The exposure time was not noted for the images. Our assumed exposure time is based on that of the other nighttime experiment and the aquarium experiments; however there is no way to know if it is correct. As a result, the conversion factor we use to extract the spectral radiance from the image may be incorrect. While the spectral radiances seem reasonable, they necessarily are only our best guess.

Lights from the nearby town at the horizon and causing light pollution in the sky also made it difficult to determine the radiance of the beam alone. While we subtracted the background radiance around the beam, this signal still may have caused problems. Near the base of the beam, at the horizon, the beams sometimes directly overlapped nearby light sources, which would contribute to the radiance of the beam and not be fully captured in our background patch of the image. In the green channel, the radiance of the sky is very strong, and sometimes overpowers the radiance of the laser itself, which, when the background radiance is subtracted, results in less scattering. A more remote location such as dark sky preserve may have yielded better results, or taking a background image without any lasers which we could then subtract to get just the laser.

The position of the laser was also not truly vertical, as it was intended to be. The laser or camera may have been jostled in the case, or the accuracy of the setup may not have been perfect. As a result, we have had to determine the tilt of the laser based on the beam's position in the image. Characterising the position of the laser with respect to the camera to a higher level of precision will be necessary in deriving the liquid water concent with respect to height, as well as getting accurate scattering angles to observe scattering behaviour.

The method we used to determine the pixel coordinates of the laser beam on the image itself (described

in Section 5.2.5) was also flawed due both to this mispointing and to the non-equiangular characteristics of the lens, which we are unable to account for in this work. The magnitude of this effect is not quantifiable, as we cannot account for the distortion from the lens which caused the modelled beam to not line up with the imaged laser beam (Figure 5.22). Due to the lack of any accurate camera model for this setup, we were were forced to assume a distance along the beam at each of the manually selected points to be the same as those on the modelled beam at the same elevation angle. We found the difference in azimuth and elevation from the modelled beam points and the manually selected points for all three images was no greater than 1.38° and 0.29°, respectively.

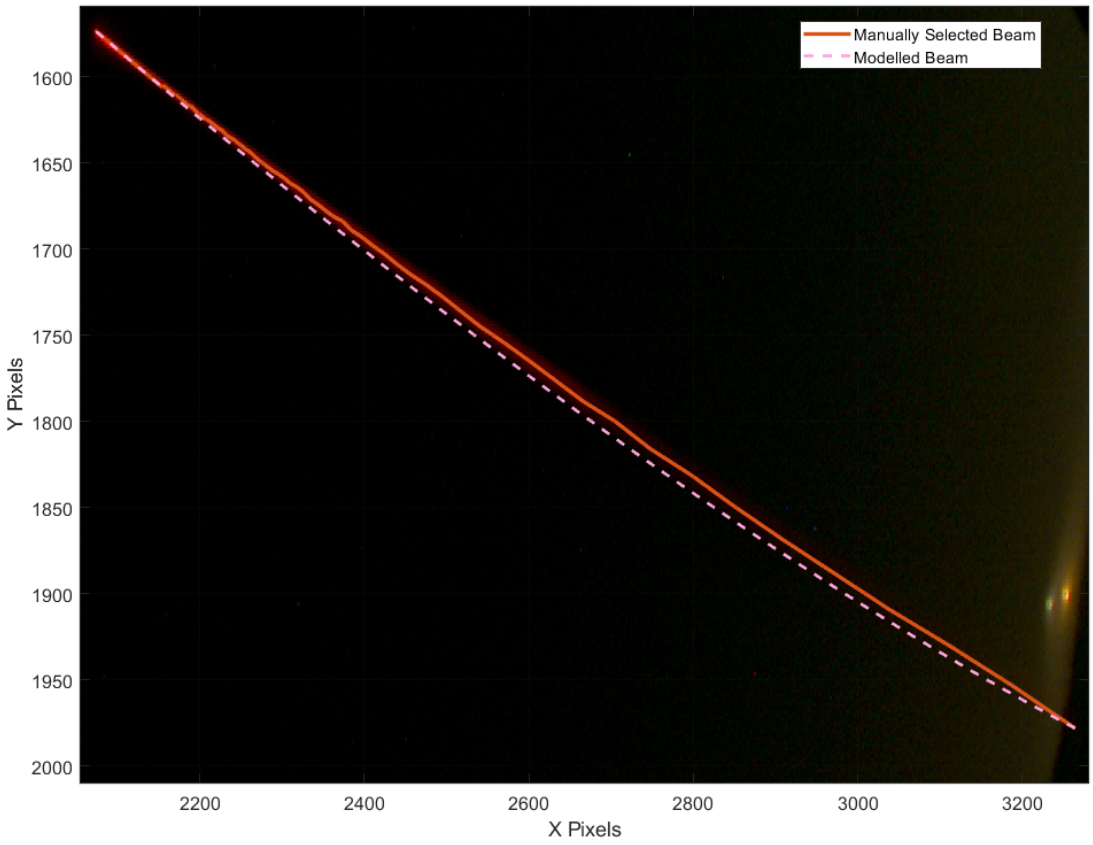


Figure 5.22: The modelled (pink dashed line) and manually selected (red solid line) beams plotted over the image of the red laser beam. Where the beams overlap at the top and bottom, we used the pixel coordinates from the model. The maximum distance on the image between the modelled and the manually selected beams for this image was 9.3 pixels.

Determining the cartesian geometry of the scene from the image was further hampered by the unknown nature of the lens used with the camera. Campbell (2024) attempted to characterise the geometry of the lens using grid patterns, concluding that the lens was approximately equiangualr. In the absence of any information about the lens, we must assume that it is equiangular, however it does seem that there is a small amount of angular distortion which we discovered when we attempted to fit a synthetic beam to the Argentia

images. Properly and completely characterising the camera and its lens will be essential in gaining usable results from any furture instrument.

As discussed in Section 5.3.3, the geometry of the setup also meant that the majority of the beam captured by the camera was below 10 metres. The higher parts of the beam took up only the top section of the laser beam and by only a few tens of metres the laser beam had converged on a single pixel. This impedes our ability to capture the backscattered radiance at greater altitudes and examine aerosols at these altitudes. Changing the geometry of the laser with respect to the camera can change how much of the beam we see in terms of altitude.

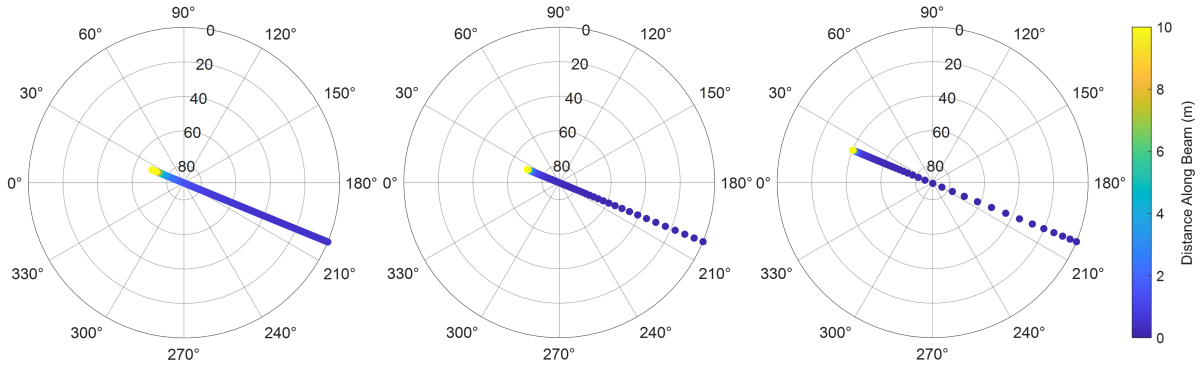


Figure 5.23: Examples of three laser beam geometries. The middle beam is tilted 20° directly towards the camera, with the laser 10 cm from the camera. The leftmost beam is tilted 20° directly towards the camera, but with the laser 50 cm from the camera. The rightmost beam is tilted 50° towards the camera with the laser 10 cm from the camera. We impose a limit on the colourbar so that everything above 50 km is coloured lightest yellow.

Figure 5.23 shows three different geometries with the amount of tilt of the laser and the distance of the laser from the camera changed. The middle modelled beam has the laser positioned 10 cm from the camera, as it was in the Argentia setup. The beam is tilted 20° directly towards the camera. When we keep the same distance between the camera and the laser but tilt the laser to 50° (rightmost in Figure 5.23), we don't see much difference in the spread of distances we can see along the beam. However, based on the June 29 beams, the red beam with the least amount of tilt saw the greatest height. When we keep the 20° tilt but move the laser 0.5 m from the camera (leftmost in Figure 5.23), there is less compression of the beam in the pixels near the top. Thus, moving the laser further from the camera may allow us to see backscatter from higher aerosols.

5.4.5 Implications for Future Instruments

The results and lessons learned through the laboratory and field experiments and subsequent analysis can inform future iterations of a low-powered laser setup for planetary aerosol investigations.

First and most importantly, we see that we are able to extract particle scattering properties such as

extinction and the scattering phase function using this setup. While similar results are easy to extract with lidar itself (E.g. Whiteway et al., 2008) as well as through imaging of the lidar beam (E.g. Moores et al., 2011), we are able to extract this information with simple low-powered lasers and an off-the-shelf camera. The aquarium results are perhaps the most dramatic, with both the extinction of the beam and the phase function at each reflection clear in the plotted radiance (Figure 5.13).

We were able to examine the impacts of particle size and wavelength on scattering properties with the aquarium setup. While models suggest that wavelength produces different scattering effects for smaller particles, we did not see this as strongly in the aquarium results. Indeed, the main differences between wavelengths observed seem to be in magnitude, and are likely a result of a combination of laser power and the responsiveness of the camera. However, further work characterising the camera and the lasers could be undertaken to fully understand this effect. We are still able to see that smaller particles will extinct the laser beam quicker, which is to be expected.

We also observed the behaviour of the camera affecting our field results. In Argentia, we saw a lot of background brightness in the green channel (Figure 5.16), which made distinguishing the beam more difficult and resulted in a lack of agreement on brighter portions of the beam with the red and blue lasers (Section 5.3.3). We look only at the channel in the image that the laser beam falls within to extract spectral radiances, but it may be worth looking at a combination of channels both for the beam and for subtracting the background.

An all-sky camera may not be the best instrument if we want to be able to view higher parts of the laser. As discussed in Section 5.4.4, the majority of the beam seen in the image is below 10 m along the beam. However, Moores et al. (2011) was able to see high portions of the beam due in part to the greater separation between the SSI and the lidar but also potentially because of the SSI's smaller field of view (13.7°).

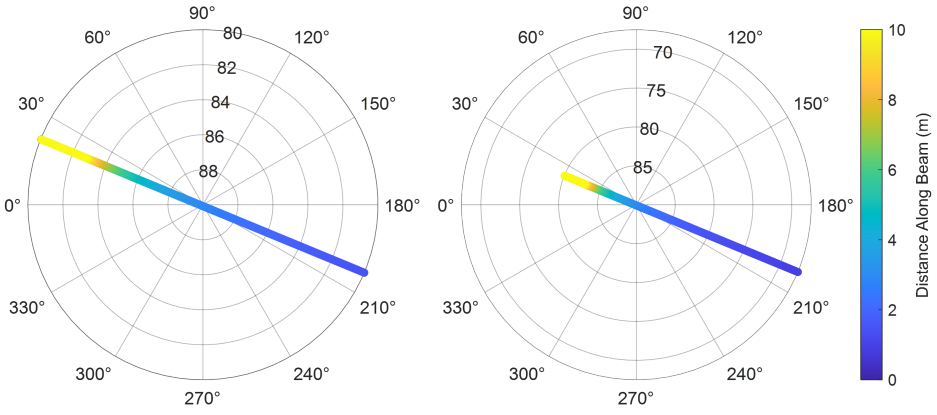


Figure 5.24: Portion of the laser beam captured by a camera with a Field of view of 45° (left) and 20° (right). The laser is tilted 10° toward the camera at a distance of 0.5 m away. The higher portions of the beam take up more of the image at smaller fields of view.

Restricting the field of view with known geometry of the laser beam may allow us to see higher parts of the laser beam. While the lower regions of the beam would be cut off in these configurations, depending on the laser spacing from the camera, areas quite close to the base of the laser beam are still captured. For instance, in the examples in Figure 5.24, the lowest seen distance in the 45° FoV is ~ 0.5 m and the lowest in the 20° FoV is a little over 1 m. If we are more interested in aerosol properties at a greater distance from the ground, this seems to be an acceptable trade.

An alternate solution may be to use two cameras, an all-sky camera to provide context and capture the entire beam and another with a more constrained FoV to capture more information in the top of the beam.

The fact that we were unable to see the laser beam even in thick fog during the daytime in Argentia (Campbell, 2024) suggests that the backscattered radiance was less than that of the background sky. We can estimate the needed laser power based on the power of the backscattered radiance by the fog at nighttime and power of the lasers. The average spectral radiances (before phase function correction) of each laser beam are 0.0034 W/m^2/Sr/nm at 638 nm, 0.0047 W/m^2/Sr/nm at 514 nm and 0.0058 W/m^2/Sr/nm at 452 nm.

We determine a sky radiance in comparable fog by taking the average radiance from a daytime image of the sky taken on July 4 at Argentia. The average sky spectral radiance in the red channel is 0.0182 W/m^2/Sr/nm, in the green is 0.0362 W/m^2/Sr/nm and in the blue is 0.0297 W/m^2/Sr/nm. The power needed to produce laser backscatter of a higher spectral radiance than the sky can be approximated as scaling linearly with the increase in spectral radiance. Thus, the red laser would need a power of ~ 29.4 mW, the green laser a power of ~ 37.9 mW and the blue laser a power of ~ 21.6 mW.

We can extend this to determine the approximate laser power we would need to see backscatter from aerosols of comparable concentration on other planetary bodies, namely Mars, Venus and Titan. For Mars, we can get an average spectral radiance overhead using a zenith image from the MSL Navcams (see Section 1.5). Averaging the spectral radiance of a ZM frame from sol 4480, an image with clouds, we get 0.0071 W/m^2/Sr/nm. The Navcams cover 600-850 nm, which overlaps the wavelength of the red laser. Thus, a 638 nm laser would need a power of ~ 11.5 mW to resolve backscatter from aerosols of a similar concentration in the daytime. This is about four times less than the power of the Phoenix lidar (Whiteway et al., 2008), which was able to resolve cloud and fog.

For Venus, Kulkarni et al. (2025) examined downward radiance profiles from Venera 13, one of the only four spacecraft to have returned data from Venus' surface. The lowest recorded wavelength at the surface is ~ 550 nm, so we can compare at the red laser wavelength of 638 nm. The downward spectral radiance recorded by Venera 13 at this wavelength is ~ 0.0308 W/m^2/Sr/nm. To overcome this brightness, the laser power would need to be ~ 49.9 mW, or about 10 mW more powerful than the Phoenix lidar.

We can also look at the values at Venus at the cloud deck at around 50-60 km where we might also deploy

an instrument on a floating spacecraft. Here at 638 nm the spectral radiance is ~ 0.4241 W/m^2/Sr/nm, which would require a much higher laser power of over 686 mW.

For Titan, Smith et al. (2016) looked at the radiance from surface images taken by Cassini-Huygens' Descent Imager/Spectrometer Radiometer. Taking an average radiance of 0.069 W/m^2/Sr and dividing by the 340 nm bandpass of the imager (660-1000 nm, Tomasko et al., 2002) gives a spectral radiance of 0.20×10^{-3} W/m^2/Sr/nm. With such a small sky radiance, we do not need a very powerful laser at all to overcome the sky brightness. Comparing with the red laser, which is the closest in wavelength, the laser power needed would be ~ 0.32 mW. These spectral radiances and the corresponding laser powers needed to overcome them are given in Table 5.6.

Table 5.6: *Background spectral radiances in the daytimes on four planetary bodies and the laser powers at a wavelength of 638 nm required to overcome them.*

Body	**Background Spectral Radiance (W/m^2/Sr/nm)**	**Laser Power (mW)**
Earth	18.2×10^{-3}	29.4
Mars	7.1×10^{-3}	11.5
Venus (Surface)	30.8×10^{-3}	49.9
Venus (Cloud Deck)	424×10^{-3}	686
Titan	0.20×10^{-3}	0.32

Chapter 6

Variability of Methane Plumes and Implications for Martian Exploration

6.1 Motivation & Author Contribution

As discussed in Section 1.6, methane measurements in the martian atmosphere, especially in-situ measurements by SAM-TLS, have revealed seasonal and diurnal cycles of background methane as well as occasional, transient methane plumes likely originating from microseepage from the martian subsurface. However, the relative scarcity of methane measurements makes characterising its behaviour difficult, especially on relatively short timescales. The appearance and subsequent rapid dispersal of methane plumes (e.g. Webster et al., 2021) make it clear that methane variability occurs on short timescales. However, the infrequent measurement cadence of SAM-TLS, as well as the time required for a single enrichment measurement, hinders our ability to understand this short-scale variability. Indeed, no methane plume has ever been observed from its initiation through its dissipation.

There is currently no flight instrument capable of acquiring the high-frequency, long-term measurements that are needed to understand the sub-diurnal behaviour of martian methane. Despite the questions and controversies surrounding martian methane, there is a desire within the community to understand methane fluctuation and variability (Banfield et al., 2025; National Academies of Sciences, Engineering, and Medicine, 2023). Understanding the short-term behaviour of methane plumes will be critical in developing the next generation of methane sampling instruments, and in planning future campaigns to better understand martian methane. To that end, this chapter aims to to understand short timescale methane variation under real-world conditions. We examine the spatial and temporal variability of point-source methane plumes on sub-hourly timescales in a martian analogue environment in the Canadian high arctic.

This chapter is based on Innanen et al. (2025b), with some alterations and additions to the text and additional figures. The paper and the section of this dissertation were written entirely by me, based on experiments that I designed and led. Data were collected by me alone in 2022, and by L. Beckering Vinckers

Stofer in 2024 based on instructions I provided. All analysis was completed by me.

6.2 Methods

6.2.1 The OA-ICOS Instrument

We used an off-the-shelf Off-Axis Integrated Cavity Optical Spectrometer (*OA-ICOS*) ultraportable instrument developed by ABB Inc. The OA-ICOS is capable of performing frequent, sub-ppbv measurements of a variety of trace gases. The measurement chamber of the instrument consists of a gas cell with highly reflective mirrors capable of producing optical path lengths of over a kilometre (Walters et al., 2024).

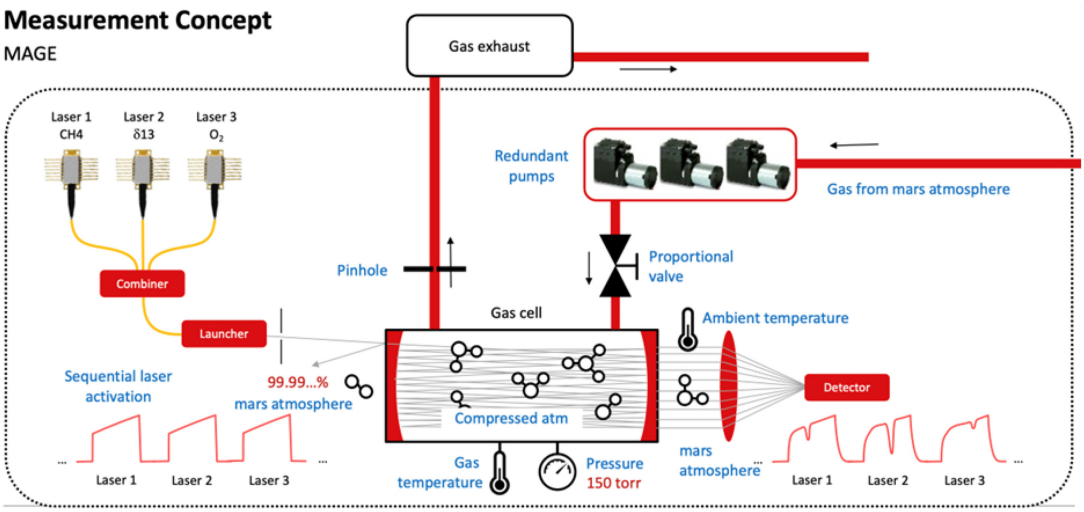


Figure 6.1: A schematic of the ABB ICOS system which is employed in the ultraportable instrument used in this study. Figure 1 in Walters et al. (2024).

The ultraportable was enclosed within a small Pelican case of 30 x 14 x 28 cm weighing about 5 kg in total (Figure 6.2). It is capable of sampling at frequencies from 20 to 0.01 Hz. This setup enables near-continuous sampling of methane and the detection of variability on small time scales. The ultraportable includes an air inlet which continuously draws surrounding air into the analysis chamber by means of a Parker Hannifin miniature diaphragm pump.



Figure 6.2: The ultraportable OA-ICOS instrument used in this study. The left photo shows the interior of the instrument with the analysis chamber at the very front. The right photo shows the ultraportable in use at Wolf Spring (Section 6.2.2).

6.2.2 Study Location

We considered two methane point sources from hypersaline cold springs on Umingmat Nunaat (Axel Heiberg Island), located at approximately 80° N in the Canadian arctic. While the air temperatures on Umingmat Nunaat can fluctuate a great deal over the course of a year, the temperatures of these springs remain fairly constant, with temperatures fluctuating less than 0.5°C (Pollard et al., 1999).

The Gypsum Hill Springs (79°24'30"N, 90°43'05"W) are located alongside the Expedition River. There are approximately forty springs along an area 300 m in length by 30 m wide at the base of the southeast slope of Gypsum Hill. They have a typical temperature of 3.9°C, a salinity between 8 and 9% and a pH of 6.9-7.4 (Pollard et al., 1999). We specifically examined a single spring, shown in Figure 6.3. This spring flowed into another downslope, which may have also had similar methane activity.

Wolf Spring (79°04'38"N, 90°12'45'W), sometimes referred to as Lost Hammer Spring, is located inside a cone-shaped structure around 2.5 m tall and 3 m in diameter (Battler et al., 2013). It has a mean temperature between -5.9 and -4.7°C, a salinity of 22-26% and a pH of 5.96-7.38 (Lay et al., 2012).

These springs have been proposed as an analogue for the creation of geologically young martian fluvial features (Andersen et al., 2002). It has been suggested that features such as those described in Malin and Edgett (2000) could have been formed by subsurface brines (Hoffman, 2000), similar to those seen in the springs which flow through the arctic permafrost (Andersen et al., 2002). Additionally, these springs act as a source of methane, which could provide an explanation for martian methane plumes (Niederberger et al.,

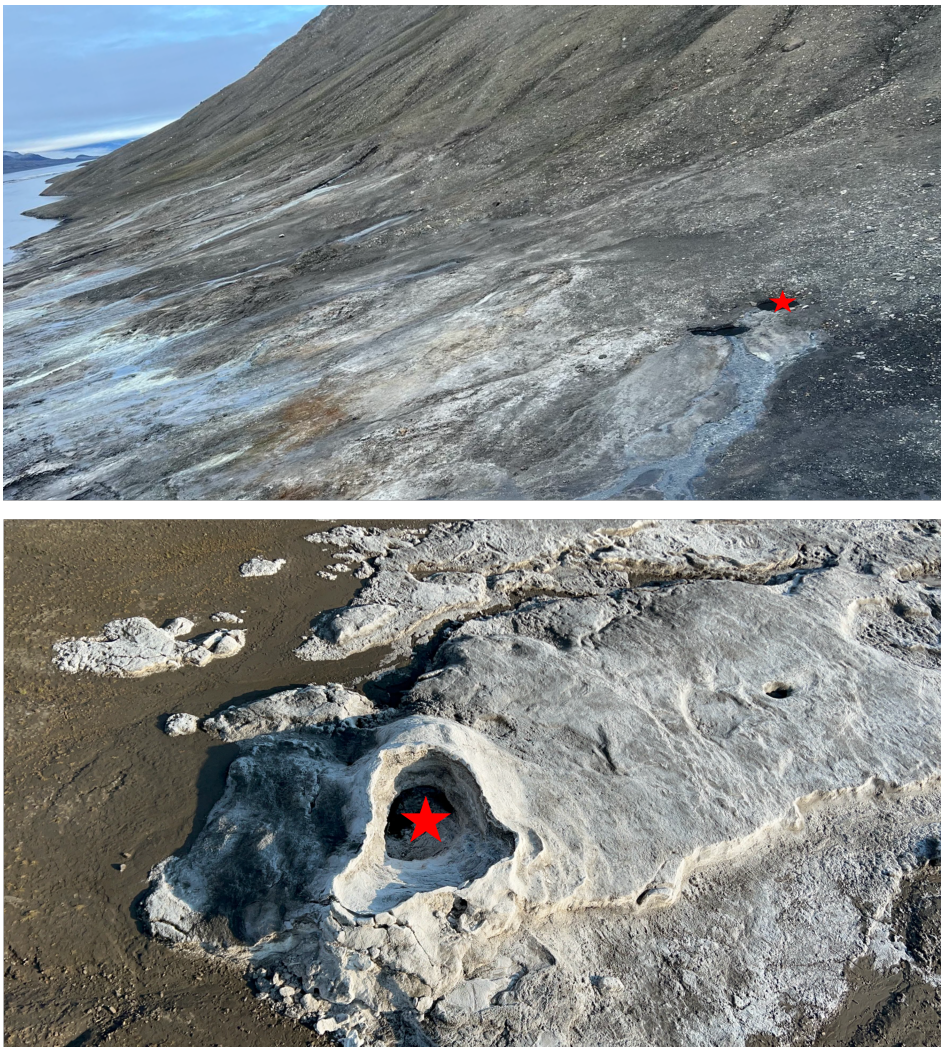


Figure 6.3: The Gypsum Hill Spring (top) and Wolf Spring (bottom) locations seen from above . The specific sites of the springs used in this study are indicated by a red star. Wolf Spring consists of a single high-intensity source whereas Gypsum Hill contained a large number of proximate low-intensity sources. We used the upper Gypsum Hill Spring shown as our point source, however the lower spring a metre or so away was also acting as a methane source.

2010). The continuous release of methane from the springs provided an opportunity to study variations in methane concentration over small time scales.

While the atmospheric dynamics around the springs will differ from the methane sources we observe on Mars (further discussed in Section 6.4.4), we assume that methane will be well mixed in the atmosphere near to the surface on both Earth and Mars. To ensure that our assumption of a well mixed atmosphere on both Earth and Mars is accurate, we can calculate the Knudsen number for both near-surface atmospheres, given by $Kn = \frac{\lambda}{L}$, where λ is the mean free path and L is the characteristic scale length (here on order 10s of metres). The mean free path is given by:

$$\lambda = \frac{k_B T}{\sqrt{2}\pi d^2 p} \tag{6.1}$$

where k_B is the Boltzmann constant, T is the temperature, d is the diameter of a methane molecule and p is the atmospheric pressure. The quantities of temperature and pressure used for Earth and Mars and the corresponding mean free paths are given in Table 6.1. For Mars we use the average near-surface temperature and pressure, while on Earth we use average surface pressure and the average temperature experienced during the 2022 study period.

Table 6.1: *The mean free paths of near-surface methane on Earth and Mars.*

	Temperature (K)	**Pressure (Pa)**	**Mean Free Path (m)**
Earth	280	101325	5.4×10^{-8}
Mars	210	610	6.7×10^{-6}

The corresponding Knudsen numbers for Earth and Mars are therefore on the order of 10^{-7} and 10^{-9} respectively. This places both in the continuum regime ($Kn < 0.1$) (Katz, 2010), which supports our assumption of a well-mixed near-surface atmosphere.

6.2.3 Sampling Procedure

In the 2022 season, we examined three study locations: Gypsum Hill and Wolf Springs and the McGill Arctic Research Station (*MARS*). Each measurement run followed the same procedure. The instrument was placed at the sampling position with the inlet perpendicular to the wind direction. It was then powered on and remained in that position for the duration of the run. The total run time was around 12 minutes, which resulted in a 9-10 minute sampling duration following a 120 second boot-up sequence. Following a run, the instrument was powered off and moved to the next position. In the absence of any dedicated meteorological equipment, the wind direction was estimated based on my observations, which were repeated throughout the course of the experiment to ensure the wind direction had not noticeably changed.

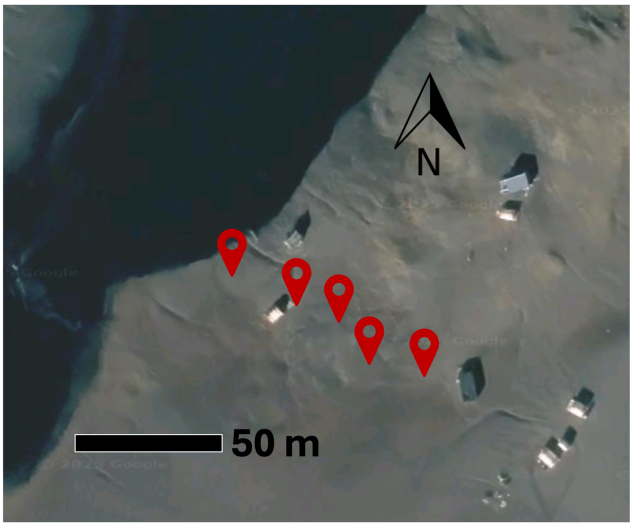


Figure 6.4: Approximate location of background methane measurements taken at MARS (79° 26' N, 90° 46' W) on July 13, 2022.

The MARS measurements were intended to determine the background methane concentration on the island at the time of year of our study. We conducted five measurements downhill towards Colour Lake

covering a total distance of 77.6 m and spaced between 15 and 25 metres apart. As there are no known springs at this location, we were able to average these measurements to derive a representative background methane concentration, as well as the variability we can expect in the background methane.

At both methane sources, we performed wind-direction transects across the springs. At Wolf Spring, this work consisted of three runs — one 12 m upwind of the cone, one 13 m downwind, and one next to the spring within the gypsum cone. At Gypsum Hill Springs, we used a single spring, seen in Figure 6.3 and located at (79° 24.25' N, 90° 44.00' W), as our reference point. The wind direction transect consisted of a measurement run just above the spring, and two runs each upwind and downwind at distances of 5 and 10 metres. We also performed an additional transect unaligned with the wind direction from the spring down towards the Expedition River in five steps of 5 m each. While moving perpendicular to the wind direction was not possible due to topographic constraints, we moved in a generally diagonal line down towards the river from the spring on the downwind side of the spring.

In 2024, a different field team returned to Wolf Spring to complete another sampling campaign designed by me (Figure 6.5). This aimed to sample the methane signal from Wolf Spring in a two-dimensional grid around the spring in order to gain a clearer understanding of the two-dimensional dispersal of methane. The sampling procedure was the same as in 2022, with each run acquiring 9–10 minutes of methane signal at each location. A total of 16 runs were completed by a Master's student in and around the spring. Additionally, these measurements were paired with meteorological data acquired by a Kestrel 5500 Weather Meter. This allowed precise wind directions to accompany each measurement run.

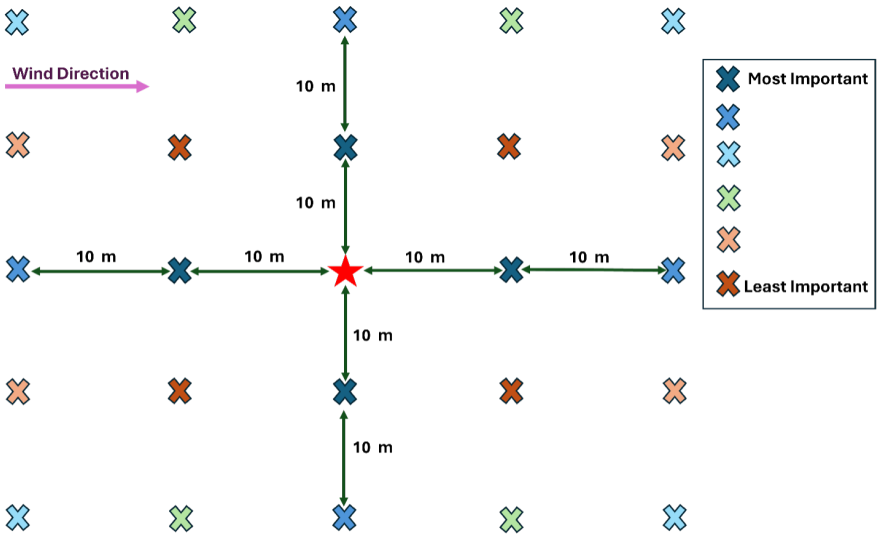


Figure 6.5: Sampling plan for the 2024 Wolf Spring campaign. The Wolf Spring methane source is indicated by a red star in the centre, with sampling locations in a grid around the source and wind direction indicated. While the plan included a total of 25 sampling locations, only 16 were sampled in 2024 due to timing constraints. The relative priorities of the sampling locations are given by the colour-coded legend.

6.3 Results

6.3.1 Background Methane Measurements

While the background measurements were taken over 77.6 m downslope, we did not observe any systematic changes with either elevation or proximity to the lake (Figure 6.6). Thus, we can simply average these measurements to understand the background concentration of and variation in methane. These five measurements have an average concentration of 1.958 ppmv with the methane signal varying on average 0.5% from the mean over the course of the measurements. For the 2022 season, we use this value as representative of methane behaviour at locations which are not influenced by spring activity.

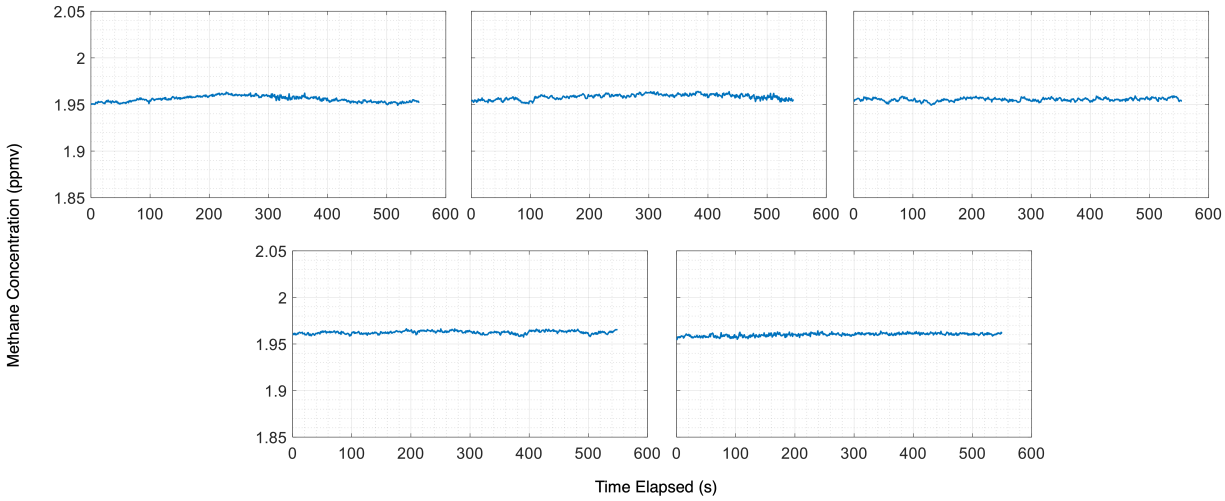


Figure 6.6: Measured methane concentrations taken at five locations at MARS as described in Section 6.2.3 with the upper left plot furthest from the lake and the lower right closest. We observe very low variability and overall concentrations around 1.958 ppmv.

6.3.2 Gypsum Hill Springs

We performed measurements described in Section 6.2.3 at Gypsum Hill on July 17, 2022. The wind was moving approximately parallel to the Expedition River and opposite to the direction of the water's flow. As described in Section 6.2.3, we performed two transects at Gypsum Hill Springs over the course of around 2.5 hours.

The first set of measurements was the wind direction transect. A summary of the measurements is given in Table 6.2. The methane concentration over the course of each run alongside their time averages are given in Figure 6.7. Time averages are calculated for a window size of about one minute.

Table 6.2: *Summary of measurements taken at Gypsum Hill traveling along the wind direction.*

Measurement ID	**Distance from source* (m)**	**Time of measurement (CDT)**	**Duration of measurement (s)**	**Average CH_4 (ppmv)**	**Standard Deviation**	**Range as a percent of mean value**
GH-WD-01	-10	13:15	549	1.998	0.0238	5.6%
GH-WD-02	-5	13:01	551	1.987	0.0181	6.3%
GH-WD-03	0	12:47	549	1.993	0.0182	6.3%
GH-WD-04	5	13:30	550	1.976	0.0057	1.8%
GH-WD-05	10	13:44	556	1.968	0.0036	1.4%

**positive values indicate distance upwind, while negative indicate distance downwind*

Our first measurement (GH-WD-03) was taken above the spring (Figure 6.7) with the inlet pointed towards the river and approximately 0.5 metres from the edge of the pool. We maintained this inlet orientation for each subsequent run. For this run, the time average is relatively flat, but we can see repeated spikes in the concentration above the mean.

We moved five metres downwind (GH-WD-04) in as straight a line as the terrain allowed. As in the previous case, we see a relatively flat time average with spikes in concentration above the mean, though the frequency of these spikes seems decreased compared to GH-WD-03 (Figure 6.7). We also see a decrease in average methane concentration at this location (Table 6.2).

A further five metres downwind (GH-WD-05), we do not see the relatively flat time average as in the previous two cases. Instead, the average concentration appears to increase gradually over the course of the run (Figure 6.7). It is difficult to say what may be the cause of this increase. It could be that the wind became stronger, carrying more methane further, though this would also dilute that methane, or that a parcel of air arrived containing methane from another location. There was no noticeable change in wind recorded during the course of the run, but in the absence of meteorological data, it is difficult identify a cause with certainty. This increase in concentration also results in the average concentration being higher than both GH-WD-03 and -04, as seen in Table 6.2, though the variation in concentration decreases.

We next moved five metres upwind of the spring (GH-WD-02), again attempting to continue in a straight line. As well as being upwind from the spring, this location was on a slight uphill from the spring with an elevation change of less than five metres. The mean methane concentration is much closer to, though still higher than, the background methane concentration. The variation in methane is also much smaller, though still higher than that of the background. While it is unlikely that the measurement at this location is being influenced much by the spring we selected, the Gypsum Hill area has approximately 40 springs, so it is likely that we are seeing the effects of these other springs throughout the course of these measurements.

The final measurement of this set was taken ten metres upwind of the spring (GH-WD-01). For approximately the first 320 s of the run, we see the same behaviour as in GH-WD-02, with very little variation in

the methane signal and mean concentration around that of the background. After this time, the average methane signal increases and then begins to decrease again near the end of the run. The variation in the signal, however, remains fairly constant. As in GH-WD-05, this could be the case of an air parcel moving past the inlet bringing methane from elsewhere. To estimate a representative mean concentration, we removed this section of the run and used only the first 320 seconds.

The second set of measurements that were acquired at this location were taken from the spring in the direction of the river. The path these measurements took traveled past the lower spring, which can be seen in Figure 6.8 below our study spring. All measurements were taken on the leeward side of the springs and their outflow channels. The measurements are summarised in table 6.3.

Table 6.3: *Summary of measurements taken at Gypsum Hill traveling from the spring towards the Expedition River.*

Measurement ID	**Distance from source (m)**	**Time of measurement (CDT)**	**Duration of measurement (s)**	**Average CH_4 (ppmv)**	**Standard Deviation**	**Range as a percent of mean value**
GH-UA-01	5	13:58	549	2.103	0.061	16.2%
GH-UA-02	10	14:11	559	2.025	0.022	6.2%
GH-UA-03	15	14:25	549	1.999	0.019	5.7%
GH-UA-04	20	14:40	549	1.997	0.008	2.4%
GH-UA-05	25	14:53	570	2.002	0.009	2.9%

In the first measurement (GH-UA-01), taken five metres away from the spring and towards the river, we see that the average methane concentrations are higher than those taken at the spring itself (GH-WD-03), as is the percent variation in methane. This is likely due to the fact that GH-UA-01 is downwind of not only the study spring but also the lower spring, as can be seen in the top panel of Figure 6.8, whereas GH-WD-03 was not (middle panel of Figure6.7).

For the following measurements, we see that the amount of methane stays around 2 ppmv, and the percent variation does not drop below 2%. In GH-UA-02 and -03, we are still seeing variability from the mean that is consistent with what we saw directly downwind of the spring. Additionally, GH-UA-03 sees a local increase in methane concentration between about 250 and 400 seconds which resembles the one we saw in GH-WD-01. These measurements were taken as we passed the lower spring.

In GH-UA-04 and -05, the amount of variation was closer to that we saw upwind of the spring, as were the methane concentrations, though they were still higher than those we observed for the background.

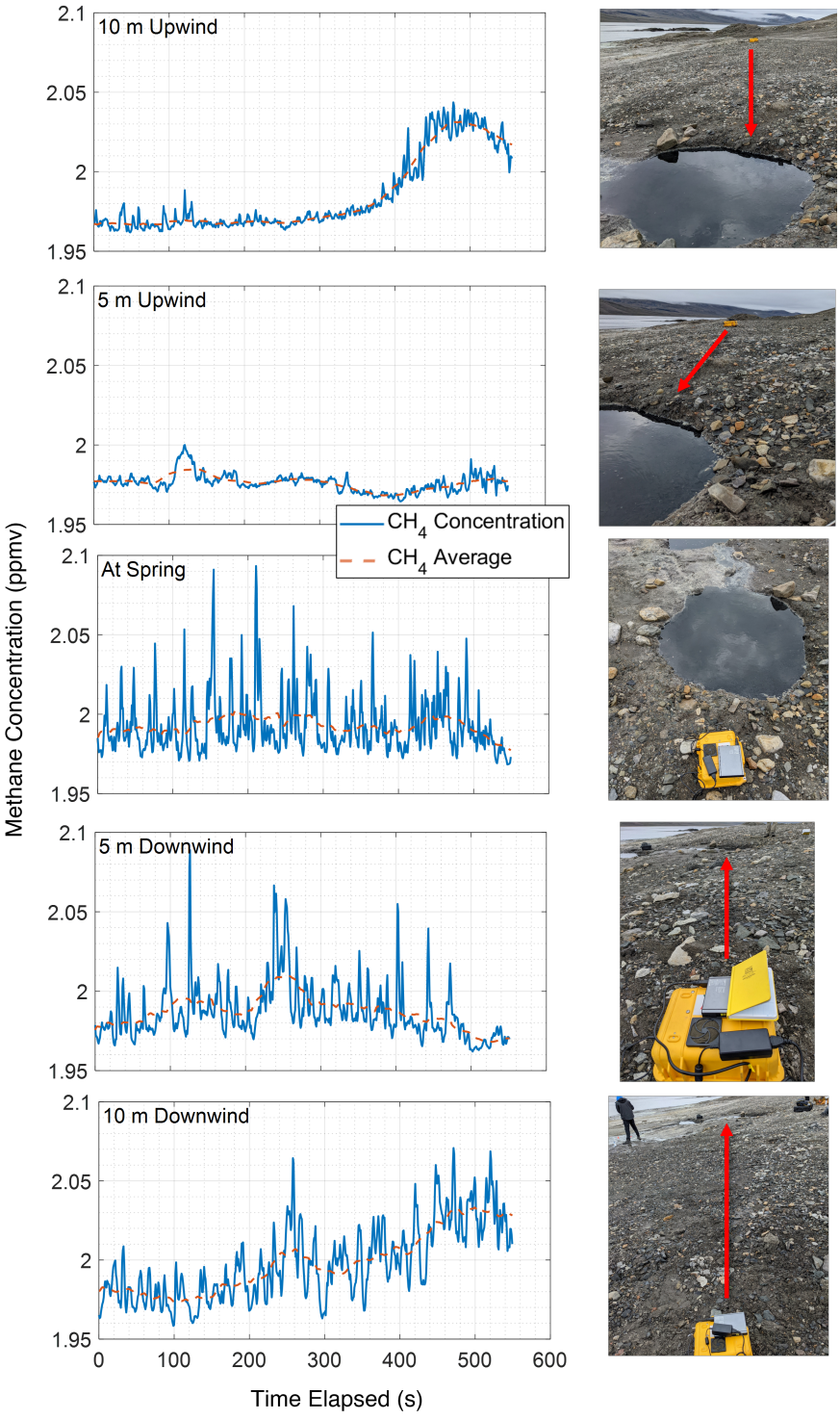


Figure 6.7: Measured methane concentrations at Gypsum Hill Spring taken at distances of 5 and 10 metres upwind and downwind and at the spring itself. The methane measurements are given by the solid blue lines and a time average is given by the orange dashed lines. Plots are shown alongside photos showing the placements of the instrument for their corresponding measurement runs. Red arrows on photos indicate the direction from the ICOS to the spring. Downwind plots show considerably more high-frequency variation as compared to upwind plots.

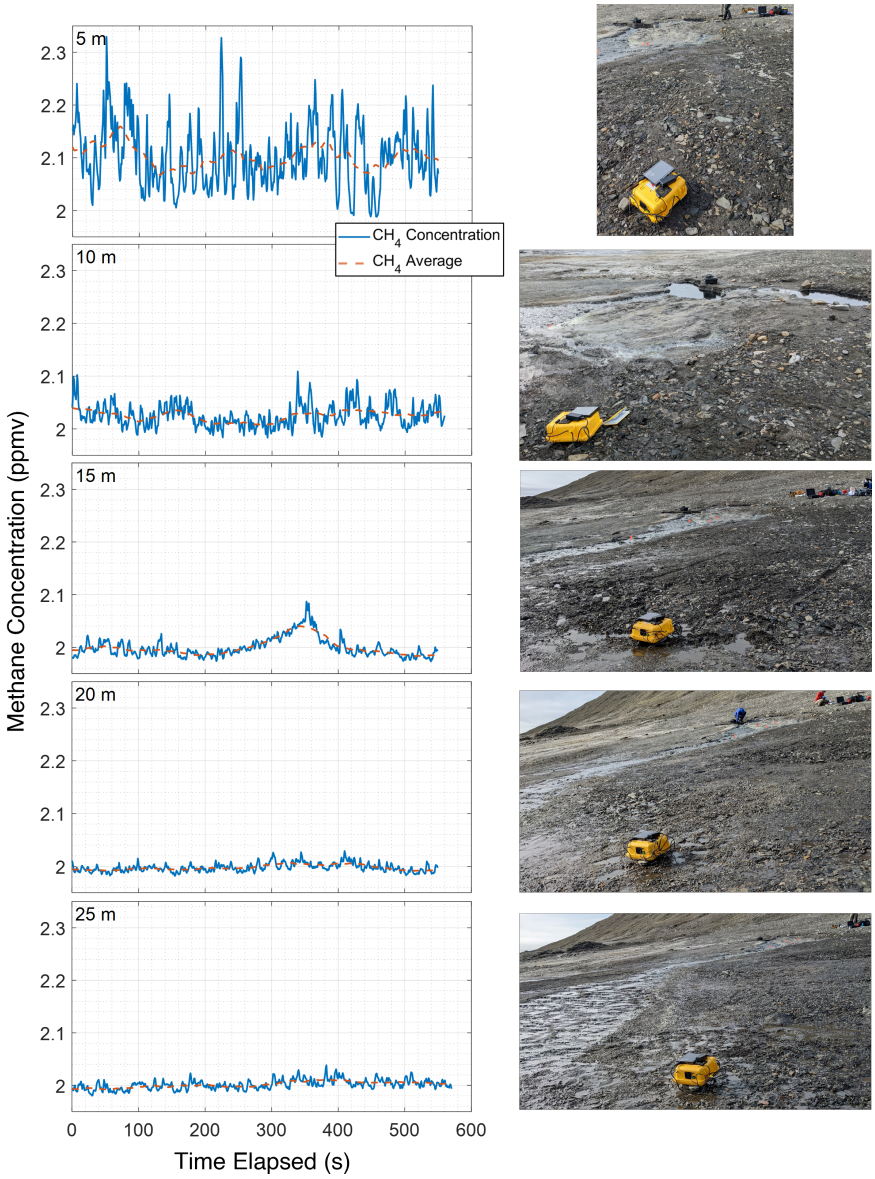


Figure 6.8: Measured methane concentrations at Gypsum Hill moving downstream towards the Expedition River. The methane measurements are given by the solid blue lines and a time average is given by the orange dashed lines. Plots are shown alongside photos showing the placements of the instrument for their corresponding measurement runs. Even travelling in an unaligned direction to the wind, the variability of the methane signal lessened as the measurement site receded from the spring.

6.3.3 Wolf Spring

6.3.3.1 2022 Measurements

The Wolf Spring measurements were taken on July 14, 2022. The wind was travelling from the southeast. The three measurements (described in Section 6.2.3) were taken over the course of around 1.5 hours. A summary of the measurements is given in Table 6.4, and methane concentration time series are given in Figure 6.9.

Table 6.4: *Summary of measurements taken at Wolf Spring in 2022.*

Measurement ID	**Distance from source* (m)**	**Time of measurement (CDT)**	**Duration of measurement (s)**	**Average CH_4 (ppmv)**	**Standard Deviation**	**Range as a percent of mean value**
WS-22-01	-13	12:59	559	2.019	0.044	9.3%
WS-22-02	0	13:58	627	12.065	3.80	255%
WS-22-03	12	14:27	559	1.944	9.57 x $10^{-}4$	0.3%

**positive values indicate distance upwind, while negative indicate distance downwind*

The first measurement we performed, WS-22-03, was downwind of the source, about 13 m away from the base of the cone structure. As at the Gypsum Hill site, we see an average concentration above background levels and higher fluctuations in the methane concentration at Wolf Spring. The time average also fluctuates more at this site than at the Gypsum Hill site.

The next measurement, WS-22-02, was taken within the cone structure, next to the spring. We see a very high average concentration of 12.065 ppmv and spikes in methane over 35 ppmv. The minimum methane concentration observed within the cone at Wolf Spring is 5.65 ppmv, much higher than the background methane concentration of around 1.95 ppmv. While the springs at the Gypsum Hill site were level with the terrain, at the Wolf site the spring is sheltered within the cone structure. This suggests that the methane is able to build up within the cone without being immediately mixed into the atmosphere at large, which could be why we record these much higher methane concentrations.

The final measurement taken at the Wolf site, WS-22-01, was taken upwind of the spring, about 12 metres from the base of the cone. Here we see a much lower methane concentration of 1.944 ppmv, close to that of the background, and very little fluctuation in that concentration. Unlike at Gypsum Hill, Wolf Spring is the only spring in the area, providing a cleaner signal uncontaminated by any other nearby point sources of methane.

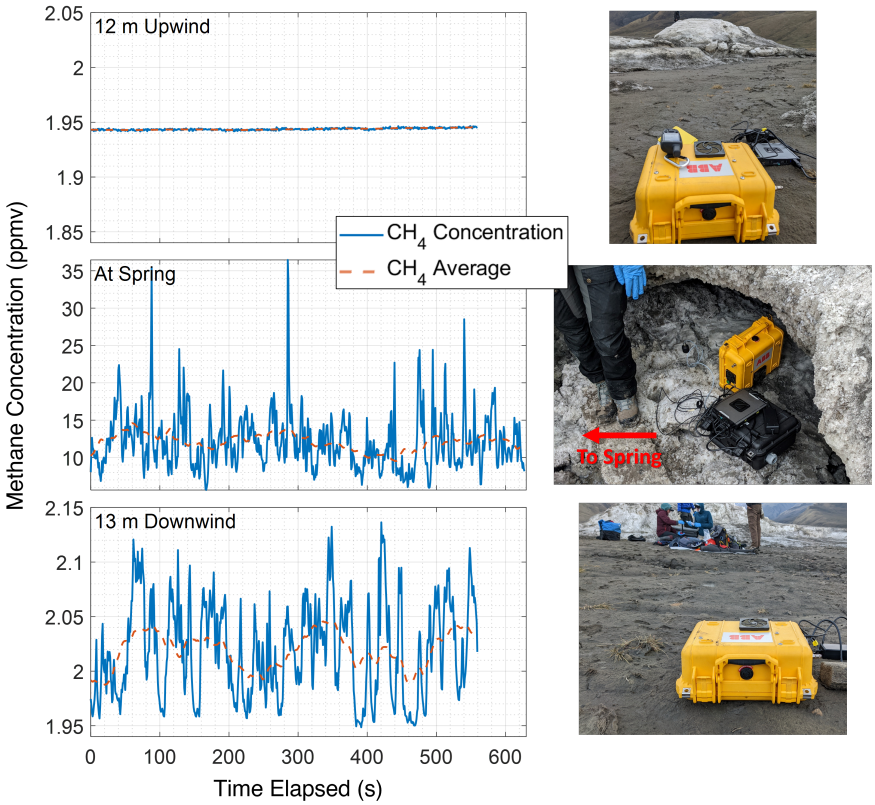


Figure 6.9: Measured methane concentrations at Wolf Spring taken at upwind and downwind and at the spring itself. The methane measurements are given by the solid blue lines and a time average is given by the orange dashed lines. Note that while the scale of y-axes of the upwind and downwind plots are the same, they are centred at different points, and that the scale of the y-axis of the plot taken at the spring is much larger. Plots are shown alongside photos showing the placements of the instrument for their corresponding measurement runs. As at Gypsum Hill, there is greater variation in the methane concentration within the spring and downwind from the spring as compared to measurements made upwind of the spring.

6.3.3.2 2024 Measurements

Unlike in 2022, in 2024 we sought to better understand the dispersal of methane in two dimensions by making measurements across a full grid rather than two transects. As such, in July 2024, an additional set of measurements were acquired at Wolf Spring using the same ultraportable instrument. Additionally, the measurements were acquired alongside meteorological measurements from a Kestrel 5500 Weather Meter. A total of 15 measurements were acquired in and around Wolf Spring, as shown in Figure 6.10. The data are summarised in Table 6.5 below. Concentration time series for each measurement are given in Appendix C.

Sometime between 2022 and 2024, the behaviour of the instrument changed for unclear reasons. The ultraportable arrived from the factory in 2022 where it was calibrated. However, in the intervening years several changes to the instrument took place including general wear and tear and replacement of some components of the instrument. As a result, we have observed drift over time in the methane concentration

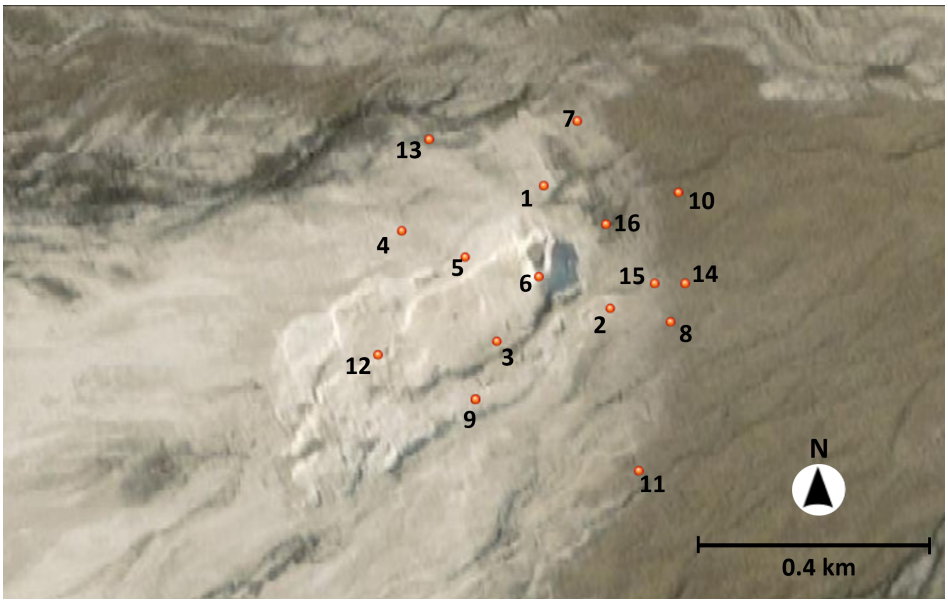


Figure 6.10: Position of each measurement taken in 2024 at Wolf Spring plotted in ArcGIS. Locations are marked with the final digits of the measurement ID. WS-24-06 was acquired inside the gypsum cone beside the spring.

reported by the instrument to higher values. Despite this, the relative instrument results over short timescales remain robust, and we can still examine the relative behaviour between locations sampled at Wolf Spring.

As in 2022, at the different locations, we see changes in both average concentration values and the variation of the methane signal (Table 6.5).

Table 6.5: *Summary of measurements taken at Wolf Spring in 2024.*

Measurement ID	**Time of measurement (CDT)**	**Duration of measurement (s)**	**Distance from source (m)**	**Angle to wind direction (°)**	**Average CH_4 (ppmv)**	**Standard Deviaiton**	**Range as a percent of mean value**
WS-24-01	11:02	764.40	15.4	52.75	2.250	0.005	1.10%
WS-24-02	11:24	640.92	13.5	15.44	2.296	0.089	27.41%
WS-24-03	11:03	700.04	13.3	148.17	2.286	0.015	3.73%
WS-24-04	12:03	664.62	24.8	173.95	2.257	0.003	0.85%
WS-24-05	12:21	690.91	13.3	178.41	2.251	0.005	1.53%
WS-24-06	12:37	694.49	0	0	17.677	6.935	343.18%
WS-24-07	12:56	694.50	28	17.42	2.256	0.005	1.54%
WS-24-08	13:15	714.49	23.8	7.90	2.262	0.008	4.89%
WS-24-09	13:33	679.98	23.7	156.90	2.254	0.005	1.31%
WS-24-10	14:22	650.00	28.1	40.29	2.262	0.035	11.92%
WS-24-11	14:37	649.16	37.8	40.35	2.260	0.005	1.37%
WS-24-12	14:53	435.82	30.6	169.28	2.251	0.003	0.56%
WS-24-13	15:13	659.19	30.1	178.54	2.251	0.004	1.15%
WS-24-14	15:40	664.57	25.1	5.13	2.279	0.041	10.05%
WS-24-15	16:06	669.97	19.9	15.52	2.376	0.094	17.79%
WS-24-16	16:22	615.52	14.3	7.19	2.272	0.050	12.98%

6.4 Discussion

6.4.1 Relative Frequency of Methane Spikes

As discussed in Section 6.3, we see spikes of varying magnitudes in methane concentration over the course of the measurement runs. We examined the power spectral density (PSD) for each signal and saw that the signals resembled pink noise (Figure 6.11). Pink noise or 1/f noise is observed in both natural and anthropogenic systems and represents many random processes in these systems (Keshner, 1982).

We can also use the PSD to infer the relative frequencies of spikes of various sizes. We fit a curve of the form $P = \frac{a}{(f-k)^b} + h$ to the Wolf Spring PSD to estimate how frequently we may expect to see methane spikes of differing sizes. We saw that instead of true pink noise, the best fit to our data was of the form $1/f^2$, known as 'Brownian noise' and characteristic of diffusive processes (Uhlenbeck and Ornstein, 1930; Grunwald and Steel, 1994). By capturing the methane spikes through high temporal resolution measurements, we are able to predict how likely we are to see spikes of different magnitudes, which on Mars could help in determining a sampling plan based on when it is likely to see methane spikes of certain magnitudes.

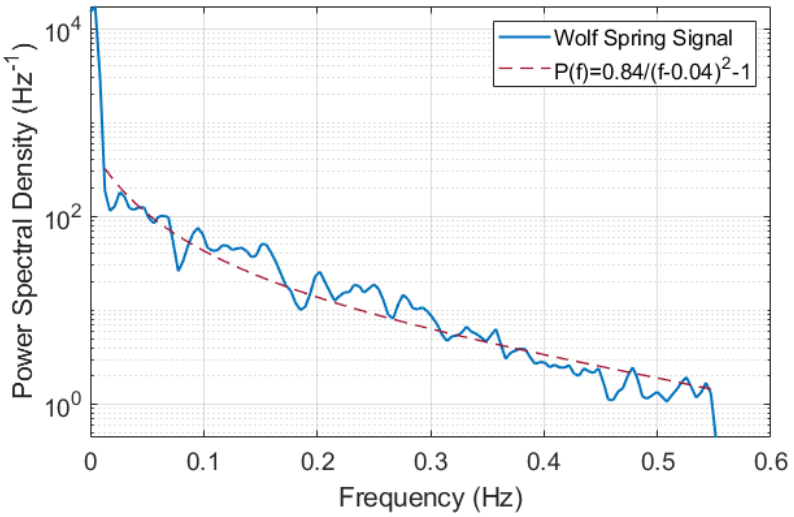


Figure 6.11: Power spectral density estimate for WS-22-02 (blue solid line). The red dashed line is fit to the PSD curve for Wolf Spring, excluding the low frequency peak. The fit dashed curve has an R^2 value of 0.95.

Based on the Brownian noise fit to the power spectral density curve, we would expect that the size of events increases as the inverse square of their frequency (or as the square of the average time between events). To give an example, SAM-TLS (Webster et al., 2015) observed plumes of approximately 5 ppbv on sols 306 and 466 at Gale crater, 160 sols apart. If this spacing is representative of the actual frequency of such events, then, using our analysis, we would predict that 1 ppbv plumes occurred at least every 70 sols, 0.1 ppbv

plumes at least every 22 sols and so forth.

6.4.2 Variation in Methane Signal with Respect to Source

Terrestrial efforts to model plume dispersion date back to the early 20th Century, with the simplest of these solutions being the "Gaussian Plume Solution". The Gaussian solution considers a plume emitted from a point source in a uni-directional wind, and is widely used to date in studying industrial and other human-made emissions as well as emissions from natural systems such as volcanoes (Stockie, 2011). We take a much similar approach to describing the methane plume, only considering the dispersion fo the plume in two dimensions and envisioning it as approximately parallel to the ground.

We can take distance from the source divided by the cosine of the angle to the wind direction (Figure 6.12) in order to show these changes with changing distance from the methane plume (Figure 6.13). We select this formalism because we expect that, as methane is dispersed from the source, it will be advected along the wind direction while diffusing perpendicular to the wind direction, travelling in an expanding fan. As such, the concentration should decrease both with distance from the source and with angle from the wind direction. For this reason, we also exclude any measurement points with wind angles greater than 90°, as we would not expect these points to 'see' any methane from the source. This approach combines our knowledge gained from the two transects at Gypsum Hill in 2022 into a single variable related to the dispersion of the plume.

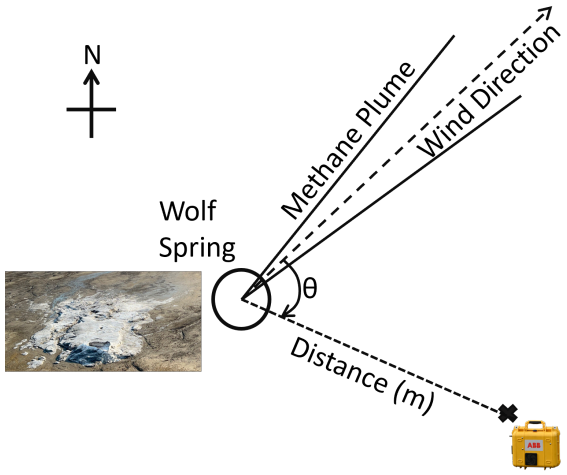


Figure 6.12: Methane plume produced from Wolf Spring diffusing in the wind direction. Measurement locations (indicated by the x) were taken a given distance away from the spring and at a given wind angle (θ) to the wind direction.

Both the average concentration of methane and the variation in methane, here represented as the standard deviation within the data, decrease as we move away from both the methane source and the plume. This

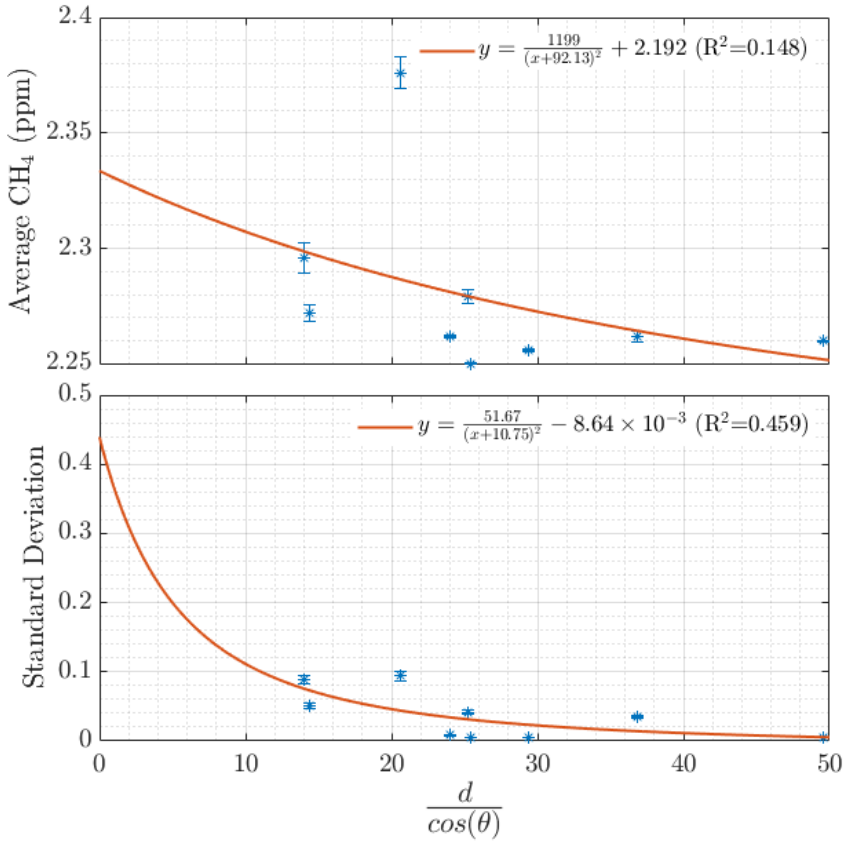


Figure 6.13: Average methane and standard deviation in measurements varying with increasing distance (d) divided by the cosine of the wind angle from the source as defined in Figure 7. Fit curves are given by $y = \frac{1199}{(x+92.13)^2} + 2.192$ (R^2=0.148) for the average value and $y = \frac{51.67}{(x+10.75)^2} - 8.64 \times 10^{-3}$ (R^2=0.459) for the standard deviation.

decrease in methane concentration with increasing distance from the source is similar to what we saw in the 2022 data. We were able to model these data (shown in Figure 6.13), which suggest either mean or standard deviation may be used in localising a methane source.

The quality of the fits is relatively poor with R^2 values of 0.148 and 0.459, respectively. This likely arises from the changing environmental conditions over the time required to acquire the measurements in the 2024 season since each point was acquired separately over the course of over five hours. However, despite these difficulties, we can see that the R^2 value is higher for the standard deviation, which suggests that methane variability is a more reliable indicator of proximity to the methane plume. This observation could be helpful to future landed operations on Mars.

6.4.3 Implications for Future Martian Missions

We can apply our findings from these analogue locations to the search for methane plumes on Mars in future missions. Based on our observations at the study sites, it is clear that high frequency methane measurements are important in characterising methane plumes. The addition of wind direction data also proved important in methane localisation. Thus, future attempts to characterise martian methane should be capable of sampling at high frequencies and would work best in concert with other meteorological measurements.

When detecting methane, amounts at or near the background methane concentration can be assumed to be upwind of or not sufficiently close to a methane source. At concentrations above the background, it will be difficult to localise the source with a single detection. Thus, at least two spatially separated detections would be needed to determine the direction of a methane source. To get a sense of how near to a source we would need to be to detect it, we can use the relation given by Figure 6.13. If we assume an instrument able to detect variability of 0.5% and that we are measuring in the exact downwind direction, we would expect to be able to observe variation in the methane signal as far as 50 m distant from the source.

Orbital missions will likely be unable to fully characterise small plumes, which we would expect would make up the majority of the methane plumes we would see. In the arctic, we observed changes in the methane concentration on minute timescales, such as in GH-WD-01, as well as the second-scale variations in the signal. An orbiter would likely not be able to capture these very small time-scale variations; however it could capture a plume of sufficient strength dissipating from a point source at a single moment in time, or even the break-up of this plume into smaller air parcels. While instruments such as ACS (Korablev et al., 2017) and NOMAD (Vandaele et al., 2018) are capable of detecting very small concentrations of methane, an orbiter's large footprint, rapid translation across the planet and relatively long revisit period to a single location would make it ill-suited to observing rapid variability in a methane signal.

For surface or near-surface missions, a stationary lander would be able to capture high-frequency methane measurements and could combine these with wind direction measurements and back-trajectory modelling to constrain the possible origin locations of the methane source (e.g. Luo et al., 2021). However, an inability to move would hamper localisation of the source itself, and any detections it might make would rely on the presence of a sufficiently detectable methane source nearby. A network of several stationary landers could provide better localisation for methane sources.

A rover, on the other hand, would have a much greater ability to localise a methane source. For this situation, the variability is of great importance, and the rover would need the ability to capture high frequency measurements, as well as wind direction data. While this work only considered the two-dimensional movement of methane along the ground, we expect methane to diffuse from the point source in three dimensions. Thus,

a helicopter could act much in the same way as a rover, but with the added dimension of height to assist in localising a methane source, similarly to how drones have been used to localise methane sources in earth-based applications (e.g. Soskind et al., 2023).

6.4.4 Limitations of the Experiment

There were a number of challenges and limitations associated with this experiment. Our lack of meteorological data in 2022, especially wind speed and direction, meant that, while we attempted to perform a transect along the path of the wind direction, we could only deduce the wind direction by inspection. We were also not able to see if other variations in temperature, pressure, or humidity could have correlated with methane behaviour.

We were also limited in the field by power and timing constraints. We were only able to visit each site once within the 2022 field season, and the greater distance from MARS at Wolf Spring meant that we had a limited amount of time on-site. Additionally, the batteries used were only able to power the instrument for a few hours on a single charge. This limitation meant we had to trade the length of the measurement runs with the number of total measurements we wanted to take, resulting in measurements of between nine and ten minutes. It also meant we were not able to build up diurnal data or to see longer-term variations at a single site. Additionally, the length of time over which the measurements were acquired likely meant that environmental or spring conditions were changing over the course of the total study period. This is especially pertinent in 2024, when the measurements were acquired over more than five hours.

A limitation of the instrument is that it is a point detector. Consequently, we are only able to observe methane behaviour at the instrument and we could not see methane behaviour occurring away from the instrument. For instance, while we are able to see increases in methane concentration which could indicate methane travelling in from another source, we are unable to retrieve any spatial information about this methane to confirm that interference.

Another limitation is that our study sites are analogues for martian conditions. We observed the behaviour of methane in Earth's atmosphere, which has different dynamics. While near-surface methane will be well mixed in both atmospheres, as discussed in Section 6.2.2, the martian atmosphere is much thinner, colder and drier than that of Earth. Additionally, the overall amount of methane in Earth's atmosphere is much higher than on Mars. Though we did not examine the role of topography in our study, it likely impacted methane diffusion.

The methane sources that we studied in the arctic may also not accurately reflect the methane sources on Mars. While the methane produced by the springs is likely biological in origin (Niederberger et al., 2010), the

source of martian methane remains uncertain. If the martian methane's source is different, then the patterns we observed in methane production and emission at the springs may not transfer over to the martian source. However, since we are more interested in the behaviour once the methane has been released, the mechanism of release may not be relevant to localising the source. Finally, the cold springs were a continuous source of methane throughout our study, whereas local plume sources on Mars may only emit methane occasionally.

Chapter 7

Conclusions

7.1 Summary of the Dissertation

This dissertation characterises and explores variability in different aspects of the martian atmosphere with the goal of better understanding these aspects. It begins with an existing water-ice clouds dataset taken from the surface of Mars in Gale Crater by the Mars Science Laboratory and looked at the scattering properties of these water-ice clouds, which has implications for radiative transfer and the radiation budget of the planet. We then further examine clouds properties from both the surface with MSL and orbit with the CaSSIS imager, in order to see how the scattering properties, namely the opacity, of optically thin clouds impact CaSSIS' ability to see to the surface, or to image optically thin clouds. We carry on this analysis of atmospheric aerosols' impact on orbital instruments by looking at how dust and water-ice clouds at Gale Crater impede the Mars Climate Sounder's ability to retrieve climate data at lower altitudes. As these lower altitudes may be missed by orbiters, we then evaluate the performance of a simple, low-cost instrument for the analysis of near-surface aerosols, both on Mars and potentially on other planets. Finally, we continue to motivate future measurements and instrumentation for the study of the near-surface martian atmosphere by studying how variability in methane plumes can be used to localise their source. The summaries of our findings for each of these projects are given in the following sections.

7.2 The Water-ice Cloud Phase Function at Gale Crater

We constructed single scattering phase functions using five Mars years of ACB cloud observations by MSL at Gale Crater. These observations spanned $L_s \sim 40 - 160°$ through MYs 34-38, covering morning hours between 06:00 and 09:30 and afternoon hours between 14:30 and 18:00 LTST. We were able to extract values of the single scattering phase function for scattering angles between 45° to around 160°. We assessed phase function variability and water-ice crystal habit.

We see little to no variability in the mean phase function over interannual, seasonal and diurnal timescales. The shape of the curve remains extremely consistent Mars year to Mars year, aligning with the high repeata-

bility of the ACB. When we split our observations into three seasonal bins representing the early, middle and late ACB, we see that the phase function has little seasonal dependence for each Mars year. However, we note that there is a hint of interannual variability in the early ACB ($L_s = 40 - 80°$), with the curves for MYs 37 and 38 being flatter than those of MYs 34-36. Comparing morning and afternoon observations, we see little diurnal variability in MYs 35-38, consistent with the low diurnal variability observed in the southern ACB and specifically in cloud opacity at Gale Crater (Hayes et al., 2024b). The MY 34 diurnal phase functions, however, vary at scattering angles $< 90°$, with the afternoon phase function being slightly flatter than the morning.

We use a Henyey-Greenstein approximation to comment upon the ice crystal habit of the clouds observed at Gale Crater. The characteristics of the HG curves that we derive for each Mars year do not agree well with those of regular water-ice crystal geometries observed in Earth-based cirrus clouds, nor with any martian airborne dusts. This result suggests that the water-ice crystal habit of the ACB clouds we observe is not like those of terrestrial clouds. Additionally, the lack of good agreement with martian dust, especially that at Gale Crater, suggests that the amount of water-ice accreted onto the dust is sufficient to change its scattering properties. Our derived HG parameters align most closely with those of volcanic basalt and olivine, which exhibit irregular, roughened geometry. The water-ice crystals in the clouds we observe could likewise have some irregular geometry.

7.3 Can CaSSIS see Suboptical Clouds?

We compare images taken by CaSSIS with MSL cloud movies taken concurrently in the ACB season to determine the limits of CaSSIS' ability to observe suboptical water-ice clouds. Such clouds are very common at Gale Crater during the ACB season, and MSL has an extensive record of cloud movies and derived cloud opacities. We identified eleven CaSSIS images taken concurrently with MSL cloud movies showing water-ice clouds during the ACB season. Of these, eight were taken as part of a coordinated imaging campaign between CaSSIS and MSL during MY 38.

The MSL cloud movies show clouds with opacities from 0.04 to 0.26. We are unable to see clouds in any of the corresponding CaSSIS images. Further analysis of the BLU channel, where we would expect clouds to be most strongly reflective, does not indicate that these clouds are influencing the reflectance in that channel.

For a point of comparison, we also looked at a CaSSIS image in which obvious clouds were present and an image in which we are reasonably certain clouds are not present. In the cloudy image, the standard deviation is much higher in the BLU channel, and this could be a good indicator for the presence of clouds.

The image without clouds overlaps one of the cloudy scenes, and in comparing the two we see that the

reflectance spectra and standard deviations are very similar, with lighting effects likely responsible for the bulk of the observed differences. It seems that suboptical clouds do not have a large or obvious influence on CaSSIS images.

7.4 The Impact of Atmospheric Aerosols on MCS Retrieval Altitudes

We use the minimum altitude of MCS temperature retrievals to infer a cut-off altitude for MCS below which the atmosphere becomes too opaque for MCS to observe. For the purposes of this study, we only examined the area around Gale Crater, where we have a substantial surface meteorological record.

In the cloudy season, MCS has a preference for cut-off altitudes above 20 km, while the dusty season shows a much larger spread in cut off altitudes. However, throughout the whole Mars year, there is a preference for cut-off altitudes between 20-40 km. MSL sees ACB clouds forming between 15-30 km, so it is possible that MCS is missing lower altitude clouds or not capturing the whole extent of cloud formation. This conclusion can be seen in comparing the inferred altitudes of clouds seen by MSL on the same sol as MCS water-ice profiles were taken, where the clouds form below the lowest MCS retrieval.

In the dusty season, when water-ice clouds are less likely to be impeding MCS retrievals, we can use the cut-off altitude to track the decay of significant dust storms, such as the global dust storms of MYs 28 and 34. The cut-off altitudes do not seem to directly track dust opacity. We do not see the maxima and minima in dust opacity throughout the dusty season, and the higher cut-off altitudes observed during GDS periods take longer to return to typical than opacities do. Rather, we may be seeing the effect of persistent, high altitude small dust particles which have less of an overall impact on opacity yet still render MCS retrieval errors unacceptably high.

7.5 Determining Near-Surface Aerosol Properties using Low-Powered Lasers

We used a setup consisting of three class 3R lasers and an all-sky camera to see if we are able to characterise near-surface aerosols. In this work, we analysed images from laboratory and field experiments and were able to see the impact of differences in particle size and to examine fog properties in three different laser wavelengths.

The laboratory work looked at three sizes of polystyrene microspheres suspended in water in a large aquarium. The camera imaged each laser beam reflected several times within the aquarium, from which we

were able to derive an extinction curve and extract a scattering phase function. The phase functions do not differ dramatically between particle size and based on wavelength, though we do see a bit more variation in the phase functions of the smaller particles while those of the larger ones are smoother. This agrees with what we see when we use a mie scattering model for the microspheres. We also find that the smaller particles have greater extinction than the larger ones, which again agrees with the models and theory.

The field experiments deployed the setup in Argentia, Newfoundland to examine backscatter from thick fog. While several experiments were done there, we look only at the results from the night of June 29. We extracted the spectral radiance along the beam for up to ~ 70 m and were able to identify potential areas of thicker fog at about 1 and 4 m above the ground in all three lasers.

Working with the data from these experiments also identified several areas for improvement in a future instrument of this type. However, we were able to see that particle size impacts the laser backscatter, which means that this setup will be able to probe the sizes of near surface aerosols. We are also able to observe the backscatter increasing and decreasing in a fog bank. While the scope of this work only went so far as estimating the thicker parts of the fog, future work could use a method similar to that used by (Moores et al., 2011) to determine the liquid water content at different heights in the fog.

The field results also allow us to estimate the laser power needed to observe comparable fogs on different planets. Using sky brightnesses for daytime Earth, Mars, Venus and Titan we see that Venus and Earth require the most powerful lasers, at tens of mW, while Mars requires a laser close to 10 mW and Titan requires a laser less powerful than a typical handheld laser pointer to overcome background illumination levels.

7.6 Variability of Methane Plumes and Implications for Martian Exploration

We examine local methane variation in the Canadian arctic to understand small-scale temporal variations in methane plumes and how this may impact methane sampling on Mars. The two hyper-saline cold springs that we studied, Gypsum Hill Springs and Wolf Spring, are often used as martian analogues and produce methane plumes which may resemble those seen on Mars. We conducted transects aligned with the wind direction at both sites in 2022, as well as an additional transect unaligned with the wind direction at Gypsum Hill. Upwind of the source, methane concentrations were closer to those of the background and there was less variation in the methane signal. Downwind, both the concentration and variation in the signal increased.

We were able to observe not only variations around the mean, but also increases in the overall methane

concentration over time, as in GH-WD-05, and the arrival and departure of an airmass containing methane, as in GH-WD-01. Being able to see such small-scale temporal changes in methane, as opposed to obtaining a single measurement every so often, allows us to build up a more complete understanding of methane's behaviour. The regular, second-scale spikes of methane do not exhibit any strong periodicity, and when we examine a periodogram for the methane signal at Wolf Spring we see that the magnitude of these spikes falls off at a rate proportional to the inverse square of the frequency, which suggests the action of a diffusive process.

We took an additional series of measurements at Wolf Spring in 2024 along with wind direction data and examined the relationship between methane signal and both wind direction and distance from the source. In this way we were able to examine how the methane signal changed with proximity to the methane plume. We saw the same tendency of the methane concentration and the variation around the mean to decrease with distance from the methane plume, though our analysis indicates that the variability is a better marker of proximity. Thus, there is a benefit to collecting high temporal frequency methane measurements beyond better temporal characterisation of methane concentration. While these measurements are not currently possible on Mars, they can increase our understanding of the behaviour of methane. We can use changes in the variability of methane to estimate not only whether we may be upwind or downwind of a methane source but also our proximity to it. Additionally, we can estimate how likely we are to see methane spikes of different magnitudes which could inform further sampling plans.

Chapter 8

Future Work

8.1 The Water-ice Cloud Phase Function at Gale Crater

The five year ACB dataset has allowed a thorough study of interannual, seasonal and diurnal variability in the cloud phase function and has increased our confidence in the likely water-ice crystal habit. Continuing to build this dataset year by year will not only increase our confidence in our findings, but also allow for identification of any longer term trends in the data. For instance, we were not able to determine a reason for the diurnal difference seen in MY 34 which was not present in any other Mars year. The addition of further Mars years of data could help to pin that down. Coordinating with other instruments or examining other meteorological datasets could also help. This work has broader implications for better understanding the impact of water-ice clouds on radiative transfer.

It would also be of interest to look at a similar dataset from another landed spacecraft for comparison purposes. The Mars 2020 Perseverance rover, which is situated more in the spatial middle of the ACB, could provide a complimentary dataset to examine another part of the ACB. We already know from solar imaging that hexagonal ice crystals are present at Jezero Crater (Lemmon et al., 2022); however there is no study of the water-ice cloud crystal habit through the entire ACB season.

Finally, the operational constraints of the Navcams and over-saturation from the sun limited our ability to see the lower scattering angles. Exploring an alternate process or using a different instrument to allow us to image closer to the sun would help to fill in this missing part of the phase function, which could provide more information about both the water-ice crystal habit and also potentially its size.

8.2 Can CaSSIS see Suboptical Clouds?

The dataset that we used in this work was very limited, with only eleven paired MSL-CaSSIS cloud observations. An extended dataset may allow patterns in the channel ratio analysis to become more apparent, and potentially allow for lighting and terrain considerations to be teased apart. Additionally, we could use a different parametrisation when investigating the relationships between the different channels than a simple

ratio. We could also explore methods for estimating an optical depth from the CaSSIS images alone, such as the shadow method employed by Hoekzema et al. (2011).

This work can also be extended to other sites such as Jezero Crater where coordinated measurements could likewise be taken with Mars 2020. This work could also include future landing sites, such as that of the ExoMars Rosalind Franklin rover at Oxia Planum. Jezero Crater ends to see optically thicker clouds in the ACB, and more often sees clouds in the raw Navcam images, which is quite rare at Gale (Hayes et al., 2024a). It would be interesting to explore how optically thicker clouds are imaged by CaSSIS, and their impacts on various channels.

Future work on this could have implications for the analysis of CaSSIS images, in particular the geological analysis which these images are primarily used for. If optically thin clouds are present in the image but unable to be seen by eye, they still may nevertheless add some reflectance to the image which may or may not be significant.

8.3 The Impact of Atmospheric Aerosols on MCS Retrieval Altitudes

The findings of this work that MCS is impeded by water-ice clouds and dust has potential implications in the use of MCS for validating surface observations. This work could be extended to Mars more broadly to examine differences in topography or location and their impacts, if any, on the cut-off altitudes of MCS retrievals. Different locations are impacted differently by dust lifting and by cloud cover, with different seasonal patterns. Additionally, this work could be extended to other instruments or orbiters using different wavelengths. We could also use findings from other instruments, for instance, water-ice opacity from MARCI (Wolff et al., 2019), in conjunction with the MCS retrievals to further probe any patterns.

We could also extend the sedimentation analysis done during the GDSs by using more sophisticated particle dynamical models than Stokes flow, which assumes the particles are all spheres under viscous flow. We can consider different particle habits and sizes, as well as incorporating air currents at the relevant altitude. We could also combine this kind of model with dust opacity retrievals from MCS above the cut-off altitude to probe upper atmosphere dust.

8.4 Determining Near-Surface Aerosol Properties using Low-Powered Lasers

We have demonstrated that a simple panoramic camera imaging low-powered lasers has the ability to characterise and explore near-surface planetary aerosols, which may not be well characterised by orbiters. However, we have only begun to explore what we are able to determine from this setup.

Properly and fully understanding the camera and lasers, as well as their geometries in the setup, is crucial in the analysis. There were several instances where we needed to make assumptions or use approximations in analysing the images that could have been avoided if all the camera parameters were well known. Additionally, different setups with the lasers at different tilt angles or different distances from the camera and different fields of view of the camera itself may impact how much of the beam we are able to see. Future work should include additional experiments using different spacings between the lasers and the camera. We could also modify the setup by including multiple cameras with different FoV. Additionally, it would be helpful to perform the same analysis on images of multiple lasers at once, which would reduce the complexity and data volume of an observation.

The experiments in the aquarium could also be redone with a different experimental design and better documentation. The concentrations of microspheres were very low, and it seems that the signal from the microspheres is likely much smaller than the signal from impurities in the water. Using distilled water could remove these impurities. Likewise, having a greater concentration of microspheres may allow us to better chracterise them. It would also be helpful to understand how the laser behaviour changes in varying concentrations of particles, so being able to capture these data would be useful. In the absence of new aquarium experiments, comparing the laser behaviour in a 'water-only' scenario may help determine the effect of water impurities.

While for the field experiments the scope of this work only went so far as estimating the heights of thicker parts of the fog, future work could use a method similar to that used by Moores et al. (2011) to determine the liquid water content at different heights in the fog, using an assumed fog droplet radius.

8.5 Variability of Methane Plumes and Implications for Martian Exploration

Future work could deal with improving the localisation of methane sources. In this work, we only examined variability in two dimensions. Understanding the 3D behaviour of methane plumes may increase our ability

to localise them. Having the instrument mounted on a drone would allow us to capture 3D information about the methane plume, which is important to understand as methane diffuses through the atmosphere in all three dimensions. Furthermore, we can validate the use of a drone-mounted sensor for the detection of methane or other trace gases on Mars. Applying more sophisticated plume modelling techniques, such as a Gaussian solution, may also enhance the work.

While we just looked at methane in this work, other trace gases such as HCl (Gregory et al., 2026) may be of interest, and future work could look into determining their behaviour and if it is possible to localise them similarly to methane. Additionally, taking simultaneous measurements of different trace gases may elucidate any relationships between them. Different trace gases may be impacted by similar processes, or may impact each other, and understanding this will give us a better understanding of the chemistry and dynamics of the martian atmosphere.

Additionally, it may be of interest to capture longer term measurements. In this work, all individual observations lasted less than fifteen minutes, so we were not able to identify longer term changes in methane plume behaviour, if any exist. A methane plume on Mars has never been observed from initiation through decay, and it would be valuable to acquire more information about their behaviour. Additionally, SAM-TLS measurements suggest that methane present overnight is rapidly destroyed or diluted during the daytime (Webster et al., 2021), a finding which is supported by the non-detection of methane by TGO. Having long-term, continuous methane measurements may provide clarity on this discrepancy.

References

D. T. Andersen, W. H. Pollard, C. P. McKay, and J. Heldmann. Cold springs in permafrost on Earth and Mars. *Journal of Geophysical Research: Planets*, 107(E3):4–1–4–7, 2002. ISSN 2156-2202. doi: 10.1029/2000JE001436.

S. K. Atreya, P. R. Mahaffy, and A.-S. Wong. Methane and related trace species on Mars: Origin, loss, implications for life, and habitability. *Planetary and Space Science*, 55(3):358–369, 2007. ISSN 0032-0633. doi: 10.1016/j.pss.2006.02.005.

S. A. Atwood, M. D. Smith, K. Badri, C. S. Edwards, P. R. Christensen, M. J. Wolff, F. Forget, S. Anwar, N. Smith, and M. R. El-Maarry. Diurnal Variability in EMIRS Daytime Observations of Water Ice Clouds During Mars Aphelion-Season. *Geophysical Research Letters*, 49(15):e2022GL099654, 2022. ISSN 1944-8007. doi: 10.1029/2022GL099654.

D. Banfield, J. Stern, A. Davila, G. Martinez, C. Newman, C. Viviano, R. Citron, P. Niles, S. Do, S. Diniega, and M. Mischna. Mars Science Goals, Objectives, Investigations, and Priorities: 2025 Version. 2025.

Basler-AG. *acA4024-29uc Datasheet*. Basler Product Documentation, 2026. URL `https://docs.baslerweb.com/aca4024-29uc`.

M. M. Battler, G. R. Osinski, and N. R. Banerjee. Mineralogy of saline perennial cold springs on Axel Heiberg Island, Nunavut, Canada and implications for spring deposits on Mars. *Icarus*, 224(2):364–381, June 2013. ISSN 00191035. doi: 10.1016/j.icarus.2012.08.031.

F. Bettonvil. Fisheye lenses. *WGN, Journal of the International Meteor Organization*, 33:9–14, 2005. ISSN 1016-3115.

L. Bi and P. Yang. Accurate simulation of the optical properties of atmospheric ice crystals with the invariant imbedding T-matrix method. *Journal of Quantitative Spectroscopy and Radiative Transfer*, 138:17–35, 2014. ISSN 00224073. doi: 10.1016/j.jqsrt.2014.01.013.

G. Bischof, S. D. Guzewich, J. E. Moores, M. T. Lemmon, J. M. Battalio, D. C. Hayes, A. C. Innanen, and C. L. Smith. Dust Dynamics in Gale Crater Observed Using the Line-Of-Sight Extinction Through 3,663 Sols of the Mars Science Laboratory Mission. *Journal of Geophysical Research: Planets*, 129(10): e2024JE008349, 2024. ISSN 2169-9100. doi: 10.1029/2024JE008349.

C. F. Bohren and S. B. Singham. Backscattering by nonspherical particles: A review of methods and suggested new approaches. *Journal of Geophysical Research: Atmospheres*, 96(D3):5269–5277, 1991. ISSN 2156-2202. doi: 10.1029/90JD01138.

G. A. Briggs, W. A. Baum, and J. Barnes. Viking Orbiter imaging observations of dust in the Martian atmosphere. *Journal of Geophysical Research: Solid Earth*, 84(B6):2795–2820, 1979. ISSN 2156-2202. doi: 10.1029/JB084iB06p02795.

C. L. Campbell. *Characterizing the Martian Environment Through Surface Spacecraft Observations*. PhD thesis, York University, Toronto, 2024.

C. L. Campbell and J. E. Moores. Using imagery from the Mars Science Laboratory mission to understand wind properties of aerosols aloft. *Planetary and Space Science*, 263:106119, 2025. ISSN 0032-0633. doi: 10.1016/j.pss.2025.106119.

C. L. Campbell, A. M. Kling, S. D. Guzewich, C. L. Smith, J. L. Kloos, M. T. Lemmon, C. A. Moore, B. A. Cooper, R. M. Haberle, and J. E. Moores. Estimating the altitudes of Martian water-ice clouds above the Mars Science Laboratory rover landing site. *Planetary and Space Science*, 182:104785, 2020. ISSN 00320633. doi: 10.1016/j.pss.2019.104785.

C. L. Campbell, C. L. Smith, A. C. Innanen, J. L. Kloos, H. Stone, G. K. Benedix, S. Meka, D. Marrable, and J. E. Moores. MAPLE: Mars Atmospheric Panoramic camera and Laser Experiment. volume 2655, page 5031, Pasadena, California, 2022. LPI.

B. A. Cantor, P. B. James, M. Caplinger, and M. J. Wolff. Martian dust storms: 1999 Mars Orbiter Camera observations. *Journal of Geophysical Research: Planets*, 106(E10):23653–23687, 2001. ISSN 2156-2202. doi: 10.1029/2000JE001310.

G. Cassini. M. Cassini a reconnu que Mars tourne sur son axe,. *Journal des sçavans*, 2:259–262, 1666.

H. Chen-Chen, S. Pérez-Hoyos, and A. Sánchez-Lavega. Characterisation of Martian dust aerosol phase function from sky radiance measurements by MSL engineering cameras. *Icarus*, 330:16–29, 2019. ISSN 0019-1035. doi: 10.1016/j.icarus.2019.04.004.

R. T. Clancy and S. W. Lee. A new look at dust and clouds in the Mars atmosphere: analysis of emission-phase-function sequences from global viking IRTM observations. *Icarus*, 93(1):135–158, 1991. ISSN 00191035. doi: 10.1016/0019-1035(91)90169-T.

R. T. Clancy, A. W. Grossman, M. J. Wolff, P. B. James, D. J. Rudy, Y. N. Billawala, B. J. Sandor, S. W. Lee, and D. O. Muhleman. Water Vapor Saturation at Low Altitudes around Mars Aphelion: A Key to Mars Climate? *Icarus*, 122(1):36–62, 1996. ISSN 0019-1035. doi: 10.1006/icar.1996.0108.

R. T. Clancy, B. J. Sandor, M. J. Wolff, P. R. Christensen, M. D. Smith, J. C. Pearl, B. J. Conrath, and R. J. Wilson. An intercomparison of ground-based millimeter, MGS TES, and Viking atmospheric temperature measurements: Seasonal and interannual variability of temperatures and dust loading in the global Mars atmosphere. *Journal of Geophysical Research: Planets*, 105(E4):9553–9571, 2000. ISSN 01480227. doi: 10.1029/1999JE001089.

R. T. Clancy, M. J. Wolff, and P. R. Christensen. Mars aerosol studies with the MGS TES emission phase function observations: Optical depths, particle sizes, and ice cloud types versus latitude and solar longitude. *Journal of Geophysical Research*, 108(E9):5098, 2003. ISSN 0148-0227. doi: 10.1029/2003JE002058.

B. A. Cooper, J. E. Moores, D. J. Ellison, J. L. Kloos, C. L. Smith, S. D. Guzewich, and C. L. Campbell. Constraints on Mars Aphelion Cloud Belt phase function and ice crystal geometries. *Planetary and Space Science*, 168:62–72, 2019. ISSN 00320633. doi: 10.1016/j.pss.2019.01.005.

M. de la Torre Juárez, J. M. Battalio, C. E. Newman, T. del Río Gaztelurrutia, R. Hueso, and A. Sánchez-Lavega. Signatures of the Martian Polar CO2 Cycle on Surface Pressures at Gale and Jezero. volume 3064, page 6060, July 2024.

S. Fonti and G. A. Marzo. Mapping the methane on Mars. *Astronomy & Astrophysics*, 512:A51, 2010. ISSN 0004-6361, 1432-0746. doi: 10.1051/0004-6361/200913178.

V. Formisano, S. Atreya, T. Encrenaz, N. Ignatiev, and M. Giuranna. Detection of Methane in the Atmosphere of Mars. *Science*, 306:1758–1761, 2004.

H. B. Franz, M. G. Trainer, C. A. Malespin, P. R. Mahaffy, S. K. Atreya, R. H. Becker, M. Benna, P. G. Conrad, J. L. Eigenbrode, C. Freissinet, H. L. K. Manning, B. D. Prats, E. Raaen, and M. H. Wong. Initial SAM calibration gas experiments on Mars: Quadrupole mass spectrometer results and implications. *Planetary and Space Science*, 138:44–54, 2017. ISSN 0032-0633. doi: 10.1016/j.pss.2017.01.014.

A. Geminale, V. Formisano, and G. Sindoni. Mapping methane in Martian atmosphere with PFS-MEX data. *Planetary and Space Science*, 59(2):137–148, 2011. ISSN 0032-0633. doi: 10.1016/j.pss.2010.07.011.

P. Gierasch, P. Thomas, R. French, and J. Veverka. Spiral clouds on Mars: A new atmospheric phenomenon. *Geophysical Research Letters*, 6(5):405–408, 1979. ISSN 1944-8007. doi: 10.1029/GL006i005p00405.

P. J. Gierasch and R. M. Goody. The Effect of Dust on the Temperature of the Martian Atmosphere. *Journal of the Atmospheric Sciences*, 29(2):400–402, 1972. ISSN 0022-4928, 1520-0469. doi: 10.1175/1520-0469(1972)029<0400:TEODOT>2.0.CO;2.

M. Giuranna, P. Wolkenberg, D. Grassi, A. Aronica, S. Aoki, D. Scaccabarozzi, B. Saggin, and V. Formisano. The current weather and climate of Mars: 12 years of atmospheric monitoring by the Planetary Fourier Spectrometer on Mars Express. *Icarus*, 353:113406, 2021. ISSN 00191035. doi: 10.1016/j.icarus.2019.113406.

B. Gregory, K. Olsen, E. Millour, M. Brown, P. Streeter, K. Rajendran, and M. Patel. Modelling the Variation of HCl in the Martian Atmosphere. Technical Report EGU26-18786, Copernicus Meetings, Mar. 2026.

E. Grunwald and C. Steel. Distinguishability of liquid environments in the presence of brownian noise. *Journal of Physical Organic Chemistry*, 7(12):734–742, 1994. ISSN 1099-1395. doi: 10.1002/poc.610071212.

S. D. Guzewich, C. E. Newman, M. D. Smith, J. E. Moores, C. L. Smith, C. Moore, M. I. Richardson, D. Kass, A. Kleinböhl, M. Mischna, F. J. Martín-Torres, M.-P. Zorzano-Mier, and M. Battalio. The Vertical Dust Profile Over Gale Crater, Mars. *Journal of Geophysical Research: Planets*, 122(12):2779–2792, 2017. ISSN 2169-9100. doi: 10.1002/2017JE005420.

S. D. Guzewich, M. Lemmon, C. L. Smith, G. Martínez, Á. de Vicente-Retortillo, C. E. Newman, M. Baker, C. Campbell, B. Cooper, J. Gómez-Elvira, A.-M. Harri, D. Hassler, F. J. Martin-Torres, T. McConnochie, J. E. Moores, H. Kahanpää, A. Khayat, M. I. Richardson, M. D. Smith, R. Sullivan, M. de la Torre Juarez, A. R. Vasavada, D. Viúdez-Moreiras, C. Zeitlin, and M.-P. Zorzano Mier. Mars Science Laboratory Observations of the 2018/Mars Year 34 Global Dust Storm. *Geophysical Research Letters*, 46(1):71–79, 2019. doi: 10.1029/2018GL080839.

S. D. Guzewich, G. Martínez, A. Innanen, J. Pla-García, M. Ruíz-Pérez, M. de la Torre Juárez, C. E. Newman, M. Lemmon, G. Bischof, M. I. Richardson, J. Moores, E. Mason, J. M. Battalio, Á. de Vicente-Retortillo, T. McConnochie, D. Hayes, A. A. Fraeman, A. Vasavada, and MSL Environmental Science Theme Group. 10 Years of Environmental Science in Gale Crater. volume 2806, page 2054, 2023a.

S. D. Guzewich, E. L. Mason, M. T. Lemmon, C. E. Newman, and K. W. Lewis. Dust Lifting Observations With the Mars Science Laboratory Navigation Cameras. *Journal of Geophysical Research: Planets*, 128 (10):e2023JE007959, 2023b. ISSN 2169-9100. doi: 10.1029/2023JE007959.

R. A. Hanel, B. J. Conrath, W. A. Hovis, V. Kunde, P. D. Lowman, C. Prabhakara, B. Schlachman, and G. V. Levin. Infrared spectroscopy experiment for Mariner Mars 1971. *Icarus*, 12(1):48–62, 1970. ISSN 0019-1035. doi: 10.1016/0019-1035(70)90031-X.

J. E. Hansen and L. D. Travis. Light scattering in planetary atmospheres. *Space Science Reviews*, 16(4): 527–610, 1974. ISSN 0038-6308, 1572-9672. doi: 10.1007/BF00168069.

B. Hapke. Bidirectional reflectance spectroscopy 7: The single particle phase function hockey stick relation. *Icarus*, 221(2):1079–1083, 2012a. ISSN 0019-1035. doi: 10.1016/j.icarus.2012.10.022.

B. Hapke. *Theory of Reflectance and Emittance Spectroscopy*. Cambridge University Press, 2 edition, 2012b. ISBN 978-0-521-88349-8 978-1-139-02568-3. doi: 10.1017/CBO9781139025683.

D. C. Hayes. Mars, 2025. URL `https://dchayes.ca/mars/`.

D. C. Hayes, A. C. Innanen, M. T. Lemmon, G. M. Martínez, and J. E. Moores. Aphelion Cloud Belt Opacities over Jezero Crater Through the First 1000 Sols of the Mars 2020 Mission. volume 3007, page 3307, July 2024a.

D. C. Hayes, J. L. Kloos, A. C. Innanen, C. L. Campbell, H. M. Sapers, and J. E. Moores. Five Mars Years of Cloud Observations at Gale Crater: Opacities, Variability, and Ice Crystal Habits. *The Planetary Science Journal*, 5(2):51, 2024b. ISSN 2632-3338. doi: 10.3847/PSJ/ad2202.

D. C. Hayes, J. L. Kloos, A. C. Innanen, C. L. Campbell, H. M. Sapers, and J. E. Moores. Six Mars Years of Gale Crater Cloud Opacity Measurements. volume 3007, page 3130, July 2024c.

N. G. Heavens, J. L. Benson, D. M. Kass, A. Kleinböhl, W. A. Abdou, D. J. McCleese, M. I. Richardson, J. T. Schofield, J. H. Shirley, and P. M. Wolkenberg. Water ice clouds over the Martian tropics during northern summer: MARTIAN TROPICAL WATER ICE CLOUDS. *Geophysical Research Letters*, 37(18): L18202, 2010. ISSN 00948276. doi: 10.1029/2010GL044610.

N. G. Heavens, M. I. Richardson, A. Kleinböhl, D. M. Kass, D. J. McCleese, W. Abdou, J. L. Benson, J. T. Schofield, J. H. Shirley, and P. M. Wolkenberg. The vertical distribution of dust in the Martian atmosphere during northern spring and summer: Observations by the Mars Climate Sounder and analysis of zonal average vertical dust profiles. *Journal of Geophysical Research: Planets*, 116(E4), 2011. ISSN 2156-2202. doi: 10.1029/2010JE003691.

W. Herschel. On the Remarkable Appearances at the Polar Regions of the Planet Mars, the Inclination of Its Axis, the Position of Its Poles, and Its Spheroidical Figure; With a Few Hints Relating to Its Real Diameter and Atmosphere. By William Herschel, Esq. F. R. S. *Philosophical Transactions of the Royal Society of London*, 74:233–273, 1784. ISSN 0261-0523. Publisher: The Royal Society.

D. P. Hinson, M. Pätzold, S. Tellmann, B. Häusler, and G. L. Tyler. The depth of the convective boundary layer on Mars. *Icarus*, 198(1):57–66, 2008. ISSN 0019-1035. doi: 10.1016/j.icarus.2008.07.003.

N. Hoekzema, M. Garcia-Comas, O. Stenzel, E. Petrova, N. Thomas, W. Markiewicz, K. Gwinner, H. Keller, and W. Delamere. Retrieving optical depth from shadows in orbiter images of Mars. *Icarus*, 214(2):447–461, Aug. 2011. ISSN 00191035. doi: 10.1016/j.icarus.2011.06.009. URL `https://linkinghub.elsevier.com/retrieve/pii/S0019103511002181`.

N. Hoffman. Ideas About the Surface Runoff Features on Mars. *Science*, 290(5492):711–714, Oct. 2000. doi: 10.1126/science.290.5492.711c.

F. Hourdin, P. L. Van, F. Forget, and O. Talagrand. Meteorological Variability and the Annual Surface Pressure Cycle on Mars. *Journal of the Atmospheric Sciences*, 50(21):3625–3640, 1993. ISSN 0022-4928, 1520-0469. doi: 10.1175/1520-0469(1993)050<3625:MVATAS>2.0.CO;2.

A. C. Innanen, B. A. Cooper, D. C. Hayes, C. L. Campbell, J. L. Kloos, S. D. Guzewich, and J. E. Moores. Three Years of ACB Phase Function Observations from the Mars Science Laboratory: Interannual and Diurnal Variability and Constraints on Ice Crystal Habit. *The Planetary Science Journal*, 5(3):72, 2024a. ISSN 2632-3338. doi: 10.3847/PSJ/ad2990.

A. C. Innanen, J. E. Moores, M. E. Landis, and V. Concepcion. Minimum Mars Climate Sounder Retrieval Altitudes Reveal Cloud Altitudes at Aphelion and Stranded High-altitude Dust Following the MY34 Global Dust Storm on Mars. *Research Notes of the AAS*, 8(4):117, 2024b. ISSN 2515-5172. doi: 10.3847/2515-5172/ad43d8.

A. C. Innanen, D. C. Hayes, B. E. Koch Nichol, and J. E. Moores. Four Mars Years of ACB Phase Function Observations from the Mars Science Laboratory Show Low Interannual and Diurnal Variability and Suggest Irregular Water–ice Crystal Geometry. *Icarus*, 429:116437, 2025a. ISSN 0019-1035. doi: 10.1016/j.icarus.2024.116437.

A. C. Innanen, J. E. Moores, H. Sapers, L. Beckering Vinckers Stofer, E. Dong, and K. Axelrod. Variability of Methane Plumes at an Arctic Analogue Site with Implications for Marian Exploration. *Acta Astronautica*, 235:223–234, 2025b. doi: 10.1016/j.actaastro.2025.05.039.

G. A. Isaac, T. Bullock, J. Beale, and S. Beale. Characterizing and Predicting Marine Fog Offshore Newfoundland and Labrador. *Weather and Forecasting*, 35(2):347–365, 2020. ISSN 1520-0434, 0882-8156. doi: 10.1175/WAF-D-19-0085.1.

J. R. Johnson, J. Sohl-Dickstein, W. M. Grundy, R. E. Arvidson, J. Bell III, P. Christensen, T. Graff, E. A. Guinness, K. Kinch, R. Morris, and M. K. Shepard. Radiative transfer modeling of dust-coated Pancam calibration target materials: Laboratory visible/near-infrared spectrogoniometry. *Journal of Geophysical Research: Planets*, 111(E12), 2006. ISSN 2156-2202. doi: 10.1029/2005JE002658.

M. A. Kahre, J. R. Murphy, C. E. Newman, R. J. Wilson, B. A. Cantor, M. T. Lemmon, and M. J. Wolff. The Mars Dust Cycle. In R. M. Haberle, R. T. Clancy, F. Forget, M. D. Smith, and R. W. Zurek, editors, *The Atmosphere and Climate of Mars*, pages 295–337. Cambridge University Press, Cambridge, 2017. ISBN 978-1-139-06017-2. doi: 10.1017/9781139060172.010.

J. Katz. *Introductory Fluid Mechanics*. Cambridge University Press, 1 edition, Aug. 2010. ISBN 978-0-521-19245-3 978-0-511-76134-8 978-1-107-61713-1. doi: 10.1017/CBO9780511761348.

M. Keshner. 1/f noise. *Proceedings of the IEEE*, 70(3):212–218, 1982. ISSN 1558-2256. doi: 10.1109/PROC.1982.12282.

H. H. Kieffer, B. M. Jakosky, and C. W. Snyder. The planet Mars: from antiquity to the present. In *Mars*, pages 1–33. 1992.

A. Kleinböhl, J. T. Schofield, D. M. Kass, W. A. Abdou, C. R. Backus, B. Sen, J. H. Shirley, W. G. Lawson, M. I. Richardson, F. W. Taylor, N. A. Teanby, and D. J. McCleese. Mars Climate Sounder limb profile retrieval of atmospheric temperature, pressure, and dust and water ice opacity: MCS RETRIEVALS. *Journal of Geophysical Research: Planets*, 114(E10):E10006, 2009. ISSN 01480227. doi: 10.1029/2009JE003358.

J. L. Kloos, J. E. Moores, M. Lemmon, D. Kass, R. Francis, M. de la Torre Juárez, M.-P. Zorzano, and F. J. Martín-Torres. The first Martian year of cloud activity from Mars Science Laboratory (sol 0–800). *Advances in Space Research*, 57(5):1223–1240, 2016. ISSN 02731177. doi: 10.1016/j.asr.2015.12.040.

J. L. Kloos, J. E. Moores, J. A. Whiteway, and M. Aggarwal. Interannual and Diurnal Variability in Water Ice Clouds Observed from MSL Over Two Martian Years. *Journal of Geophysical Research: Planets*, 123 (1):233–245, 2018. ISSN 2169-9100. doi: 10.1002/2017JE005314.

O. Korablev, F. Montmessin, A. Trokhimovskiy, A. A. Fedorova, A. V. Shakun, A. V. Grigoriev, B. E. Moshkin, N. I. Ignatiev, F. Forget, F. Lefèvre, K. Anufreychik, I. Dzuban, Y. S. Ivanov, Y. K. Kalinnikov, T. O. Kozlova, A. Kungurov, V. Makarov, F. Martynovich, I. Maslov, D. Merzlyakov, P. P. Moiseev, Y. Nikolskiy, A. Patrakeev, D. Patsaev, A. Santos-Skripko, O. Sazonov, N. Semena, A. Semenov, V. Shashkin, A. Sidorov, A. V. Stepanov, I. Stupin, D. Timonin, A. Y. Titov, A. Viktorov, A. Zharkov, F. Altieri, G. Arnold, D. A. Belyaev, J. L. Bertaux, D. S. Betsis, N. Duxbury, T. Encrenaz, T. Fouchet, J.-C. Gérard, D. Grassi, S. Guerlet, P. Hartogh, Y. Kasaba, I. Khatuntsev, V. A. Krasnopolsky, R. O. Kuzmin, E. Lellouch, M. A. Lopez-Valverde, M. Luginin, A. Määttänen, E. Marcq, J. Martin Torres, A. S. Medvedev, E. Millour, K. S. Olsen, M. R. Patel, C. Quantin-Nataf, A. V. Rodin, V. I. Shematovich, I. Thomas, N. Thomas, L. Vazquez, M. Vincendon, V. Wilquet, C. F. Wilson, L. V. Zasova, L. M. Zelenyi, and M. P. Zorzano. The Atmospheric Chemistry Suite (ACS) of Three Spectrometers for the ExoMars 2016 Trace Gas Orbiter. *Space Science Reviews*, 214(1):7, 2017. ISSN 1572-9672. doi: 10.1007/s11214-017-0437-6.

V. A. Krasnopolsky, J. P. Maillard, and T. C. Owen. Detection of methane in the martian atmosphere: evidence for life? *Icarus*, 172(2):537–547, 2004. ISSN 0019-1035. doi: 10.1016/j.icarus.2004.07.004.

S. V. Kulkarni, P. G. J. Irwin, C. F. Wilson, and N. I. Ignatiev. A Search for the Near-Surface Particulate Layer Using Venera 13 In Situ Spectroscopic Observations. *Journal of Geophysical Research: Planets*, 130 (4):e2024JE008728, 2025. ISSN 2169-9100. doi: 10.1029/2024JE008728.

C.-Y. Lay, N. Mykytczuk, T. Niederberger, C. Martineau, C. Greer, and L. Whyte. Microbial diversity and activity in hypersaline high Arctic spring channels. *Extremophiles : life under extreme conditions*, 16: 177–91, Mar. 2012. doi: 10.1007/s00792-011-0417-9.

R. B. Leighton, B. C. Murray, R. P. Sharp, J. D. Allen, and R. K. Sloan. Mariner IV Photography of Mars: Initial Results. *Science*, 149(3684):627–630, 1965. ISSN 0036-8075. URL `https://www.jstor.org/stable/1716664`.

M. Lemmon, S. Guzewich, J. Battalio, M. Malin, A. Vicente-Retortillo, M.-P. Zorzano, J. Martín-Torres, R. Sullivan, J. Maki, M. Smith, and J. Bell. The Mars Science Laboratory record of optical depth measurements via solar imaging. *Icarus*, 408:115821, 2024a. ISSN 00191035. doi: 10.1016/j.icarus.2023.115821.

M. T. Lemmon. Monitoring Aerosol Optical Depth Through Sky Imaging. volume 3007, page 3326, July 2024. URL https://ui.adsabs.harvard.edu/abs/2024LPICo3007.3326L. ADS Bibcode: 2024LPICo3007.3326L.

M. T. Lemmon, M. J. Wolff, J. F. Bell, M. D. Smith, B. A. Cantor, and P. H. Smith. Dust aerosol, clouds, and the atmospheric optical depth record over 5 Mars years of the Mars Exploration Rover mission. *Icarus*, 251:96–111, 2015. ISSN 0019-1035. doi: 10.1016/j.icarus.2014.03.029.

M. T. Lemmon, D. Toledo, V. Apestigue, I. Arruego, M. J. Wolff, P. Patel, S. Guzewich, A. Colaprete, Á. Vicente-Retortillo, L. Tamppari, F. Montmessin, M. de la Torre Juarez, J. Maki, T. McConnochie, A. Brown, and J. F. Bell. Hexagonal Prisms Form in Water-Ice Clouds on Mars, Producing Halo Displays Seen by Perseverance Rover. *Geophysical Research Letters*, 49(17), 2022. ISSN 0094-8276, 1944-8007. doi: 10.1029/2022GL099776.

M. T. Lemmon, C. L. Campbell, C. A. Wolfe, D. Viúdez-Moreiras, R. D. Lorenz, J. N. Maki, J. Moores, A. Spiga, and D. Banfield. Results from the InSight atmospheric imaging campaign. *Icarus*, 421:116248, 2024b. ISSN 0019-1035. doi: 10.1016/j.icarus.2024.116248.

M. T. Lemmon, A. Vicente-Retortillo, S. D. Guzewich, M. d. l. T. Juárez, A. C. Innanen, C. L. Campbell, J. N. Maki, M. C. Malin, and J. E. Moores. Iridescence Reveals the Formation and Growth of Ice Aerosols in Martian Noctilucent Clouds. *Geophysical Research Letters*, 51(23):e2024GL111183, 2024c. ISSN 1944-8007. doi: 10.1029/2024GL111183.

K.-N. Liou. *An introduction to atmospheric radiation*. Number v. 84 in International geophysics series. Academic Press, Amsterdam ; Boston, 2nd ed edition, 2002. ISBN 978-0-12-451451-5.

Y. Luo, M. A. Mischna, J. C. Lin, B. Fasoli, X. Cai, and Y. L. Yung. Mars Methane Sources in Northwestern Gale Crater Inferred From Back Trajectory Modeling. *Earth and Space Science*, 8(11):e2021EA001915, 2021. ISSN 2333-5084. doi: 10.1029/2021EA001915.

P. Machado, H. Eira, V. Bickel, F. Brasil, J. Silva, N. Thomas, M. Almeida, D. Tirsch, J. Carter, A. Cardesin-Moinelo, P. Martin, and C. Wilson. Winds and Waves on Mars' atmosphere using ExoMars/TGO CaSSIS. Technical Report EPSC-DPS2025-550, Copernicus Meetings, July 2025.

A. Macke, M. I. Mishchenko, and B. Cairns. The influence of inclusions on light scattering by large ice particles. *Journal of Geophysical Research: Atmospheres*, 101(D18):23311–23316, 1996. ISSN 2156-2202. doi: 10.1029/96JD02364.

J.-B. Madeleine, F. Forget, A. Spiga, M. J. Wolff, F. Montmessin, M. Vincendon, D. Jouglet, B. Gondet, J.-P. Bibring, Y. Langevin, and B. Schmitt. Aphelion water-ice cloud mapping and property retrieval using the OMEGA imaging spectrometer onboard Mars Express. *Journal of Geophysical Research: Planets*, 117 (E11), 2012. ISSN 2156-2202. doi: 10.1029/2011JE003940.

W. C. Maguire. Martian isotopic ratios and upper limits for possible minor constituents as derived from Mariner 9 infrared spectrometer data. *Icarus*, 32(1):85–97, 1977. ISSN 0019-1035. doi: 10.1016/0019-1035(77)90051-3.

P. R. Mahaffy, C. R. Webster, M. Cabane, P. G. Conrad, P. Coll, S. K. Atreya, R. Arvey, M. Barciniak, M. Benna, L. Bleacher, W. B. Brinckerhoff, J. L. Eigenbrode, D. Carignan, M. Cascia, R. A. Chalmers, J. P. Dworkin, T. Errigo, P. Everson, H. Franz, R. Farley, S. Feng, G. Frazier, C. Freissinet, D. P. Glavin, D. N. Harpold, D. Hawk, V. Holmes, C. S. Johnson, A. Jones, P. Jordan, J. Kellogg, J. Lewis, E. Lyness, C. A. Malespin, D. K. Martin, J. Maurer, A. C. McAdam, D. McLennan, T. J. Nolan, M. Noriega, A. A. Pavlov, B. Prats, E. Raaen, O. Sheinman, D. Sheppard, J. Smith, J. C. Stern, F. Tan, M. Trainer, D. W. Ming, R. V. Morris, J. Jones, C. Gundersen, A. Steele, J. Wray, O. Botta, L. A. Leshin, T. Owen, S. Battel, B. M. Jakosky, H. Manning, S. Squyres, R. Navarro-González, C. P. McKay, F. Raulin, R. Sternberg, A. Buch, P. Sorensen, R. Kline-Schoder, D. Coscia, C. Szopa, S. Teinturier, C. Baffes, J. Feldman, G. Flesch, S. Forouhar, R. Garcia, D. Keymeulen, S. Woodward, B. P. Block, K. Arnett, R. Miller, C. Edmonson, S. Gorevan, and E. Mumm. The Sample Analysis at Mars Investigation and Instrument Suite. *Space Science Reviews*, 170(1):401–478, 2012. ISSN 1572-9672. doi: 10.1007/s11214-012-9879-z.

J. Maki, D. Thiessen, A. Pourangi, P. Kobzeff, T. Litwin, L. Scherr, S. Elliott, A. Dingizian, and M. Maimone. The Mars Science Laboratory Engineering Cameras. *Space Science Reviews*, 170(1-4):77–93, 2012. ISSN 0038-6308. doi: 10.1007/s11214-012-9882-4.

M. C. Malin and K. S. Edgett. Evidence for Recent Groundwater Seepage and Surface Runoff on Mars. *Science*, 288(5475):2330–2335, June 2000. doi: 10.1126/science.288.5475.2330.

D. J. McCleese, J. T. Schofield, F. W. Taylor, S. B. Calcutt, M. C. Foote, D. M. Kass, C. B. Leovy, D. A. Paige, P. L. Read, and R. W. Zurek. Mars Climate Sounder: An investigation of thermal and water vapor structure, dust and condensate distributions in the atmosphere, and energy balance of the polar regions. *Journal of Geophysical Research*, 112(E5):E05S06, 2007. ISSN 0148-0227. doi: 10.1029/2006JE002790.

A. F. McGuire and B. W. Hapke. An Experimental Study of Light Scattering by Large, Irregular Particles. *Icarus*, 113(1):134–155, 1995. ISSN 00191035. doi: 10.1006/icar.1995.1012.

H. J. Melosh. *Planetary Surface Processes*. Cambridge University Press, 1 edition, 2011. ISBN 978-0-521-51418-7 978-0-511-97784-8. doi: 10.1017/CBO9780511977848.

L. Montabone, F. Forget, E. Millour, R. J. Wilson, S. R. Lewis, B. Cantor, D. Kass, A. Kleinböhl, M. T. Lemmon, M. D. Smith, and M. J. Wolff. Eight-year climatology of dust optical depth on Mars. *Icarus*, 251:65–95, 2015. ISSN 0019-1035. doi: 10.1016/j.icarus.2014.12.034.

F. Montmessin, F. Forget, P. Rannou, M. Cabane, and R. M. Haberle. Origin and role of water ice clouds in the Martian water cycle as inferred from a general circulation model. *Journal of Geophysical Research: Planets*, 109(E10), 2004. ISSN 2156-2202. doi: 10.1029/2004JE002284.

F. Montmessin, O. I. Korablev, A. Trokhimovskiy, F. Lefèvre, A. A. Fedorova, L. Baggio, A. Irbah, G. Lacombe, K. S. Olsen, A. S. Braude, D. A. Belyaev, J. Alday, F. Forget, F. Daerden, J. Pla-Garcia, S. Rafkin, C. F. Wilson, A. Patrakeev, A. Shakun, and J. L. Bertaux. A stringent upper limit of 20 pptv for methane on Mars and constraints on its dispersion outside Gale crater. *Astronomy & Astrophysics*, 650:A140, 2021. ISSN 0004-6361, 1432-0746. doi: 10.1051/0004-6361/202140389.

J. E. Moores, M. T. Lemmon, P. H. Smith, L. Komguem, and J. A. Whiteway. Atmospheric dynamics at the Phoenix landing site as seen by the Surface Stereo Imager. *Journal of Geophysical Research (Planets)*, 115(24):E00E08, 2010. doi: 10.1029/2009JE003409.

J. E. Moores, L. Komguem, J. A. Whiteway, M. T. Lemmon, C. Dickinson, and F. Daerden. Observations of near-surface fog at the Phoenix Mars landing site. *Geophysical Research Letters*, 38(4), 2011. ISSN 0094-8276. doi: 10.1029/2010GL046315.

J. E. Moores, T. Ha, M. T. Lemmon, and H. P. Gunnlaugsson. Martian airfall dust on smooth, inclined surfaces as observed on the Phoenix Mars Lander telltale mirror. *Planetary and Space Science*, 116:6–17, 2015. ISSN 00320633. doi: 10.1016/j.pss.2015.01.001.

J. E. Moores, M. T. Lemmon, S. C. R. Rafkin, R. Francis, J. Pla-Garcia, M. de la Torre Juárez, K. Bean, D. Kass, R. Haberle, C. Newman, M. Mischna, A. Vasavada, N. Rennó, J. Bell, F. Calef, B. Cantor, T. H. Mcconnochie, A.-M. Harri, M. Genzer, M. Wong, M. D. Smith, F. Javier Martín-Torres, M.-P. Zorzano, O. Kemppinen, and E. McCullough. Atmospheric movies acquired at the Mars Science Laboratory landing site: Cloud morphology, frequency and significance to the Gale Crater water cycle and Phoenix mission results. *Advances in Space Research*, 55(9):2217–2238, 2015. doi: 10.1016/j.asr.2015.02.007.

J. E. Moores, P. L. King, C. L. Smith, G. M. Martinez, C. E. Newman, S. D. Guzewich, P.-Y. Meslin, C. R. Webster, P. R. Mahaffy, S. K. Atreya, and A. C. Schuerger. The Methane Diurnal Variation and Microseepage Flux at Gale Crater, Mars as Constrained by the ExoMars Trace Gas Orbiter and Curiosity Observations. *Geophysical Research Letters*, 46(16):9430–9438, 2019. ISSN 1944-8007. doi: 10.1029/2019GL083800.

R. V. Morris, D. C. Golden, D. W. Ming, T. D. Shelfer, L. C. Jørgensen, J. F. Bell III, T. G. Graff, and S. A. Mertzman. Phyllosilicate-poor palagonitic dust from Mauna Kea Volcano (Hawaii): A mineralogical analogue for magnetic Martian dust? *Journal of Geophysical Research: Planets*, 106(E3):5057–5083, 2001. ISSN 2156-2202. doi: 10.1029/2000JE001328.

M. J. Mumma, G. L. Villanueva, R. E. Novak, T. Hewagama, B. P. Bonev, M. A. DiSanti, A. M. Mandell, and M. D. Smith. Strong Release of Methane on Mars in Northern Summer 2003. *Science*, 323(5917): 1041–1045, 2009. ISSN 0036-8075, 1095-9203. doi: 10.1126/science.1165243.

D. T. F. Möhlmann, M. Niemand, V. Formisano, H. Savijärvi, and P. Wolkenberg. Fog phenomena on Mars. *Planetary and Space Science*, 57(14):1987–1992, 2009. ISSN 0032-0633. doi: 10.1016/j.pss.2009.08.003.

National Academies of Sciences, Engineering, and Medicine. *Origins, Worlds, and Life: A Decadal Strategy for Planetary Science and Astrobiology 2023-2032*. The National Academies Press, Washington, DC, 2023. ISBN 978-0-309-47578-5. doi: 10.17226/26522.

C. E. Newman, C. Lee, M. A. Mischna, M. I. Richardson, and J. H. Shirley. An initial assessment of the impact of postulated orbit-spin coupling on Mars dust storm variability in fully interactive dust simulations. *Icarus*, 317:649–668, 2019. ISSN 0019-1035. doi: 10.1016/j.icarus.2018.07.023.

T. D. Niederberger, N. N. Perreault, S. Tille, B. S. Lollar, G. Lacrampe-Couloume, D. Andersen, C. W. Greer, W. Pollard, and L. G. Whyte. Microbial characterization of a subzero, hypersaline methane seep in the Canadian High Arctic. *The ISME Journal*, 4(10):1326–1339, 2010. ISSN 1751-7362. doi: 10.1038/ismej.2010.57.

D. Z. Oehler and G. Etiope. Methane Seepage on Mars: Where to Look and Why. *Astrobiology*, 17(12): 1233–1264, 2017. ISSN 1531-1074. doi: 10.1089/ast.2017.1657.

K. S. Olsen, F. Lefèvre, F. Montmessin, A. Trokhimovskiy, L. Baggio, A. Fedorova, J. Alday, A. Lomakin, D. A. Belyaev, A. Patrakeev, A. Shakun, and O. Korablev. First detection of ozone in the mid-infrared at Mars: implications for methane detection. *Astronomy & Astrophysics*, 639:A141, July 2020. ISSN 0004-6361, 1432-0746. doi: 10.1051/0004-6361/202038125. URL `https://www.aanda.org/articles/aa/abs/2020/07/aa38125-20/aa38125-20.html`.

P. Patel, L. Tamppari, M. d. l. T. Juárez, M. Lemmon, A. Coates, M. Wolff, D. Toledo, G. Branduardi-Raymont, G. Jones, C. Campbell, J. Moores, J. Maki, and J. Ryan. Geometric Properties of Water-ice Clouds as Observed from Jezero Crater in the First 600 sols with the NavCam Instrument On Board the Mars2020 Rover, Perseverance. *The Planetary Science Journal*, 4(12):226, 2023. ISSN 2632-3338. doi: 10.3847/PSJ/acfc35.

H. Perko, J. Nelson, and J. Green. Review of Martian Dust: Composition, Transport, Deposition, Adhesion and Removal. *Space 2002 and Robotics 2002*, 2002. doi: 10.1061/40625(203)25.

A. Petrosyan, B. Galperin, S. E. Larsen, S. R. Lewis, A. Määttänen, P. L. Read, N. Renno, L. P. H. T. Rogberg, H. Savijärvi, T. Siili, A. Spiga, A. Toigo, and L. Vázquez. The Martian Atmospheric Boundary Layer. *Reviews of Geophysics*, 49(3), 2011. ISSN 1944-9208. doi: 10.1029/2010RG000351.

S. Piqueux, S. Byrne, H. H. Kieffer, T. N. Titus, and C. J. Hansen. Enumeration of Mars years and seasons since the beginning of telescopic exploration. *Icarus*, 251:332–338, 2015. ISSN 0019-1035. doi: 10.1016/j.icarus.2014.12.014.

J. B. Pollack, D. Colburn, R. Kahn, J. Hunter, W. Van Camp, C. E. Carlston, and M. R. Wolf. Properties of aerosols in the Martian atmosphere, as inferred from Viking Lander imaging data. *Journal of Geophysical Research (1896-1977)*, 82(28):4479–4496, 1977. ISSN 2156-2202. doi: 10.1029/JS082i028p04479.

W. Pollard, C. Omelon, D. Andersen, and C. McKay. Perennial spring occurrence in the Expedition Fiord area of western Axel Heiberg Island, Canadian High Arctic. 36, 1999.

Polysciences, Inc. *Polybead® Polystyrene Microspheres*. Technical Data Sheet 238, Feb. 2009.

V. G. Rangarajan and L. L. Tornabene. Assessment of the Detection Capability of Ices in the VNIR from the Colour and Stereo Surface Imaging System (CaSSIS). In *Ices in the Solar System 2026*, volume 4011, 2026.

S. W. Ruff and P. R. Christensen. Bright and dark regions on Mars: Particle size and mineralogical characteristics based on Thermal Emission Spectrometer data. *Journal of Geophysical Research: Planets*, 107 (E12):2–1–2–22, 2002. ISSN 2156-2202. doi: 10.1029/2001JE001580.

K. Sassen and K.-N. Liou. Scattering of Polarized Laser Light by Water Droplet, Mixed-Phase and Ice Crystal Clouds. Part I: Angular Scattering Patterns. *Journal of the Atmospheric Sciences*, 36(5):838–851, 1979. ISSN 0022-4928, 1520-0469. doi: 10.1175/1520-0469(1979)036<0838:SOPLLB>2.0.CO;2.

J. T. Schofield, J. R. Barnes, D. Crisp, R. M. Haberle, S. Larsen, J. A. Magalhães, J. R. Murphy, A. Seiff, and G. Wilson. The Mars Pathfinder Atmospheric Structure Investigation/Meteorology (ASI/MET) Experiment. *Science*, 278(5344):1752–1758, 1997. doi: 10.1126/science.278.5344.1752.

C. L. Smith, B. A. Cooper, and J. E. Moores. Possible ground fog detection from SLI imagery of Titan. *Icarus*, 271:269–278, 2016. ISSN 0019-1035. doi: 10.1016/j.icarus.2016.02.002.

M. G. Soskind, N. P. Li, D. P. Moore, Y. Chen, L. P. Wendt, J. McSpiritt, M. A. Zondlo, and G. Wysocki. Stationary and drone-assisted methane plume localization with dispersion spectroscopy. *Remote Sensing of Environment*, 289:113513, 2023. ISSN 0034-4257. doi: 10.1016/j.rse.2023.113513.

A. Souchon, P. Pinet, S. Chevrel, Y. Daydou, D. Baratoux, K. Kurita, M. Shepard, and P. Helfenstein. An experimental study of Hapke's modeling of natural granular surface samples. *Icarus*, 215(1):313–331, 2011. ISSN 00191035. doi: 10.1016/j.icarus.2011.06.023.

A. Spiga. The Planetary Boundary Layer of Mars. In *Oxford Research Encyclopedia of Planetary Science*, page 130. 2019. ISBN 978-0-19-064792-6. doi: 10.1093/acrefore/9780190647926.013.130.

A. Stcherbinine, M. Vincendon, F. Montmessin, M. J. Wolff, O. Korablev, A. Fedorova, A. Trokhimovskiy, A. Patrakeev, G. Lacombe, L. Baggio, and A. Shakun. Martian Water Ice Clouds During the 2018 Global Dust Storm as Observed by the ACS-MIR Channel Onboard the Trace Gas Orbiter. *Journal of Geophysical Research: Planets*, 125(3), 2020. ISSN 2169-9097, 2169-9100. doi: 10.1029/2019JE006300.

J. M. Stockie. The Mathematics of Atmospheric Dispersion Modeling. *SIAM Review*, 53(2):349–372, 2011. ISSN 0036-1445, 1095-7200. doi: 10.1137/10080991X.

L. K. Tamppari, R. W. Zurek, and D. A. Paige. Viking-era diurnal water-ice clouds. *Journal of Geophysical Research: Planets*, 108(E7), 2003. ISSN 2156-2202. doi: 10.1029/2002JE001911.

N. Thomas, G. Cremonese, R. Ziethe, M. Gerber, M. Brändli, G. Bruno, M. Erismann, L. Gambicorti, T. Gerber, K. Ghose, M. Gruber, P. Gubler, H. Mischler, J. Jost, D. Piazza, A. Pommerol, M. Rieder, V. Roloff, A. Servonet, W. Trottmann, T. Uthaicharoenpong, C. Zimmermann, D. Vernani, M. Johnson, E. Pelò, T. Weigel, J. Viertl, N. De Roux, P. Lochmatter, G. Sutter, A. Casciello, T. Hausner, I. Ficai Veltroni, V. Da Deppo, P. Orleanski, W. Nowosielski, T. Zawistowski, S. Szalai, B. Sodor, S. Tulyakov, G. Troznai, M. Banaskiewicz, J. C. Bridges, S. Byrne, S. Debei, M. R. El-Maarry, E. Hauber, C. J. Hansen, A. Ivanov, L. Keszthelyi, R. Kirk, R. Kuzmin, N. Mangold, L. Marinangeli, W. J. Markiewicz, M. Massironi, A. S. McEwen, C. Okubo, L. L. Tornabene, P. Wajer, and J. J. Wray. The Colour and Stereo Surface Imaging System (CaSSIS) for the ExoMars Trace Gas Orbiter. *Space Science Reviews*, 212(3):1897–1944, 2017. ISSN 1572-9672. doi: 10.1007/s11214-017-0421-1.

J. Thøgersen, E. N. Bak, K. Finster, P. Nørnberg, H. J. Jakobsen, and S. J. Knak Jensen. Light on windy nights on Mars: A study of saltation-mediated ionization of argon in a Mars-like atmosphere. *Icarus*, 332: 14–18, 2019. ISSN 0019-1035. doi: 10.1016/j.icarus.2019.06.025.

J. E. Tillman, N. C. Johnson, P. Guttorp, and D. B. Percival. The Martian annual atmospheric pressure cycle: Years without great dust storms. *Journal of Geophysical Research: Planets*, 98(E6):10963–10971, 1993. ISSN 2156-2202. doi: 10.1029/93JE01084.

D. Tirsch, J. Hernández-Bernal, A. S. Lavega, P. Machado, F. Brasil, A. Nair, and M. D. S. Encarnacao. Cloud Morphologies on Mars: A Closer Look through the HRSC Cloud Atlas. Technical Report EPSC-DPS2025-295, Copernicus Meetings, July 2025.

M. Tomasko, D. Buchhauser, M. Bushroe, L. Dafoe, L. Doose, A. Eibl, C. Fellows, E. M. Farlane, G. Prout, M. Pringle, B. Rizk, C. See, P. Smith, and K. Tsetsenekos. The Descent Imager/Spectral Radiometer (DISR) Experiment on the Huygens Entry Probe of Titan. *Space Science Reviews*, 104(1):469–551, 2002. ISSN 1572-9672. doi: 10.1023/A:1023632422098.

L. L. Tornabene, F. P. Seelos, A. Pommerol, N. Thomas, C. M. Caudill, P. Becerra, J. C. Bridges, S. Byrne, M. Cardinale, M. Chojnacki, S. J. Conway, G. Cremonese, C. M. Dundas, M. R. El-Maarry, J. Fernando, C. J. Hansen, K. Hansen, T. N. Harrison, R. Henson, L. Marinangeli, A. S. McEwen, M. Pajola, S. S. Sutton, and J. J. Wray. Image Simulation and Assessment of the Colour and Spatial Capabilities of the Colour and Stereo Surface Imaging System (CaSSIS) on the ExoMars Trace Gas Orbiter. *Space Science Reviews*, 214(1):18, 2017. ISSN 1572-9672. doi: 10.1007/s11214-017-0436-7.

A. Trokhimovskiy, A. Fedorova, O. Korablev, F. Montmessin, J.-L. Bertaux, A. Rodin, and M. D. Smith. Mars' water vapor mapping by the SPICAM IR spectrometer: Five martian years of observations. *Icarus*, 251:50–64, 2015. ISSN 00191035. doi: 10.1016/j.icarus.2014.10.007.

G. E. Uhlenbeck and L. S. Ornstein. On the Theory of the Brownian Motion. *Physical Review*, 36(5):823–841, 1930. doi: 10.1103/PhysRev.36.823.

A. C. Vandaele, J.-J. Lopez-Moreno, M. R. Patel, G. Bellucci, F. Daerden, B. Ristic, S. Robert, I. R. Thomas, V. Wilquet, M. Allen, G. Alonso-Rodrigo, F. Altieri, S. Aoki, D. Bolsée, T. Clancy, E. Cloutis, C. Depiesse, R. Drummond, A. Fedorova, V. Formisano, B. Funke, F. González-Galindo, A. Geminale, J.-C. Gérard, M. Giuranna, L. Hetey, N. Ignatiev, J. Kaminski, O. Karatekin, Y. Kasaba, M. Leese, F. Lefèvre, S. R. Lewis, M. López-Puertas, M. López-Valverde, A. Mahieux, J. Mason, J. McConnell, M. Mumma, L. Neary, E. Neefs, E. Renotte, J. Rodriguez-Gomez, G. Sindoni, M. Smith, A. Stiepen, A. Trokhimovsky, J. Vander Auwera, G. Villanueva, S. Viscardy, J. Whiteway, Y. Willame, M. Wolff, and the NOMAD Team. NOMAD, an Integrated Suite of Three Spectrometers for the ExoMars Trace Gas Mission: Technical Description, Science Objectives and Expected Performance. *Space Science Reviews*, 214(5):80, 2018. ISSN 1572-9672. doi: 10.1007/s11214-018-0517-2.

Virtual Photonics Technology Initiative. *Mie Simulator GUI*. University of California, Irvine, Beckman Laser Institute, 2025.

S. Viscardy, D. C. Catling, and K. Zahnle. Questioning the Reliability of Methane Detections on Mars by the Curiosity Rover. *Journal of Geophysical Research: Planets*, 130(4):e2024JE008441, 2025. ISSN 2169-9100. doi: 10.1029/2024JE008441. URL `https://onlinelibrary.wiley.com/doi/abs/10.1029/2024JE008441`. _eprint: https://agupubs.onlinelibrary.wiley.com/doi/pdf/10.1029/2024JE008441.

M. Walters, J. E. Moores, F. Grandmont, M. Gordon, and H. Sapers. Water vapor condensation in optical instruments on Mars. *Acta Astronautica*, 218:232–239, May 2024. ISSN 0094-5765. doi: 10.1016/j.actaastro.2024.02.031.

H. Wang and A. P. Ingersoll. Martian clouds observed by Mars Global Surveyor Mars Orbiter Camera. *Journal of Geophysical Research: Planets*, 107(E10):8–1–8–16, 2002. ISSN 2156-2202. doi: 10.1029/2001JE001815.

C. R. Webster, P. R. Mahaffy, S. K. Atreya, G. J. Flesch, K. A. Farley, O. Kemppinen, N. Bridges, J. R. Johnson, M. Minitti, D. Cremers, J. F. Bell, L. Edgar, J. Farmer, A. Godber, M. Wadhwa, D. Wellington, I. McEwan, C. Newman, M. Richardson, A. Charpentier, L. Peret, P. King, J. Blank, G. Weigle, M. Schmidt, S. Li, R. Milliken, K. Robertson, V. Sun, M. Baker, C. Edwards, B. Ehlmann, K. Farley, J. Griffes, J. Grotzinger, H. Miller, M. Newcombe, C. Pilorget, M. Rice, K. Siebach, K. Stack, E. Stolper, C. Brunet, V. Hipkin, R. Léveillé, G. Marchand, P. S. Sánchez, L. Favot, G. Cody, A. Steele, L. Flückiger, D. Lees, A. Nefian, M. Martin, M. Gailhanou, F. Westall, G. Israël, C. Agard, J. Baroukh, C. Donny,

A. Gaboriaud, P. Guillemot, V. Lafaille, E. Lorigny, A. Paillet, R. S. Pérez, Muriel, C. Yana, C. Armiens-Aparicio, J. C. Rodríguez, I. C. Blázquez, F. G. Gómez, J. G. Elvira, S. Hettrich, A. L. Malvitte, M. M. Jiménez, J. Martínez-Frías, J. M. Soler, F. J. Martín-Torres, A. M. Jurado, L. Mora-Sotomayor, G. M. Caro, S. N. López, V. Peinado-González, J. Pla-García, J. A. R. Manfredi, J. J. F. Romeral-Planelló, Sara Alejandra Sans, E. S. Martinez, J. T. Redondo, R. Urqui-O'Callaghan, M.-P. Z. Mier, S. Chipera, J.-L. Lacour, P. Mauchien, J.-B. Sirven, H. Manning, A. Fairén, A. Hayes, J. Joseph, S. Squyres, R. Sullivan, P. Thomas, A. Dupont, A. Lundberg, N. Melikechi, A. Mezzacappa, J. DeMarines, D. Grinspoon, G. Reitz, B. Prats, E. Atlaskin, M. Genzer, A.-M. Harri, H. Haukka, H. Kahanpää, J. Kauhanen, O. Kemppinen, M. Paton, J. Polkko, W. Schmidt, T. Siili, C. Fabre, J. Wray, M. B. Wilhelm, F. Poitrasson, K. Patel, S. Gorevan, S. Indyk, G. Paulsen, S. Gupta, D. Bish, J. Schieber, B. Gondet, Y. Langevin, C. Geffroy, D. Baratoux, G. Berger, A. Cros, C. d'Uston, O. Forni, O. Gasnault, J. Lasue, Q.-M. Lee, S. Maurice, P.-Y. Meslin, E. Pallier, Y. Parot, P. Pinet, S. Schröder, M. Toplis, É. Lewin, W. Brunner, E. Heydari, C. Achilles, D. Oehler, B. Sutter, M. Cabane, D. Coscia, G. Israël, C. Szopa, G. Dromart, F. Robert, V. Sautter, S. Le Mouélic, N. Mangold, M. Nachon, A. Buch, F. Stalport, P. Coll, P. François, F. Raulin, S. Teinturier, J. Cameron, S. Clegg, A. Cousin, D. DeLapp, R. Dingler, R. S. Jackson, S. Johnstone, N. Lanza, C. Little, T. Nelson, R. C. Wiens, R. B. Williams, A. Jones, L. Kirkland, A. Treiman, B. Baker, B. Cantor, M. Caplinger, S. Davis, B. Duston, K. Edgett, D. Fay, C. Hardgrove, D. Harker, P. Herrera, E. Jensen, M. R. Kennedy, G. Krezoski, and D. Krysak. Low Upper Limit to Methane Abundance on Mars. *Science*, 342(6156):355–357, 2013. doi: 10.1126/science.1242902.

C. R. Webster, P. R. Mahaffy, S. K. Atreya, G. J. Flesch, M. A. Mischna, P.-Y. Meslin, K. A. Farley, P. G. Conrad, L. E. Christensen, A. A. Pavlov, J. Martín-Torres, M.-P. Zorzano, T. H. McConnochie, T. Owen, J. L. Eigenbrode, D. P. Glavin, A. Steele, C. A. Malespin, P. D. Archer, B. Sutter, P. Coll, C. Freissinet, C. P. McKay, J. E. Moores, S. P. Schwenzer, J. C. Bridges, R. Navarro-Gonzalez, R. Gellert, M. T. Lemmon, and t. M. S. Team. Mars methane detection and variability at Gale crater. *Science*, 347(6220):415–417, 2015. ISSN 0036-8075, 1095-9203. doi: 10.1126/science.1261713.

C. R. Webster, P. R. Mahaffy, S. K. Atreya, J. E. Moores, G. J. Flesch, C. Malespin, C. P. McKay, G. Martinez, C. L. Smith, J. Martin-Torres, J. Gomez-Elvira, M.-P. Zorzano, M. H. Wong, M. G. Trainer, A. Steele, D. Archer, B. Sutter, P. J. Coll, C. Freissinet, P.-Y. Meslin, R. V. Gough, C. H. House, A. Pavlov, J. L. Eigenbrode, D. P. Glavin, J. C. Pearson, D. Keymeulen, L. E. Christensen, S. P. Schwenzer, R. Navarro-Gonzalez, J. Pla-García, S. C. R. Rafkin, Á. Vicente-Retortillo, H. Kahanpää, D. Viudez-Moreiras, M. D. Smith, A.-M. Harri, M. Genzer, D. M. Hassler, M. Lemmon, J. Crisp, S. P. Sander, R. W. Zurek, and A. R. Vasavada. Background levels of methane in Mars' atmosphere show strong seasonal variations. *Science*, 360(6393):1093–1096, 2018. ISSN 0036-8075, 1095-9203. doi: 10.1126/science.aaq0131.

C. R. Webster, P. R. Mahaffy, S. K. Atreya, G. J. Flesch, C. A. Malespin, and A. R. Vasavada. Curiosity Mars methane measurements are not confused by ozone. *Astronomy & Astrophysics*, 641:L3, Sept. 2020. ISSN 0004-6361, 1432-0746. doi: 10.1051/0004-6361/202038815. URL `https://www.aanda.org/articles/aa/abs/2020/09/aa38815-20/aa38815-20.html`.

C. R. Webster, P. R. Mahaffy, J. Pla-Garcia, S. C. R. Rafkin, J. E. Moores, S. K. Atreya, G. J. Flesch, C. A. Malespin, S. M. Teinturier, H. Kalucha, C. L. Smith, D. Viúdez-Moreiras, and A. R. Vasavada. Day-night differences in Mars methane suggest nighttime containment at Gale crater. *Astronomy & Astrophysics*, 650:A166, 2021. ISSN 0004-6361, 1432-0746. doi: 10.1051/0004-6361/202040030.

J. Whiteway, M. Daly, A. Carswell, T. Duck, C. Dickinson, L. Komguem, and C. Cook. Lidar on the Phoenix mission to Mars. *Journal of Geophysical Research: Planets*, 113(E3), 2008. ISSN 2156-2202. doi: 10.1029/2007JE003002.

J. A. Whiteway, L. Komguem, C. Dickinson, C. Cook, M. Illnicki, J. Seabrook, V. Popovici, T. J. Duck, R. Davy, P. A. Taylor, J. Pathak, D. Fisher, A. I. Carswell, M. Daly, V. Hipkin, A. P. Zent, M. H. Hecht, S. E. Wood, L. K. Tamppari, N. Renno, J. E. Moores, M. T. Lemmon, F. Daerden, and P. H. Smith. Mars Water-Ice Clouds and Precipitation. *Science*, 325(5936):68–70, 2009. ISSN 0036-8075, 1095-9203. doi: 10.1126/science.1172344.

R. J. Wilson and S. D. Guzewich. Influence of water ice clouds on nighttime tropical temperature structure as seen by the Mars Climate Sounder. *Geophysical Research Letters*, 41(10):3375–3381, 2014. ISSN 1944-8007. doi: 10.1002/2014GL060086.

M. J. Wolff, J. F. Bell, P. B. James, R. T. Clancy, and S. W. Lee. Hubble Space Telescope observations of the Martian aphelion cloud belt prior to the Pathfinder mission: Seasonal and interannual variations. *Journal of Geophysical Research: Planets*, 104(E4):9027–9041, 1999. ISSN 0148-0227. doi: 10.1029/98je01967.

M. J. Wolff, R. T. Clancy, M. A. Kahre, R. M. Haberle, F. Forget, B. A. Cantor, and M. C. Malin. Mapping water ice clouds on Mars with MRO/MARCI. *Icarus*, 332:24–49, 2019. ISSN 00191035. doi: 10.1016/j.icarus.2019.05.041.

M. J. Wolff, A. Fernando, M. D. Smith, F. Forget, E. Millour, S. A. Atwood, A. R. Jones, M. M. Osterloo, R. Shuping, M. Al Shamsi, C. Jeppesen, and C. Fisher. Diurnal Variations in the Aphelion Cloud Belt as Observed by the Emirates Exploration Imager (EXI). *Geophysical Research Letters*, 49(18):e2022GL100477, 2022. ISSN 1944-8007. doi: 10.1029/2022GL100477.

P. Wolkenberg, M. Giuranna, M., D. Grassi, and M. Amoroso. Similarities and Differences of Global Dust Storms in MY 25, 28, and 34. *Journal of Geophysical Research: Planets*, 125(3):e2019JE006104, 2020. ISSN 2169-9097. doi: 10.1029/2019je006104.

P. Yang and K. N. Liou. Geometric-optics–integral-equation method for light scattering by nonspherical ice crystals. *Applied Optics*, 35(33):6568, 1996. ISSN 0003-6935, 1539-4522. doi: 10.1364/AO.35.006568.

P. Yang, L. Bi, B. A. Baum, K.-N. Liou, G. W. Kattawar, M. I. Mishchenko, and B. Cole. Spectrally Consistent Scattering, Absorption, and Polarization Properties of Atmospheric Ice Crystals at Wavelengths from 0.2 to 100 m. *Journal of the Atmospheric Sciences*, 70(1):330–347, 2013. ISSN 0022-4928, 1520-0469. doi: 10.1175/JAS-D-12-039.1.

X. Zhang, D. Berkinsky, C. R. Markus, S. R. Chitturi, F. J. Grieman, M. Okumura, Y. Luo, Y. L. Yung, and S. P. Sander. Reaction of methane and UV-activated perchlorate: Relevance to heterogeneous loss of methane in the atmosphere of Mars. *Icarus*, 376:114832, 2022. ISSN 0019-1035. doi: 10.1016/j.icarus.2021.114832.

List of Acronyms and Abbreviations

ACB Aphelion Cloud Belt

ACS Atmospheric Chemistry Suite

CaSSIS Colour and Stereo Surface Imaging System

CW Continuous Wave

FOV Field of View

FWHM Full Width Half Maximum

GDS Global Dust Storm

HG Henyey-Greenstein

HRSC High Resolution Stereo Camera

LMST Local Mean Solar Time

L_s Solar Longitude

LST Local Solar Time

LTST Local True Solar Time

LWC Liquid Water Content

MAPLE Mars Atmospheric Panoramic camera and Laser Experiment

Mastcam Mast Camera

MARCI Mars Colour Imager

MARS McGill Arctic Research Station

MCS Mars Climate Sounder

MFS Mean Frame Subtraction

MGS Mars Global Surveyor

MRO Mars Reconnaissance Orbiter

MSL Mars Science Laboratory

MY Mars year

Navcam Navigation Camera

NOMAD Nadir and Occultation for MArs Discovery

OA-ICOS Off-Axis Integrated Cavity Optical Spectrometer

PBL Planetary Boundary Layer

PFS Planetary Fourier Spectrometer

PFSS Phase Function Sky Survey

ppbv Parts per billion by volume

ppmv Parts per million by volume

PSD Power Spectral Density

RSM Remote Sensing Mast

SAM-TLS Sample Analysis at Mars Tunable Laser Spectrometer

SCET Spacecraft Event Time

TGO Trace Gas Orbiter

WIC Water-Ice Cloud

Appendix A

CaSSIS Images Aquired over Gale Crater

Table A1: *CaSSIS images acquired over Gale Crater.*

Image ID	L_s (°)	Imaging Time (SCET)	LST	Incidence Angle (°)	Phase Angle (°)	Filters Used
MY34_002158_354_2	177.839	2018-05-18T18:22:44.635	16:56:52	74.378	76.3317	PAN-NIR-BLU
MY34_002444_354_1	191.201	2018-06-11T04:06:04.582	11:35:44	6.04315	16.4022	PAN-RED-NIR
MY34_002444_354_2	191.201	2018-06-11T04:06:51.728	11:36:25	5.87696	9.7428	PAN-RED-BLU
MY34_004092_186_1	274.827	2018-10-24T00:01:52.280	15:58:04	60.3075	62.9212	PAN-NIR-BLU
MY34_004092_186_2	274.827	2018-10-24T00:02:38.557	15:58:48	60.517	56.5784	PAN-RED-BLU
MY34_004179_186_1	279.269	2018-10-31T02:54:29.546	14:14:16	37.9425	45.1952	PAN-NIR-BLU
MY34_004179_186_2	279.269	2018-10-31T02:55:15.825	14:14:59	38.1472	35.4761	PAN-RED-BLU
MY34_004769_354_1	308.52	2018-12-18T10:39:11.201	14:35:14	40.2144	33.7472	PAN-RED-NIR-BLU
MY34_004769_354_2	308.52	2018-12-18T10:39:55.613	14:35:48	40.3068	45.7775	PAN-BLU
MY34_005055_355_1	321.979	2019-01-10T20:23:34.202	9:10:28	42.9763	43.7778	PAN-RED-NIR-BLU
MY35_007380_357_0	55.0203	2019-07-20T03:23:12.889	14:45:47	47.898	50.4631	PAN-RED-NIR-BLU
MY35_007467_357_0	58.1497	2019-07-27T06:21:12.054	13:15:01	31.6811	32.4868	PAN-RED-NIR-BLU
MY35_008785_354_0	105.681	2019-11-12T04:22:11.551	14:13:50	44.1697	48.0421	PAN-NIR-BLU
MY35_009687_188_0	140.538	2020-01-24T23:59:57.938	10:36:02	30.3121	28.6562	PAN-NIR-BLU
MY35_010364_354_0	169.394	2020-03-20T11:18:05.931	10:29:10	24.8802	24.0248	PAN-RED-NIR-BLU
MY35_011856_357_0	242.365	2020-07-20T15:15:47.631	7:37:59	65.3999	68.8699	PAN-NIR-BLU
MY35_012099_186_0	254.965	2020-08-09T11:52:15.407	15:16:10	50.7964	52.5807	PAN-NIR-BLU
MY35_012472_186_0	274.245	2020-09-09T00:50:51.559	8:15:13	57.5306	60.1047	PAN-NIR-BLU
MY35_012559_187_0	278.692	2020-09-16T03:48:59.147	6:39:17	78.7916	82.254	PAN-NIR-BLU
MY35_014094_354_0	350.578	2021-01-19T21:11:30.723	14:50:27	42.5026	43.8631	PAN-RED-NIR-BLU
MY36_014467_352_0	5.91632	2021-02-19T10:11:19.910	8:24:11	54.4565	57.1561	PAN-RED-NIR-BLU
MY36_015083_185_0	29.7874	2021-04-10T19:46:30.666	9:52:14	36.1249	28.8916	PAN-RED-NIR-BLU
MY36_018708_356_0	167.346	2022-02-01T16:15:45.161	8:42:07	50.4359	41.4058	PAN-NIR-BLU
MY36_019666_354_1	212.688	2022-04-21T02:50:17.286	16:51:53	72.4388	71.522	PAN-NIR-BLU
MY36_019666_354_2	212.688	2022-04-21T02:51:03.677	16:52:33	72.5801	79.9781	PAN-NIR-BLU
MY36_019977_356_3	228.463	2022-05-16T14:00:00.927	11:36:06	14.9996	21.8322	PAN-RED-NIR-BLU
MY36_020089_355_3	234.226	2022-05-25T18:05:10.750	9:41:07	36.5364	40.1586	PAN-RED-NIR-BLU
MY36_020201_355_3	240.017	2022-06-03T22:10:59.813	7:46:12	63.435	65.7404	PAN-RED-NIR-BLU
MY36_020780_185_0	270.021	2022-07-21T07:03:01.583	9:47:19	37.7561	43.787	PAN-RED-NIR-BLU
MY36_021047_353_0	283.686	2022-08-12T04:39:25.561	17:00:32	74.3394	69.6183	PAN-RED-NIR-BLU
MY36_021358_356_0	299.197	2022-09-06T15:49:26.378	11:41:45	17.5809	25.3086	PAN-RED-NIR-BLU
MY36_021582_354_3	310.048	2022-09-25T00:00:24.501	7:53:28	61.549	63.2294	PAN-RED-NIR-BLU
MY37_022851_355_0	5.67972	2023-01-06T21:44:09.972	11:04:37	16.1162	13.3446	PAN-RED-NIR-BLU
MY37_023542_187_0	32.3758	2023-03-04T10:42:56.109	12:10:03	18.9821	3.19233	PAN-RED-NIR-BLU
MY37_023654_185_0	36.543	2023-03-13T14:48:15.694	10:20:25	31.4498	23.6245	PAN-RED-NIR-BLU
MY37_024120_353_0	53.5741	2023-04-20T19:28:01.435	14:40:28	46.7484	57.4848	PAN-RED-NIR-BLU
MY37_024431_355_3	64.7415	2023-05-16T06:37:49.709	9:39:26	44.4107	35.1228	PAN-RED-NIR-BLU

Image ID	L_s (°)	Imaging Time (SCET)	LST	Incidence Angle (°)	Phase Angle (°)	Filters Used
MY37_024923_187_3	82.3247	2023-06-25T12:33:07.428	13:50:41	40.28	49.7819	PAN-NIR-BLU
MY37_025035_185_0	86.349	2023-07-04T16:37:52.892	12:01:55	30.0475	15.8884	PAN-RED-NIR-BLU
MY37_025501_352_0	103.321	2023-08-11T21:17:38.005	16:14:46	68.8253	75.162	PAN-RED-NIR-BLU
MY37_025613_353_0	107.469	2023-08-21T01:23:28.309	14:28:04	46.1696	51.2972	PAN-RED-NIR-BLU
MY37_025812_353_0	114.929	2023-09-06T08:26:38.915	11:08:25	30.8924	44.7203	PAN-RED-NIR-BLU
MY37_026036_353_1	123.492	2023-09-24T16:37:56.546	7:33:05	70.3662	81.4203	PAN-RED-NIR-BLU
MY37_026036_353_2	123.492	2023-09-24T16:38:42.634	7:33:53	70.2321	68.8266	PAN-RED-NIR-BLU
MY37_026416_186_3	138.485	2023-10-25T18:28:39.209	13:30:34	31.0978	38.476	PAN-RED-NIR-BLU
MY37_027081_352_0	166.608	2023-12-19T06:10:43.174	14:25:54	38.1545	47.0821	PAN-RED-NIR-BLU
MY37_027193_353_0	171.604	2023-12-28T10:16:39.857	12:36:48	12.3772	25.8541	PAN-RED-NIR-BLU
MY37_027417_352_1	181.836	2024-01-15T18:27:23.721	8:59:12	45.4042	53.9537	PAN-RED-NIR-BLU
MY37_027417_352_2	181.836	2024-01-15T18:28:09.719	9:00:00	45.2134	47.9765	PAN-RED-NIR-BLU
MY37_027504_356_0	185.896	2024-01-22T21:26:26.902	7:29:16	67.5588	56.7761	PAN-RED-NIR-BLU
MY37_027685_188_0	194.471	2024-02-06T16:12:45.296	16:45:07	70.8565	70.7886	PAN-RED-NIR-BLU
MY37_027797_187_0	199.889	2024-02-15T20:18:04.609	14:55:45	43.8405	35.3098	PAN-RED-NIR-BLU
MY37_027909_189_0	205.379	2024-02-25T00:24:08.988	13:04:05	16.5428	10.6272	PAN-RED-NIR-BLU
MY37_027996_186_0	209.689	2024-03-03T03:20:49.201	11:27:02	10.8992	23.8418	PAN-RED-NIR-BLU
MY37_028108_186_0	215.293	2024-03-12T07:26:16.664	9:36:22	36.5993	41.9389	PAN-RED-NIR-BLU
MY37_028462_352_0	233.364	2024-04-10T08:00:28.480	15:25:27	51.8787	47.325	PAN-RED-NIR-BLU
MY37_028574_353_1	239.151	2024-04-19T12:06:20.510	13:30:11	27.6903	22.4132	PAN-RED-NIR-BLU
MY37_028574_353_2	239.151	2024-04-19T12:07:06.580	13:30:50	27.7396	37.1391	PAN-RED-NIR-BLU
MY37_028686_356_0	244.958	2024-04-28T16:12:24.911	11:34:26	18.6728	24.819	PAN-RED-NIR-BLU
MY37_028798_355_0	250.777	2024-05-07T20:18:19.196	9:43:36	37.6579	50.677	PAN-RED-NIR-BLU
MY37_028885_356_0	255.297	2024-05-14T23:16:21.598	8:05:43	59.5176	56.1992	PAN-RED-NIR-BLU
MY37_029265_185_1	274.905	2024-06-15T01:05:04.947	13:37:36	30.4415	44.8154	PAN-RED-NIR-BLU
MY37_029265_185_2	274.905	2024-06-15T01:05:51.064	13:38:19	30.6581	33.7026	PAN-RED-NIR-BLU
MY37_029377_186_0	280.62	2024-06-24T05:10:58.319	11:39:55	21.0881	14.5456	PAN-NIR-BLU
MY37_029489_185_0	286.287	2024-07-03T09:16:23.566	9:43:44	37.9175	43.0328	PAN-NIR-BLU
MY37_030154_355_3	318.635	2024-08-26T21:00:09.373	10:14:57	27.928	25.5388	PAN-RED-NIR-BLU
MY37_030758_189_0	345.63	2024-10-15T07:01:07.949	12:34:06	8.50774	9.54042	PAN-RED-NIR-BLU
MY37_030870_187_0	350.391	2024-10-24T11:06:21.773	10:43:03	19.2563	25.4795	PAN-RED-NIR-BLU
MY37_031069_185_0	358.674	2024-11-09T18:09:33.149	7:25:47	68.5854	63.5085	PAN-RED-NIR-BLU
MY38_031224_353_0	4.99464	2024-11-22T11:40:05.890	16:45:44	71.7282	77.5817	PAN-RED-NIR-BLU
MY38_031336_353_0	9.47261	2024-12-01T15:45:44.618	15:01:11	46.1663	46.9191	PAN-RED-NIR-BLU
MY38_031647_354_1	21.6068	2024-12-27T02:54:35.706	9:58:32	33.5039	38.9724	PAN-RED-NIR-BLU
MY38_031647_354_2	21.6071	2024-12-27T02:55:22.084	9:59:12	33.3982	23.1383	PAN-RED-NIR-BLU
MY38_031871_356_0	30.109	2025-01-14T11:06:47.149	6:30:21	83.5328	86.9851	PAN-RED-NIR-BLU
MY38_033831_184_0	101.1	2025-06-23T21:48:50.685	10:49:34	33.6	20.9	PAN-RED-NIR-BLU
MY38_034055_185_0	109.4	2025-07-12T06:00:17.051	7:16:07	74.7	78.1	PAN-RED-NIR-BLU
MY38_034297_353_0	118.5	2025-08-01T02:28:45.245	15:04:01	52.7	60.8	PAN-RED-NIR-BLU
MY38_034409_354_0	122.8	2025-08-10T06:34:38.555	13:16:07	31.8	39.4	PAN-RED-NIR-BLU
MY38_034521_354_1	127.2	2025-08-19T10:40:12.782	11:29:36	25.7	37.9	PAN-NIR-BLU
MY38_034521_354_2	127.2	2025-08-19T10:40:58.901	11:30:20	25.7	17	PAN-RED-BLU
MY38_034901_190_0	142.3	2025-09-19T12:30:54.292	17:27:58	83.9	87	PAN-RED-NIR-BLU
MY38_035125_187_0	151.6	2025-10-07T20:41:43.957	13:52:48	32.6	32.2	PAN-RED-NIR-BLU

Appendix B

Analysis of CaSSIS ACB Cloud Images

Figure B1 compares the coefficients of variation in the BLU channel to the optical depths. As discussed in Section 3.4.1, we see little good agreement between higher optical depths and higher coefficients of variation.

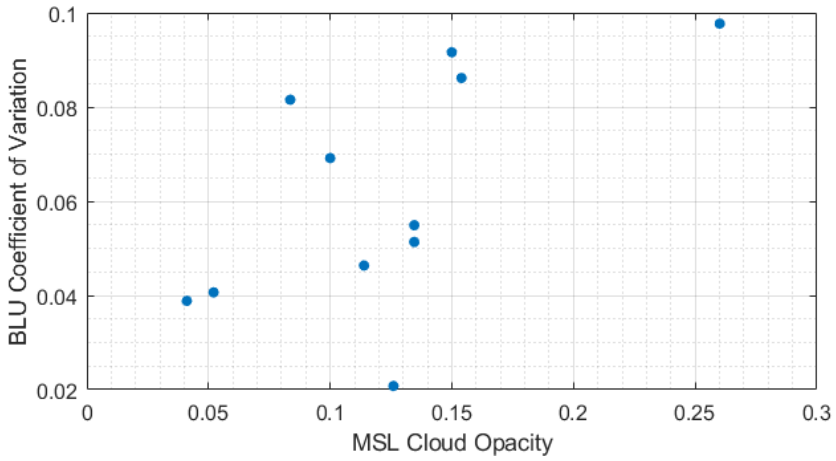


Figure B1: Coefficients of variation in the BLU channel versus MSL-derived cloud optical depths.

Section 3.4.1 shows the NPB image for MY38_035125_187_0 as well as the BLU and NIR channels alone and the ratio of the BLU to NIR. Additionally, we show the mean I/F and standard deviation across the whole image for each channel. This section shows the same figures for each of the remaining ten ACB cloud images listed in Table 3.3. We are unable to see evidence of clouds in any of the images. Note that scales differ between figures.

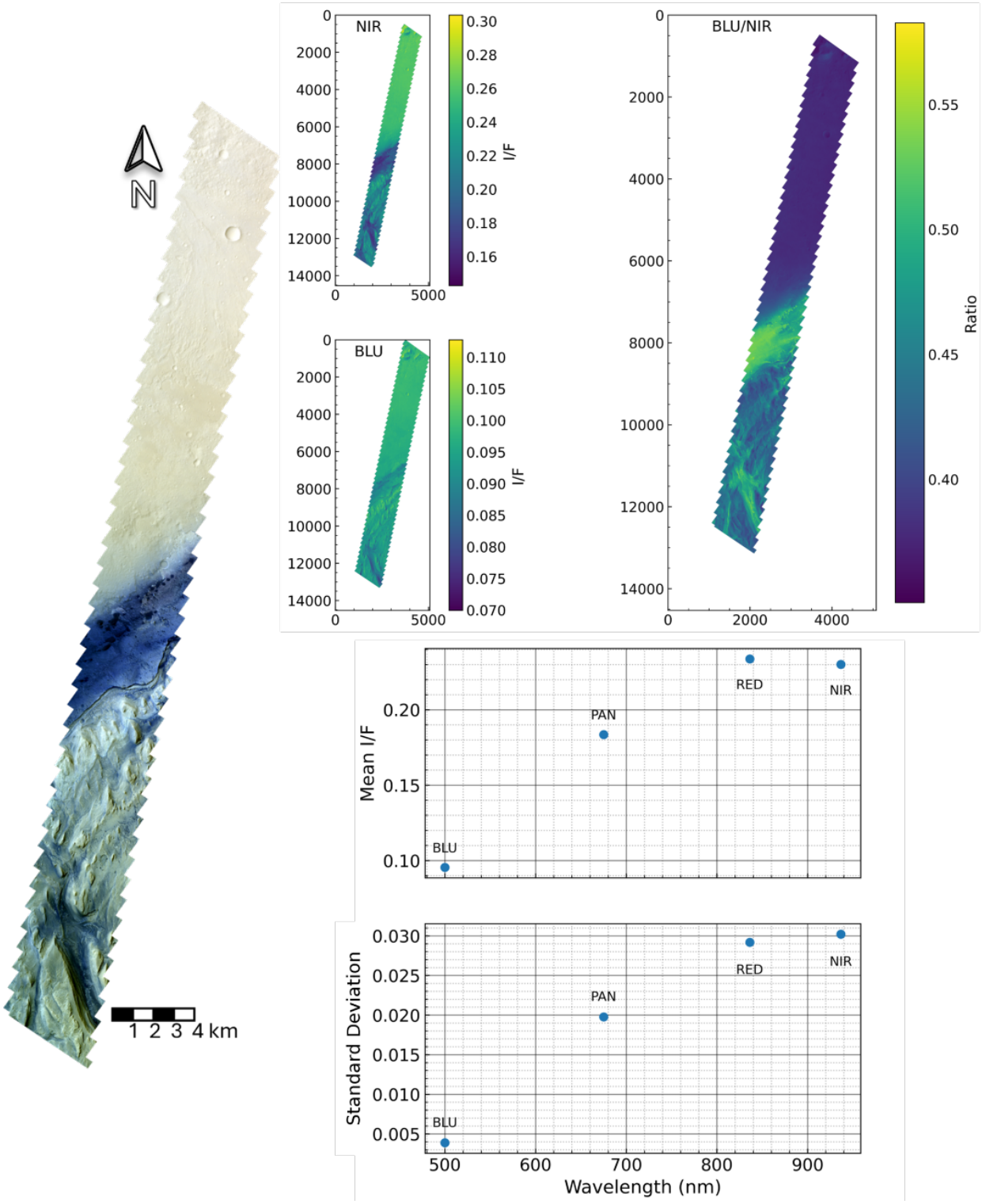


Figure B2: Left: the NPB image of MY35_007380_357_0. Upper right: the I/F across the NIR and BLU channels and the ratio of the BLU to NIR channel. Lower right: Mean I/F and standard deviation for each channel over the whole image.

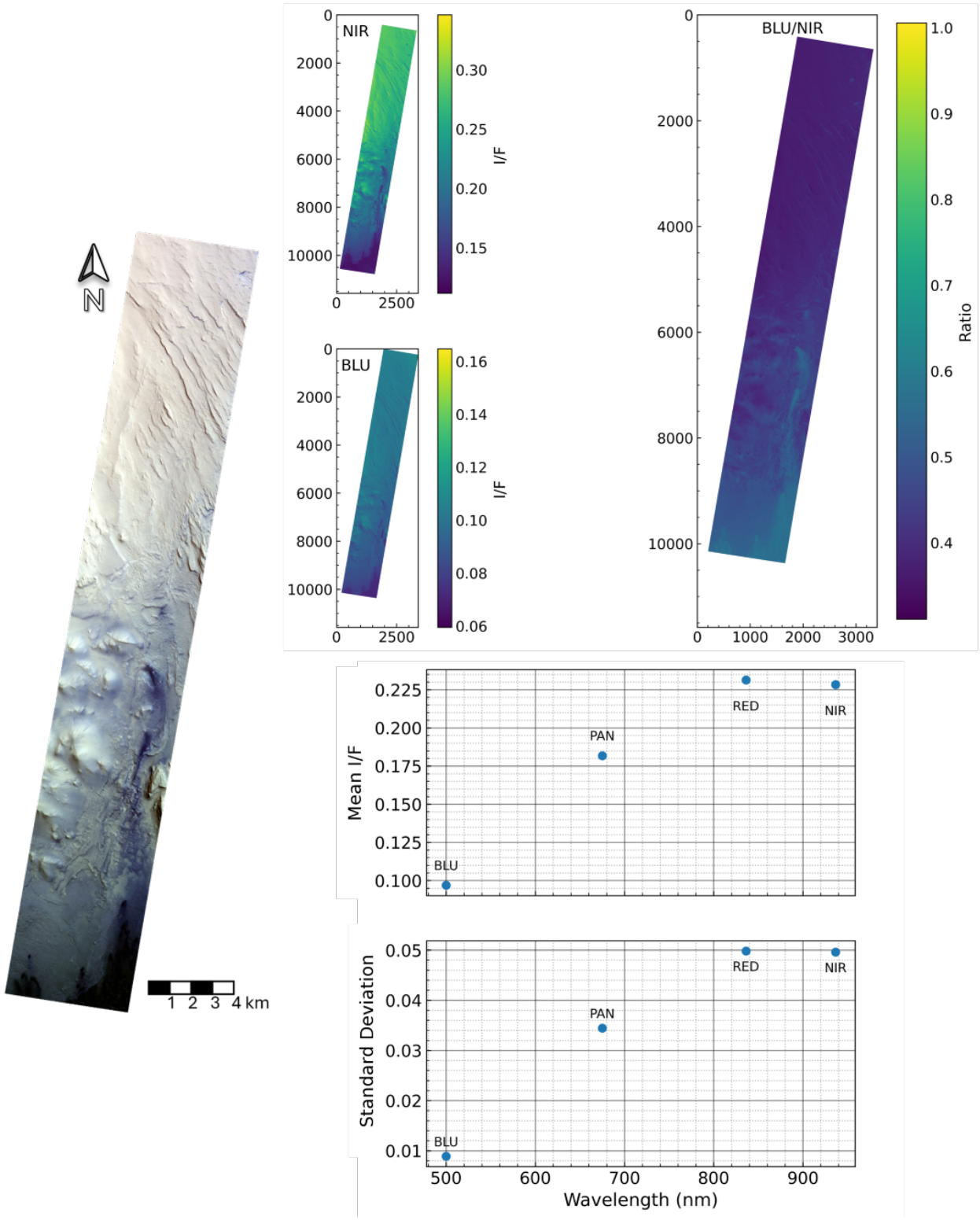


Figure B3: Left: the NPB image of MY37_024431_355_3. Upper right: the I/F across the NIR and BLU channels and the ratio of the BLU to NIR channel. Lower right: Mean I/F and standard deviation for each channel over the whole image.

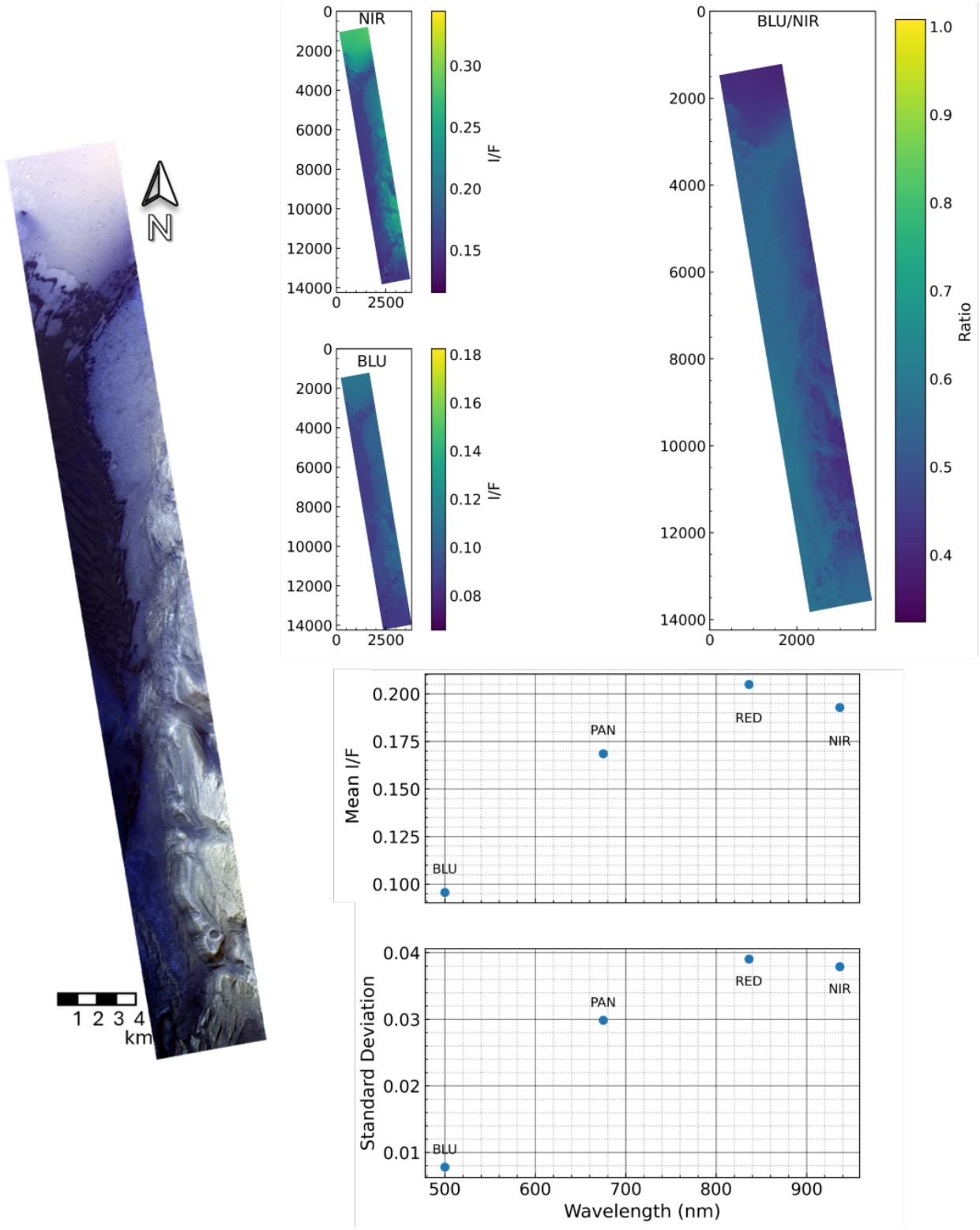


Figure B4: Left: the NPB image of MY37_026416_186_3. Upper right: the I/F across the NIR and BLU channels and the ratio of the BLU to NIR channel. Lower right: Mean I/F and standard deviation for each channel over the whole image.

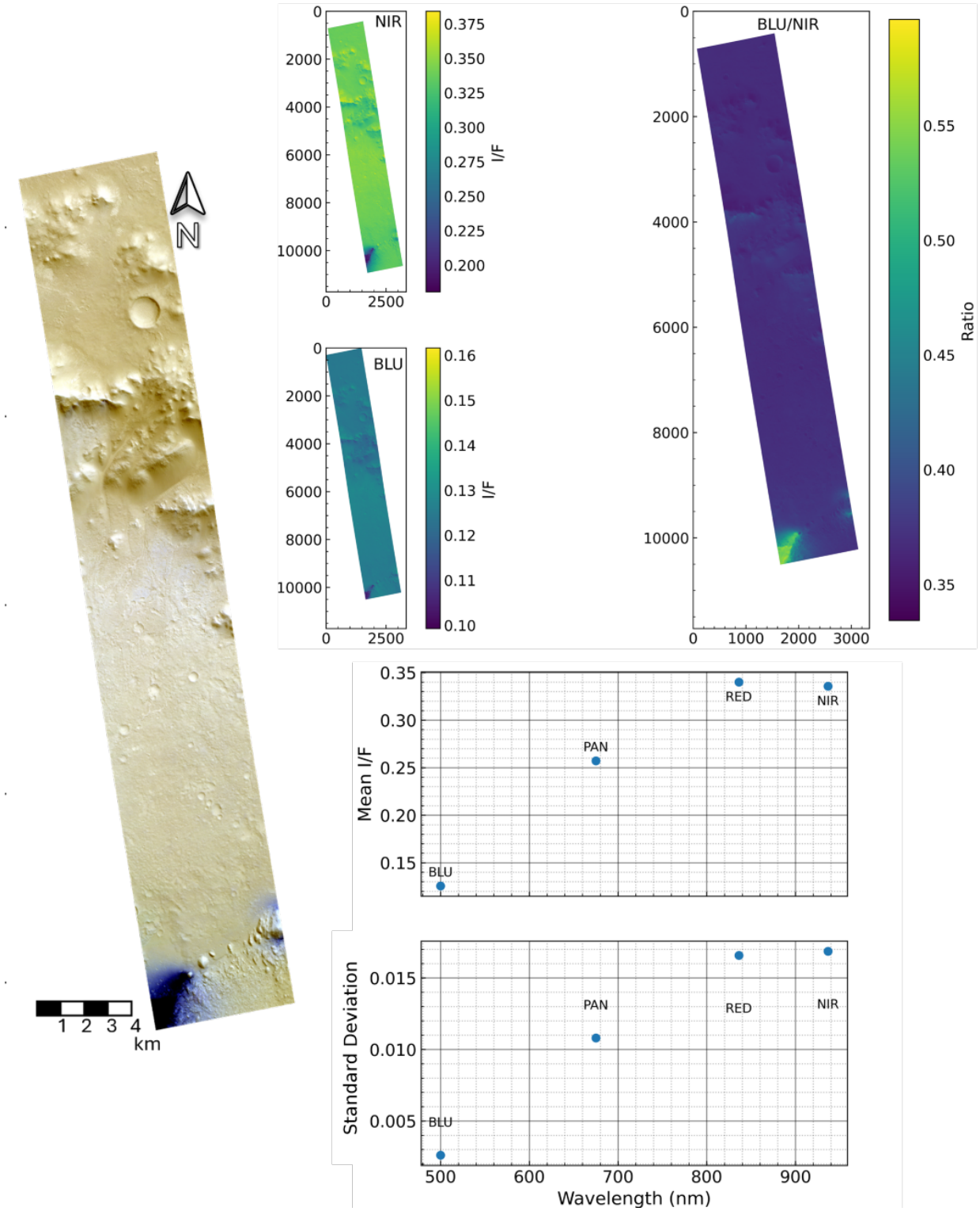


Figure B5: Left: the NPB image of MY38_033831_184_0. Upper right: the I/F across the NIR and BLU channels and the ratio of the BLU to NIR channel. Lower right: Mean I/F and standard deviation for each channel over the whole image.

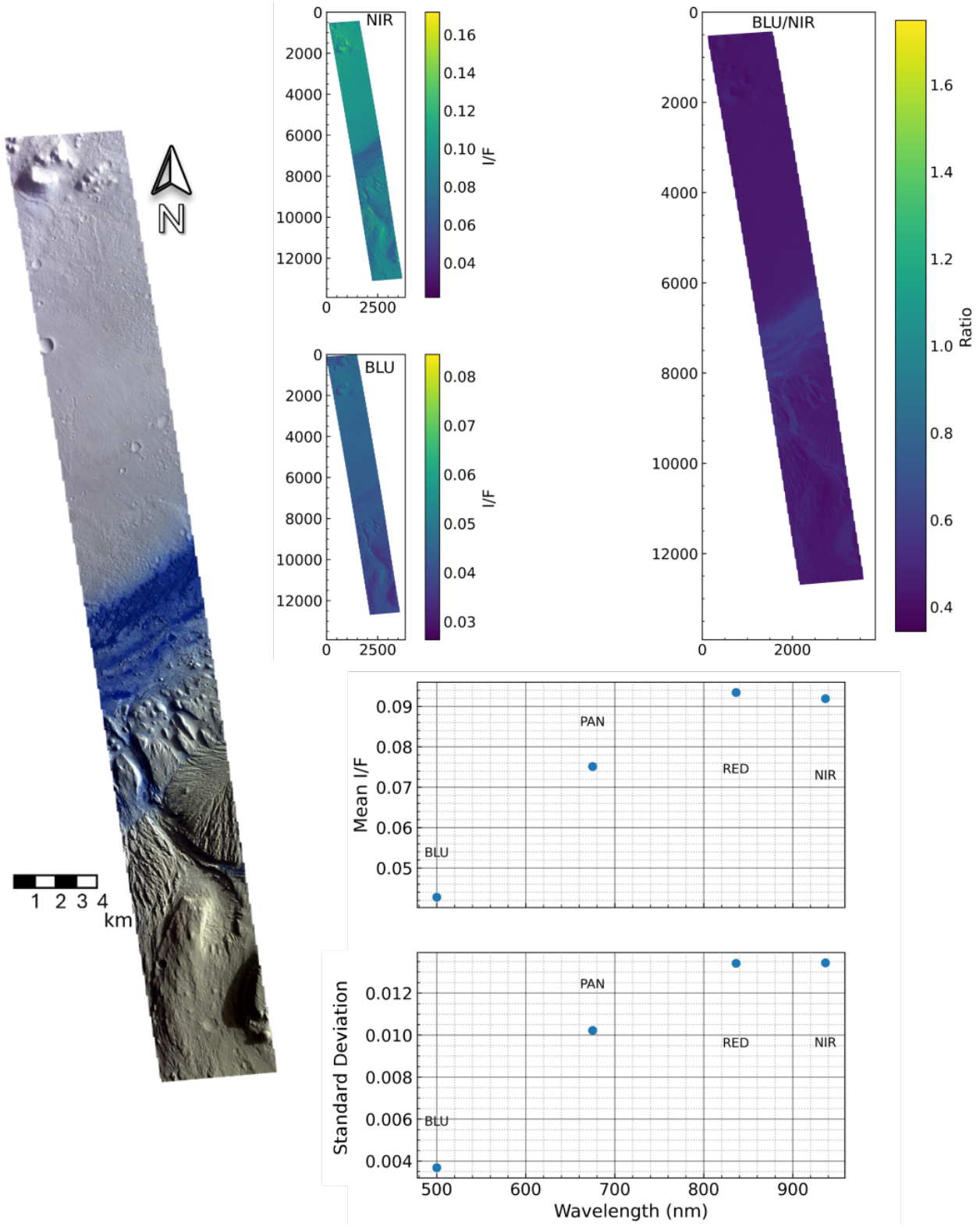


Figure B6: Left: the NPB image of MY38_034055_185_0. Upper right: the I/F across the NIR and BLU channels and the ratio of the BLU to NIR channel. Lower right: Mean I/F and standard deviation for each channel over the whole image.

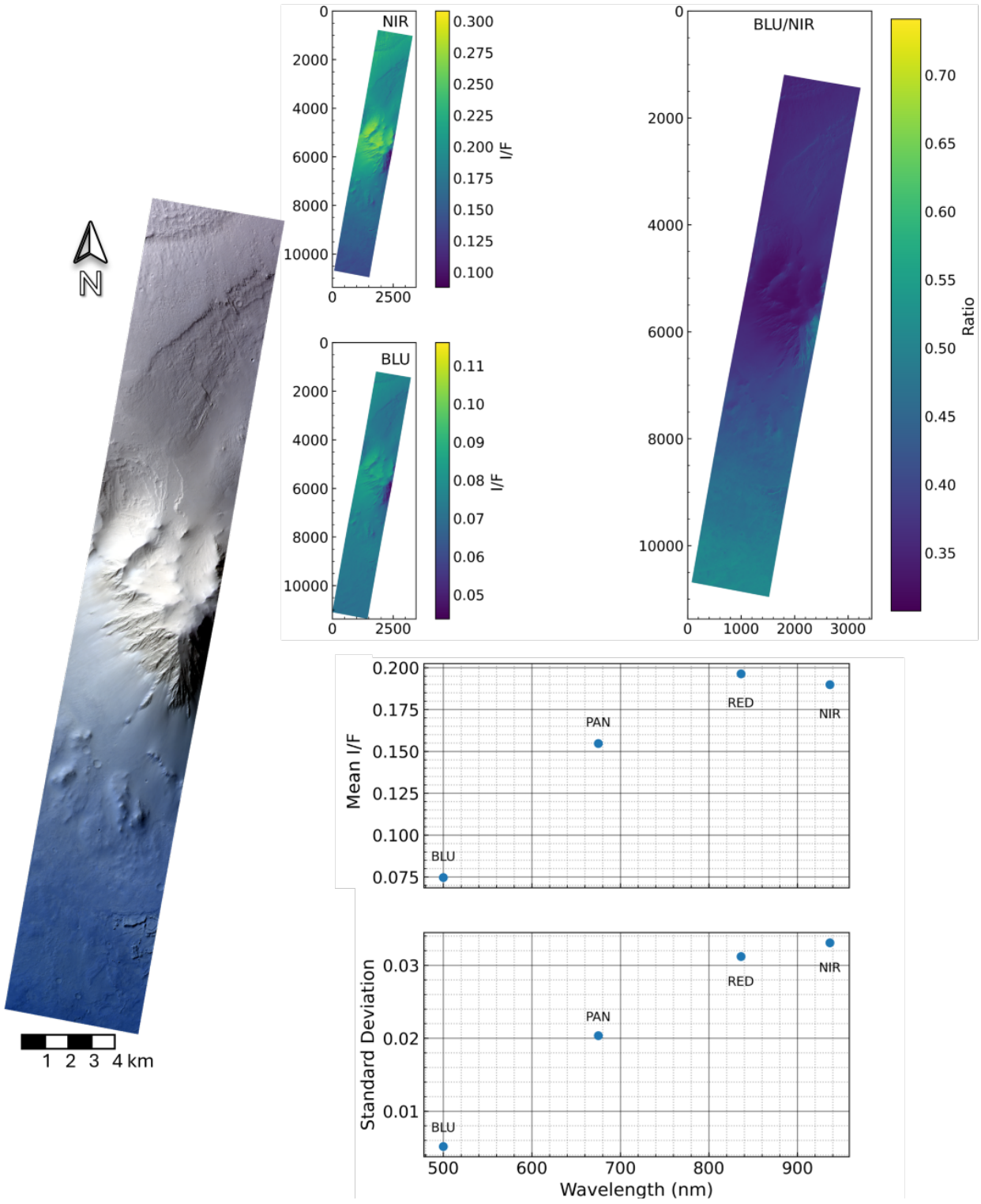


Figure B7: Left: the NPB image of MY38_034297_353_0. Upper right: the I/F across the NIR and BLU channels and the ratio of the BLU to NIR channel. Lower right: Mean I/F and standard deviation for each channel over the whole image.

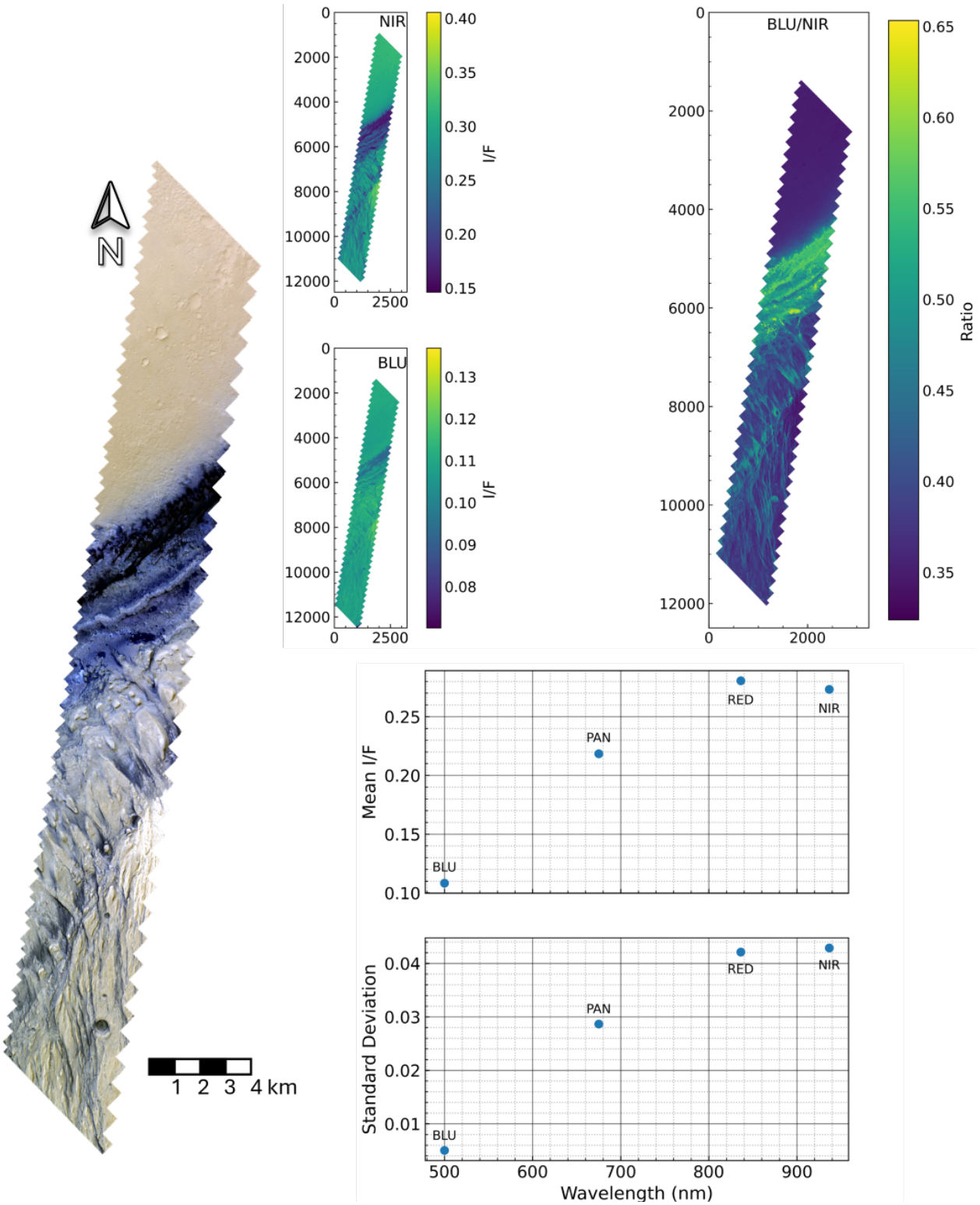


Figure B8: Left: the NPB image of MY38_034409_354_0. Upper right: the I/F across the NIR and BLU channels and the ratio of the BLU to NIR channel. Lower right: Mean I/F and standard deviation for each channel over the whole image.

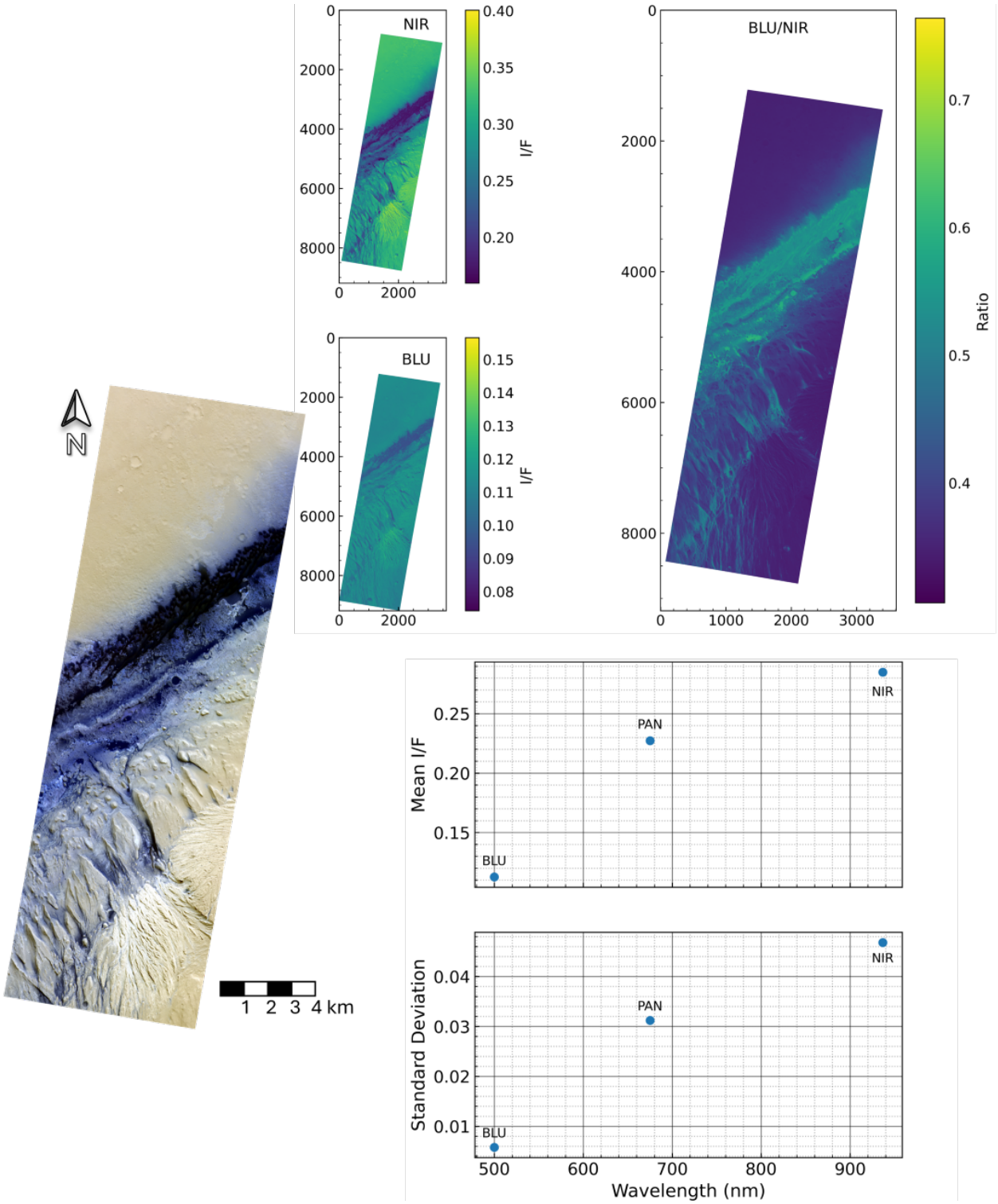


Figure B9: Left: the NPB image of MY38_034521_354_1, the first of a stereo pair with B10. Upper right: the I/F across the NIR and BLU channels and the ratio of the BLU to NIR channel. Lower right: Mean I/F and standard deviation for each channel over the whole image.

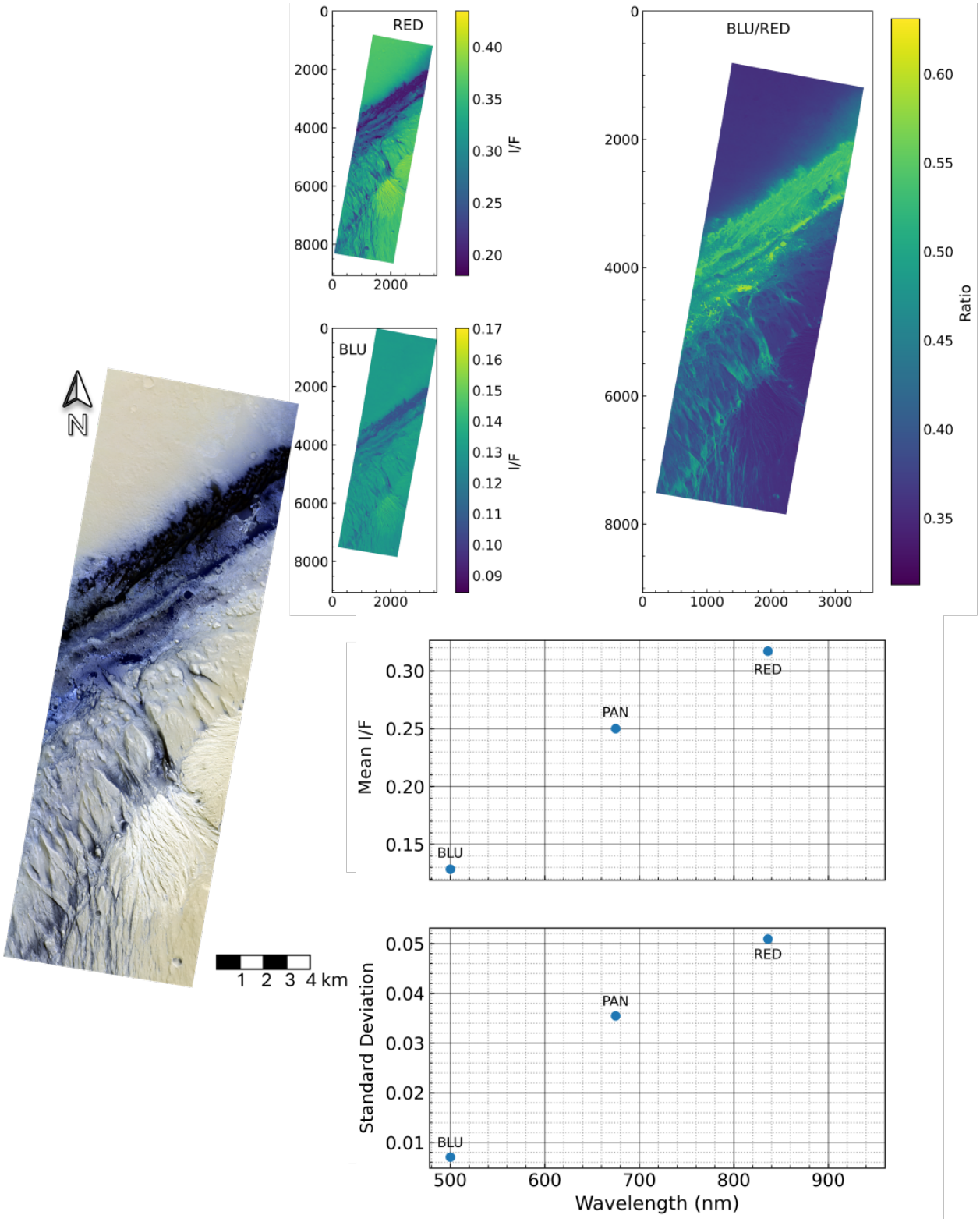


Figure B10: Left: the RPB image of MY38_034521_354_2, the second of a stereo pair with B9. Upper right: the I/F across the RED and BLU channels and the ratio of the BLU to RED channel. Lower right: Mean I/F and standard deviation for each channel over the whole image.

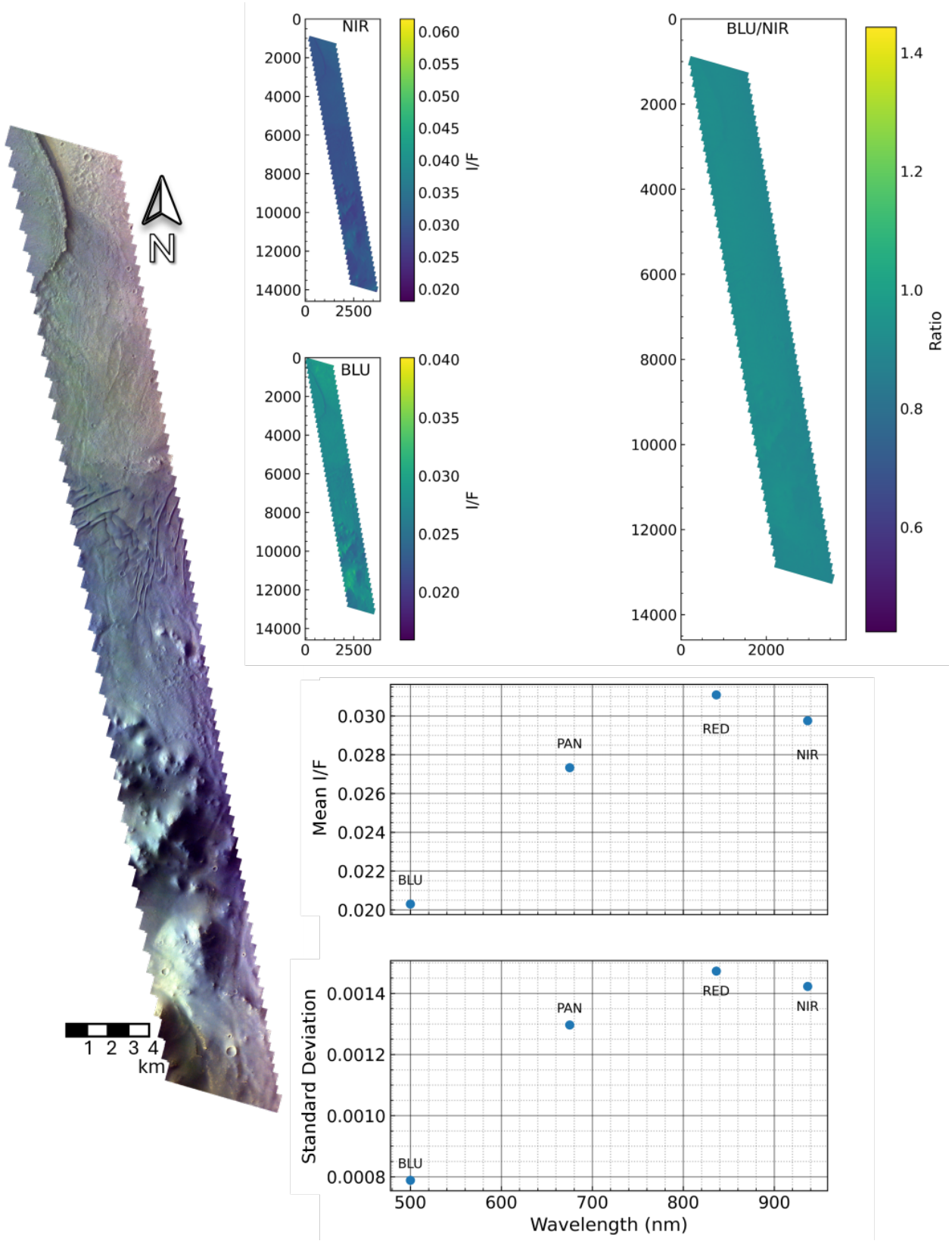


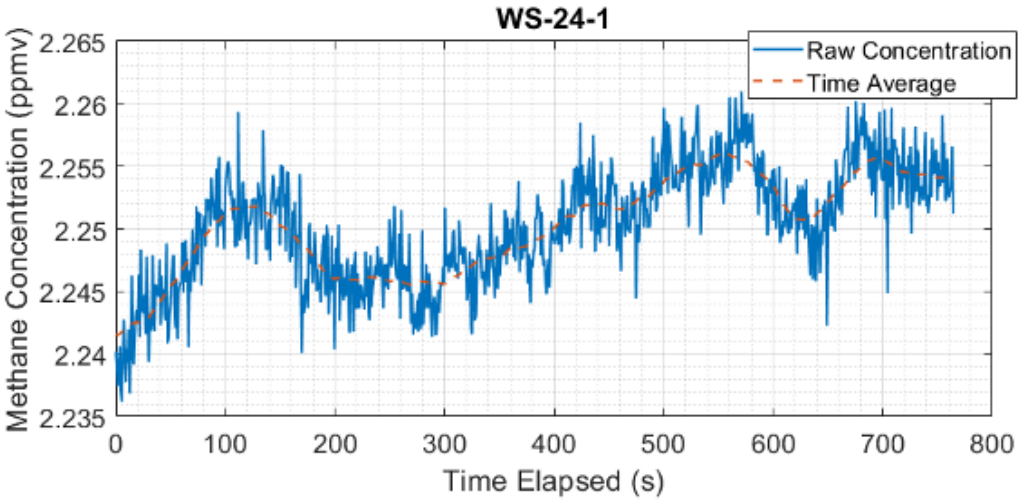
Figure B11: Left: the NPB image of MY38_034901_190_0. Upper right: the I/F across the NIR and BLU channels and the ratio of the BLU to NIR channel. Lower right: Mean I/F and standard deviation for each channel over the whole image.

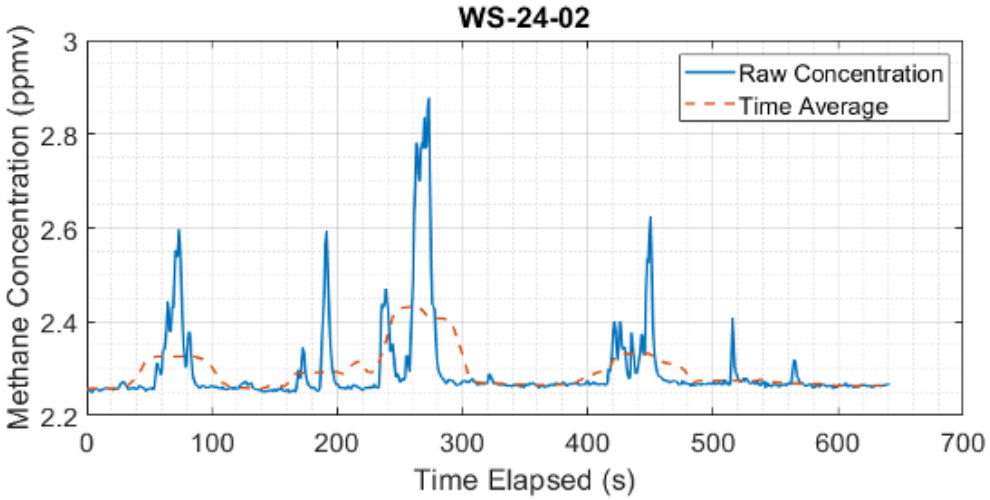
Appendix C

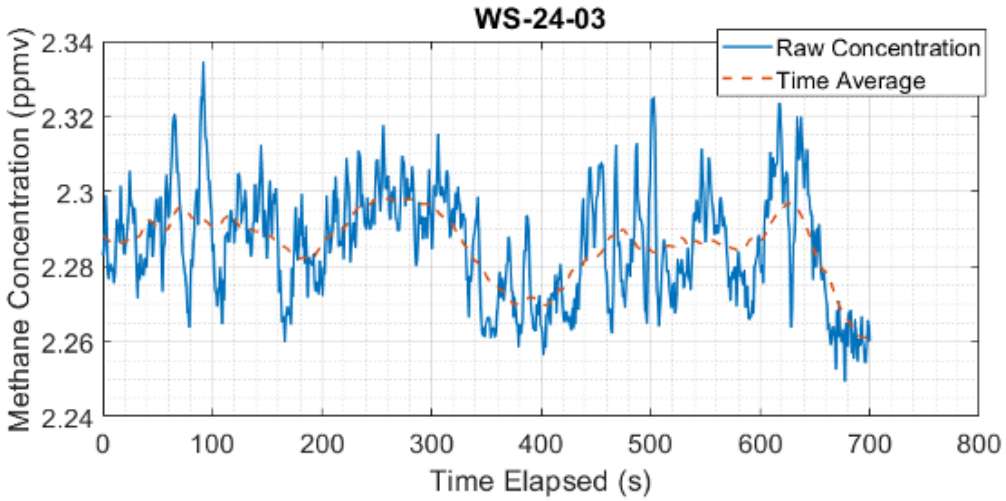
Methane Concentration at Wolf Spring in 2024

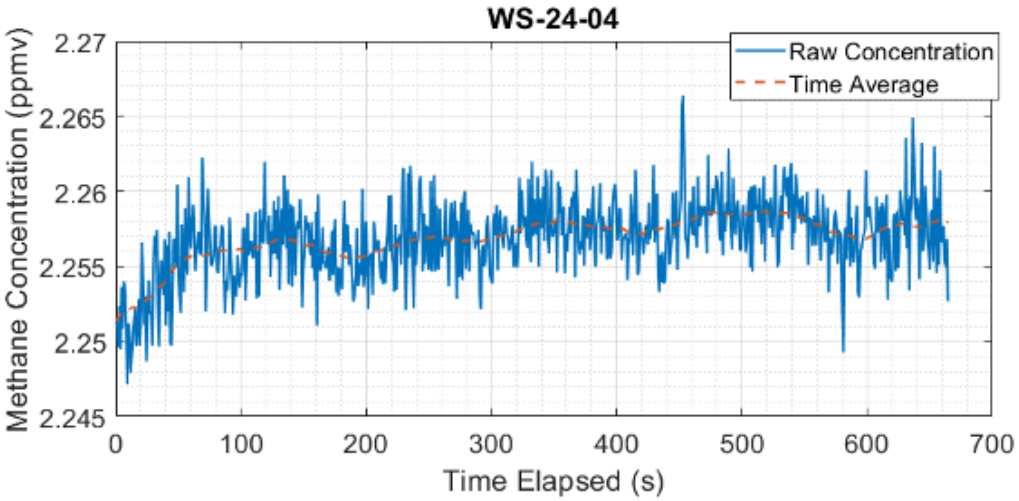
The concentration time series for each measurement acquired in 2024 at Wolf Spring are given below. The measurements are summarised in Section 6.3.3, Table 6.5. A running average with a window size of one minute is plotted alongside the raw concentration. Note the different axes for each figure.

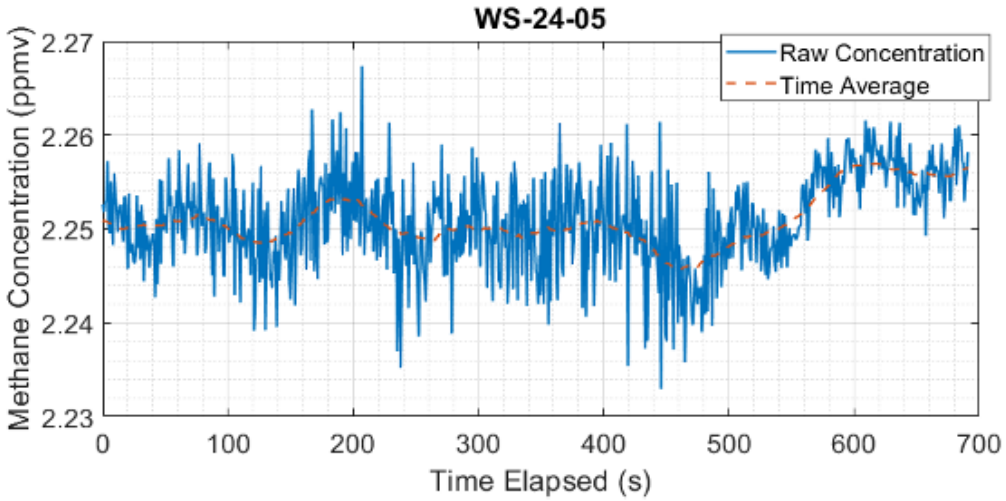
This appendix is reproduced from the supplementary material from Innanen et al. (2025b). All figures and text were generated by me.

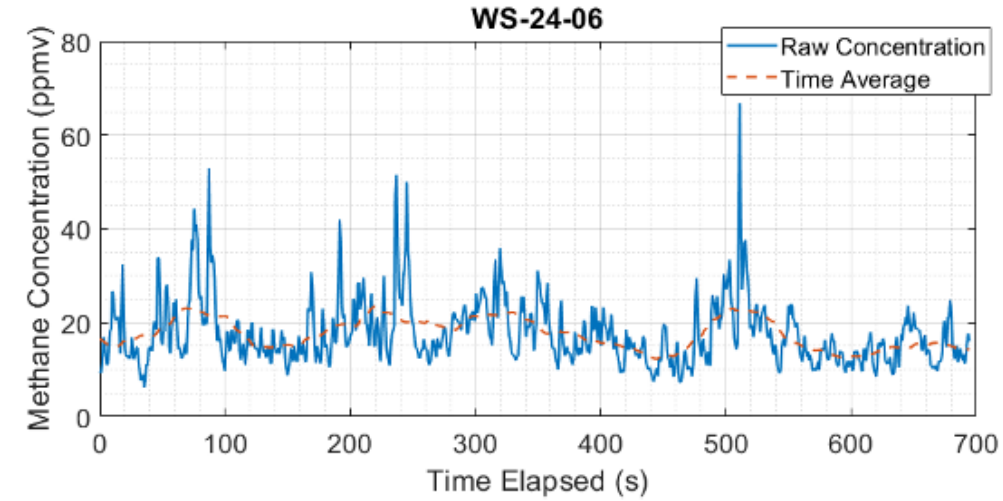


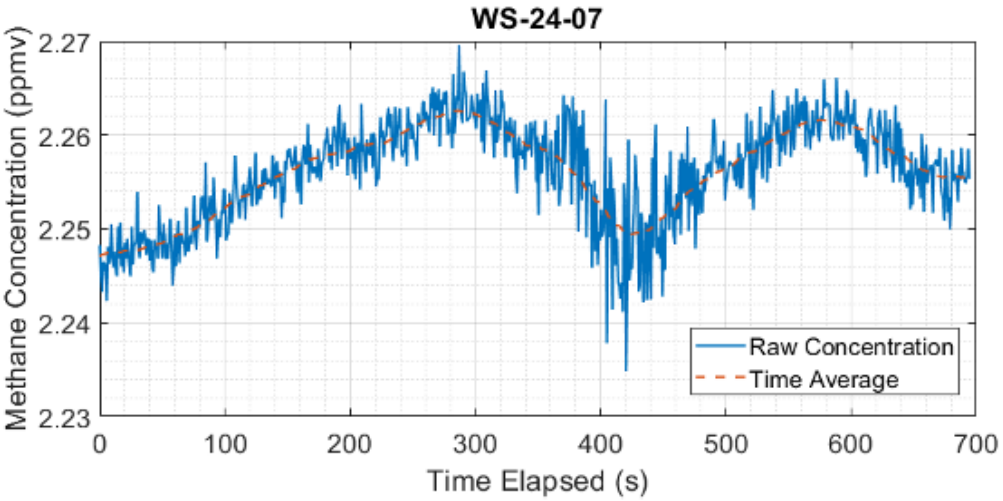


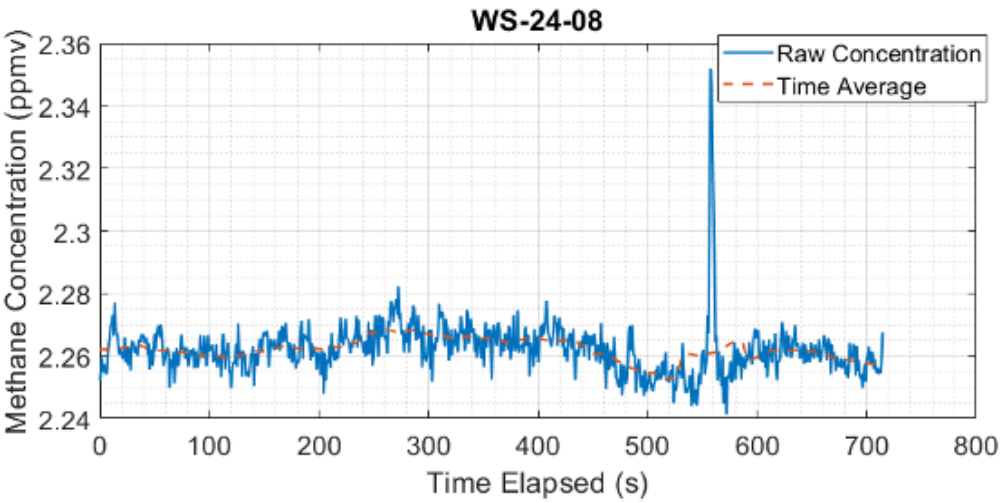

WS-24-03
Raw Concentration
Time Average
Methane Concentration (ppmv)
2.34
2.32
2.3
2.28
2.26
2.24
0
100
200
300
400
500
600
700
800
Time Elapsed (s)

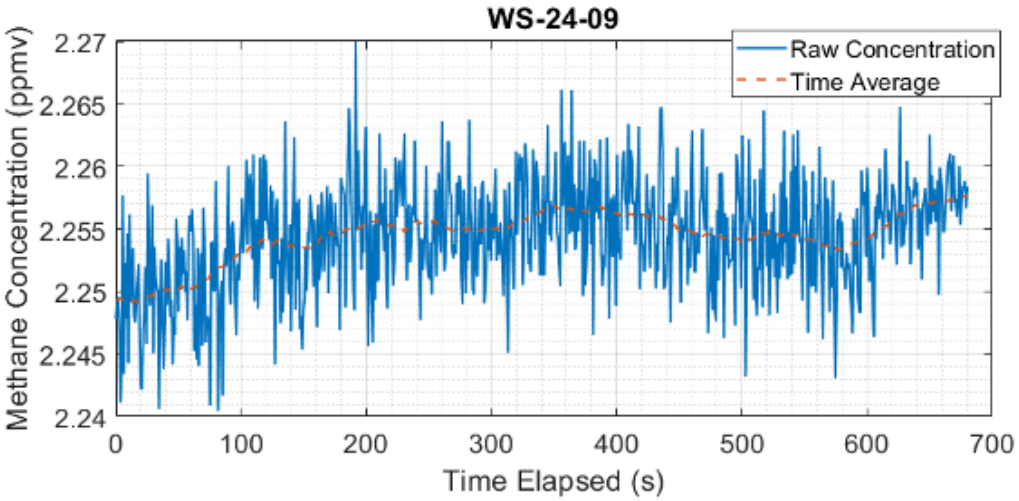

WS-24-04
Raw Concentration
Time Average
Methane Concentration (ppmv)
2.27
2.265
2.26
2.255
2.25
2.245
0
100
200
300
400
500
600
700
Time Elapsed (s)

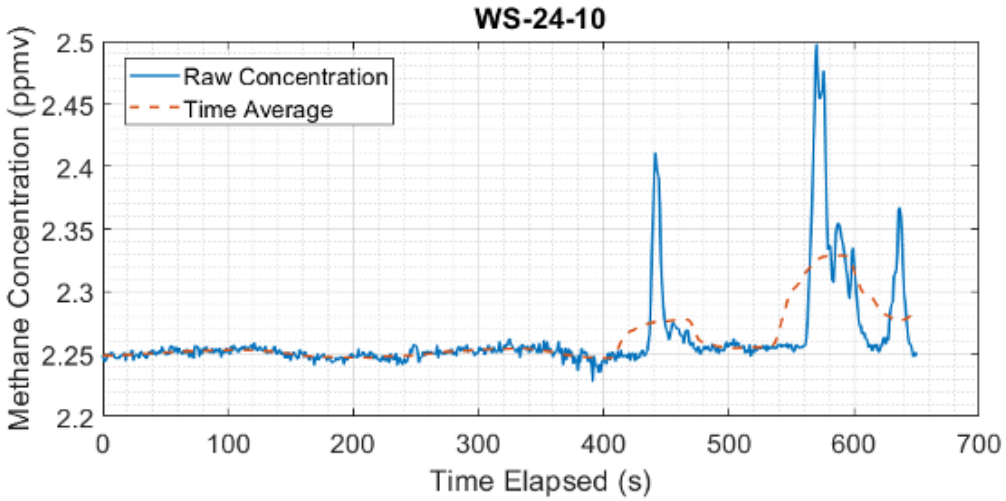

WS-24-05
Raw Concentration
Time Average
Methane Concentration (ppmv)
2.27
2.26
2.25
2.24
2.23
0
100
200
300
400
500
600
700
Time Elapsed (s)

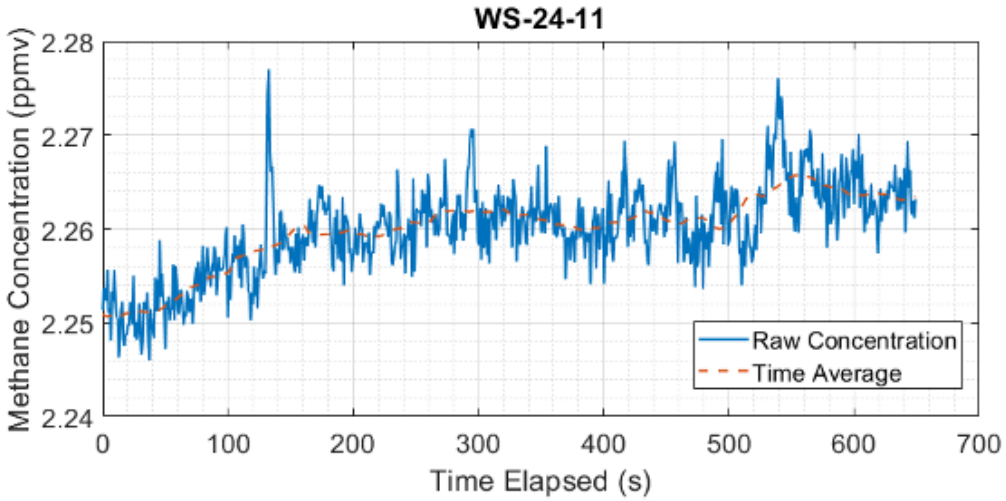

WS-24-06
Raw Concentration
Time Average
Methane Concentration (ppmv)
Time Elapsed (s)
0
20
40
60
80
0
100
200
300
400
500
600
700

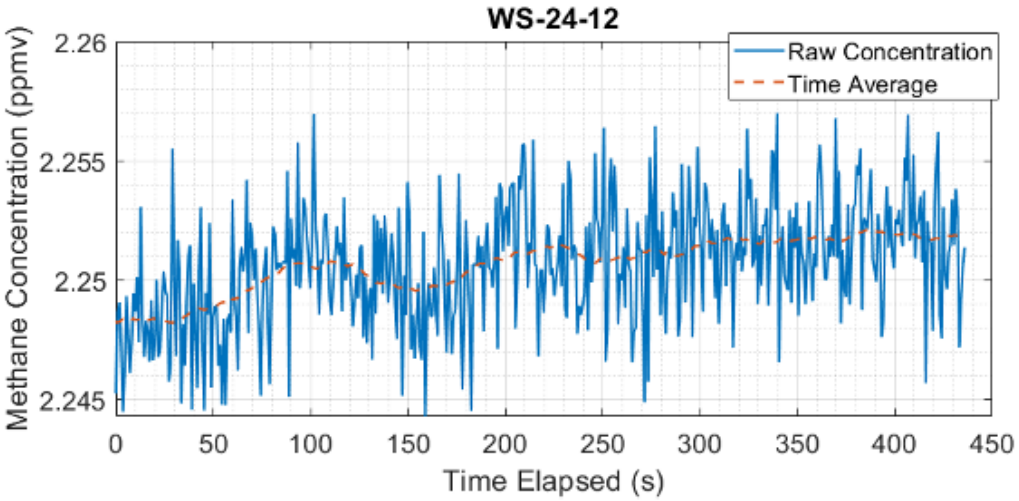

WS-24-07
Raw Concentration
Time Average
Methane Concentration (ppmv)
Time Elapsed (s)
2.23
2.24
2.25
2.26
2.27
0
100
200
300
400
500
600
700

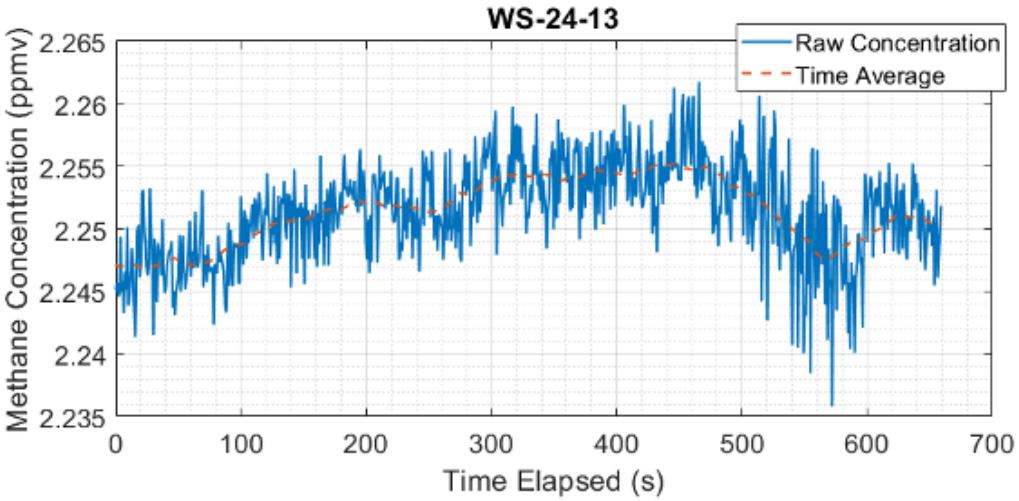

WS-24-08
Raw Concentration
Time Average
Methane Concentration (ppmv)
Time Elapsed (s)
2.24
2.26
2.28
2.3
2.32
2.34
2.36
0
100
200
300
400
500
600
700
800

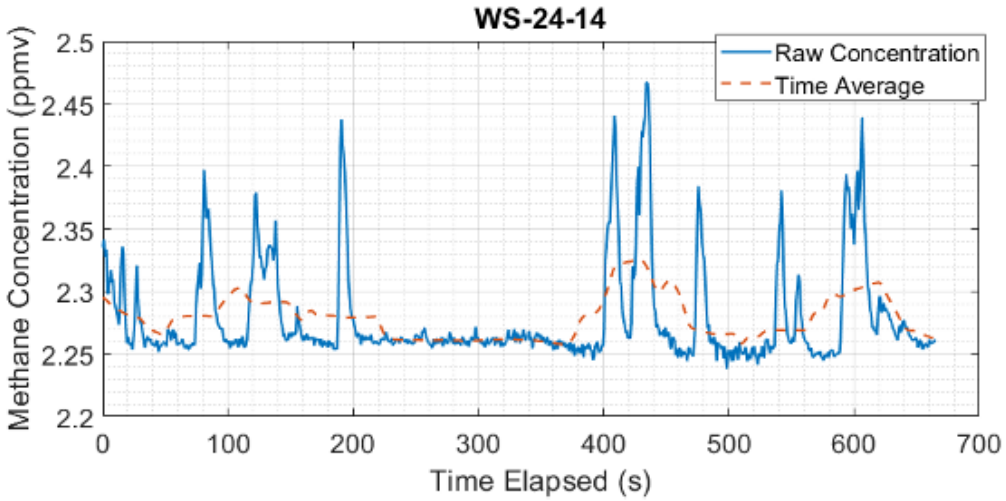

WS-24-09
Raw Concentration
Time Average
Methane Concentration (ppmv)
2.27
2.265
2.26
2.255
2.25
2.245
2.24
0
100
200
300
400
500
600
700
Time Elapsed (s)


WS-24-10
Raw Concentration
Time Average
Methane Concentration (ppmv)
2.5
2.45
2.4
2.35
2.3
2.25
2.2
0
100
200
300
400
500
600
700
Time Elapsed (s)


WS-24-11
Raw Concentration
Time Average
Methane Concentration (ppmv)
2.28
2.27
2.26
2.25
2.24
0
100
200
300
400
500
600
700
Time Elapsed (s)


WS-24-12
Raw Concentration
Time Average
Methane Concentration (ppmv)
2.26
2.255
2.25
2.245
0
50
100
150
200
250
300
350
400
450
Time Elapsed (s)


WS-24-13
Raw Concentration
Time Average
Methane Concentration (ppmv)
2.265
2.26
2.255
2.25
2.245
2.24
2.235
0
100
200
300
400
500
600
700
Time Elapsed (s)


WS-24-14
Raw Concentration
Time Average
Methane Concentration (ppmv)
2.5
2.45
2.4
2.35
2.3
2.25
2.2
0
100
200
300
400
500
600
700
Time Elapsed (s)

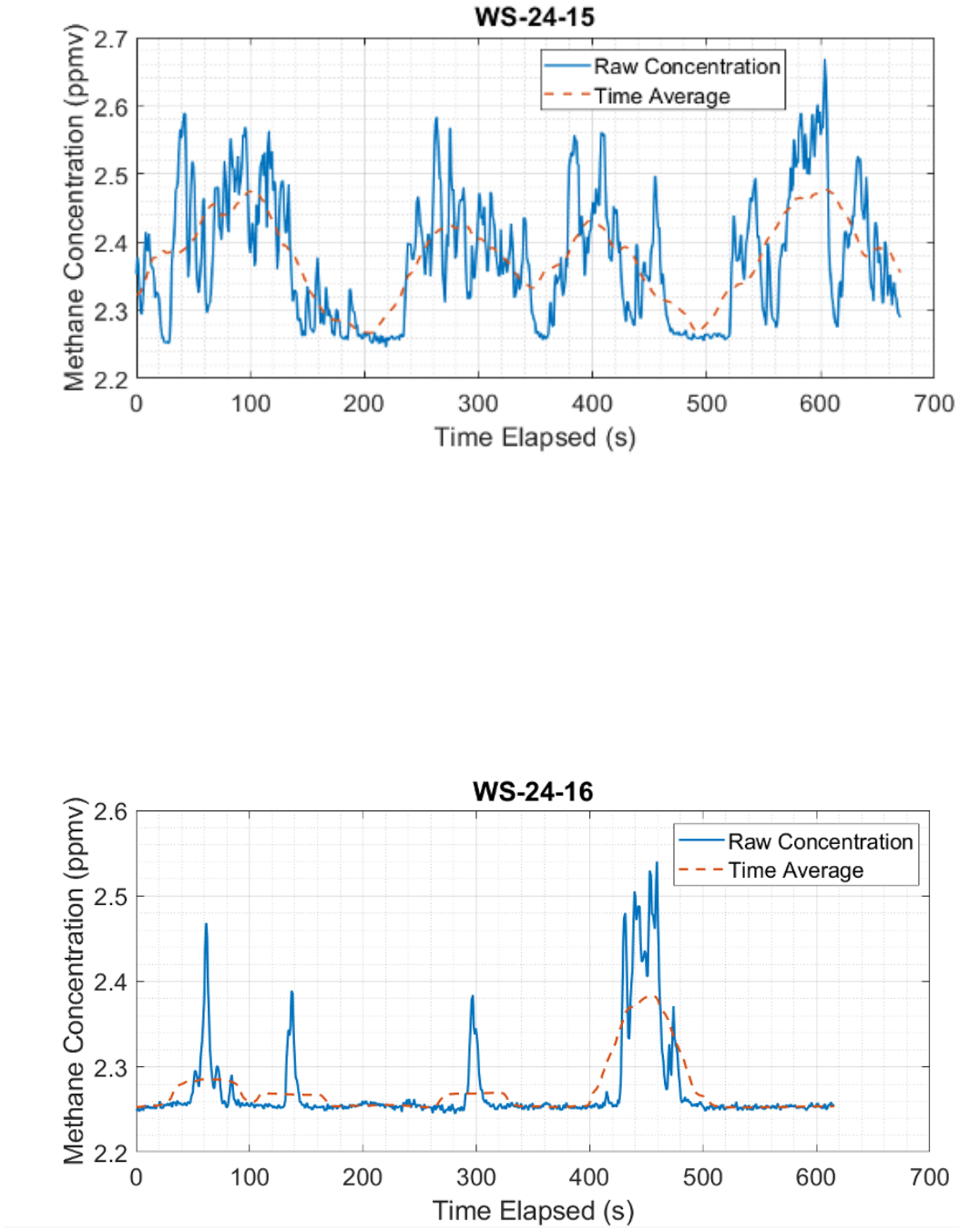


Figure C1: Measured methane concentrations at Wolf Spring acquired in 2024.